UNIVERSIDADE ESTADUAL DE CAMPINAS
Faculdade de Engenharia Mecânica

CAIO HENRIQUE RUFINO

Conceptual study of an internal combustion engine with adjustable cubic capacity and compression ratio

Estudo conceitual de um motor com cilindrada e taxa de compressão ajustáveis

CAMPINAS
2020

CAIO HENRIQUE RUFINO

Conceptual study of an internal combustion engine with adjustable cubic capacity and compression ratio

Estudo conceitual de um motor com cilindrada e taxa de compressão ajustáveis

Thesis presented to the School of Mechanical Engineering of the University of Campinas in partial fulfillment of the requirements for the degree of Doctor, in Mechanical Engineering, the field of Solid mechanics and Mechanical project.

Tese apresentada à Faculdade de Engenharia Mecânica da Universidade Estadual de Campinas como parte dos requisitos exigidos para a obtenção do título de Doutor em Engenharia Mecânica, na Área de Mecânica dos sólidos e Projeto Mecânico.

Supervisor: Prof. Dr. Janito Vaqueiro Ferreira

ESTE EXEMPLAR CORRESPONDE À VERSÃO FINAL DA TESE DEFENDIDA PELO ALUNO CAIO HENRIQUE RUFINO, E ORIENTADA PELO PROF. DR. JANITO VAQUEIRO FERREIRA.

CAMPINAS

2020

Ficha catalográfica
Universidade Estadual de Campinas
Biblioteca da Área de Engenharia e Arquitetura
Luciana Pietrosanto Milla - CRB 8/8129

R839c

Rufino, Caio Henrique, 1993-
Conceptual study of an internal combustion engine with adjustable cubic capacity and compression ratio / Caio Henrique Rufino. – Campinas, SP : [s.n.], 2020.

Orientador: Janito Vaqueiro Ferreira.
Tese (doutorado) – Universidade Estadual de Campinas, Faculdade de Engenharia Mecânica.

1. Motores de combustão interna - Termodinâmica. 2. Motores de combustão interna - Modelos matemáticos. 3. Motores a álcool. I. Ferreira, Janito Vaqueiro, 1961-. II. Universidade Estadual de Campinas. Faculdade de Engenharia Mecânica. III. Título.

Informações para Biblioteca Digital

Título em outro idioma: Estudo conceitual de um motor com cilindrada e taxa de compressão ajustáveis
Palavras-chave em inglês:
Internal combustion engines - Thermodynamics
Internal combustion engines - Mathematical modelling
Alcohol fuelled engines
Área de concentração: Mecânica dos Sólidos e Projeto Mecânico
Titulação: Doutor em Engenharia Mecânica
Banca examinadora:
Janito Vaqueiro Ferreira [Orientador]
Rogerio Gonçalves dos Santos
Carlos Eduardo Keutenedjian Mady
José Antonio Andrés Velásquez Alegre
José Eduardo Mautone Barros
Data de defesa: 19-02-2020
Programa de Pós-Graduação: Engenharia Mecânica

Identificação e informações acadêmicas do(a) aluno(a)
- ORCID do autor: https://orcid.org/0000-0002-4564-5377
- Currículo Lattes do autor: http://lattes.cnpq.br/8526204483675376

UNIVERSIDADE ESTADUAL DE CAMPINAS
FACULDADE DE ENGENHARIA MECÂNICA

TESE DE DOUTORADO

Conceptual study of an internal combustion engine with adjustable cubic capacity and compression ratio

Estudo conceitual de um motor com cilindrada e taxa de compressão ajustáveis

Autor: Caio Henrique Rufino.

Orientador: Prof. Dr. Janito Vaqueiro Ferreira

A Banca Examinadora composta pelos membros abaixo aprovou esta Tese:

Prof. Dr. Janito Vaqueiro Ferreira, Presidente
DMC/FEM/UNICAMP

Prof. Dr. Rogerio Gonçalves dos Santos
DE/FEM/UNICAMP

Prof. Dr. Carlos Eduardo Keutenedjian Mady
DE/FEM/UNICAMP

Prof. Dr. José Antonio Andrés Velásquez Alegre
DAMEC/UTFPR

Prof. Dr. José Eduardo Mautone Barros
DEMEC/UFMG

A Ata de defesa com as respectivas assinaturas dos membros encontra–se no processo de vida acadêmica do aluno.

Campinas, 19 de fevereiro de 2020.

Agradecimentos

Este trabalho não poderia ser concluído sem a ajuda das seguintes pessoas e instituições, às quais expresso o meu agradecimento:

Ao Conselho Nacional de Pesquisa (CNPq), pela oportunidade concedida através do programa de Iniciação Científica PIBIC, que gerou o embrião deste trabalho.

À Fundação de Amparo à Pesquisa do Estado de São Paulo (FAPESP), pelo apoio através do processo No. 2018/18859-1.

À PSA Peugeot Citroën, pelo apoio financeiro ao Laboratório de Motores Biocombustíveis.

Ao prof. Clayton do Instituto Mauá de Tecnologia, pelo aprendizado com a parte experimental e os experimentaos realizados.

Aos colegas de laboratório dos tempos de iniciação científica: André Bosso, Gustavo Santos Lopes e Nelson Cró pela aprendizagem e ajuda.

Aos colegas do Laboratório de Motores Biocombustíveis (LMB): Ana Paula, Alessandro, Felipe, Jair e Fazal pelo trabalho em conjunto.

Às pessoas que não estão relacionadas ao projeto que desenvolvi, mas me acompanharam nesta fase da minha vida: minhas professoras e colegas do Conservatório de Salto por terem me ajudado a me reencontrar na música. Também aos colegas da equipe de espaçomodelismo Antares, pelo companheirismo e pelo desenvolvimento de projetos, trazendo aprendizados em múltiplos aspectos e boas risadas, seja nos horários de oficina ou em sessões de D&D.

À Beatriz pela ajuda, orientação e conselhos com relação aos aspectos financeiros e administrativos do projeto.

À Beth, pela paciência, carinho e apoio desde o meu ingresso na Unicamp em 2011.

Ao prof. Gallo, pela coordenação do grupo e por possibilitar o LMB crescer como uma equipe.

Ao prof. Janito Vaqueiro Ferreira pela orientação, pelo reconhecimento e investimento em meu trabalho desde o início de minha graduação.

Aos meus familiares pelo apoio desde o princípio.

“The answer is 42.”

Answer to the Ultimate Question of Life, the Universe, and Everything.

Resumo

Motores de combustão interna ainda possuem um longo futuro no setor de transportes por apresentar grandes vantagens em termos de autonomia, preço e peso em comparação à suas tecnologias concorrentes. Além disso, o uso desses motores pode ser estendido devido a novos avanços tecnológicos, trazendo melhorias em eficiência e emissões, somados à possibilidade de operar com combustíveis de origem renovável, o que reduziria consideravelmente a emissão de gases efeito estufa.

Com esta motivação uma solução é proposta com o objetivo de permitir maior flexibilidade a um motor de ignição por centelha. A solução inovativa consiste de um mecanismo *multi–link* que permite o controle sobre a cinemática do pistão, e com este controle torna–se possível ajustar razão de compressão e cilindrada. O objetivo deste estudo é apresentar os resultados preliminares obtidos através de simulações, indicando os ganhos da implementação da solução proposta. Para realizar este estudo, primeiramente foi desenvolvido um modelo cinemático do mecanismo. O modelo cinemático foi então incorporado a um modelo termodinâmico de simulação, denominado modelo preditivo. Este modelo termodinâmico consiste em um modelo fenomenológico de duas zonas de combustão, o qual permite prever o desempenho do motor e também prever a ocorrência da detonação. Para verificar a acurácia do modelo de simulação, um diagnóstico de combustão foi executado em dados experimentais obtidos de um motor comercial. O diagnóstico forneceu dados fundamentais para o entendimento do comportamento da combustão em relação a diversos parâmetros do motor, tais como avanço, carga, rotação e razão ar–combustível. Os dados obtidos no diagnóstico de combustão foram utilizados na modelagem da combustão, implementada no modelo preditivo. Após a implementação do modelo de combustão, o modelo preditivo pôde ser validado comparando resultados obtidos na simulação com os resultados experimentais obtidos do motor comercial ensaiado em bancada. Com o modelo de simulação validado, uma calibração baseada em simulação foi realizada para o motor proposto operando com etanol em condição estequiométrica, indicando a combinação ótima de pressão no coletor de admissão, cilindrada, razão de compressão e avanço com o objetivo de maximizar eficiência térmica indicada do motor.

Resultados indicaram que a principal vantagem em se controlar a razão de compressão fica evidente em médias e altas rotações, condições em que a detonação não é crítica. Um motor convencional com razão de compressão fixa opera com baixa eficiência devido à sua razão de compressão fixada nas condições críticas para a detonação enquanto um motor com razão de compressão variável pode sempre operar com a razão de compressão ótima. As vantagens de se controlar cilindrada ficam mais evidentes em condições de carga parcial, nas quais as perdas por bombeamento devido ao fechamento da válvula borboleta são mitigadas pela redução na cilindrada. Combinando o controle de razão de compressão e cilindrada, foi

possível obter até 20% de ganho em eficiência em cargas plenas e alta rotação e um ganho entre 10% e 20% de eficiência em condições de cargas parciais.

Palavras–chave: Motor de ignição por centelha; razão de compressão variável; Deslocamento variável; etanol.

Abstract

Internal combustion engines still possess a long future in the transportation sector as they present significant advantages in terms of mileage, costs and mass as compared to their competitor technologies. Besides, the use of those engines can be extended owing to new technological advances, bringing improvements in efficiency and pollutant emissions, adding to the possibility of operating with fuels from renewable sources, considerably reducing the emission of greenhouse effect gases.

Given this motivation, a solution is proposed, with the objective of permitting higher flexibility for a spark–ignition engine. The innovative solution presented here consists of a multi–link mechanism, which allows the control on the piston kinematics, thus adjusting compression ratio and cubic capacity. The objective of this study is to present preliminary results obtained by simulations, indicating the gains of implementing the proposed solution. To perform the study, a kinematic model of the mechanism was firstly developed. The kinematic model was then incorporated to a thermodynamic model for simulation, known as the predictive model. This model consists of a phenomenological model of two–zones of combustion, which predicts the engine performance and knock onset. To ensure model accuracy, a combustion diagnosis was performed on experimental data obtained from a commercial engine. The diagnosis provided fundamental data for the understanding of combustion behaviour related to diverse engine parameters such as spark timing, load, engine speed, and air–fuel ratio. Additionally, a comparison between ethanol and gasoline was performed as a mean to indicate the differences between both fuels. The data obtained from the combustion diagnosis were used in the combustion modelling, implemented in the predictive model. After the implementation of the combustion model, the predictive model was validated by comparing results obtained from the simulation for the commercial engine using data obtained from the bench tests. With the validated simulation model, a calibration based on simulation was performed for the proposed engine operating with ethanol at stoichiometric condition in order to indicate the optimal combination of intake manifold pressure, cubic capacity, compression ratio, and spark timing with the objective of maximising indicated thermal efficiency for the engine.

Results demonstrated that the main advantage of controlling compression ratio becomes evident at medium to high engine speeds, conditions at which the knock onset is not critical. A conventional engine with fixed compression ratio operates with low compression ratio as its compression ratio is fixed because of the critical conditions for knock onset whereas a variable compression ratio engine can operate with an optimal compression ratio in all conditions. The advantages of controlling cubic capacity become more evident for partial load conditions, at which the pump losses caused by throttling are mitigated by the reduced cubic capacity. By combining the control of compression ratio and cubic capacity, it was possible to

obtain up to 20% of efficiency increase for full load conditions and high engine speed as also an increase in efficiency between 10% and 20% for partial load conditions.

Keywords: Spark ignition engine; variable compression ratio; variable stroke engine; ethanol.

List of Figures

List of Tables

Nomenclature

Latin letters

$\bar{c}_p$	Specific heat at constant pressure in molar basis
$\bar{R}$	Universal constant of gases
$\ddot{\vec{w}}$	Acceleration vector
$\dot{\vec{w}}$	Velocity vector
$\dot{m}$	Mass flow
$\dot{W}$	Power
$\mathcal{T}$	Torque
$\mathcal{X}, \mathcal{Y}$	Arbitrary parameters
$\vec{w}$	Position vector
A	Area
a	Constant for interpolation
A_K	Constant for knock prediction
A_p	Length of piston rod
B	Lever length
b	Constant for interpolation
B_K	Constant for knock prediction
C	Lever length
c	Constant for interpolation
C_D	Coefficient of discharge

c_p	Specific heat at constant pressure
c_v	Specific heat at constant volume
CC	Cubic capacity
CR	Compression ratio
D_c	Cylinder diameter
D_v	Valve diameter
f_m	Molar fraction
H	Extensive enthalpy
h	Intensive enthalpy
h^{HT}	Heat transfer coefficient
H_{comb}	Extensive combustion enthalpy
h_{comb}	Intensive combustion enthalpy
$imep$	Indicated mean effective pressure
J	Eccentricity of the piston
k	Specific heat ratio
K_I	Knock index
L	Constant for calculation of SOC
L_{cr}	Connecting rod length
M	Molecular weight
m	Mass
N	Engine speed
n	Form factor
n_K	Constant for knock prediction
ON	Octane number
P	Pressure

P^*	Non-dimensional Pressure
Q	Heat interaction
R	Gas constant
R_{cs}	Crank length
T	Temperature
t	Time
U	Internal energy
V	Volume
v	Specific volume
v_m	Mean velocity of the piston
W	Work interaction
W_h	Horizontal position of the pivot
W_v	Vertical position of the pivot
x	Volumetric fraction
x_b	Mass fraction burn
Y	Valve lift
y	Mass fraction

Greek letters

α	Angle of Lever
$\Delta\theta_b$	Combustion duration
η	Efficiency
η_r	Maximum mass fraction burn
γ	Angle of Connecting rod
λ	Relative air–fuel ratio
ν	Gas velocity

ω	Angular velocity
ϕ	Arbitrary property
ρ	Density
τ	Auto ignition delay
θ	Crank position
θ_o	SOC
	Subscripts and superscripts
10	10% of MFB
50	50% of MFB
90	90% of MFB
adm	Admitted
atm	Atmospheric
b	Burned
CD	Combustion duration
$comb$	Combustion
$cycle$	Engine cycle
ds	Downstream
em	Exhaust manifold
et	Ethanol
ex	Exhaust
$fuel$	Fuel
i, j	Arbitrary indexes
im	Intake manifold
in	Intake
iso	Isoentropic flow

max Maximum

min Minimum

P Pressure

p Combustion products

r Reactants

$real$ Real flow

sat Saturation

T Temperature

u Unburned

us Upstream

v Valve

w Cylinder wall

x X component

y Y component

Acronyms

$aTDC$ After top dead centre

BDC Bottom dead centre

CA Crank Angle

CI Compression Ignition

ECU Electronic Control Unit

EOC End of combustion

EVC Exhaust valve closing

EVO Exhaust valve opening

FCR Fixed compression ratio engine

GHG Green House Gases

ICE Internal Combustion Engine

IVC Intake valve closing

IVO Intake valve opening

MAP Manifold Absolute Pressure

MFB Mass Fraction Burn

SI Spark Igntion

SOC Start of combustion

TDC Top dead centre

VCR Variable compression ratio engine

VSE Variable stroke engine

Contents

1. Introduction

1.1 Motivation

Internal combustion engines (ICE) are widely used in many sectors from transportation to electrical power generation. Owing to high energy capacity of fuels, ICEs are currently the unique solution for freighting, agricultural machines, naval transportation, aviation and electricity production. Nevertheless, the use of ICE has been pondered as most of it is dependent on fossil fuels, collaborating to the emission of greenhouse gases (GHG). Thus the electric vehicles have recently gained territory in the automotive market. However, electric vehicles still present many challenges in their development such as technological challenges: battery recycling and mileage. Moreover, there are strategical challenges regarding the implementation of electric vehicles, as the electrification consists itself in changing the source of power from a local power plant, installed in the vehicle, to the electric power plants. Thus, the electric generation system must be improved in order to supply the new demand on electricity by electric cars. Consequently, the complete electrification of the vehicles fleet only makes sense as means for mitigating GHG emission if the electricity generation process becomes utterly independent of fossil fuels. In conclusion, an universal solution for a sustainable automotive fleet does not exist. Therefore, there is a demand on the development of multiple technologies and their combination, resulting in hybrid systems and more flexible vehicles, which are capable of operating with electricity and/or diverse renewable fuels according to the fuel or electricity availability of each locality.

The illustration of propulsion system composition is presented in Figure 1.1. Researchers from the MIT foresee that almost 80% of the vehicles to be sold by 2050 will still be equipped with an ICE (AKERLIND *et al.*, 2015).

Discussions and concerns regarding the effects of ICE on the environment can be tracked in the literature from the 1940's (HEYWOOD, 1988). Firstly, health concerns have motivated the development of more efficient engines emitting lower levels of pollutants. Many efforts have been invested in engine development and great advances were accomplished, *e.g.*,

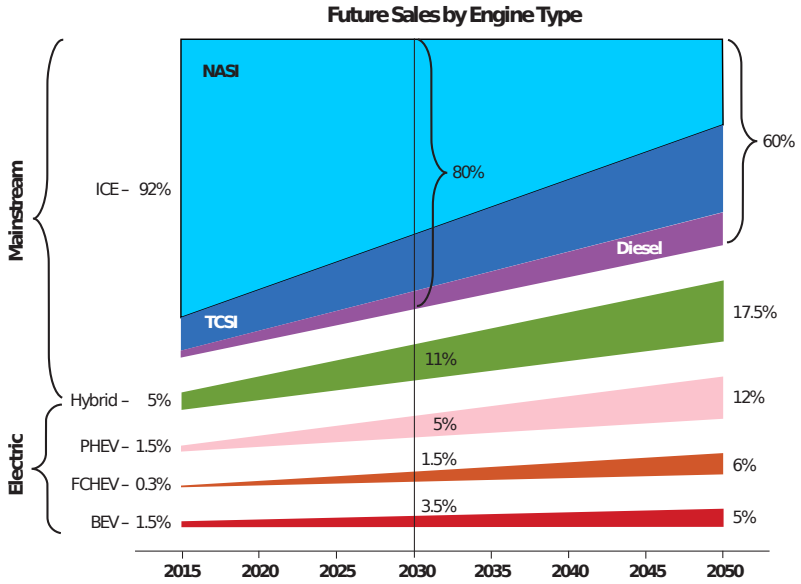

Figure 1.1: Prediction for propulsion of the vehicles to be sold. Source: AKERLIND *et al.* (2015).

the development of the Electronic Control Unit (ECU) and more recently, the control over components and actuations which were fixed until short time ago, such as valve timing, compression ratio, and the direct injection of fuel. These technologies have improved significantly the emission of pollutants, such as carbon monoxide, nitric oxides, hydrocarbons, and particulate matter thus enabling to meet the demands of policies, such as the Corporative Average Fuel Economy from the Environment Protection Agency from USA, the Euro Standards, and the Brazilian Proconve.

Although reducing pollutant emission is still one objective of the automotive industry, the focus of engine research has change to the emission of GHG nowadays. In order to reduce emission, the most obvious action is to cease the use of fossil fuels. MACLEAN and LAVE (2003) made an detailed review on the automotive propulsion systems. The major challenge in substituting fossil fuel based engines is the price. Many other alternatives are not profitable enough to dispute market with the gasoline or diesel fuelled engines. As industry develops products motivated by the profit of that product, the ICE fuelled by fossil fuel will continue to thrive, unless regulations and standards for GHG emission restrain the sales of gasoline or diesel engines. Both electric and biomass fuelled vehicles offer alternatives to fossil fuel driven vehicles. There is a distinction between battery electric vehicles (BEV) and hybrid electric vehicles (HEV), which still use an ICE coupled to an electric motor. This type of vehicle has the advantage of combining both electric and combustion systems, obtaining a greater driving range. On the other side, the BEV is much simpler than the HEV, with the disadvantage of low driving range. There is no universal answer for lowering GHG emission based only on electric vehicles or on biomass (MACLEAN and LAVE, 2003). The report published by AKERLIND *et al.* (2015) provide several recommendations for GHG emission mitigation.

Among those recommendations there is the change in transportation modes, the development of both alternative fuels and electric vehicles. Regarding the issue of competitiveness between technologies, AKERLIND *et al.* (2015) suggest the fossil fuel tax increasing for fossil. However, it is highlighted that the prices should be established not only based on the local emissions, but on the overall emission for each propulsion system. For example, most countries still posses an electric matrix based on fossil fuels. In those countries, vehicles fuelled by biomass would be a better alternative for mitigating GHG emission.

Biomass is considered to allow a "null" GHG emission because the carbon contained in its molecules are captured from the atmosphere by the process of photosynthesis. Although this affirmation is not strictly true since the production and processing of biomass involve the use of machines mainly fuelled by diesel, the potential of biomass for GHG mitigation is evident. In Brazil, the ethanol is the most promising biofuel. Its usage has begun in 1975 with the program Pró–Álcool as a substitute for gasoline. In 1993, anhydrous ethanol started being used as anti–knock agent in gasoline in Brazil. This blend has become known as gasohol later. In 2003, Brazilian automotive industries started producing the flex–fuel engines, allowing the use of gasohol, hydrous ethanol or a mixture of both in any proportion (BALAT and BALAT, 2009). Currently, Brazilian market for fuels offers E27, gasohol with 27% of anhydrous ethanol in volume, and E95h, hydrous ethanol with 5% of water in volume and flex–fuel engines have reached up to 90% of the vehicles sold until 2011 (BRINKMAN *et al.*, 2018).

The key issue of this type of engine is the fact that it is chiefly used in light duty vehicles (LDV). The development of engines for LDV represents a challenge for the automotive industry as an engine for this application is required to be capable of working efficiently in urban traffic conditions. The wide variability presented in the duty of the engine leads to the necessity of a machine capable of adapting itself to each condition of operation, such as speed, load, acceleration and deceleration and yet be capable of a quick cold start and stable idle operation. This issue is more clearly observed in flex–fuel engines. Ethanol has different characteristics from gasoline, having a higher heat of vaporisation, requiring a higher value of compression ratio, while the gasoline has a lower Octane Number (value related to the sensibility to auto-ignition), requiring a lower compression ratio. Consequently, flex–fuel engines often operate with less efficiency in both conditions, when fuelled with ethanol working at low compression ratio and when fuelled with gasoline by retarding the spark at knock condition that now happens under more operational conditions. Another strategy to be used would be a VCR engine. The VCR concept is based on the fact that it can continuously adjust to operate in the MBT (Maximum Brake Torque) condition, which depends not only on the spark advance but also on the compression ratio according to each load condition, speed, stoichiometry and characteristics of the fuel. By such means, there is no need to sacrifice efficiency by retarding the spark or adopting a low fixed compression ratio.

To the understanding of the researchers, the development of a more flexible engine is a direction to be explored in order to reduce fuel consumption. Also, flexible engines can attend the market trends on fuels and permitting the use of one type of engine in multiple locations, in which fuels may present different properties. Based on the Brazilian context, the Laboratory of Biofuel Engines of the University of Campinas has participated from 2015 to 2018 in the Professor Ernesto Urbano Stumpf Research Centre, an initiative from FAPESP and PSA Group for the development of biofuel engines. The Research Centre investigates many technological solutions for improving ethanol engine efficiency. Among the studied technologies, the theme of innovative solutions for controlling compression ratio motivated the conception of a proposal for the engine, which comprises a *multilink* mechanism that allows the real time, continuous control on both cubic capacity and compression ratio individually. This mechanism is denominated as Variable Stroke Engine (VSE) and its conceptual study is covered by the doctoral research presented in this Thesis.

1.2 The VSE mechanism

The redesign of the engine and its components consist in the challenge presented by the development of a VSE. SIEGLA and SIEWERT (1978) stated that a VSE ideally should provide the capacity to vary the stroke length without adding weight, volume, and mechanical losses due to friction. However, the design of a minimalist mechanism that allows the real–time control over piston's kinematics is not a trivial task. Any mechanism that seeks improvement towards controllability will present more complexity and a higher amount of components compared to the simple crank–rod mechanism used in conventional engines. Although the addition of components could look like a contradiction to the downsizing trend in the automotive industry, the increase of efficiency justifies the use of smaller engines, compensating their increase of components.

The mechanism proposed on FERREIRA and RUFINO (2014) adopts a lever connecting the piston to the crank–rod mechanism (Fig. 1.2). Differently from most VSE mechanisms, the proposed mechanism allows the independent control of cubic capacity and compression ratio. Additionally, these both parameters can be continuously adjusted in real time and individually for each cylinder, contrarily from many mechanisms described in the literature review, which can only achieve two levels of compression ratio or set the same compression ratio for all cylinders.

The addition of a lever modifies the kinematics of the piston. Many *multilink* mechanism cause this modification, altering velocity and acceleration of the piston around Top Dead Centre (TDC) and Bottom Dead Centre (BDC). However, there is no consensus in the literature on how the piston's kinematic affects the combustion. Hence, it is assumed that the kinematics

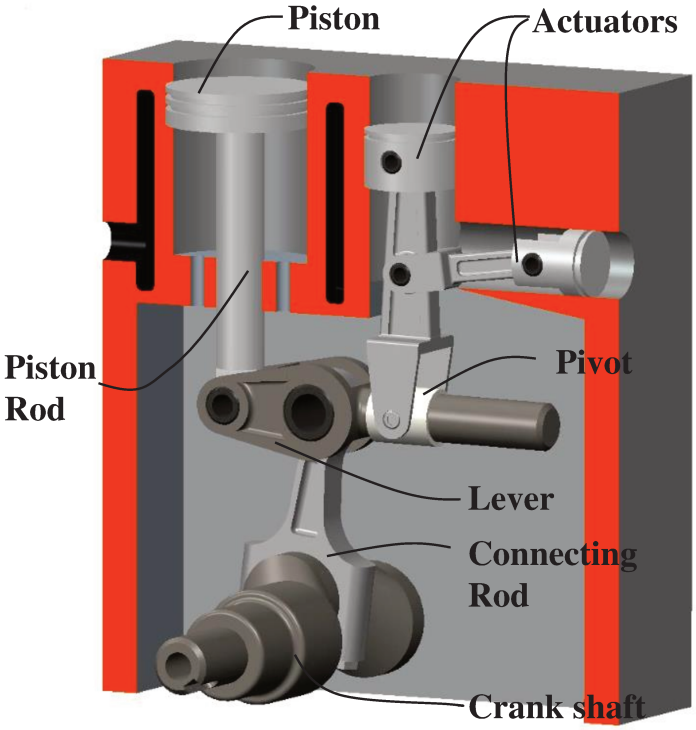

Figure 1.2: Conception of the mechanism.

of the proposed mechanism is desired to be similar to the conventional crank–rod mechanism. That hypothesis is taken since further evaluation on the effects of kinematics on the development of combustion would require a complex multidimensional simulation or experimental tests. The present work consists of a conceptual study with the objective of predicting the performance of such engine without considering further details on geometry and construction of the engine. Detailed studies on the influence of piston kinematics on charge motion will be comprehended in future works.

Note that there are two actuators to control horizontal and vertical displacement of the pivot, since the mechanism has three degrees of freedom. The arrangement illustrated in Figure 1.2 is only one possibility. It is highlighted that there are many forms of controlling the pivot's displacement. Thus, the study presented here will assume that somehow the pivot position is being defined by an actuation system, the layouts and arrangements of which are not detailed here.

The piston is cohesively attached to a rod, which does not execute a pendular motion. Consequently, the lateral forces that act on the side of the piston's head are absorbed by the rod, since it is in direct contact with the crank case (Figure 1.2). This characteristic is highlighted as another advantage of the proposed mechanism because the reduction of lateral forces on the piston can increase durability. Moreover, the lever amplifies the motion of the crank–rod mechanism to the piston. That means that the crank length has to be shorter than it is in the conventional mechanism, resulting in a weight reduction.

As the position of the pivot of the lever can be altered, the arm length of the lever can be adjusted, and the stroke length is controlled (Figs. 1.3 and 1.3). Furthermore, the inclination of the lever determines the position of the Top Dead Centre, controlling compression ratio by regulating the clearance volume (Figs. 1.5 and 1.5).

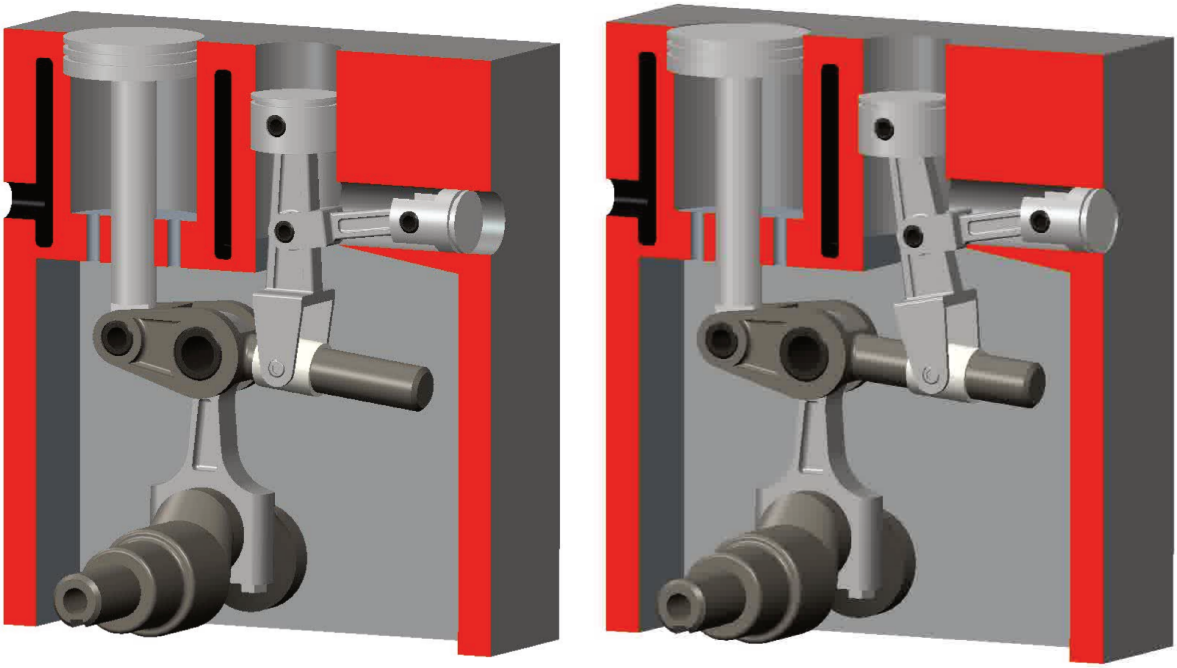

(a) High cubic capacity.

(b) Low cubic capacity.

Figure 1.3: Top dead centre for different cubic capacity.

When the mechanism is set for maximum cubic capacity (Fig. 1.7), the pivot (point e) is moved near to the superior connecting rod axis (point b). The pivot is fixed and as the crank (point a) performs one revolution, the rest of the lever (points b and c) perform a reciprocating movement. Since the connection between the piston rod and the lever (point c) must perform a purely vertical reciprocating movement, the distance between b and e cannot be constant along one crank revolution, exposing the necessity of the sliding connection between pivot and lever. However, the distance between points c and b is constant. The top of the piston (point d) follows point c. Therefore, the stroke length (trajectory of point d) is influenced by the ratio between the distance c to b and the initial distance b to e. Hence, in order to reduce cubic capacity, point e must be pushed away from point b (Fig. 1.8).

As cubic capacity is being changed, the clearance volume has to change in order to keep a constant compression ratio. Moreover, the proposed mechanism also has the objective of adjusting compression ratio independently of the cubic capacity. Thus, a three degree of freedom mechanism is required and the pivot not only has to be moved horizontally, but also vertically. The vertical position of point e defines the inclination of the lever. As point e is moved downwards and point b is fixed to the connecting rod, point d is moved upwards. Conse-

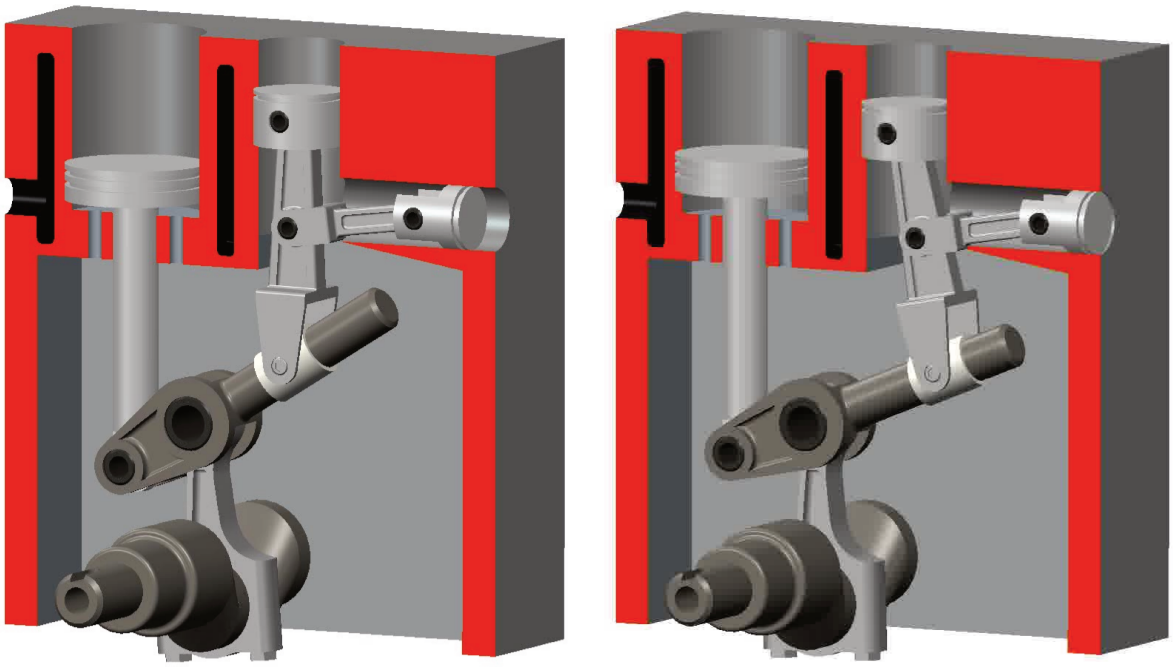

(a) High cubic capacity.

(b) Low cubic capacity.

Figure 1.4: Bottom dead centre for different cubic capacity.

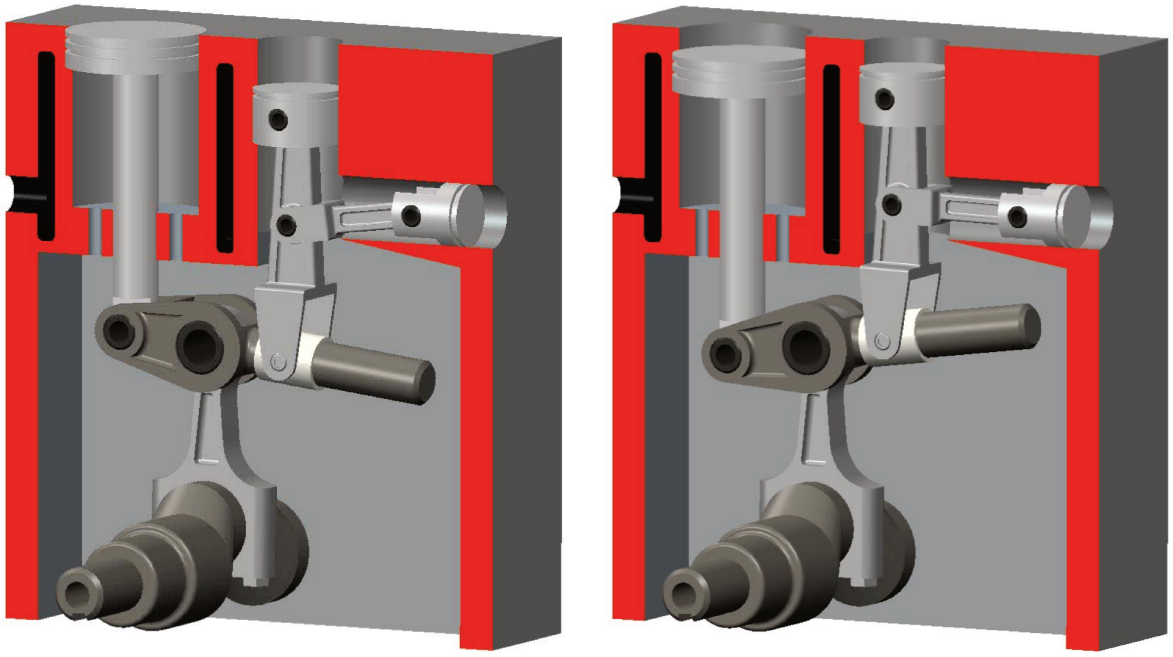

(a) High compression ratio.

(b) Low compression ratio.

Figure 1.5: Top dead centre for different compression ratio.

quently, the TDC is moved towards the head, reducing clearance volume and the compression ratio is increased. Contrarily, if the pivot is moved upwards, TDC is moved downwards, increasing clearance volume and, thus, compression ratio is decreased. This is a simplified exposure of the kinematic strategy of the mechanism since compression ratio is not strictly influenced by

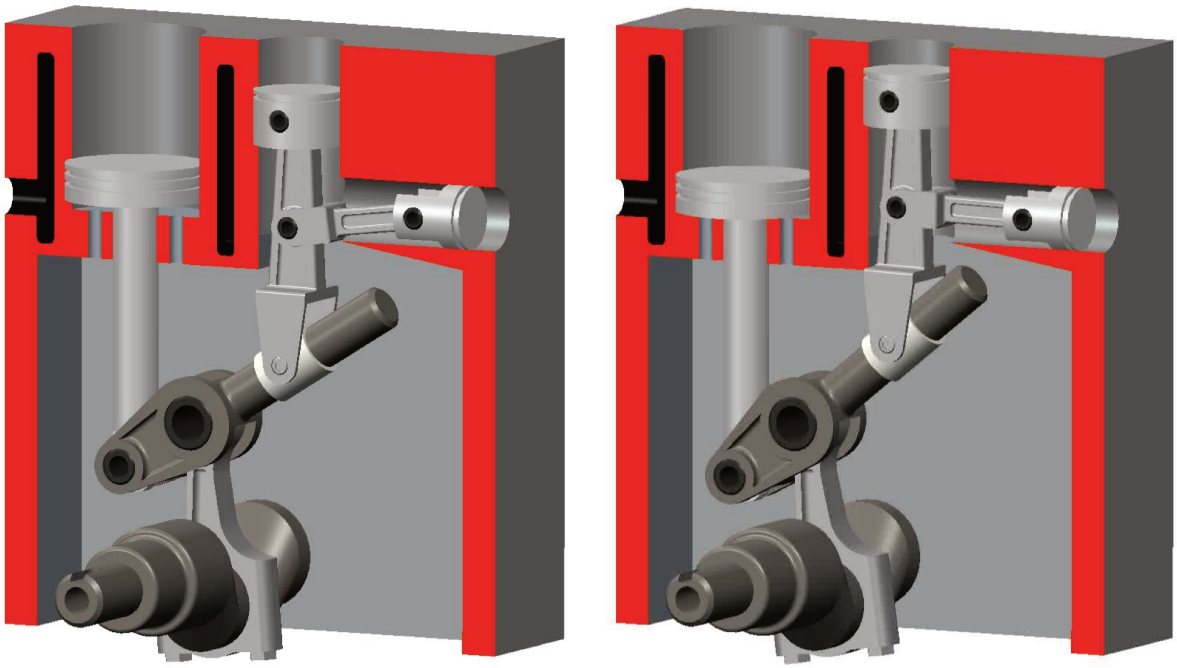

(a) High compression ratio.

(b) Low compression ratio.

Figure 1.6: Bottom dead centre for different compression ratio.

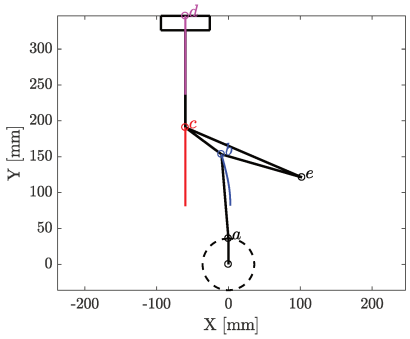

Figure 1.7: Trajectory of each point at maximum cubic capacity

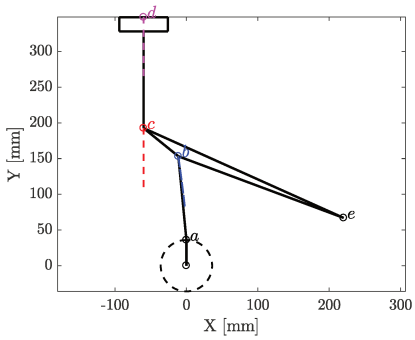

Figure 1.8: Trajectory of each point at minimum cubic capacity

the vertical position of the pivot and stroke length is not strictly influenced by the horizontal position of the pivot due to non–linearities. Further details on the kinematics are given in Chapter

3.

1.3 The proposed work

The main purpose of this work is to conduct a conceptual study on the proposed mechanism, *i.e.*, to perform an evaluation in the operation of a spark–ignition engine with the VSE mechanism, according to the established objectives:

- Understand the strategies for VSE calibration;
- Evaluate the benefits of adjusting compression ratio;
- Evaluate the benefits of adjusting cubic capacity;
- Quantify the gains stemming from the VSE technology.

This Thesis is organised according to the development of the study on the proposed engine. The work is divided into the development of:

1. Kinematic model of the mechanism;
2. Combustion model;
3. Phenomenological model;
4. Calibration strategy.

As the mechanism is different from the conventional crank–rod used in the conventional engines, the development of a kinematic model is necessary. The model indicates the relation between lever position and piston motion. Moreover, the model allows to calculate the pivot position according to a desired set of compression ratio and cubic capacity. This model has two objectives: to compare the motion of the proposed mechanism to a conventional one, highlighting differences and establishing the characteristics of the VSE in a qualitative approach. The second objective is to allow the calculation of instantaneous volume, area and the volume differential, informations required by the phenomenological model in order to evaluate the thermodynamic state of the gases in the cylinder and, thus, calculate the pressure profile used in the prediction of performance.

In order to obtain reliable results from the phenomenological simulation, it is necessary to develop a model for the combustion. Therefore, a combustion diagnosis was performed. Data obtained from a commercial engine was used to evaluate the effects of engine's operational conditions on ethanol combustion, providing information used in the implementation of the simulation model.

The Phenomenological model is implemented thereafter by solving the laws of thermodynamics, mass balance and equations of state for a system comprised of the in–cylinder gases. Once the thermodynamic states are evaluated along the engine cycle, the performance can be predicted, indicating power output, efficiency and knock onset for the engine operating at a certain condition.

The performance of the engine rely on the calibration strategy. Therefore, it is necessary to generate calibration maps in order to optimise the operation of the engine. To perform this calibration task, the simulation was carried out for several conditions, searching for the optimum set of engine parameters aiming the efficiency maximisation. With the calibration maps generated in the virtual process, called simulation based calibration, it was possible to made comparisons between the existing technologies and the proposed VSE.

Therefore, a Bibliographic revision is provided in Chapter 2 presenting the development of the mechanism for VSE solution and other strategies for load control. Then, a revision on phenomenological methods is made, presenting methods used in the literature for simulating spark ignition engines. Following, a revision on combustion diagnosis is performed, presenting alternatives for evaluating combustion development based on experimental pressure data. Finally, a revision on model based calibration is presented, exposing different techniques for predicting engine's optimum performance based on simulated data.

The development of the Kinematic model is presented on Chapter 3. Equation for piston motion are derived and the effects of controlling compression ratio and stroke length are evaluated in this Chapter. Comparisons between a conventional crank–rod mechanism and the proposed VSE mechanism are presented indicating the main differences.

The development of the diagnosis model and the diagnosis of ethanol combustion is given in Chapter 4. A brief comparison with gasohol is also provided in this Chapter. More details on the development of the diagnosis model are presented in Appendix C. Additional results of the combustion diagnosis are provided in Appendix D.

In Chapter 5, the predictive model is explained, describing the phenomenological approach adopted. A validation of the algorithm is presented in the end of the Chapter. More details on the predictive model are provided in Appendix B. Constants used in the algorithm are provided in Appendix A.

The description of the simulations performed and the strategy adopted for the calibration of the VSE are described in Chapter 6. Also in this Chapter, a detailed revision on the results found is made and a comparison between the VSE, a VCR and a conventional engine is presented indicating the gains in efficiency obtained from the implementation of each technology.

The Conclusion summarizes the findings of this study and also brings a discussion on the next steps for the research, exposing each tool developed in the research.

2. Bibliographic revision

A literature overview is presented in this Chapter. Firstly, a revision on *Variable Stroke Engine* (VSE) and *Variable Compression Ratio* (VCR) mechanisms is exposed, together with literature view on this type of engine. Afterwards, the bibliographic revision focuses on the tools developed for the analysis of the VSE engine:

1. Combustion diagnosis;
2. Phenomelogical models for simulation;
3. Simulation based calibration.

2.1 Variable Stroke Engines and Variable Compression Ratio technologies

There are only few studies about VSE in the literature. There is much more efforts on research on VCR engines. Since the purpose of this thesis is the study on a mechanism that allows the adjustment of both compression ratio and stroke length, a historical and technical review on both VSE and VCR is herein presented.

Before the development of the Electronic Control Unit (ECU), engines were optimised for a strictly narrow range of operational conditions. Therefore, the search for a higher degree of flexibility was convenient before the 1980's. After the implementation of the ECU in engines, audacious technologies like VCR and VSE were put aside. Recently, the environment protection politics have motivated the research on those type of solutions in order to achieve the emission and fuel consumption levels established by standards.

Strategies for VCR and VSE require the control over piston trajectory and, thus, the redesign of the whole engine or, at least, some components is mandatory. Consequently, several solutions were proposed over the years since the invention of the reciprocating engines, however, only few were produced and until nowadays there is no commercial implementation

of the VSE engine while the VCR engine is beginning to be inserted in the automobile market. The reasons for this issue are discussed through this literature review.

WELSH and RILEY (1971) exposed the issues of throttling in their work. This solution consists in closing a valve, known as throttle and thus limiting the admitted amount of air in the cylinder. It has been used unanimously in engines as mean for load control. However, the throttling process generates a vacuum pressure in the intake manifold. Consequently, the intake process requires a greater amount of work. This work is known as pump work or pump losses, since it does not collaborate to the power output of the engine. Therefore, the higher the pump work, the lower the engine's efficiency. A solution for load control without throttling could mitigate this problem. By reducing cubic capacity it is possible to produce a lower level of power. The most intuitive mean for reducing cubic capacity of a reciprocating engine is the reduction on piston's stroke. Hence, Variable Stroke Engines bring the promise of increasing efficiency since they adopt a different strategy than throttling for load control. Moreover, WELSH and RILEY (1971) also indicated that a conventional engine has a constant stroke length and since engine friction is chiefly originated by the sliding movement of the piston in the cylinder, friction is constant independently of the load. A VSE presents a lower stroke for partial loads conditions, yielding a lower level of friction.

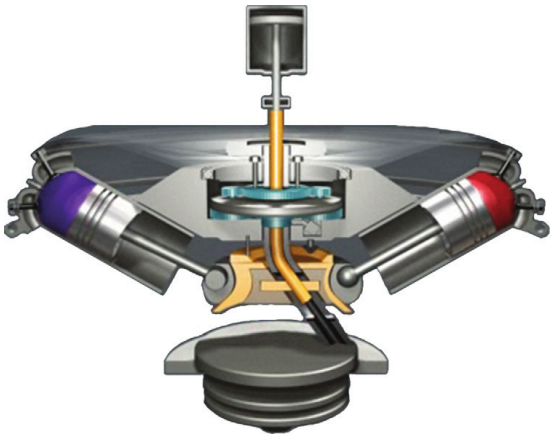

Figure 2.1: Axial piston VSE. Source: TAVARES *et al.* (2011).

SIEGLA and SIEWERT (1978) have presented a review, indicating that the first patent for VSE dates from 1890's. They have described in their work the axial piston mechanisms of WELSH and RILEY (1971) (Figure 2.1) and the radial piston mechanism of POULIOT *et al.* (1977) (Figure 2.2), being the later the pioneer physical prototype of a VSE, tested in the Sandia Laboratories. It has been stated the desired characteristics of a VSE: the capability of controlling stroke length without adding more weight to the engine. However, this task characterises itself as an utopia since the piston trajectory control requires more components in order to be performed. Additionally, the advantages on friction reduction with stroke shortening can be overwhelmed by the additional bearings in the mechanism of the VSE. Another concern is

the effect of the stroke length on the compression ratio. If the engine has only one degree of freedom (DOF), it is possible to control only compression ratio or stroke length. Since compression ratio is a function of the displacement, the clearance volume has to be adjusted together with stroke length in order to keep a constant compression ratio. It is highlighted that the first studies on VSE did not aim to compression ratio control besides stroke length, as it will be explored ahead in this review.

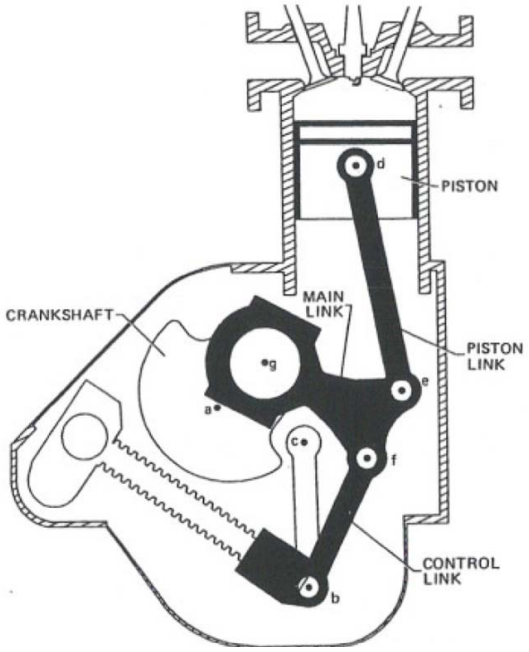

Figure 2.2: Pouliot VSE mechanism. Source: ROSSO *et al.* (2006).

SIEGLA and SIEWERT (1978) have experimentally tested a conventional engine with modifications in order to test different strokes lengths, simulating the VSE. Insights on the effects of shortening the stroke length have been found in that work. Although a fuel economy of 20% has been found for the engine operating under the conditions of the cycles Highway and EPA, emissions were increased.

A complementary study has been presented by SIEWERT (1978) simultaneously to the previous cited work. The main issue of shortening stroke length stems from the reduction of stroke length/bore diameter ratio (S/B). It was been verified that for very low values of S/B, the ratio of area/volume (A/V) of the cylinder is increased and, consequently, the heat transfer losses are very high. Blow–by and exhaust temperature were observed to increase with S/B reduction. Additionally, combustion was verified to be slower for those conditions. Those characteristics lead to an increase in hydrocarbons (HC) emissions. On the other hand, nitric oxides (NOx) were verified to reduce in low S/B conditions. The hypothesis behind those results was that shortened stroke reduce the level of turbulence inside the cylinder, harming flame propagation. In order to solve the observed issues, SIEWERT (1978) proposed the redesign of the combustion chamber aiming the decrease of A/V ratio and the increase of turbulence.

Few years later, FUKUI *et al.* (1983) presented another technique for solving the pumping losses. It consisted in turning off one or more cylinders in order to reduce engine's cubic capacity. This can be done by either only turning off the fuel injection, deactivating valves, turning off fuel injection and circulating air in wide open throttle (WOT) condition or recirculate exhaust gases in the cylinder. It was concluded that the deactivation of valves is the most convenient strategy.

The evolution of computers resulting in the possibility of performing extensive simulations have exposed the VSE to more intensive analyses. ALSTERFALK *et al.* (1997) proposed the comparison between conventional engines and VSE by using non–dimensional simulations, exposing the fact that it is not possible to completely eliminate the throttling, mainly for idle and braking conditions. Modifications suggested by ALSTERFALK *et al.* (1997) include the adjustment of valve lift to improve intake process. The results of the simulations had confirmed the hypothesis that the shortened stroke length affects turbulence, leading to a slower combustion, mainly in the fast burning phase. Moreover, the flame area is reduced in low S/B conditions, collaborating to a longer combustion. Effects of stroke length on friction were confirmed since sliding is responsible for 60 % of the total friction of an engine. For a conventional engine, load reduction leads to a lower in–cylinder pressure, resulting in a lower lateral force on the piston. Therefore, there is indeed a reduction on friction for partial loads in conventional engines, although it is not comparable to the friction reduction in a VSE. ALSTERFALK *et al.* (1997) concluded that the benefits of VSE are more evident at partial load conditions, between 30% to 70% at the full load condition.

TSUCHIDA *et al.* (2007) proposed the use of longer stroke length in order to avoid the problems of low S/B ratio, inducing higher levels of turbulence and decreasing the A/V ratio. When increasing the stroke length, the VSE had presented an identical level of friction compared to that presented by the conventional engine.

The application of VSE have been explored recently with other technologies. TAVARES *et al.* (2011) studied the use of an axial piston VSE together with vehicle hybridisation. JIANG and SMITH (2014) used mechanisms synthesis in order to convert VCR in VSE. Similarly, CASTAÑEDA *et al.* (2018) coupled genetic algorithms with mechanism synthesis methods to optimise the layout of a VSE.

Besides the cited mechanisms, other solutions for VSE can be found in the literature. Most of them do not permit the control on the compression ratio and, in some cases, the compression ratio varies within fixed conditions with stroke length adjusting, as the mechanism presented in Figure 2.3. YAMIN and DADO (2004) described a mechanism composed by alternating pistons which allows the variation on stroke length, however, the mechanism does not allow the control on the compression ratio. DORIĆ and KLINAR (2014) described a VSE composed by a toroidal combustion chamber.

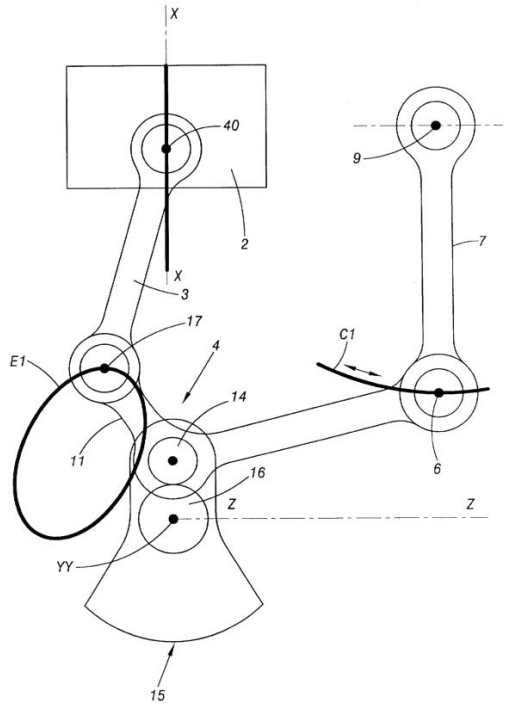

Figure 2.3: VSE proposal with only 1 DOF. Source: BEROFF (2000).

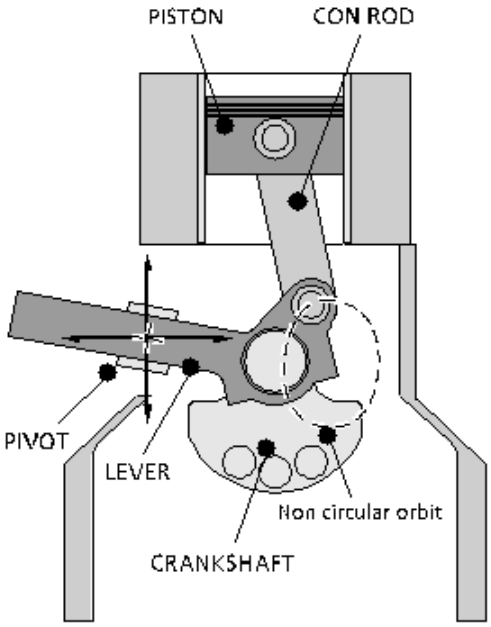

Figure 2.4: Mayflower VSE. Source: ROBERTS (2003).

The combination of VSE with VCR is very scarce in the literature. In order to control stroke length and compression ratio independently, the mechanism must have 2 DOF. ROBERTS (2003) described the Mayflower mechanism (Figure 2.5). However, the authors could not find further academic publications about this specific mechanism. ROSSO *et al.*

(2006) proposed a multi-link mechanism which was considered a success (Figure 2.5), being vibration the only issue found during the experiments. ROSSO *et al.* (2006) also mentioned the implementation of a variable valvetrain as means for fully optimisation of the VSE.

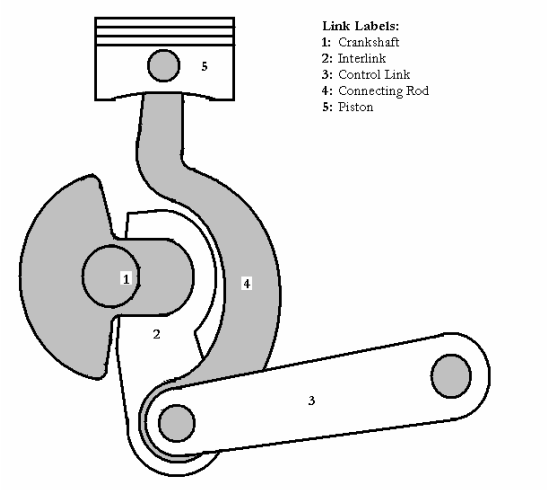

Figure 2.5: Michigan Tech VSE. Source: ROSSO *et al.* (2006).

As mentioned before, VCR mechanisms received a greater attention in the literature. Similar to the VSE mechanisms, the VCR mechanisms have been proposed since the beginning of the use of reciprocating engines. The first patent dates from the decade of 1900 (ASTHANA *et al.*, 2016). ADAMS *et al.* (1987) bring a brief review of VCR proposals of that time (indications shown in Figure 2.6):

- Auxiliary chamber (E and F);
- Movable piston crown (B);
- Adjustable head height (A);
- Adjustable length of con–rod (Not presented in Fig. 2.6);
- Multi–link mechanisms (D);
- Eccentric crank bearings (C-3).

ADAMS *et al.* (1987) exposed the need for VCR. Fixed Compression Ratio engines (FCR), or conventional engines, have their compression ratio limited by the full load conditions, sacrificing efficiency in partial loads. The VCR solution is proposed in order to adjust compression ratio for optimised performance in all conditions of loads. ADAMS *et al.* (1987) also conducted experiments using an auxiliary chamber type VCR. This configuration had been criticized for harming combustion development due to modifications in the combustion chamber. ADAMS *et al.* (1987) argued that the redesign of the combustion chamber could mitigate this

issue. Moreover, it had been concluded that there is a limit of 15:1 in compression ratio since above the temperature of in–cylinder gases leads to heat losses that overwhelm the benefits of increasing compression ratio.

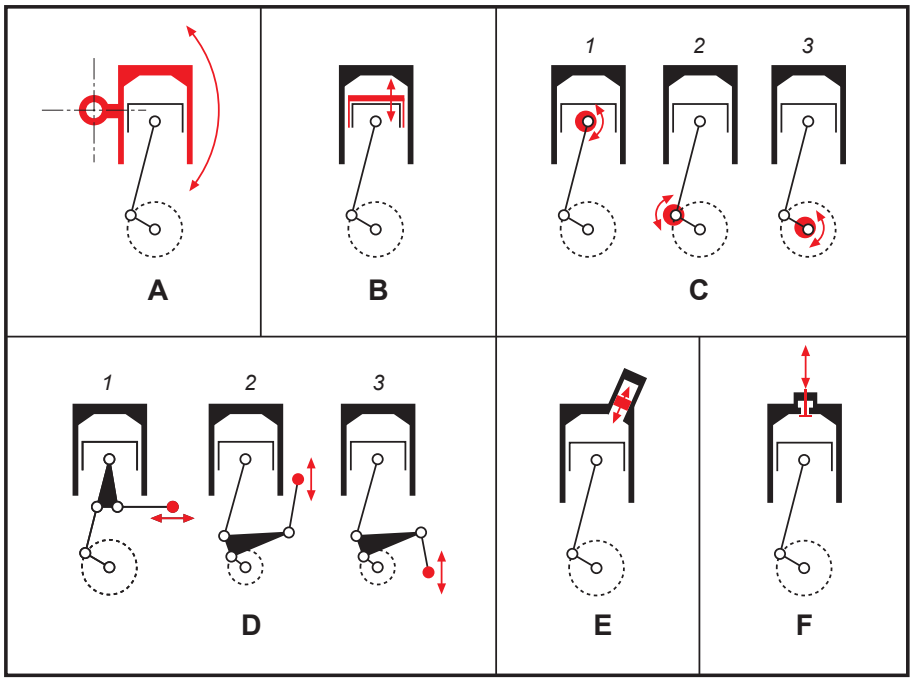

Figure 2.6: Possible layouts for VCR engines. Source: RABHI *et al.* (2004)

WIRBELEIT *et al.* (1990) explained in more details the strategy for VCR. Compression ratio (CR) is a geometrical parameter that plays a fundamental role on the thermodynamic process. The higher the CR, the more efficient a motor cycle will be. In a more qualitative approach, Spark–ignition (SI) engines execute a sequence of thermodynamic processes defined after the ideal cycle Otto (aside from few exceptions that follows the ideal cycles Atkinson or Miller, which will be mentioned ahead). In the Otto cycle, the compression ratio is equal to the expansion ratio. Consequently, a higher compression ratio also means a higher expansion ratio and since the positive work of an expansion process is always higher than the negative work of a compression process in a power cycle, the efficiency will be proportional to the CR (SHAIK *et al.*, 2007). However, technical characteristics of the engines and chemical characteristics of the fuel create a barrier for the CR. Higher compression ratios leads to higher end–gas temperature during the combustion process, which can induce knock onset. Therefore, CR is defined for the critical condition for knock onset, *i.e.*, full load and low engine speed. For other conditions, it would be possible to operate under higher efficiency if the CR could be adjusted, justifying the research on VCR. WIRBELEIT *et al.* (1990) also cited other solutions, such as the eccentric axes for the con–rod (solutions C1 and C2 in Figure 2.6). Moreover, the increase of temperature induced by higher CR would improve cold start conditions.

DRANGEL *et al.* (2002) explored the advantages of VCR beyond partial loads con-

ditions. Higher CR would also solve the issue of combustion variability in very lean conditions or the exploration of Exhaust Gases Recirculation (EGR) as means for controlling load. Experiments consisted in constructing a supercharged downsized engine with an adjustable cylinder head. By combining VCR with supercharging, it was found a fuel economy between 30 % and 35 %.

ROBERTS (2003) presented a review of several VCR mechanisms, pointing out the commercial barriers for VCR implementation in vehicles. The greatest challenge does not consist in the additional components in the engine, but the modifications in the facilities and machinery to produce VCR. The review also presents a discussion on the role of compression ratio on the calibration process. The calibration maps of the VCR must include maps for CR combined to the spark timing for each condition of load and engine speed. Additionally, strategies for transient conditions must be defined in order to control CR. Another challenge is the actuation of the mechanism. The transition from low to high CR can be easily performed, however, the transition from high to low CR is a critical procedure and has to be performed quickly, requiring the development of more efficacious actuation systems. Finally, ROBERTS (2003) pointed out the direct injection as the major opponent solution for the VCR since it allows to increase the fixed CR in conventional engines and avoiding knock onset by changing the strategies of injection.

MOTEKI *et al.* (2003) had divided the VCR mechanisms according to the function of the modified components. Hence, there are two categories of VCR: modifying fixed components, such as cylinder head, crank case and bearings, and modifying movable components such as piston, crankshaft and con–rod. MOTEKI *et al.* (2003) introduced the multi–link mechanism for VCR. In those mechanisms, the con–rod is divided into, at least, two parts. A lever is used to adjust the relative positions between the two parts of the con–rod, altering the position of the Top Dead Centre (TDC) and the Bottom Dead Centre (BDC) and, thus, adjusting the CR.

RABHI *et al.* (2004) introduced another solution for VCR (Figure 2.7). The solution consists in adding a gear to the engine. This gear has its center pinned to the upper axis of the con–rod. On one side, an actuator is geared while on the other side the piston is geared. This solution promises to preserve the piston trajectory produced by the crank–rod mechanism and allowing to control the CR continuously over a wide range of values. RABHI *et al.* (2004) indicated some considerations on the design process of components for a VCR, among those the fact that the in–cylinder pressure can reach levels around 100 bar at high CR.

SUGIYAMA *et al.* (2007) pointed out another application for VCR. Variable valvetrains are another technology aiming the increase in efficiency. The variation on valve opening and closing events allowed the control of air intake. This strategy is commonly referred as “Atkinson cycle”. However, the early intake valve closing leads to a lower effective CR. Therefore, it was suggested the use of VCR with variable valvetrain in order to avoid this issue.

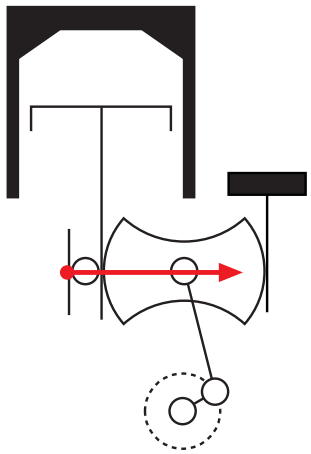

MCE-5

Figure 2.7: Gear based solution for VCR. Source: RABHI *et al.* (2004).

SHAIK *et al.* (2007) presented a review on VCR, indicating other benefits directly related to combustion. The increase in CR leads to a faster flame development, resulting in a more efficient combustion. Older works on VCR had only pointed the improvement on efficiency as major benefit of the VCR. SHAIK *et al.* (2007) also pointed out the use of VCR in order to increase power output of an engine, being the benefits more evident in turbocharged engines. The VCR would also allow the operation at idle condition on very low engine speed due to the misfire suppressing in high CR operation. Additionally, the existence of a trade–off between spark timing and CR for VCR was mentioned. It was believed that the VCR will become economically favourable since the environmental laws will encourage more audacious solutions for fuel economy. SHAIK *et al.* (2007) also introduced the VCR as a solution for multi–fuel engines since each type of fuel has a different sensibility for knock onset.

Most VCR solutions aim for SI engines because of knock onset. However, WITTEK *et al.* (2009) has indicated the use of VCR for compression–ignition (CI) engines. In the case of CI, knock is not an issue. However, the CR is also limited because of engine structural resistance and emissions, which are critical for specific conditions, being possible to operate at higher CR on not critical conditions. WITTEK *et al.* (2009) divided the VCR solutions in two–stage and continuous. Two–stage solutions allow the CR variation in only two levels, arguing that those solutions are simpler and enough for the purposes of VCR. Continuous VCR technology allows the continuous control of CR between two levels of CR and it requires a more complex system for controlling CR.

PEŠIĆ *et al.* (2010) presented a work about the application of VCR systems for CI engines. For very high levels of CR, a trade–off between thermal efficiency and mechanical efficiency appears since the in–cylinder pressures are very high. Moreover, another trade–off for CR exists concerning emissions. Suppression of particulates and NOx is favoured by low

CR whereas suppression of HC and CO is favoured by high CR.

Variable Compression mechanisms have also been used for other strategies. BORETTI *et al.* (2011) described a mechanism that varies the TDC in order to obtain ER different from the CR, creating an approximation of the ideal "Miller cycle". However, WOS *et al.* (2012) defined the VCR technology as mechanisms that allow the non–periodic variation of CR, which excludes the engine described by BORETTI *et al.* (2011) as a VCR engine. WOS *et al.* (2012) presented a review on VCR technologies, pointing out the use of VCR for new combustion strategies, such as Homogeneous Charge Compression Ignition (HCCI), Controlled Auto–Ignition (CAI) and Low Temperature Combustion (LTC). WOS *et al.* (2012) brought a very comprehensive discussion on the pros and cons of each VCR solution (Figure 2.8).

VCR design case:	a)	b)	c)	d)	e)	f)	g)	h)
CR varying principle	articulated monohead	piston deck height varying	eccentrics on main bearings	eccentrics on rod-end bearings	multilink rod-crank mechanism	additional small chamber	gear-based crank mechanism	shifted monohead
Engine layout	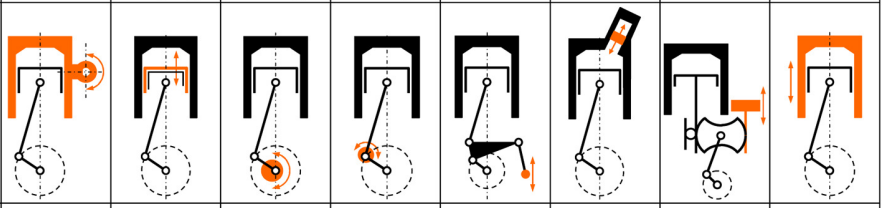							
Combustion chamber integrity	preserved	preserved	preserved	preserved	preserved	significantly deteriorated	preserved	preserved
Crankshaft-piston assembly kinematics	slightly changed	not changed	slightly changed	slightly changed	significantly changed	not changed	significantly changed	not changed
Mechanical losses	not changed	not changed	not changed	not changed	significantly deteriorated	not changed	slightly improved	not changed
Engine overall rigidity	deteriorated	preserved	preserved	preserved	preserved	preserved	preserved	deteriorated
CR varying effect on engine displacement	null	null	null	null	significant	null	null	null
CR control accuracy	good	poor	good	poor	very good	good	very good	good
Capability to control CR cylinder by cylinder	low	medium	null	medium	high	high	high	low
Suitability for converting a stock engine into VCR one	high	medium	high	medium	low	high	null	very high

Figure 2.8: Comparison for different VCR strategies. Source: WOS *et al.* (2012)

ASTHANA *et al.* (2016) listed the commercial implementations of VCR in commercial engines, such as Mercedes Benz, Nissan, Ford and Peugeot. and also summarizing the technical development of mechanisms from MCE-5, FEV and Gomecsys. Moreover, ASTHANA *et al.* (2016) described a solution which consists of a variable height piston. The piston has a chamber, which can be filled with a incompressible fluid, changing its height.

Beyond the application of VCR in commercial engines, there are application that have been already implemented for academic purposes. ROMERO and CASTAÑEDA (2019) recently described the process of construction of a Cooperative Fuel Research (CFR) engine with VCR technology for research on alternative fuels and teaching purposes. ROMERO and CASTAÑEDA (2019) stated that the academic community has the responsibility for developing alternative solutions for new engines and the process of design for those engines creates techni-

cal solutions and improvements that must be implemented in the industrial sector afterwards.

In Brazil, the development of VCR solutions were encouraged by the INOVAR AUTO program (LOPES and FERREIRA, 2014). The use of flex–fuel engines in Brazil brings a promising possibility of implementing VCR with the objective of optimising engines for many types of fuels. Among Brazilian studies on VCR, it is worth mentioning the analysis of effect of CR on flex–fuel engine performance, carried out by COSTA and SODRÉ (2011), the structural analysis of a VCR mechanism presented by CASSIANI *et al.* (2009) and the new proposal for VCR engines presented by LOPES and FERREIRA (2014).

Some of the cited mechanism in this review are listed on Table 2.1, together with additional patents for VCR and VSE mechanism.

Table 2.1: List of VSE and VCR mechanisms

Reference	Description
ADAMS *et al.* (1987)	Variable geometry of the combustion chamber - VCR
WIRBELEIT *et al.* (1990)	Piston with movable head - VCR
WITTEK *et al.* (2009)	Eccentric Rod pin - VCR
ROBERTS (2003)	Multi-link mechanism - VSE
ROBERTS (2003)	Eccentric crank pin - VCR
WIRBELEIT *et al.* (1990)	Piston position controlled by a gear - VCR
DRANGEL *et al.* (2002)	Head - VCR
POULIOT *et al.* (1977)	Multi-link mechanism - VSE
WELSH and RILEY (1971)	Axial engine - VSE
ROSSO *et al.* (2006)	Multi-link mechanism - VSE
RIETTI (1914)	Multi-link mechanism - VSE
PIERCE (1914)	Multi-link mechanism - VSE
WILDHABER (1951)	Axial engine - VSE
BIERMANN (1955)	Multi-link mechanism - VSE
CRISE (1978)	Multi-link mechanism - VSE
FREUNDENSTEIN and MAKI (1981)	Balanceable engine assembly - VSE
HENIGES (1984)	Scotch yoke with variable stroke length - VSE
NELSON (1985)	Multi-link mechanism - VSE
PAL and PAL (1990)	Multi-link mechanism - VSE
GONZALEZ (1999)	Eccentric Crank pin - VSE
BOGGS (2001)	Multi-link mechanism - VSE
RAO *et al.* (2002)	Eccentric Rod axe - VCR
FUJIMOTO and MOTEKI (2003)	Multi-link mechanism - VCR
YAMADA and SATO (2004)	Multi-link mechanism - VCR
PATTAKOS *et al.* (2012)	Geared piston head - VCR
RIES (2010)	Multiple piston device - VCR
BEROFF (2000)	Multi-link mechanism - VSE

2.2 Diagnosis models

Combustion diagnosis is a powerful tool employed in internal combustion engines providing information about combustion characteristics in a thermodynamic approach. It is performed by using the measured in–cylinder pressure since it is the most accessible thermodynamic property in the cylinder (GUEZENNEC and HAMAMA, 1999). Combustion effect on in–cylinder pressure can be isolated from other phenomena such as blow–by, heat transfer, internal energy change and work (GATOWSKI *et al.*, 1984). The output of the procedure is known as Apparent Heat Release (AHR) and the Heat Release Rate (HRR) profiles. Start of combustion (SOC), end of combustion (EOC), and other secondary parameters as combustion duration, ignition delay and form factor of combustion can be deduced from the AHR profile. Therefore, it possible to perform this analysis in order to determine the effect on combustion of design parameters, such as piston geometry, compression ratio, valve timing, and operational parameter, which are constantly adjusted by the electronic control unit (ECU) during the operation of the engine, such as air–fuel ratio, spark timing and load. From the HRR profile it is also possible to understand the effect of each tested parameter on the phases of combustion, specifically, flame development (usually the phase in which until 10% of the fuel is burnt), fast burn phase (burnt fuel is from 10 to 90%), and quenching phase (ABBASZADEHMOSAYEBI and GANIPPA, 2014).

Researchers have begun to determine Start and End of Combustion from pressure data by tracing the logarithmic pressure–volume diagram and identifying the lines representing compression and expansion (D'AMBROSIO *et al.*, 2015), as demonstrated on Fig. 2.9. The pioneer method to determine heat release from experimental data was developed by Rasswiler and Withrow (RW), which consists in correlate MFB to pressure rise fraction caused by combustion ($P_{comb,RW}$) (MUELLER *et al.*, 1983), by subtracting the pressure rise due to a polythropic expansion with polythropic index n_p from the measured pressure (Eq. 2.1). D'AMBROSIO *et al.* (2015) list modifications performed on the RW method, such as the assumption that the fraction of fuel burnt is proportional to the polytropic constant. Moreover, other methods can be derived by evaluating the ratio between the firing pressure profile and the motoring pressure profile, such as the Pressure Ratio Management and the Pressure Departure Ratio. A more elaborated method was proposed by Krieger and Borman (KB), described by GATOWSKI *et al.* (1984), which is based on the energy conservation law applied to the in–cylinder gases (Fig. 2.10) allowing the inclusion of heat transfer (δQ_{ht}) and blow–by effects (dm_{cr}). By separating the phenomena and allowing the use of temperature dependent properties, it is possible to obtain a more accurate result, besides the possibility of a more comprehensive analysis (CHEUNG and HEYWOOD, 1993). A comparison between the methods was carried out by BRUNT and EMTAGE (1997) demonstrating that the KB method presents higher reliability and accuracy since

its does not depend on the estimation of a polythropic index. However, when the amount of heat release is low, *i.e.*, at partial load condition, RW method presents more robustness to noise and uncertainties because of its simplicity, being preferred by some researchers until nowadays. A detailed description of the heat release analysis for a spark–ignition engine was made by MACHADO (2012).

Other methods can be based on other parameters beyond pressure signal. One example is the use of the ion signal measured in the spark plug for determining MFB (DANIELS, 1998). Many researchers expanded both methods to a two–zone approach, in which reactants and combustion products are separately analysed. STONE and GREEN-ARMYTAGE (1987) and BALL *et al.* (1998) have described two–zone models based on the RW method, in which each zone is assumed to undergo a polythropic compression/expansion. Note that this method uses the intake temperature as initial value for the unburnt gases and the exhaust temperature as final value for the burnt gases. Hence, the burnt fraction must be calculated from the end of the cycle to the SOC.

$$P_{comb,RW} = P_i - P_{i-1}\left(\frac{V_i}{V_i - 1}\right)^{n_p} \tag{2.1}$$

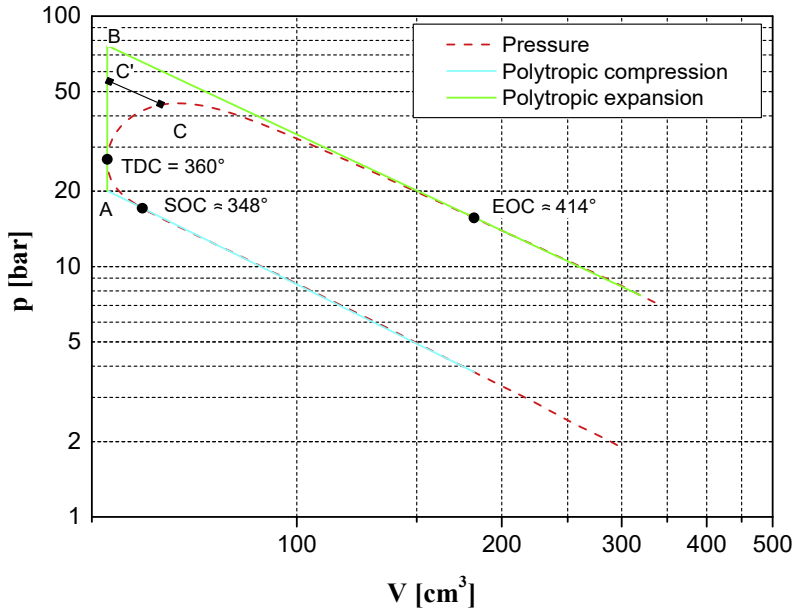

Figure 2.9: Determination of SOC and EOC from logarithmic Pressure-Volume diagram. Source: D'AMBROSIO *et al.* (2015).

Other combustion diagnosis methods based on two–zone approach are developed based on thermodynamic relations and energy conservation law (GUEZENNEC and HAMAMA, 1999; KAMIMOTO *et al.*, 1997; CATANIA *et al.*, 2003). The first law of thermodynamics is applied for each of the zones. Usually, the adiabatic flame temperature is assumed as initial value for burnt gases temperature.

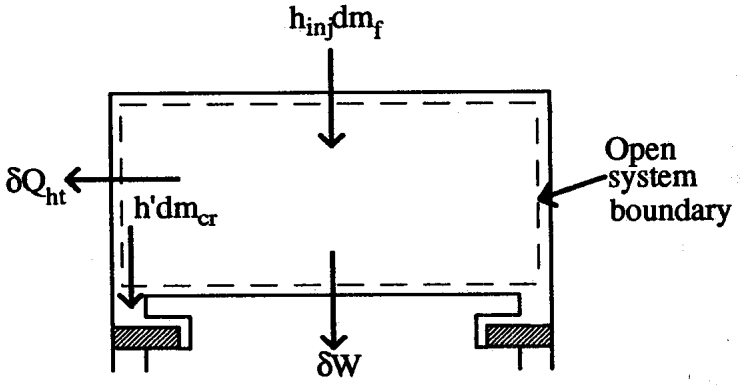

Figure 2.10: Cylinder model for the KB method. Source: CHEUNG and HEYWOOD (1993).

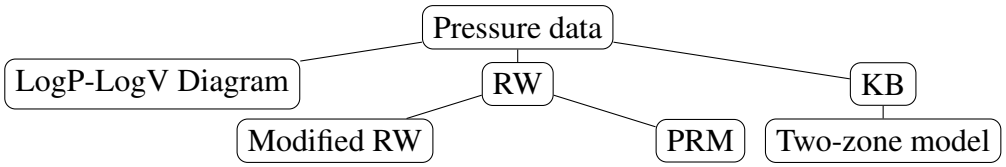

Figure 2.11: Methods for Combustion diagnosis.

The combustion diagnosis can be performed on both compression–ignition and spark–ignition (SI) engines. Commonly, the heat release analysis is applied to compression ignition. When fuel amount and energy content are known, it is possible to obtain the mass fraction burnt (MFB). The MFB or burn rate analysis provides the profile of the fraction of fuel burnt, from 0 to 1 (BRUNT *et al.*, 1998).

Other methods can characterize combustion on a more detailed and microscopic approach. For example, flame growth, structure and speed can be measured in optical engines or closed vessels providing the effects of specific parameters on combustion, *e.g.*, air–fuel ratio (ALEIFERIS *et al.*, 2013), diluent concentration (EISAZADEH-FAR *et al.*, 2011b) and temperature (KONNOV *et al.*, 2011). Those analyses can also present a comparison between different types of fuels (GÜLDER, 1984; ALEIFERIS and BEHRINGER, 2015). However, determining the effect of the combined variation of many parameters within the wide operational conditions of an engine can be a difficult task. Thus, combustion diagnosis is still a reliable tool to characterize combustion, which can be used in parallel to those methods based on a more theoretical approach. Moreover, combustion diagnosis can provide data for data–based MFB models for engine simulation. The most frequently used correlation that describes the MFB profile is the Wiebe function (GHOJEL, 2010) for engine research application. Consequently, several studies of combustion diagnosis have evaluated combustion characteristics by fitting parameters of the Wiebe function to the studied case (BONATESTA *et al.*, 2010; YELIANA *et al.*, 2011; ABBASZADEHMOSAYEBI and GANIPPA, 2014; YELIANA *et al.*, 2008).

The exposed type of analysis has been used for a wide variety of applications. Most applications use the information provided in the analysis to evaluate the influence of operational

and design parameters on combustion behaviour. Moreover, the evaluation regarding effects of implementing new technologies or strategies relies on the combustion diagnosis, such as the effects of a secondary injection of natural gas on compression–ignition engines (LI *et al.*, 2015), or the effect of using blends of ethanol and n–butanol in diesel (RAKOPOULOS *et al.*, 2011). Some investigations suggest the implementation of such models on real–time diagnosis to assist engine control, such as determining the beginning of combustion in compression-ignition engines (OH *et al.*, 2015) or combustion duration in spark–ignition engines (MITTAL *et al.*, 2009). Another case is its application in homogeneous charge compression ignition and spark-assisted compression ignition , where the model must consider the effect of auto-ignition with that of flame propagation ORTIZ-SOTO *et al.* (2014). Another application that can be highlighted is the study of turbo lag effects (ASSANIS *et al.*, 2000). As one example of the work developed by BUENO *et al.* (2004), combustion diagnosis can also be performed based on the second law of thermodynamics, known as exergetic diagnosis. Other applications include the calibration of predictive models, *i.e.*, simulation models of engines (GUEZENNEC and HAMAMA, 1999) and the use of this type of analysis for educational purposes in engineering education (DEPCIK *et al.*, 2007).

Combustion diagnosis is a considerably contributive analysis in the research of alternative fuels. Owing to the possibility of substituting fossil fuels, bioethanol has been extensively studied (REITZ, 2013). Besides being produced from renewable sources, ethanol presents a higher heat of vaporisation and faster flame speed, leading to a higher resistance to knock onset and, thus, facilitate downsizing through turbocharging (REITZ, 2013; BAE and KIM, 2017). The studies of performance, emission, and combustion characterization of engines operating with hydrous ethanol, gasohol blends, and wet ethanol (ethanol with high water content) are summarized in a review conducted by EL-FAROUG *et al.* (2016). As examples, works on ethanol combustion have evaluated the following: anhydrous and hydrous ethanol combustion in port fuel injection (PFI) and direct injection (DI) engines (AUGOYE and ALEIFERIS, 2014), effects of spark timing and compression ratio on gasohol blends (COONEY *et al.*, 2009), and effect of water content on DI engines (LANZANOVA *et al.*, 2016).

Combustion diagnosis has been used in Brazil for evaluating the performance of hydrous ethanol as fuel. For example, COSTA and SODRÉ (2010) compared gasohol and hydrous ethanol operation in terms of their brake specific consumption, thermal efficiency, and emission in a wide range of speed under full load conditions. Subsequently, COSTA and SODRÉ (2011) studied the effects of compression ratio for a flexfuel ratio with ethanol on a specific fuel consumption, brake mean effective pressure, brake power, brake torque, and thermal efficiency under the same conditions of the previous study. Another work was performed by MELO *et al.* (2011), who measured brake thermal efficiency and emissions on a flexfuel engine operating at a constant torque under different speed conditions. Further investigations of the same en-

gine were performed to evaluate the effect of hydrous ethanol and gasohol blends on knock, cyclic variability, and combustion duration at a constant torque and under three–speed conditions (MELO *et al.*, 2012b). Another investigation expanded the cited study by evaluating the effects of hydrous ethanol and gasohol blend on heat release and emissions under two-load conditions and three speeds under stoichiometric and rich conditions (MELO *et al.*, 2012a).

2.3 Phenomenological models for simulation

The books for internal combustion engines, such as HEYWOOD (1988), FERGUSON and KIRKPATRICK (2015), and STONE (1999), bring several definitions and classifications for predictive models. Unfortunately, there is no consensus in the literature about the classification of the methods for computationally prediction of engines performance and behaviour. The author makes an attempt to unify the classification here. BAYRAKTAR (2003) divided the models into two main categories: thermodynamic and fluid mechanics. Both models are based on conservation laws for energy and mass. Those models do not consider local effects. Fluid mechanics models include the momentum conservation and consider local effects. Therefore, other authors have mentioned the fluid mechanics models as multi-dimensional models. Some authors mention the thermodynamic models as phenomenological models (BLUMBERG *et al.*, 1979) as most phenomena involved in the simulation are usually formulated by empirical or semi–empirical models rather than the laws of Thermodynamics, such as combustion, heat transfer, knock onset or pollutant formation. The phenomenological models can be divided into single–zone or zero–dimensional, which considers a homogeneous mixture between burned and unburned gases, and the multi–zone or quasi–dimensional models, which separates the gases into various zones, each under its thermodynamic state and composition. The most usual quasi–dimensional model is the two–zone model. In this model, the burned and unburned gases are assumed to be divided by the flame front. There are also simulation models which include spatial effects, called Multidimensional models. BUTLER *et al.* (1981) presented a review on multidimensional models. The main discussion on multidimensional models is focused on the dimension of the simulation, being 1-D, 2-D or 3-D. For the cases 1-D and 2-D, hypotheses on symmetry must be assumed. The advantages of assuming symmetry is the simplicity of the model since a reduced approach can be sufficient depending on the objectives of the simulation. Examples of Multidimentional simulations are: Reynolds Averaged Navier Stokes (RANS) (RICHARD *et al.*, 2007; VERMOREL *et al.*, 2009), Large Eddy Simulations (LES) (RUTLAND, 2011) and Direct Numerical Solution (DNS) (CHAKRABORTY *et al.*, 2007).

In 1985, Phil Myers published an article entitled “The art of choosing a model” (MYERS, 1985). Although it has been more than 30 year since the publication of the article,

it presented some useful insights until the present. The article presents a review on the models available at that moment. The review begins with the ideal air–standard cycle Otto. This cycle has been used before the development of computers for approximating the processes in the cylinder to ideal processes. Much of the analyses carried out by using this model assumes air as working fluid and combustion is neglected, being replaced by an addition of heat at constant volume. After the evolution of computer programming, this model had become obsolete and its use was not justified. The inclusion of time as a variable in engines simulation begun with the thermodynamic models. MYERS (1985) defined the development of the thermodynamic models in three tasks: the mathematical based on the conservation laws for a transient process, the improvement of this mathematical with submodels for specific phenomena and the implementation of a second law analysis for a more strict evaluation of the processes. (MYERS, 1985) also highlighted his scepticism with respect to multidimensional models.

The first thermodynamic models had appear in the 1960's. PHILLIPPS and ORMAN (1966) proposed the discrete approach for solving a thermodynamic process for an engine in a digital computer. Hence, the cycle is divided into time steps and in each step the thermodynamic state of the working fluid is determined based on the mathematical model. The discrete approach became universal thereafter. The reason for this approach is the complexity that appears in the modelling of the many phenomena involved in the engine processes, what makes the analytical solution impossible to be obtained (BUTLER *et al.*, 1981). In the next year, ZACHARIAS (1967) made a fundamental contribution by evaluating the importance of choosing an adequate state equation for the working fluid. Although engines operate at high levels of pressure, the temperature is also high. Consequently, the author had concluded that the hypothesis of ideal gas behaviour is accurate enough for engine simulation by comparing the ideal gas law to the Beattie–Bridgemann state equation.

BENSON *et al.* (1975) described the development of models for closed–phases in CI engines, and proposed a model for gases exchange in SI engines. BLUMBERG *et al.* (1979) and BUTLER *et al.* (1981) argued on the role of engine simulations. Computer simulation can perform a prediction of engine performance as function of design parameters, providing information for *a priori* analyses. Those models do not intend to substitute experiments, but to indicate trends, being helpful in the execution of the experimental tests, which provide the results for the *a posteriori* analyses. Moreover, the development of mathematical models brings a benefit for the researcher in order to understand phenomena related to engine operation and indicates the benefits of novel technologies and strategies. BLUMBERG *et al.* (1979) introduced the term phenomenological for thermodynamic models since the model is focused on the description of phenomena. Hence, the researcher has the freedom of choosing the submodels used in the mathematical model. The disadvantages of the phenomenological models is the inaccurate relation between submodels and the omission of local effects. These issues are covered by

the multi–dimensional models. Although BLUMBERG *et al.* (1979) had made a distinction between phenomenological and multidimensional models, the multidimensional models are also phenomenological in a certain degree since they consider constant properties for a discrete location in space. RAMOS (1986) described the single–zone model as inaccurate and suggests the multizone models as a solution for accuracy and simplicity. The two–zone model permits the implementation of more complex combustion models beyond the semi–empirical correlations.

ARSIE *et al.* (1998) highlighted the coupling of different methods for the same model, implementing specific approaches for different components, *e.g.*, the multidimensional model for manifolds coupled to the phenomenological model for the cylinder. Data–based models were described, which are based on empirical correlations fitted to experimental data. Those models were defined as "black box". The phenomenological were defined by the author as "grey box" because it considers the physical laws in the equations, although many phenomena are modelled by simplified correlations. The calibration process of a grey box model is much simpler than that of the black box model.

Several works are found in the literature describing simulations models and applications. The works of ALLA (2002) and VERHELST and SHEPPARD (2009) are highlighted as the most instructive descriptions for phenomenological models, as this work comprises the development of a two–zone phenomenological model. For gas exchange processes, BENSON (1982) presented three main strategies. The first and simplest is the quasi–steady flow assumption. In this method, the flow is considered to occur between cylinder and manifolds, being the manifold at constant conditions. The equations used in this model are described by many authors, being highlighted the work of SHERMAN and BLUMBERG (1977). Another method consists in assuming that a quasi–steady flow occurs from many systems. Consequently, the manifolds also behave as system and their conditions are not constant as in the previous method. Thus, a system of differential equations must be solved in order to calculate the pressure in manifolds, ports and cylinders. By these means it is possible to simulate a multicylinder engine and estimate the crossed effect of the gas exchange processes between cylinders. More complex models consist in simulating the manifolds and ports multidimensionally.

Many Brazilian Thesis were written exposing the phenomenological models. It can be cited as good source for understanding the modelling process the thesis of: GALLO (1990), ALEGRE (1993), LOPES (2014), BARROS (2003), CRUZ NETO (2013), SANTOS (2009), MELO (2007) and NUNES (2017).

Thermodynamic models can be coupled with diverse sub–models in order to simulate specific physical phenomena. The sub–models adopted in the predictive model developed in this work are:

- Heat transfer;

- Combustion;
- Knock.

2.3.1 Heat transfer

Estimation of heat transfer in internal combustion engines is a well–consolidated topic. Researchers started proposing models in the 1920's. JANEWAY (1938) was one of the pioneers in presenting a critical analysis of the heat transfer issue in engines. It has been verified that heat transfer is one of the main sources of inefficiency in engines and the author had proposed means for estimating those losses, pointing the factors that influence heat transfer, such as turbulence, difference of temperature between gases and cylinder walls and area of the cylinder. The temperature of cylinder walls had been considered by the authors as one issue in heat transfer modelling since it was difficult to obtain reliable information on this parameter. However, JANEWAY (1938) demonstrated that an error of 50 °F for the cylinder wall temperature leads to less than 2% of error in the heat transfer estimation.

After the development of phenomenological models, the need for an accurate model for heat transfer had arisen. BORMAN and NISHIWAKI (1987) presented a review on the models available in the literature at that moment, dividing the heat transfer models in empirical, semi–empirical and zonal models. Each model provides an approach for calculation of the heat transfer coefficient, which can be purely related to convection effects, or present a combination of radiation and convection effects on a global heat transfer coefficient. The empirical models were the first attempts to model the engine heat transfer, such as the works of Nusselt, Van Tyen, Brilling and Eichelberg. Semi–empirical models are more accurate and were developed between 1960's and 1980's. Most of them are used until recently, such as the models proposed by: SITKEI and RAMANAIAH (1972), WOSCHNI (1967), HOHENBERG (1979) and ANNAND (1963). BORMAN and NISHIWAKI (1987) also had described the zonal models, which consider local variation of temperature in the walls. One example of this type of model was presented by WU and KNAPP (1981), who proposed a model for the thermal circuit, including convection between gases and cylinder wall, conduction through the cylinder wall and the convection between cylinder walls and coolant.

MOREL and KERIBAR (1985) categorise the heat transfer models in three generations. The first generation comprises the empirical models, the second comprises the semi–empirical models and the third generation comprises the models which consider the charge motion on the calculation of the heat transfer coefficient. Empirical and semi–empirical models include the turbulence effects in the models through the mean velocity of the piston. The third generation models are based on the kinetic energy of the fluid in order to estimate the heat transfer coefficient. MOREL and KERIBAR (1985) proposed a third generation model which

considers the viscous dissipation and the effects of swirl and squish.

GALLO (1988) presented a review on empirical and semi–empirical models, indicating that empirical models have only a historical relevance while semi-empirical models are more suitable for engine simulation. Since the heat transfer occurring during the compression, combustion and expansion strokes is more relevant, most models are not convenient for open phase. Hence the author indicated the use of the model proposed by NISHIWAKI *et al.* (1979) for modelling heat transfer occurring during the open phases.

FINOL and ROBINSON (2006) presented a more recent review on heat transfer models, dividing models in time–averaged, spatially–averaged and local. Time–averaged models can estimate the amount of heat transfer without modelling in–cylinder processes. Spatially–averaged models comprise the empirical, semi–empirical and fluid motion models. Those are the models used in phenomenological simulations, which are sufficient for predicting engine performance. For a more detailed analysis on NOx formation, a local model would be required, since the pollutant formation process is sensible to wall temperature. The pioneer for this method was LeFeuvre in 1969. FINOL and ROBINSON (2006) also commented on the application of the model proposed by Annand. This model considers the radiation effects in the calculation of the equivalent heat transfer coefficient. However, radiation has been verified to be significant on in CI engines because of soot formation, whereas it is negligible for SI engines.

2.3.2 Combustion

FAN and REITZ (2000) divided the combustion models into three main categories:

1. Semi-empirical models;
2. Flamelet models;
3. Flame propagation models.

Semi–empirical models have been used since the beginning of the development of simulations models for internal combustion engines. BLUMBERG *et al.* (1979) presented two examples of semi–empirical correlations for combustion rate, the cosine equation, which has not been used recently, and the aforementioned Wiebe equation, used until nowadays owing to its simplicity and to the possibility of calibration.

Flamelets models consist in assuming that the flame propagation can be interpreted as the diffusion of stretched laminar flames in a flame sheet (WILLIAMS, 1994) whereas flame propagation models are based on the assumption that the turbulence affects the flame speed. Therefore, those models rely on the calculation of a laminar flame speed, which is corrected to a turbulent flame speed according to the turbulence models (MEDINA *et al.*, 2014).

The Entrainment combustion model is obtained from the hypothesis that the laminar flame entrains part of the air–fuel mixture, being consumed thereafter. This model depends on the laminar velocity of the flame and sizes of the eddies entraining the mixture (VERHELST and SHEPPARD, 2009).

For multidimensional models, combustion modelling consists in solving the chemical reaction rates for chemical kinetics schemes, such as detailed chemical kinetics schemes, reduced schemes coupled to flamelet models.

2.3.3 Knock

Knock is an undesirable phenomena verified in SI engines consisting of oscillations in the in–cylinder pressure, which can cause damage and lead to engine failure (WANG *et al.*, 2017). These oscillations are induced by the autoignition of the unburned zone, or end–gas (Figure 2.12) during the combustion process. For an autoignition cycle to lead to knock, it is necessary enough volume and fuel in order to the second flame front to propagate and generate the acoustic effects. Consequently, knock onset has been observed for autoignition occurring between 50% and 70% of the MFB (STEURS *et al.*, 2014). The autoignition can be induced by many means, such as hot spots or the reactivity of the fuel, specially at low engine speed conditions, in which the combustion is longer and the end–gas is exposed to conditions of pressure and temperature, leading to the autoignition (GRIFFITHS, 1995).

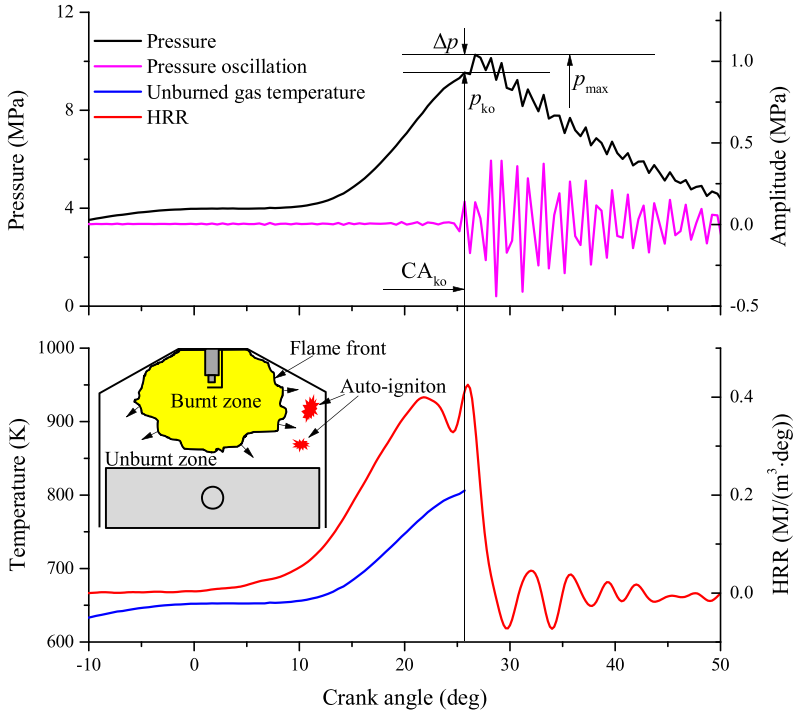

Figure 2.12: Combustion knock effects. Source: WANG *et al.* (2017).

Fuel reactivity, or sensibility to knock onset, has been tested for a long period of

time. Until recently, the parameter for indicating fuel sensibility to knock is the Octane Number (ON). There are two methods for measuring ON, the research (RON) and the motor (MON) tests (BRADLEY *et al.*, 2004; BURLUKA *et al.*, 2004). In these tests, the analysed fuel is compared to a primary research fuel (PRF), which consists of a mixture of n–heptane and iso–octane. A fuel with an ON of 0 has a knock sensibility comparable to that of the n–heptane whilst a fuel with an ON of 100 has a knock sensibility comparable to that of the iso–octane.

Methods for predicting knock onset have been suggested in the literature since the 1950's. The pioneers in presenting a model for knock onset prediction were LIVENGOOD and WU (1955). These authors proposed a hypothetical reaction, described by the Arrhenius equation, which provides a delay of autoignition for a given thermodynamic state. However, the conditions for the end–gases vary along the engine cycle, and thus the ratio between time and autoignition delay has to be integrated along the cycle. Whenever the integral reaches the unity value, the autoignition is assumed to occur. This method has become known as Knock Integral method (KIM). Experiments were conducted in a rapid compression machine in order to calibrate the model.

Other models have been proposed, among those, the model presented by HALSTEAD *et al.* (1975) and HALSTEAD *et al.* (1977), which has become known as "Shell model" (SCHREIBER *et al.*, 1994). This method consists in solving the chemical kinetics of six representative reactions for the unburned zone. More complex models can include schemes for simplified reactions mechanisms or detailed reaction mechanisms (GRIFFITHS, 1995). BURLUKA *et al.* (2004) compared the methods KIM, Shell, reduced and detailed chemical kinetics, highlighting the flexibility for calibration presented by the KIM. ELMQVIST *et al.* (2003) affirmed that knock prediction is a difficult task. However, the trends verified in simulations can bring helpful information for engine design. ELMQVIST *et al.* (2003) also indicated the simplicity of the KIM as an advantage comparing to those of the methods based on chemical kinetics.

One of the most important works on the calibration for the KIM was presented by DOUAUD and EYZAT (1978). These authors described means for including the ON in the calculation of the ignition delay, which is still used nowadays. Many revisions on the method can be found in the literature. As example, there are modifications for natural gas applications: FUIORESCU and RADU (2010), BECCARI *et al.* (2016) and SOYLU (2005), and modifications for including the effects of EGR: HOEPKE *et al.* (2012) and CHEN *et al.* (2014).

The disadvantage of this method is that there are reactions that prevail over others depending on the temperature regime. Consequently, a simple equation of Arrhenius is not sufficient for describing the effect of temperature on autoignition delay. This relation is presented in Figure 2.13. It is verified an intermediate temperature region, in which the increase of temperature leads to an increase of autoignition delay. This behaviour is known as NTC. Moreover,

n–heptane and iso–octane are paraffins, which present the NTC behaviour whereas commercial fuels can contain olefins and aromatics, which do not present the NTC behaviour (VILJOEN *et al.*, 2005). Moreover, alcohols have been used because of its renewable sources and they also do not present the NTC behaviour. Therefore, methods based only on the ON are not accurate since the ON is estimated based on a PRF composed by only two paraffin surrogates. An alternative for improving KIM accuracy would be fitting the parameters of the Arrhenius equation to the ON sensibility. The sensibility of the fuel to the method used for calculating ON can indicate the presence or absence of the NTC region in the autoignition characteristic of the fuel.

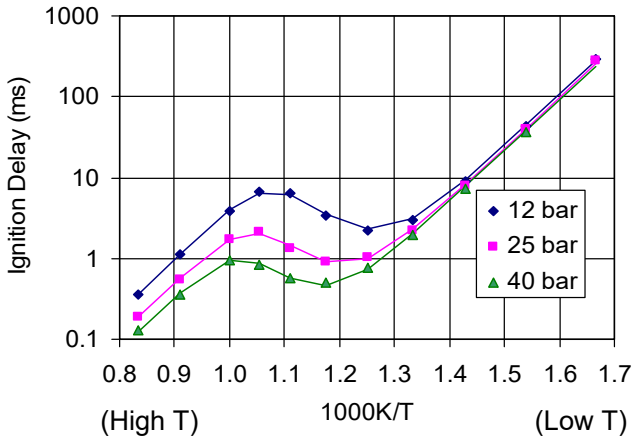

Figure 2.13: The NTC behaviour. Source: YATES *et al.* (2010).

Because of the NTC behaviour of most fuels, some authors had presented modifications for the KIM, considering many stages on the autoignition delay and calculating the knock integral by parts, such as the proposals of VILJOEN *et al.* (2005), YATES *et al.* (2010) and FANDAKOV *et al.* (2018).

ROBERT *et al.* (2015) indicated the use of multidimensional methods for knock onset prediction. RANS simulations have been used in order to predict knock for an average cycle, indicating local effects on autoignition. However, the main reason of implementing a multidimensional model would be the analysis of the stochastic behaviour of the knock onset, which cannot be performed on a RANS simulation because it relies on averaged calculations. In order to verify the stochastic nature of knock onset, the implementation of LES simulation was suggested. D'ADAMO *et al.* (2017) argued that LES simulations are computationally costly. Thus, it is possible to verify the cyclic nature of knock by running several simulations, in which the input parameters vary according to a statistical distribution.

VANCOILLIE *et al.* (2014) presented a calibration of the KIM for alcohols whilst SILEGHEM *et al.* (2015) performed a calibration of the method for blends of ethanol and iso-octane. The great advantage of alcohols on knock onset suppression is the higher heat of vaporisation compared to that of the hydrocarbons. Therefore, the MON and RON tests are

inadequate to indicate the knock sensibility of alcohols (YATES *et al.*, 2010). Moreover, alcohols increase the flame velocity, reducing combustion time whilst the autoignition delay is increased in the low temperature region (SYED *et al.*, 2011). STEURS *et al.* (2014) indicated that the advantages of higher heat of vaporisation of alcohols are more evident in direct injection engines, presenting a comparison between ethanol and iso–octane. The model proposed by YATES *et al.* (2010) was verified for ethanol by TOUGRI *et al.* (2017), obtaining satisfactory results. However, TOUGRI *et al.* (2017) highlighted that no work in the literature had systematically evaluated the knock sensibility of Brazilian hydrous ethanol, being the presence of water neglected in the previous studies.

2.4 Simulation based calibration

The task of controlling an engine consists in adjusting actuators in order to guarantee that the engine will operate under a desired condition. This condition is established according to an objective, which is chiefly determined by the manufacturer in order to reduce fuel consumption, reduce emissions and improve torque and driveability, subjected to safety restraints as maximum in–cylinder pressure and exhaust temperature (TEODOSIO *et al.*, 2017b). The objectives can be differently traced for each state of the engine, such as cold start, transient, steady full and partial load, deceleration and idle.

Under the author's view, the process of calibration can be divided in several steps. The first step consists in defining parameters directly related to an engine efficiency, performance, and emissions, such as: air–fuel ratio, spark timing, and load. However, these parameters can only be achieved by controlling engine components, such as: injectors, valves, ignition coil, and throttle. Therefore, the second step consists in determining the parameters related to the operation of engine components in order to achieve the objectives defined in the first step, such as: throttle position, dwell time, and injection pulse width. Subsequently, the final steps of calibration include the development of transient conditions, idle, cold start, and corrections. Thus, the initial phase of the calibration process consists in evaluating parameters that affects directly the thermodynamics processes, leading to the optimum performance according to the objectives of the engine's manufacturer.

The collection of parameters values for all conditions of load and engine speed create the calibration maps. Those maps are recorded into the ECU in the form of look–up tables. During the operation of the engine, the ECU receives data sent from sensors, such as oxygen concentration on exhaust gases, intake manifold pressure, air flow, water and oil temperature, and uses these data to determine the conditions (MALIKOPOULOS *et al.*, 2009). Once the engine condition is identified by the ECU, the values from the tables are loaded and corrected by using feedback signal from sensors. The final values are finally used for controlling

the actuation system of the engine.

Environmental concerns have motivated improvements in engine technology. Consequently, engines have become more complex with an increasing quantity of subsystems, including direct injection, variable valvetrain, variable compression ratio, turbocompressor control and exhaust gases recirculation (EGR). Each subsystem adds parameters that must be accounted on the calibration process. RASK and SELLNAU (2004) defined the calibration in bench as art and reaffirm that the effort for calibration grows exponentially with engine complexity. Calibration for optimum operation becomes impractical since each parameter cannot be optimised individually because of the interaction between degrees of freedom (MILLO *et al.*, 2010).

Design of Experiments (DoE) is a tool that has been explored as mean for reducing efforts for in–bech calibration (TEODOSIO *et al.*, 2017b; BOZZA *et al.*, 2017; GUERRIER and CAWSEY, 2004). Results obtained from the experiments are used for a statistical model or for a model–based optimisation. However, even with the implementation of DoE, the bench tests can be extensive for complex engines. Thus, Simulation Based Calibration (SBC) can be implemented in order to generate a pre–calibration that will help in the whole calibration process, reducing time and costs for tests in bench (TEODOSIO *et al.*, 2017b; BOZZA *et al.*, 2017; DE BELLIS *et al.*, 2013).

Therefore, SBC relies on numerical simulations, which provides data for a virtual calibration. This virtual calibration using SBC can be implemented for calibrating specific parameters, *e.g.*, optimal air–fuel ratio (LEI *et al.*, 2014), spark timing (XIAO *et al.*, 2013), and valve timing (ATASHKARI *et al.*, 2007). Moreover, SBC was also implemented for advanced calibration of engine control, including driveability issues on the process coupled with Hardware–in–the–loop simulations (DAMJI *et al.*, 2015), and the self adaptative real–time calibration in the vehicle (MALIKOPOULOS *et al.*, 2009).

There is no consensus in the literature about which type of simulation is more convenient for this application. The numerical models can be divided into data–based and physics–based models. Physics–based models are derived from the mathematical representation of the phenomena involved in the process occurring along the engine cycle. Three categories are found in the literature: the zero–dimensional or phenomenological models, which rely on the basic thermodynamic laws. This type of model can present a good accuracy compared to the data–based models but without the complexity of multi–dimensional models (GRASREINER *et al.*, 2017). Many authors present the uni–dimensional model as an intermediate solution between phenomenological models and the full computational fluid dynamics (CFD) simulation, bringing a good compromise of accuracy and computational performance (TEODOSIO *et al.*, 2017b; BOZZA *et al.*, 2017; D'ERRICO *et al.*, 2011; TEODOSIO *et al.*, 2017a). Complex three–dimensional models that couple CFD tools with chemical kinetics calculations can

be used to validate more simple models or can be implemented with DoE in order to reduce computational efforts, generating response surfaces used in the optimisation methods (BURK *et al.*, 2003). Data–based models allows a drastic reduction of computational time by using semi–empirical models or artificial intelligence schemes such as neural networks or evolutionary algorithms (ATKINSON and MOTT, 2005; ATASHKARI *et al.*, 2007). XIAO *et al.* (2013) discussed the limitation of data–based models, which have to be tuned with a good accuracy within a domain of operational conditions. Although physics–based models are developed following laws and theoretical remarks, their accuracy also depends on the validation performed with experimental data (RASK and SELLNAU, 2004).

The final task on SBC is the optimisation. After performing the simulations, an optimisation scheme has to be implemented. MILLO *et al.* (2010) divided the optimisation methods into three categories: numerical, direct search and explorative methods. Numerical methods can be implemented when an analytical expression is known. In the case of engine simulation, that can only be possible after fitting a mathematical expression on the data obtained from the simulation. Direct search are based on the identification of gradients on the objective function. Explorative methods are based on searching the optimal solution by statistical or genetic approaches. One of the challenges of calibration optimisation is the use of multi–objective functions. As mentioned before, calibration aims to reduce emissions, reduce fuel consumption and improve torque. The multi–objective aspect of calibration generates compromises, which can be evaluated by pareto methods (ATASHKARI *et al.*, 2007).

3. Kinematic model

As the proposed technology consists of a multi–link mechanism different from the conventional crank–rod mechanism. Consequently, the kinematics of the VSE engine is expected to be different from a conventional engine. Therefore, piston motion must be studied in order to perform an accurate thermodynamic simulation, which depends on instantaneous area and volume of the cylinder. Moreover, multidimensional effects that are not considered in the phenomenological model can be affected by piston kinematics, such as development of turbulence and charge motion (swirl and tumble).

Hence, the kinematics of the proposed mechanism is developed in this chapter. The equations are separated in Displacement, Velocity and Acceleration. By implementing the analytical dynamics equations of motion (SCHIEHLEN and EBERHARD, 1986), it will be shown in section 3.1 how the relations are non-linear for the displacement. The non-linearity implies that it is necessary to fit a model to determine the pivot position as a function of a given compression ratio and cubic capacity set. In addition, a comparison of the kinematics characteristics is performed between the new mechanism and the conventional one. The objective of this comparison is to indicate the changes in the motion of the piston that results from the implementation of the novel mechanism. This work will be detailed into the description of the mechanism, presentation of the strategy for controlling the stroke length and compression ratio, and the components of the mechanism. The methodology adopted for mapping and developing a relation between the input parameters and the configuration of the components is then presented. Subsequently, the kinematics of the mechanism and its comparison with a conventional engine are presented. The methods and results were published in the Journal of the Brazilian Society of Mechanical Sciences and Engineering (RUFINO and FERREIRA, 2018).

The laws of motion are written in terms of the variables displayed in Fig. 3.2. The reference points and angles indicated in the analysis are schemed in Fig. 3.2.

The dimensions defined in this work are the same of a prototype, currently being assembled. Those dimensions are given in Table 3.1:

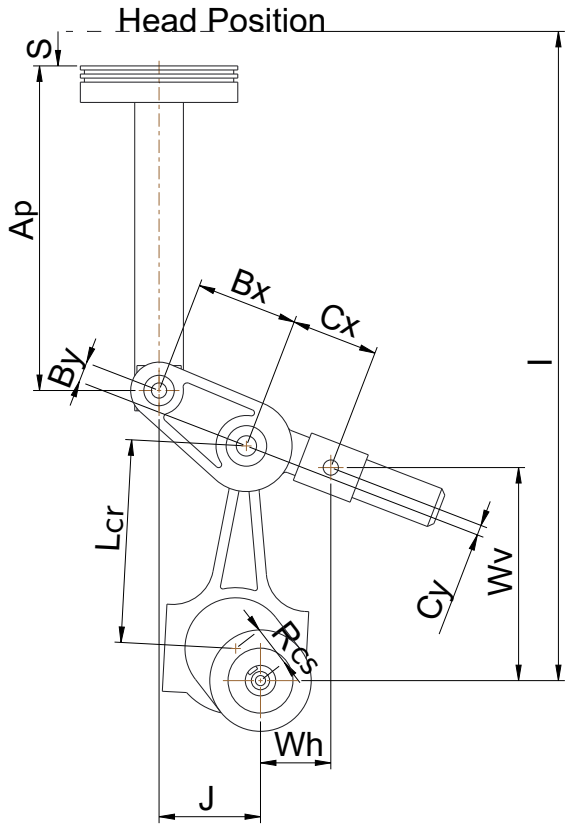

Figure 3.1: Dimensions used in the kinematic model.

Table 3.1: Dimensions of the mechanism

Dimension	Value $[mm]$
Cylinder diameter	68
A_p	155.4
B_x	60
B_y	18
C_y	8
R_{cs}	36
J	60
L_{cr}	117.8
I	356.2

3.1 Displacement

Initially, it is considered that an inertial referential is fixed with its origin coinciding with the centre of rotation of the crankshaft. According to the nomenclature herein adopted, the

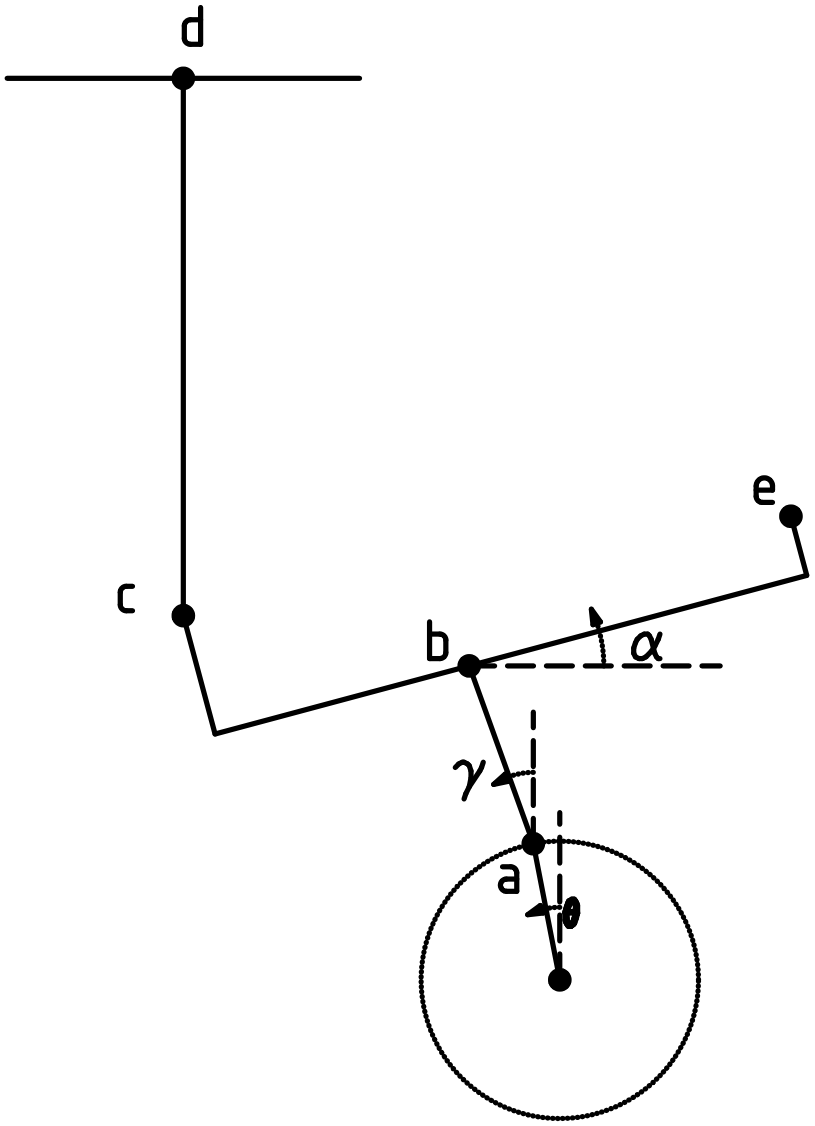

Figure 3.2: Angles and points for the kinematic analysis.

position of any point is represented by the vector $\vec{w}$.

The angular position of the crankshaft is given by θ, and the crank radius is given by R_{cs}. Hence, the position $\vec{w}_a$ (with respect to the inertial referential, which is considered to be fixed in the centre of rotation of the crankshaft) is determined in Eq. 3.1.

$$\vec{w}_a = \begin{bmatrix} \cos\theta & -\sin\theta \\ \sin\theta & \cos\theta \end{bmatrix} \begin{Bmatrix} 0 \\ R_{cs} \end{Bmatrix} = \begin{Bmatrix} -R_{cs}\sin\theta \\ R_{cs}\cos\theta \end{Bmatrix} \tag{3.1}$$

Similarly to the conventional crank-rod mechanism, the connecting rod is pinned to the crank. Its length is L_{cr}, and its inclination is given by γ, leading to the position $\vec{w}_b$ in Eq.

3.2.

$$\vec{w}_b = \vec{w}_a + \begin{bmatrix} \cos\gamma & -\sin\gamma \\ \sin\gamma & \cos\gamma \end{bmatrix} \begin{Bmatrix} 0 \\ L_{cr} \end{Bmatrix} = \begin{Bmatrix} -R_{cs}\sin\theta - L_{cr}\sin\gamma \\ R_{cs}\cos\theta + L_{cr}\cos\gamma \end{Bmatrix} \tag{3.2}$$

The point in which the piston's rod is connected moves according to the alternative displacement of the lever. By using the point b as the origin of the referential, the position $\vec{w}_c$ is given by Eq. 3.3 in which B is the length of the lever's left arm. And the position for point d is given by Eq. 3.4.

$$\vec{w}_c = \vec{w}_b + \begin{bmatrix} \cos\alpha & -\sin\alpha \\ \sin\alpha & \cos\alpha \end{bmatrix} \begin{Bmatrix} -B_x \\ B_y \end{Bmatrix} = \\ = \begin{Bmatrix} -R_{cs}\sin\theta - L_{cr}\sin\gamma - B_x\cos\alpha - B_y\sin\alpha \\ R_{cs}\cos\theta + L_{cr}\cos\gamma - B_x\sin\alpha + B_y\cos\alpha \end{Bmatrix} \tag{3.3}$$

$$\vec{w}_d = \vec{w}_c + \begin{Bmatrix} 0 \\ A_p \end{Bmatrix} = \begin{Bmatrix} -J \\ I - S \end{Bmatrix} \tag{3.4}$$

Note that the piston executes a reciprocating movement in the vertical direction. Thus, the horizontal position can be used as the boundary condition for the solution of the equations, as indicated in Eq. 3.5.

$$-R_{cs}\sin\theta - L_{cr}\sin\gamma - B_x\cos\alpha - B_y\sin\alpha = -J \tag{3.5}$$

And the piston's displacement S is given by Eq. 3.6.

$$S = I - R_{cs}\cos\theta - L_{cr}\cos\gamma + B_x\sin\alpha - B_y\cos\alpha - A_p \tag{3.6}$$

The position of the piston determines the instantaneous volume V of the combustion chamber, presented in Eq. 3.7, in which the diameter of the cylinder is represented by D_c.

$$V = S\frac{\pi D_c^2}{4} \tag{3.7}$$

The dislocated volume gives the Cubic Capacity (CC) in Eq. 3.8 and the Compression Ratio (CR) in Eq. 3.9.

$$CC = \left[\max(S) - \min(S)\right]\frac{\pi D_c^2}{4} \tag{3.8}$$

$$CR = \frac{CC}{\min(S)} + 1 \tag{3.9}$$

There are three unknown variables: α, γ and C_x. Therefore, it is necessary to obtain another two boundary conditions in order to solve the equations. The position of the pivot is imposed by the actuation system and as a result, is known. Calling the position of the pivot as a point e, its position $\vec{w}_e$ can be found by the relation presented in Eq. 3.10.

$$\vec{w}_e = \vec{w}_b + \begin{bmatrix} \cos\alpha & -\sin\alpha \\ \sin\alpha & \cos\alpha \end{bmatrix} \begin{Bmatrix} C_x \\ C_y \end{Bmatrix} = \\ = \begin{Bmatrix} -R_{cs}\sin\theta - L_{cr}\sin\gamma + C_x\cos\alpha - C_y\sin\alpha \\ R_{cs}\cos\theta + L_{cr}\cos\gamma - C_x\sin\alpha + C_y\cos\alpha \end{Bmatrix} \tag{3.10}$$

The relation in Eq. 3.10 must be equal to the imposed position of the pivot, leading to Eq. 3.11.

$$\begin{Bmatrix} -R_{cs}\sin\theta - L_{cr}\sin\gamma + C_x\cos\alpha - C_y\sin\alpha \\ R_{cs}\cos\theta + L_{cr}\cos\gamma - C_x\sin\alpha + C_y\cos\alpha \end{Bmatrix} = \begin{Bmatrix} W_h \\ W_v \end{Bmatrix} \tag{3.11}$$

As the unknown variables are trigonometric function's arguments, no analytical solution can be easily found. Therefore, it was opted to solve the system numerically by implementing the Newton–Rapshon technique.

3.2 Velocity

The velocity relations are obtained assuming that the crankshaft is rotating at a constant speeds, given by $\dot{\theta}$. Thus, the velocity of point a is given by Eq. 3.12.

$$\dot{\vec{w}}_a = \begin{bmatrix} 0 & -\dot{\theta} \\ \dot{\theta} & 0 \end{bmatrix} \begin{bmatrix} \cos\theta & -\sin\theta \\ \sin\theta & \cos\theta \end{bmatrix} \begin{Bmatrix} 0 \\ R_{cs} \end{Bmatrix} = \begin{Bmatrix} -\dot{\theta}R_{cs}\cos\theta \\ -\dot{\theta}R_{cs}\sin\theta \end{Bmatrix} \tag{3.12}$$

Adding the rotational motion of the crank with the rotational motion of the connecting rod, the velocity of point b is given by Eq. 3.13.

$$\dot{\vec{w}}_b = \dot{\vec{w}}_a + \begin{bmatrix} 0 & -\dot{\gamma} \\ \dot{\gamma} & 0 \end{bmatrix} \begin{bmatrix} \cos\gamma & -\sin\gamma \\ \sin\gamma & \cos\gamma \end{bmatrix} \begin{Bmatrix} 0 \\ L_{cr} \end{Bmatrix} = \begin{Bmatrix} -\dot{\theta}R_{cs}\cos\theta - \dot{\gamma}L_{cr}\cos\gamma \\ -\dot{\theta}R_{cs}\sin\theta - \dot{\gamma}L_{cr}\sin\gamma \end{Bmatrix} \tag{3.13}$$

And the velocity of point c can be found by summing the reciprocating motion of the lever to the motion of point b, yielding to Eq. 3.14.

$$\dot{\vec{w}}_c = \dot{\vec{w}}_b + \begin{bmatrix} 0 & -\dot{\alpha} \\ \dot{\alpha} & 0 \end{bmatrix} \begin{bmatrix} \cos\alpha & -\sin\alpha \\ \sin\alpha & \cos\alpha \end{bmatrix} \begin{Bmatrix} B_x \\ B_y \end{Bmatrix} \tag{3.14}$$

As the point d follows point c, their velocities are the same, i.e., $\dot{\vec{w}}_d = \dot{\vec{w}}_c$, and since the piston executes a reciprocating trajectory in the vertical direction, the horizontal component presented in Eq. 3.15 can be used as boundary condition.

$$\dot{\vec{w}}_c = \begin{Bmatrix} -\dot{\theta}R_{cs}\cos\theta - \dot{\gamma}L_{cr}\cos\gamma + \dot{\alpha}B_x\sin\alpha - \dot{\alpha}B_y\cos\alpha \\ -\dot{\theta}R_{cs}\sin\theta - \dot{\gamma}L_{cr}\sin\gamma - \dot{\alpha}B_x\cos\alpha - \dot{\alpha}B_y\sin\alpha \end{Bmatrix} = \begin{Bmatrix} 0 \\ -\dot{S} \end{Bmatrix} \tag{3.15}$$

Similarly to the displacement model, there are three unknown variables, being the angular velocities $\dot{\gamma}$ and $\dot{\alpha}$ and the rate of change in the arm length $\dot{C}_x$ and consequently, it is necessary to obtain three boundary conditions to solve the equations. Since this study is made to the mechanism operating at stable conditions, the pivot is assumed to be static, and thus the velocity of the pivot is null, leading to Eq. 3.16.

$$\dot{\vec{w}}_e = \dot{\vec{w}}_b + \begin{bmatrix} 0 & -\dot{\alpha} \\ \dot{\alpha} & 0 \end{bmatrix} \begin{bmatrix} \cos\alpha & -\sin\alpha \\ \sin\alpha & \cos\alpha \end{bmatrix} \begin{Bmatrix} C_x \\ C_y \end{Bmatrix} + \begin{bmatrix} \cos\alpha & -\sin\alpha \\ \sin\alpha & \cos\alpha \end{bmatrix} \begin{Bmatrix} \dot{C}_x \\ 0 \end{Bmatrix} \tag{3.16}$$

Expanding the terms in Eq. 3.16 yields to Eq. 3.17.

$$\dot{\vec{w}}_e = \begin{Bmatrix} -\dot{\theta}R_{cs}\cos\theta - \dot{\gamma}L_{cr}\cos\gamma - \dot{\alpha}C_x\sin\alpha - \dot{\alpha}C_y\cos\alpha + \dot{C}_x\cos\alpha \\ -\dot{\theta}R_{cs}\sin\theta - \dot{\gamma}L_{cr}\sin\gamma + \dot{\alpha}C_x\cos\alpha - \dot{\alpha}C_y\sin\alpha + \dot{C}_x\sin\alpha \end{Bmatrix} = \begin{Bmatrix} 0 \\ 0 \end{Bmatrix} \tag{3.17}$$

The velocity of the piston is given by Eq. 3.15. Note that this relation does not depend on $\dot{C}_x$. Therefore, using the boundary conditions given by Eqs. 3.15 and 3.17 it is possible to eliminate $\dot{C}_x$ and define $\dot{\alpha}$ and $\dot{\gamma}$ in analytical expressions indicated in Eqs. 3.18 and 3.19, respectively.

$$\dot{\alpha} = \frac{\dot{\theta}R_{cs}\sin(\theta-\alpha) + \dot{\gamma}L_{cr}\sin(\gamma-\alpha)}{C_x} \tag{3.18}$$

$$\dot{\gamma} = \frac{\dot{\theta} R_{cs}}{L_{cr}} \frac{\left(\frac{B_x \sin\alpha - B_y \cos\alpha}{C_x}\right) \sin(\theta - \alpha) - \cos\theta}{\cos\gamma - \left(\frac{B_x \sin\alpha - B_y \cos\alpha}{C_x}\right) \sin(\gamma - \alpha)} \tag{3.19}$$

For $\dot{C}_x$, one of the relations given by 3.17 is used, resulting in Eq. 3.20.

$$\dot{C}_x = \frac{\dot{\theta} R_{cs} \cos\theta + \dot{\gamma} L_{cr} \cos\gamma + \dot{\alpha} (C_x \sin\alpha + C_y \cos\alpha)}{\cos\alpha} \tag{3.20}$$

Note that any of the components of 3.17 could be used to determine $\dot{C}_x$. However, it was preferred to use the horizontal component since the relation obtained has $\cos\alpha$ as the denominator, and since α assumes values near to zero, the equation is computationally stable.

3.3 Acceleration

As mentioned above, this analysis will be carried out considering the crankshaft to be rotating at a constant speed. Consequently, the acceleration of point a is given only by the centripetal component indicated in Eq. 3.21.

$$\ddot{\vec{w}}_a = \begin{bmatrix} 0 & -\dot{\theta} \\ \dot{\theta} & 0 \end{bmatrix}^2 \begin{bmatrix} \cos\theta & -\sin\theta \\ \sin\theta & \cos\theta \end{bmatrix} \begin{Bmatrix} 0 \\ R_{cs} \end{Bmatrix} = \begin{Bmatrix} \dot{\theta}^2 R \sin\theta \\ -\dot{\theta}^2 R \cos\theta \end{Bmatrix} \tag{3.21}$$

And for point b there are centripetal and tangential components since $\dot{\gamma}$ is not constant, as indicated in Eq. 3.22, leading to Eq. 3.23.

$$\ddot{\vec{w}}_b = \ddot{\vec{w}}_a + \left(\begin{bmatrix} 0 & -\ddot{\gamma} \\ \ddot{\gamma} & 0 \end{bmatrix} + \begin{bmatrix} 0 & -\dot{\gamma} \\ \dot{\gamma} & 0 \end{bmatrix}^2 \right) \begin{bmatrix} \cos\gamma & -\sin\gamma \\ \sin\gamma & \cos\gamma \end{bmatrix} \begin{Bmatrix} 0 \\ L_{cr} \end{Bmatrix} \tag{3.22}$$

$$\ddot{\vec{w}}_b = \begin{Bmatrix} \dot{\theta}^2 R \sin\theta + \dot{\gamma}^2 L \sin\gamma - \ddot{\gamma} L_{cr} \cos\gamma \\ -\dot{\theta}^2 R \cos\theta - \dot{\gamma}^2 R \cos\gamma - \ddot{\gamma} L_{cr} \sin\gamma \end{Bmatrix} \tag{3.23}$$

Similarly, for point c ($\dot{\alpha}$ is not constant also), the aceleration is given by Eq. 3.24, leading to Eq. 3.25.

$$\ddot{\vec{w}}_c = \ddot{\vec{w}}_b + \left(\begin{bmatrix} 0 & -\ddot{\alpha} \\ \ddot{\alpha} & 0 \end{bmatrix} + \begin{bmatrix} 0 & -\dot{\alpha} \\ \dot{\alpha} & 0 \end{bmatrix}^2 \right) \begin{bmatrix} \cos\alpha & -\sin\alpha \\ \sin\alpha & \cos\alpha \end{bmatrix} \begin{Bmatrix} -B_x \\ B_y \end{Bmatrix} \tag{3.24}$$

$$\ddot{\vec{w}}_c = \left\{ \begin{array}{l} \dot{\theta}^2 R\sin\theta + \dot{\gamma}^2 L\sin\gamma - \ddot{\gamma} L_{cr}\cos\gamma + \\ -\dot{\theta}^2 R\cos\theta - \dot{\gamma}^2 R\cos\gamma - \ddot{\gamma} L_{cr}\sin\gamma - \\ \qquad + \dot{\alpha}^2\left(B_x\cos\alpha + B_y\sin\alpha\right) - \ddot{\alpha}\left(-B_x\sin\alpha + B_y\cos\alpha\right) \\ \qquad - \dot{\alpha}^2\left(-B_x\sin\alpha + B_y\cos\alpha\right) - \ddot{\alpha}\left(B_x\cos\alpha + B_y\sin\alpha\right) \end{array} \right\} \tag{3.25}$$

The relation above becomes the first boundary condition to solve the equations of acceleration, since it represents the acceleration of the piston, which is null in the horizontal component, as demonstrated in Eq. 3.26.

$$\ddot{\vec{w}}_c = \left\{ \begin{array}{c} 0 \\ -\ddot{S} \end{array} \right\} \tag{3.26}$$

To determine the remaining variables, it is used again the acceleration of point e as boundary condition. Since the arm length C_x varies, the acceleration of that point depends on the coriolis acceleration and relative acceleration besides the centripetal and tangential components, as indicated in Eq. 3.27.

$$\begin{aligned} \ddot{\vec{w}}_e = \ddot{\vec{w}}_b + \left(\left[\begin{array}{cc} 0 & -\ddot{\alpha} \\ \ddot{\alpha} & 0 \end{array} \right] + \left[\begin{array}{cc} 0 & -\dot{\alpha} \\ \dot{\alpha} & 0 \end{array} \right]^2 \right) \left[\begin{array}{cc} \cos\alpha & -\sin\alpha \\ \sin\alpha & \cos\alpha \end{array} \right] \left\{ \begin{array}{c} C_x \\ C_y \end{array} \right\} + \\ + 2 \left[\begin{array}{cc} 0 & -\dot{\alpha} \\ \dot{\alpha} & 0 \end{array} \right] \left[\begin{array}{cc} \cos\alpha & -\sin\alpha \\ \sin\alpha & \cos\alpha \end{array} \right] \left\{ \begin{array}{c} \dot{C}_x \\ 0 \end{array} \right\} + \left[\begin{array}{cc} \cos\alpha & -\sin\alpha \\ \sin\alpha & \cos\alpha \end{array} \right] \left\{ \begin{array}{c} \ddot{C}_x \\ 0 \end{array} \right\} \end{aligned} \tag{3.27}$$

By expanding the terms in Eq. 3.27, Eq. 3.28 is obtained.

$$\ddot{\vec{w}}_e = \left\{ \begin{array}{l} \dot{\theta}^2 R\sin\theta + \dot{\gamma}^2 L\sin\gamma - \ddot{\gamma} L_{cr}\cos\gamma - \dot{\alpha}^2\left(C_x\cos\alpha - C_y\sin\alpha\right) - \\ -\dot{\theta}^2 R\cos\theta - \dot{\gamma}^2 L\cos\gamma - \ddot{\gamma} L_{cr}\sin\gamma - \dot{\alpha}^2\left(C_x\sin\alpha + C_y\cos\alpha\right) + \\ \qquad - \ddot{\alpha}\left(C_x\sin\alpha + C_y\cos\alpha\right) - 2\dot{\alpha}\dot{C}_x\sin\alpha + \ddot{C}_x\cos\alpha \\ \qquad + \ddot{\alpha}\left(C_x\cos\alpha - C_y\sin\alpha\right) + 2\dot{\alpha}\dot{C}_x\cos\alpha + \ddot{C}_x\sin\alpha \end{array} \right\} = \left\{ \begin{array}{c} 0 \\ 0 \end{array} \right\} \tag{3.28}$$

Again, the unknown variables are: $\ddot{\alpha}$, $\ddot{\gamma}$ and $\ddot{C}_x$. By using the three given boundary conditions shown in Eqs. 3.29 and 3.30.

$$\ddot{\alpha} = \frac{\dot{\theta}^2 R\cos\left(\theta - \alpha\right) + \dot{\gamma}^2 L\cos\left(\gamma - \alpha\right) + \ddot{\gamma} L_{cr}\sin\left(\gamma - \alpha\right) + \dot{\alpha}^2 C_y - 2\dot{\alpha}\dot{C}_x}{C_x} \tag{3.29}$$

$$\ddot{\gamma} = \left\{ L_{cr} \left[\cos\gamma + \frac{\sin(\gamma-\alpha)}{C_x} \left(-B_x \sin\alpha + B_y \cos\alpha \right) \right] \right\}^{-1} \left\{ \dot{\theta}^2 R \sin\theta + \right.$$
$$+ \dot{\gamma}^2 L \sin\gamma + \dot{\alpha}^2 \left(B_x \cos\alpha + B_y \sin\alpha \right) -$$
$$\left. - \frac{\left(B_y \cos\alpha - B_x \sin\alpha \right)}{C_x} \left[\dot{\theta}^2 R \cos(\theta-\alpha) + \dot{\gamma}^2 L \cos(\gamma-\alpha) + \dot{\alpha}^2 C_y - 2\dot{\alpha}\dot{C}_x \right] \right\} \quad (3.30)$$

The acceleration of the piston is given by Eq. 3.26.

3.4 Interpolation of the control parameters

A model to link cubic capacity and compression ratio to the position of the pivot is described in this section. In the previous sections, it was explained why the need to develop such relation arises, since the relations of motion are not linear. Moreover, as a simulation of engine performance would require the evaluation of the mechanism operating at several different conditions, the adjustment *ad hoc* would not be convenient.

The strategy adopted was to map the entire range of operation of the mechanism, giving the compression ratio and cubic capacity to each pair of coordinates of the pivot (Fig. 3.3).

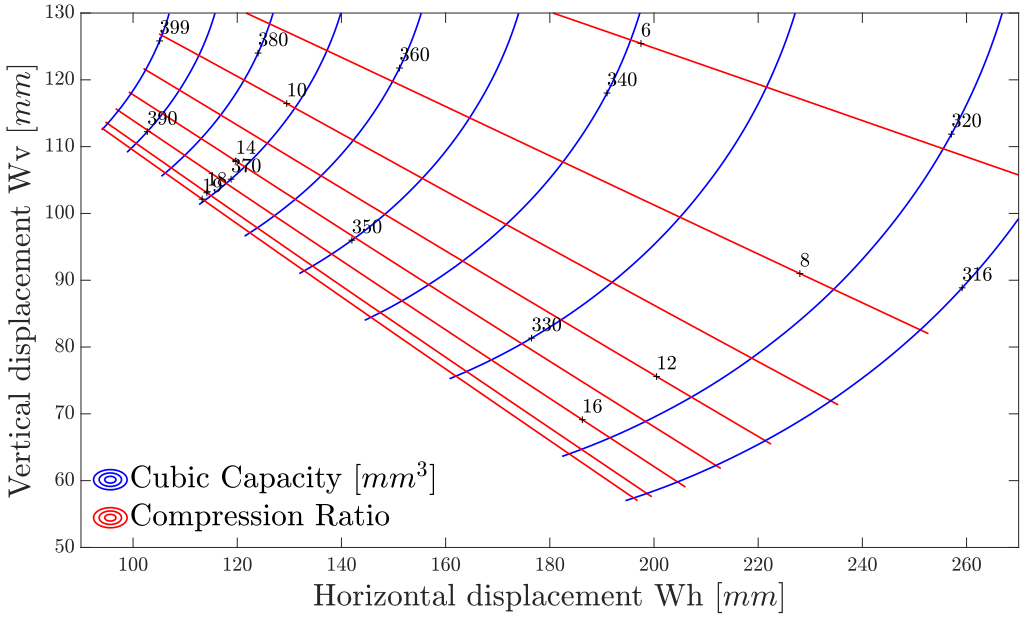

Figure 3.3: Base map for interpolation.

However, it is desired to obtain the position of the pivot as a function of cubic capacity and compression ratio instead of the other way around. Therefore, the coordinates were determined as a function of the engine parameters (Fig. 3.4).

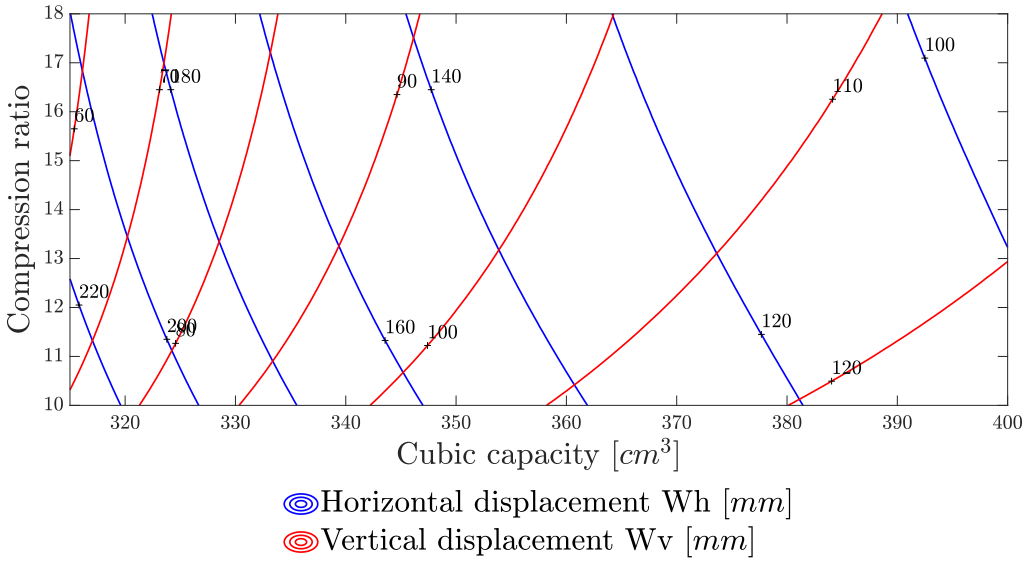

Figure 3.4: Map of set for the position of the pivot.

Although both components of the displacement have influence on both parameters, the horizontal component is strongly linked to the cubic capacity while the vertical component is strongly linked to the compression ratio. Thus, it was opted to develop two expressions in the following form:

$$W_h = W_h\left(CC, CR\right) \rightarrow W_h\left(CC, f\left(CR\right)\right) \tag{3.31}$$

and

$$W_v = W_v\left(CR, CC\right) \rightarrow W_v\left(CR, f\left(CC\right)\right) \ . \tag{3.32}$$

By performing a regression, the relation presented in Eq. 3.33 was found, wherein a_{W_h}, b_{W_h} and c_{W_h} are respectively given by Eqs. 3.34, 3.35 and 3.36.

$$W_h = a_{W_h} \exp\left(\frac{b_{W_h}}{CC} + \frac{c_{W_h}}{CC^2}\right) \tag{3.33}$$

$$a_{W_h} = {}_1a_{W_h} + {}_2a_{W_h} \ln\left(CR\right) \tag{3.34}$$

$$b_{W_h} = {}_1b_{W_h} + \frac{{}_2b_{W_h}}{CR} + \frac{{}_3b_{W_h}}{CR^2} \tag{3.35}$$

$$c_{W_h} = {}_1c_{W_h} + {}_2c_{W_h} \ln\left(CR\right) + {}_3c_{W_h} \ln^2\left(CR\right) \tag{3.36}$$

And for the vertical component, the relation presented in Eq. 3.37 was found, wherein a_{W_v}, b_{W_v} and c_{W_v} are respectively given by Eqs. 3.38, 3.38 and 3.38.

$$W_v = a_{W_v} \exp\left(\frac{b_{W_v}}{CR} + \frac{c_{W_v}}{CR^2}\right) \tag{3.37}$$

$$a_{W_v} = {}_1a_{W_v} + {}_2a_{W_v} \ln(CC) + {}_3a_{W_v} \ln^2(CC) \tag{3.38}$$

$$b_{W_v} = {}_1b_{W_v} \exp\left(\frac{{}_2b_{W_v}}{CC} + \frac{{}_3b_{W_v}}{CC^2}\right) \tag{3.39}$$

$$c_{W_v} = {}_1c_{W_v} + \frac{{}_2c_{W_v}}{CC} + \frac{{}_3c_{W_v}}{CC^2} \tag{3.40}$$

The variables proposed were determined by the implementation of the least squares method, leading to the values presented in Tab. 3.2:

Table 3.2: Parameters of the interpolation

Parameter	Value
${}_1a_{W_h}$	-224.856647
${}_2a_{W_h}$	119.792433
${}_1b_{W_h}$	-1582.807539
${}_2b_{W_h}$	7892.012552
${}_3b_{W_h}$	39677.439377
${}_1c_{W_h}$	-821563.554214
${}_2c_{W_h}$	730561.355817
${}_3c_{W_h}$	-110027.677793
${}_1a_{W_v}$	-23936.295463
${}_2a_{W_v}$	7977.219991
${}_3a_{W_v}$	-661.899957
${}_1b_{W_v}$	137589.999804
${}_2b_{W_v}$	-7830.134472
${}_3b_{W_v}$	1380900.8319
${}_1c_{W_v}$	89.819454
${}_2c_{W_v}$	-78474.864516
${}_3c_{W_v}$	17192106.2599

The relations presented an average percent deviation (STOECKER, 1980) of 0.44% for both W_h and W_v. Note that there is an error of precision between the desired set of compression ratio/cubic capacity and the effective values of both. By comparing the results obtained with the assigned values it was found an average percent deviation of 0.94% in the compression ratio and 0.17% in the cubic capacity.

The described model was implemented and run in a FORTRAN 95 code. The generated results were then loaded to the platform Matlab to perform the analysis. This analysis

consists in verifying the desired characteristics mentioned in the previous sections, and it is exposed in this section. The desired characteristics are: stroke–bore ratio, effects of cubic capacity and compression ratio variation on kinematics and a comparison with the kinematics of a conventional engine.

3.5 Stroke–bore ratio

As explained before, a small ratio of stroke–bore is undesirable since it harms efficiency. Thus, it is important to verify how the stroke-bore ratio is varying with Cubic Capacity for the configuration of the mechanism. The Stroke length was calculated to each condition of cubic capacity (Fig. 3.5).

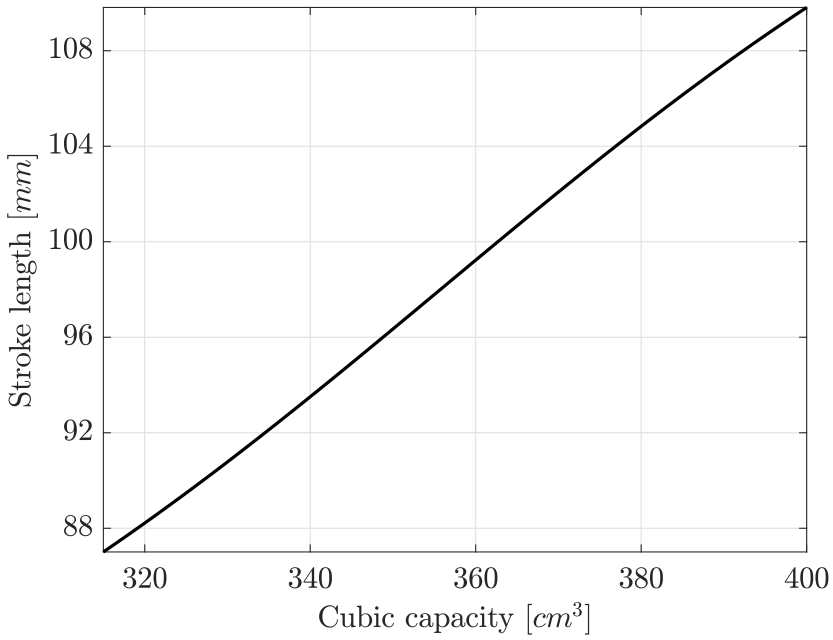

Figure 3.5: Stroke length as function of the cubic capacity.

The components of the mechanism were designed in a manner that the stroke length-bore relation would not be less than 1 for the entire range of cubic capacity (Fig. 3.6).

It is mentioned in SIEWERT (1978) that the effects of heat transfer and flame speed are only observed at small values of stroke–bore ratio (less than 0.5). Consequently, it is not expect to find issues associated to efficiency reduction owing to strok length diminishing.

3.6 Influence of compression ratio on kinematics

It was shown how the position profile of the piston behaves as the compression ratio is altered (Fig. 3.7). It was also highlighted the increasing of the clearance volume with

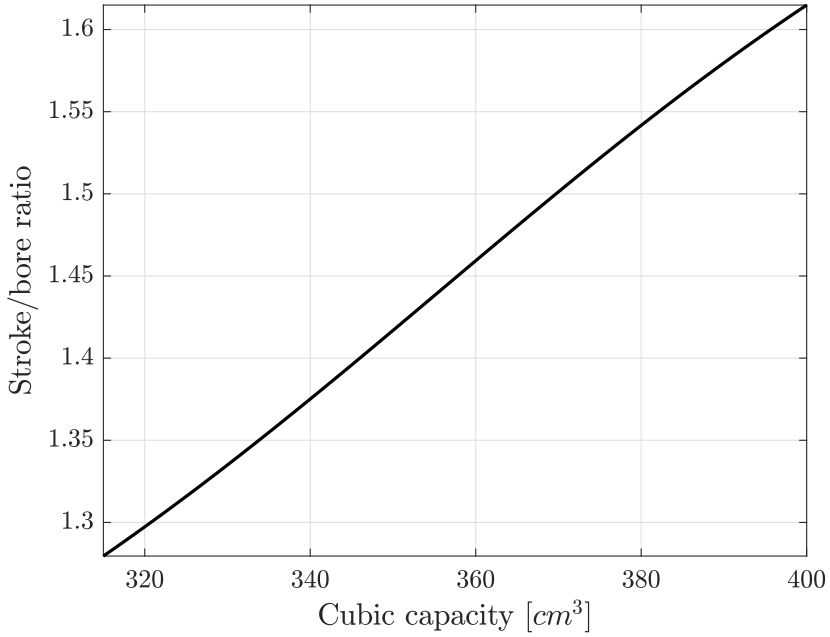

Figure 3.6: Stroke length–bore ratio.

the decrease in the compression ratio and how this relation is not linear.

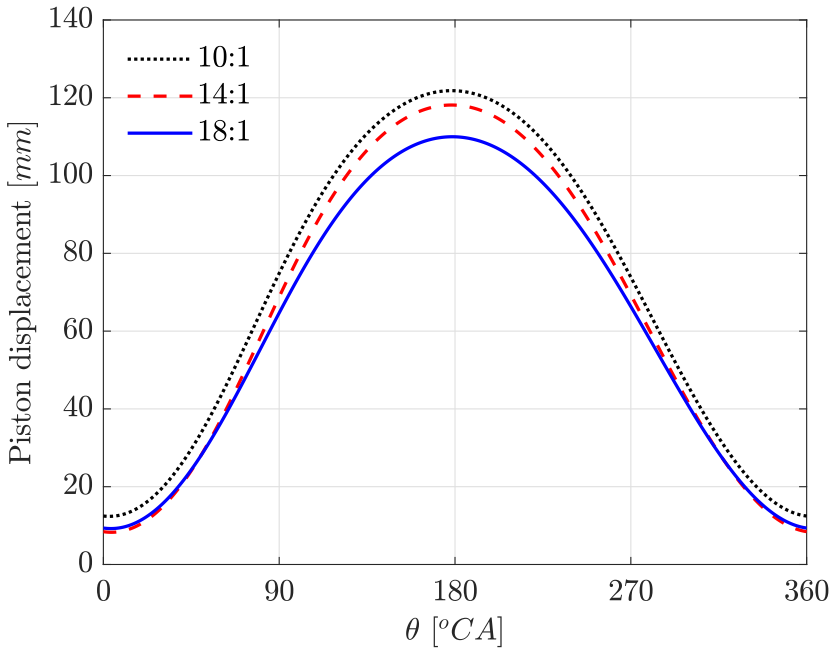

Figure 3.7: Effect of the compression ratio on the position profile of the piston.

The displacement profile practically suffered no modification with a variation on the compression ratio (Fig. 3.7). Actually, the adjustment of compression ratio is performed by altering the inclination of the lever. That causes a shift on TDC and BDC that is explained on section 3.8.

3.7 Influence of cubic capacity on kinematics

The increase in the stroke length is accompanied by an increase in cubic capacity, as stated by Eq. 3.8 (Fig. 3.8). Another aspect of the displacement when cubic capacity was adjusted is the position of TDC, which is illustrated in Section 3.8. The variation on the position of TDC occurs whenever cubic capacity was made without changing the compression ratio. That happens because compression ratio is given by the ratio between maximum volume and minimum volume (clearance volume) of the combustion chamber. If the dislocated volume is changed, the clearance volume has to vary in order to keep the ratio constant (12:1 in the case of Fig. 3.8). This feature characterises a great disadvantage of VSE mechanisms that only allow the adjustment of stroke length. In those cases, it is impossible to adjust cubic capacity maintaining compression ratio constant.

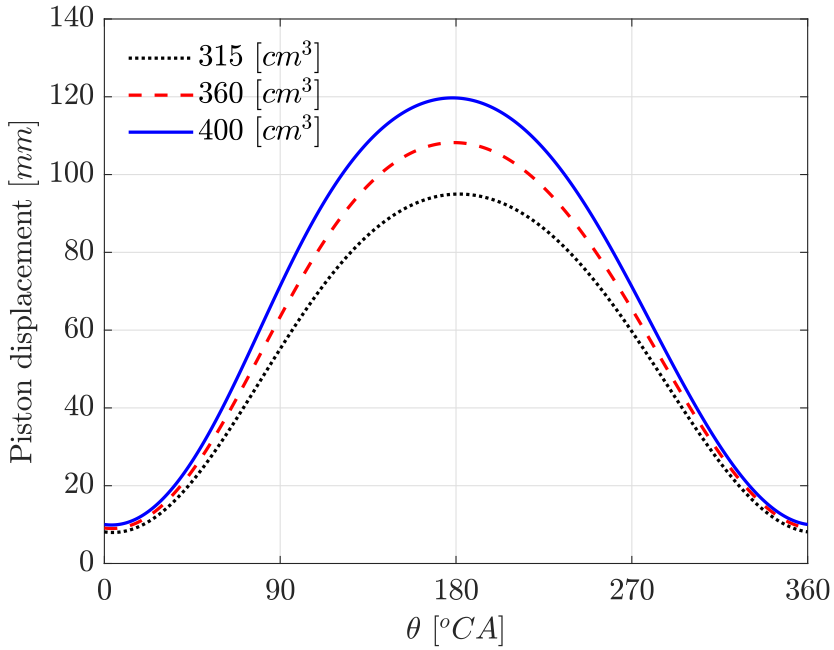

Figure 3.8: Displacement profile of the piston.

The variation of cubic capacity affects the velocity profile by increasing its amplitude as cubic capacity rises. This happens because the lengthening of the stroke requires a higher velocity for the piston to run its stroke in the same period of time (Fig. 3.9). Moreover, the position of the pivot affects the motion of the lever, changing the position of the velocity peak, around 90 °CA (Crank Angle degree). The effect of engine speed is only related to the amplitude of both velocity and acceleration. Thus, the effects on the profiles will be the same independently of the engine speed.

Similarly to the velocity profile, it was not observed significant changes in the profile of acceleration with the reduction in the stroke length unless by the decrease in the amplitude

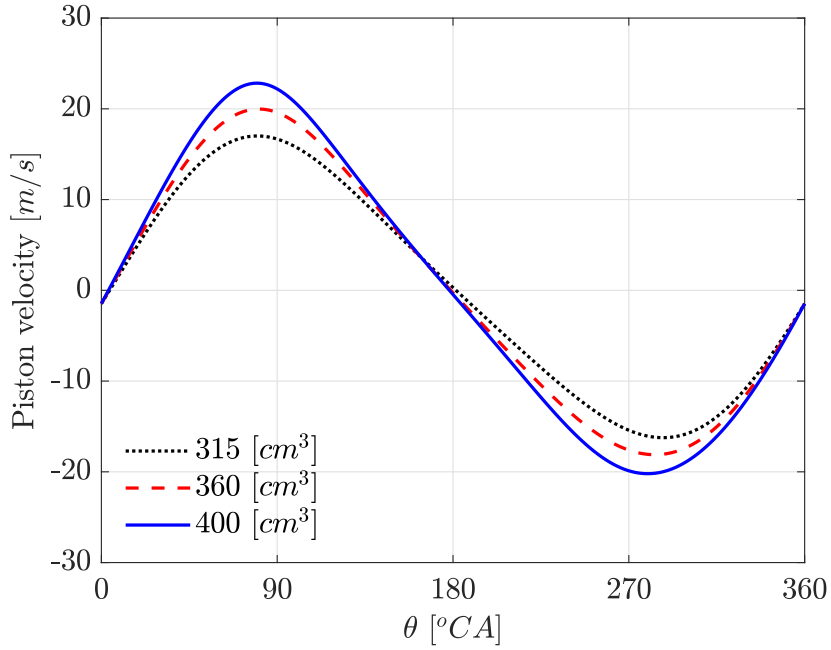

Figure 3.9: Velocity profile of the piston.

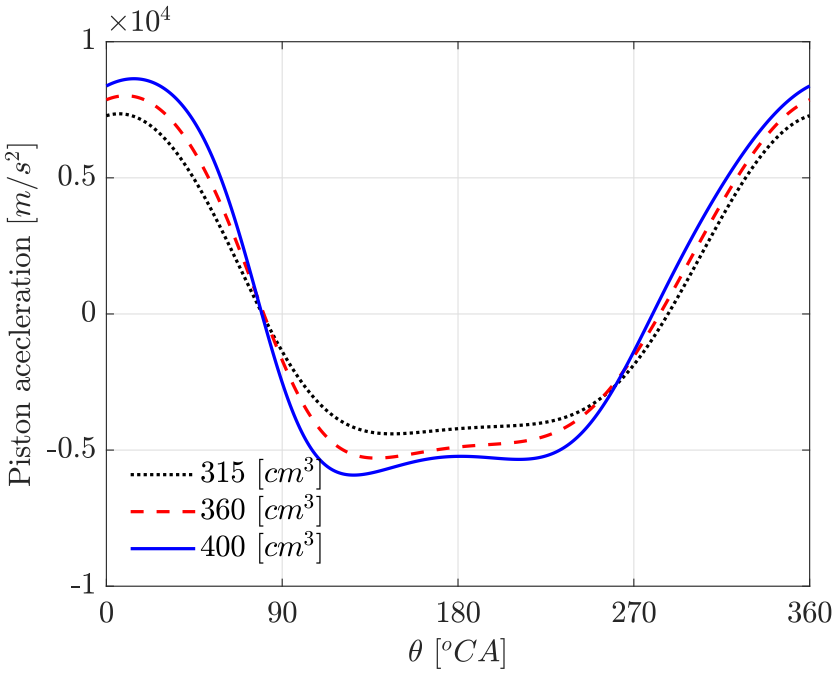

Figure 3.10: Acceleration profile of the piston.

(Fig. 3.10). Moreover, a slight asymmetry in the profile was observed.

3.8 Phase shift of TDC and BDC

When the mechanism is static at $\theta = 0°CA$, it is perceived that the connecting rod is slightly tilted, which means that the TDC does not occur at exactly $\theta = 0°CA$, neither the

BDC occurs at $\theta = 180°CA$ (Figs. 1.7 and 1.8). Therefore, it was noted that the TDC and BDC position depends on the configuration of the mechanism. For the entire range of compression ratio and cubic capacity, the phase shifts on TDC and BDC were calculated and mapped (Figs. 3.11 and 3.12).

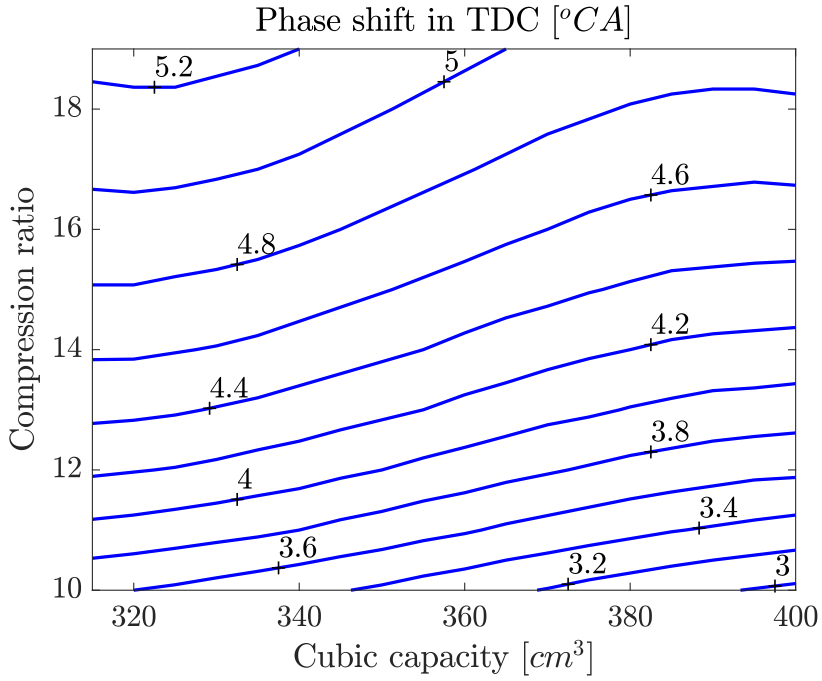

Figure 3.11: Phase shift in TDC.

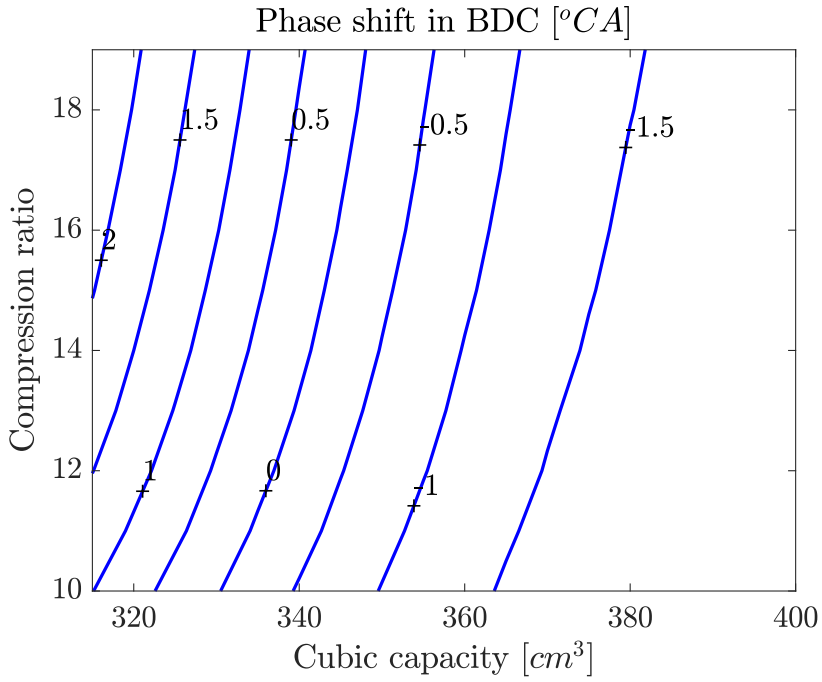

Figure 3.12: Phase shift in BDC.

The phase shift in the TDC was strongly related to the Compression ratio, assuming

values from +3 °CA to +5.2 °CA, always positive. On the other hand, it was verified that the phase shift of BDC was almost symmetric, going from -1.5 °CA to +2°CA and it was strongly dependent on Cubic Capacity.

This phase shift is not to be expected as a drawback, since the calibration of ECU can easily identify the shift and correct events dependent on TDC and BDC, such as spark timing. Even if the engine does not allow to control valve phasing, the magnitude of the phase shift in the TDC and BDC would not harm the gas exchange process. This effect of the phase shift is already observed when conventional crank–rod mechanism presents an eccentricity, *i.e.*, when the axis of the cylinder is not aligned with the crankshaft axis in order to minimise lateral forces on the piston's head.

3.9 Comparison with the conventional mechanism

One of the main concerns in the design of the proposed mechanism is to preserve the kinematics characteristics observed in a conventional crank–rod mechanism. In order to verify that, it was simulated the kinematics of a conventional mechanism with the same Cubic Capacity of the proposed mechanism in the simulated condition. As the crank length is greater in a conventional engine for reasons explained in section 1.2, the connecting rod of the model simulated was increased to keep the same ratio rod length/crank length.

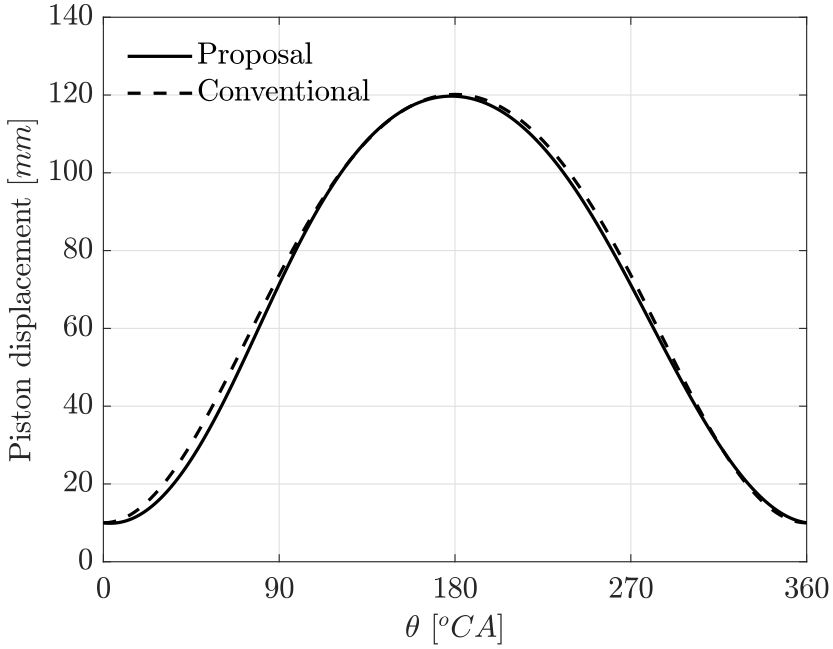

Figure 3.13: Comparison with a conventional engine, position profile.

There is a slight difference between the kinematics of a conventional engine and the proposed one (Figs. 3.13, 3.14 and 3.15). This difference was measured for all conditions of

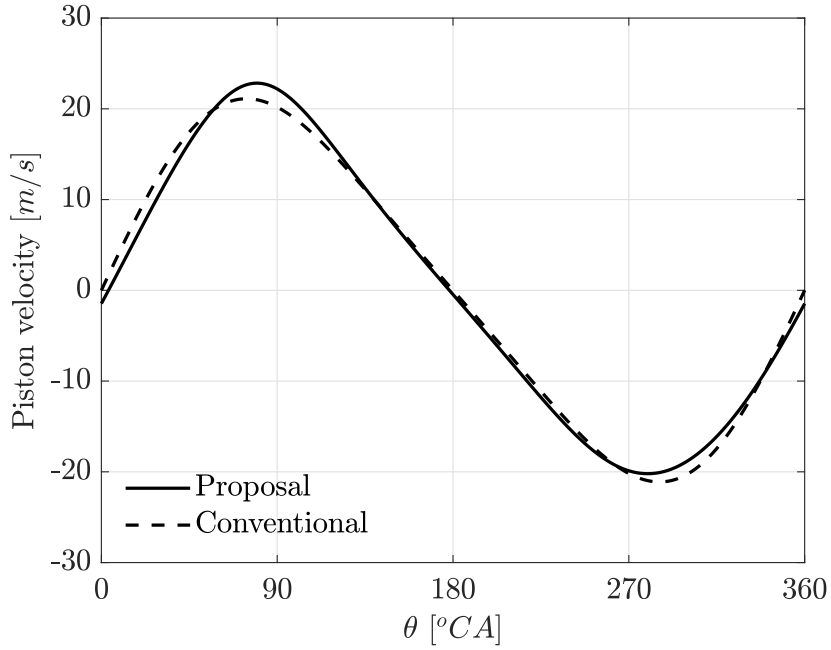

Figure 3.14: Comparison with a conventional engine, velocity profile.

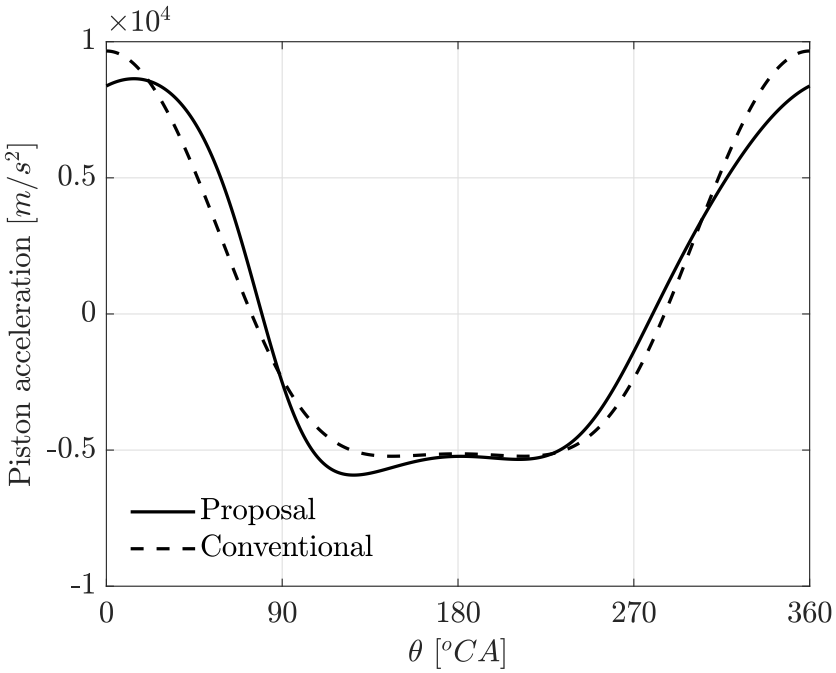

Figure 3.15: Comparison with a conventional engine, acceleration profile.

cubic capacity and compression ratio.

The compression ratio exhibited a strong relation with the minimum velocity at large cubic capacity (Fig. 3.16). That happens because of the inclination of the lever in that situation, specifically. For small values of cubic capacity, the compression ratio almost ceased its influence on the velocity. For all conditions, compression ratio had none or few influence on velocity (Fig. 3.17). It was concluded, then, that the mechanism reduces maximum velocity in

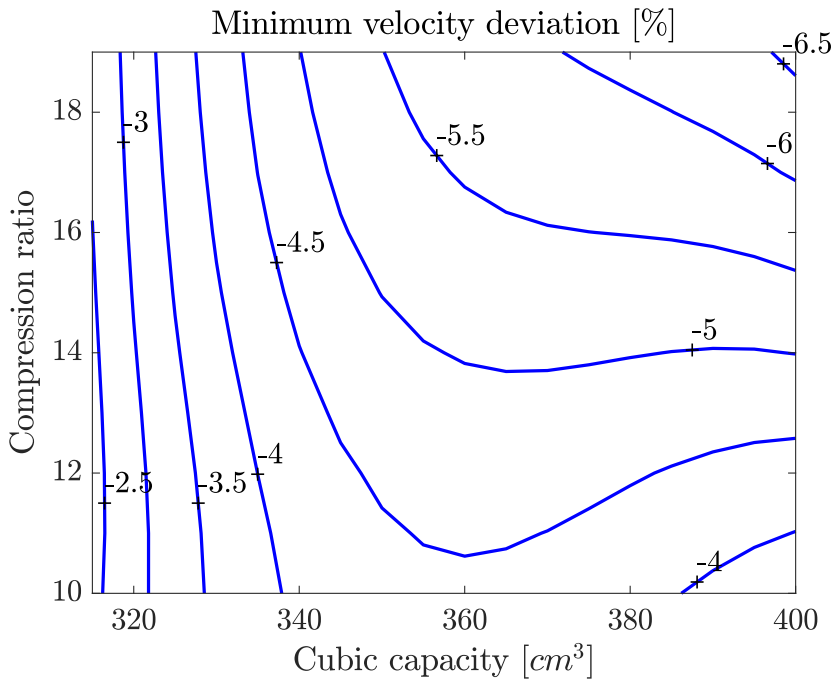

Figure 3.16: Minimum velocity deviation.

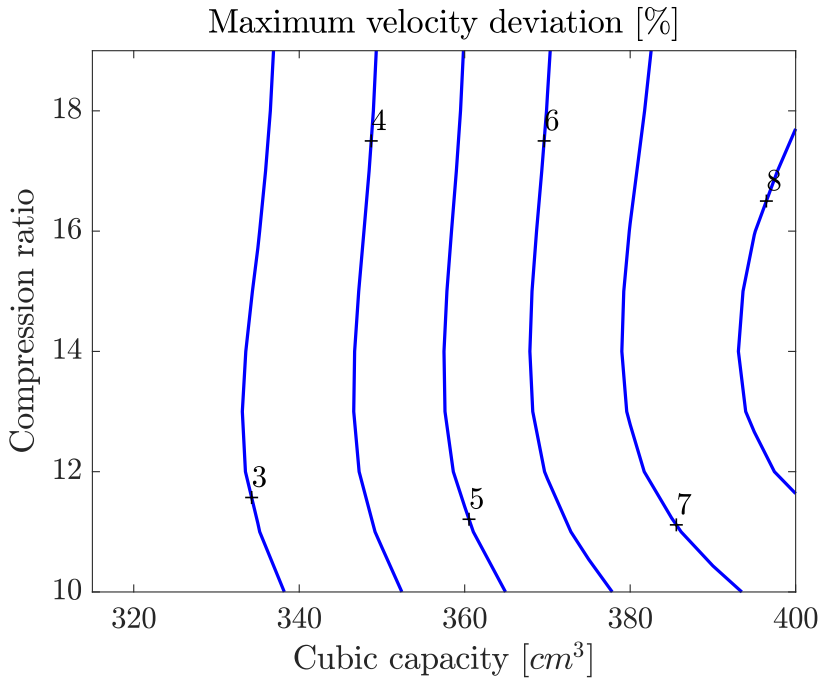

Figure 3.17: Maximum velocity deviation.

the trajectory from BDC to TDC (negative values) while it increased maximum velocity along the trajectory from TDC to BDC (positive values). In addition, an absolute deviation of 8% at the most distant condition was found. Similar effects were verified in the acceleration (Figs. 3.18 and 3.19)

A larger deviation was observed for acceleration than that verified for velocity. Even so, the maximum deviation was bellow a margin of 20%. To the understanding of the authors,

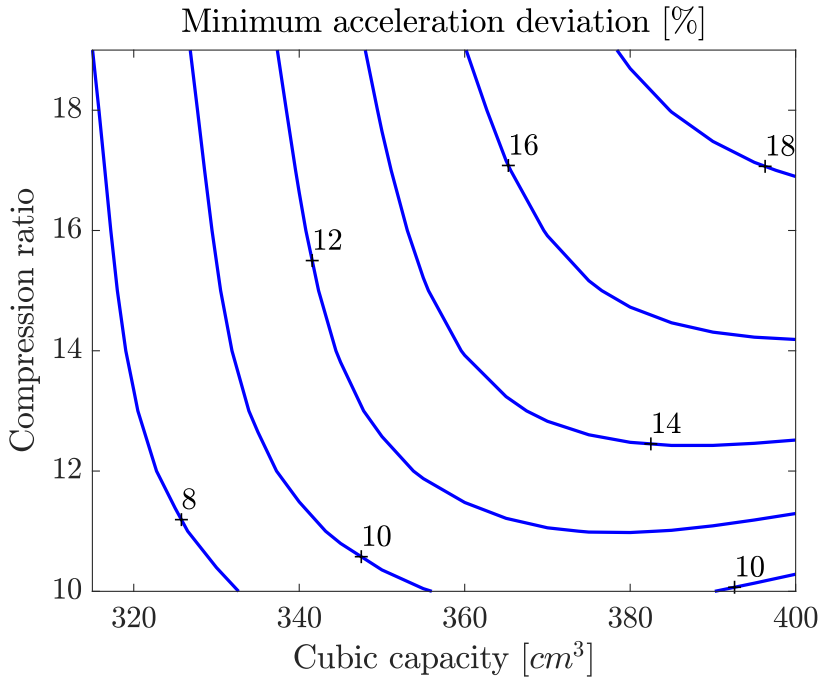

Figure 3.18: Minimum acceleration deviation.

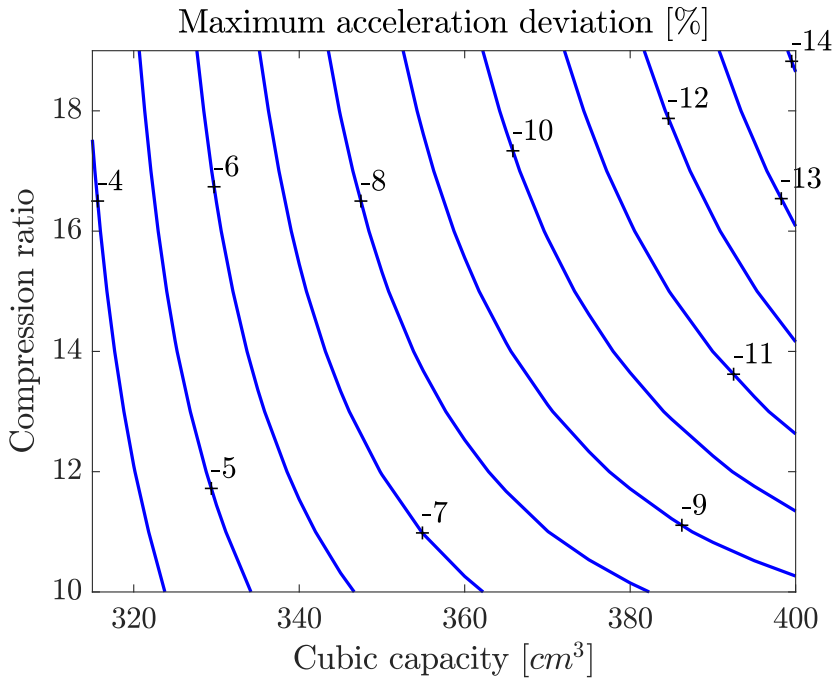

Figure 3.19: Maximum acceleration deviation.

those results present differences that are not expected to cause significant influence on the engine performance.

4. Combustion diagnosis

A combustion diagnosis was performed in order to characterise the combustion of ethanol in a flex fuel engine. Currently, the Brazilian market offers hydrous ethanol and gasohol, which are referred to as E95h and E27. Only few studies have evaluated the operation of Brazilian hydrous ethanol in flexfuel engines. For example, Costa and Sodré compared gasohol and hydrous ethanol operation in terms of their brake specific consumption, thermal efficiency, and emission in a wide range of speed under full load conditions (COSTA and SODRÉ, 2010). Subsequently, the authors studied the effects of compression ratio for a flexfuel engine operating with ethanol on a specific fuel consumption, brake mean effective pressure, brake power, brake torque, and thermal efficiency under the same conditions of the previous study (COSTA and SODRÉ, 2011). Another work was performed by Melo et. al., who measured brake thermal efficiency and emissions on a flexfuel engine operating at a constant torque under different speed conditions (MELO *et al.*, 2011). Further investigations of the same engine were performed to evaluate the effect of hydrous ethanol and gasohol blends on knock, cyclic variability, and combustion duration at a constant torque and under three–speed conditions (MELO *et al.*, 2012b). Another investigation expanded the cited study by evaluating the effects of hydrous ethanol and gasohol blend on heat release and emissions under two–load conditions and three speeds under stoichiometric and rich conditions (MELO *et al.*, 2012a). In these studies, evaluations were performed either under a full load or specific load condition, the air–fuel ratio was set to either stoichiometric condition or rich condition, and the spark timing was set to either MBT or limited knock. Moreover, there were no data related to the effect of air–fuel ratio under the lean condition and only a limited range of data can be found for analysis on the effect of load. Additionally, there is a scarcity of results for combustion characteristics for air–fuel ratio in the lean condition, which is also covered by this work. Although the catalyst operation limits the air–fuel ratio to stoichiometric and rich conditions, lean mixtures have been considered for partial load operations with the objective of reducing pumping losses (BAE and KIM, 2017).

This task aims characterise the combustion of E95h on a commercial SI PFI flexfuel engine performed by a two zone heat release model. The objectives of this study consist of eval-

uating the effects of engine parameters on hydrous ethanol combustion, correlating those effects to studies found on literature and indicating the degree of influence of each engine parameter. By those means, the comprehensive set of results provides the experimental data used for modelling hydrous ethanol combustion in the predictive model. Thus, experiments were conducted in a wide range of operational conditions of engine speed, throttle position and spark timing. In some cases, the calibration strategy of the ECU for the commercial engine was preserved. Characteristics of combustion were indicated by values of the Wiebe function parameters: combustion duration, form factor, 50% of MFB and combustion phases duration. A comparison of E95h with gasohol E27 was also performed in order to determine the differences between the characteristics of both fuels combustion. The diagnosis model developed in this work was also implemented with an exergetic model, providing results presented by RUFINO *et al.* (2018a), which were lately extended for publication in the Journal Energy Conversion and Management (RUFINO *et al.*, 2019).

4.1 Diagnosis model

A two–zone model was developed and implemented to carry out the combustion diagnosis in this work. This model implemented allows to determine the temperature of both reactants and combustion products separately and the mass fraction burned (MFB). The development of the model is detailed in Appendix C. The parameters evaluated in the analysis are obtained from the MFB profile, such as CA50, combustion duration, n and ignition delay.

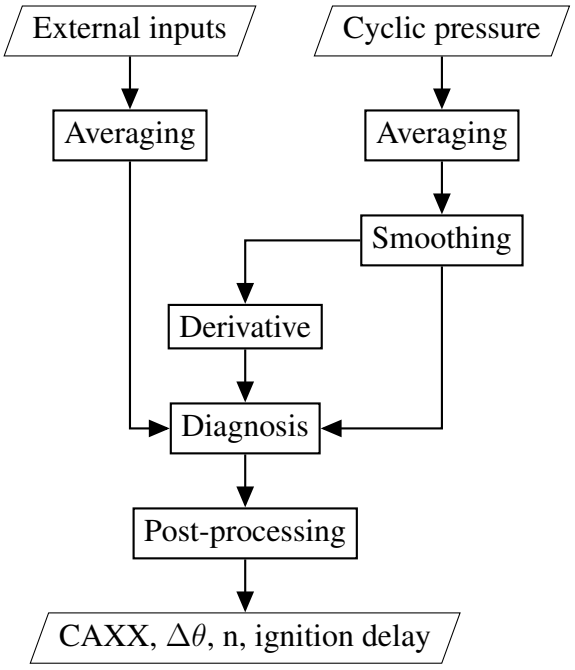

Figure 4.1: Flowchart for the procedure of combustion diagnosis.

The procedure for obtaining the combustion parameters comprises the acquisition

of experimental measurements. External parameters to the engine are measured, such as: air and fuel flows, pressure and temperature in the manifolds and atmospheric air humidity. A set of pressure profiles are also acquired for many engine cycles. All of the measurements undergo an averaging process. The averaged pressure profile has also to be smoothed in order to eliminate noise before being derived. Afterwards, the pressure profile, its derivative and the averaged external parameters are used as inputs for the diagnosis model, which provides the HRR and MFB profiles. Finally, those profiles are post–processed in order to calculate the combustion parameters (Fig. 4.1).

4.1.1 Heat release profile

The first procedure in the combustion evaluation was the determination of the in–cylinder trapped mass of the homogeneous mixture. The trapped mass in the cylinder can be calculated by measuring the instantaneous fuel flow and air–fuel ratio. Although the intake manifold design can lead to a non–homogeneous distribution of mass, the adopted hypothesis for the homogeneous distribution of mass to all cylinders closely approximated that for SI engines as reported by DEPCIK *et al.* (2007).

By neglecting blow–by, the energy balance in the crank position domain is given in Eq. 4.1.

$$\frac{\mathrm{d}U}{\mathrm{d}\theta} = \frac{\mathrm{d}Q}{\mathrm{d}\theta} - \frac{\mathrm{d}W}{\mathrm{d}\theta} \tag{4.1}$$

Work and heat transfer are the only interaction of energy exchange in the cylinder prior to ignition event. Hence, this part of the cycle can be used to estimate the temperature of cylinder wall. The energy transfer via work interaction occurred in the cylinder only because of the piston displacement, given by Eq. 4.2.

$$\frac{\mathrm{d}W}{\mathrm{d}\theta} = P\frac{\mathrm{d}V}{\mathrm{d}\theta} \tag{4.2}$$

The internal energy depends only on temperature as a consequence of the hypothesis on ideal gas, yielding Eq. 4.3, wherein $\frac{\partial u}{\partial T}$ is the specific heat at constant volume, c_v, of the mixture. Its value was fitted for all substances using data provided by the NIST thermophysical tables (see Appendix A).

$$\frac{\mathrm{d}U}{\mathrm{d}\theta} = m\frac{\partial u}{\partial T}\frac{\mathrm{d}T}{\mathrm{d}\theta} \tag{4.3}$$

Reactants were considered to be a mixture of fuel and air. Air was modelled as an ideal gas, composed of nitrogen, oxygen, carbon dioxide, and argon. Humidity was measured at the location where the tests were performed.

The heat transfer $\frac{\mathrm{d}Q}{\mathrm{d}\theta}$ was obtained by isolating it from the energy balance 4.1, leading to Eq. 4.4.

$$\frac{\mathrm{d}Q}{\mathrm{d}\theta} = P\frac{\mathrm{d}V}{\mathrm{d}\theta} + mc_v\frac{\mathrm{d}T}{\mathrm{d}\theta} \tag{4.4}$$

The differential of temperature is given by the state equation for ideal gases in Eq. 4.5, considering a fixed composition ($\frac{\mathrm{d}R}{\mathrm{d}\theta} = 0$).

$$\frac{\mathrm{d}T}{\mathrm{d}\theta} = T\left(\frac{1}{P}\frac{\mathrm{d}P}{\mathrm{d}\theta} + \frac{1}{V}\frac{\mathrm{d}V}{\mathrm{d}\theta}\right) \tag{4.5}$$

Substituting Eq. 4.5 in Eq. 4.4 and re–arranging the terms, the heat release rate is obtained, as presented in Eq. 4.6, in which the constant R is the difference between specific heats at a constant pressure and constant volume. In–cylinder gas is colder than the cylinder wall at the beginning of the compression stroke, after intake valve closing. Therefore, heat transfer occurs from the wall to the gas. Then the gas is compressed and its temperature rises, changing the direction of heat flux. Consequently, there is a moment in which the gas and the cylinder wall are at the same temperature and this instant can be determined when the heat flux is calculated as null. Cylinder walls temperature is defined in this instant as being the same as in–cylinder gases temperature. Usually, the temperature of cylinder walls is estimated. The procedure for determining the temperature of cylinder walls described here is original as there are no similar methods described in the literature.

$$\frac{\mathrm{d}Q}{\mathrm{d}\theta} = P\left(\frac{c_v}{R} + 1\right)\frac{\mathrm{d}V}{\mathrm{d}\theta} + V\frac{C_v}{R}\frac{\mathrm{d}P}{\mathrm{d}\theta} \tag{4.6}$$

Combustion energy released after the ignition cannot be differentiated from heat transfer and the equations provide the net heat release. In order to achieve a higher accuracy, many works implement the estimative of heat transfer, separating effects of combustion and heat losses and obtaining the gross heat release. In this analysis, heat release was estimated from the convection law, presented in Eq. 4.7, in which A is the area of a zone and T_w is the cylinder wall temperature. The heat transfer coefficient h^{HT} was calculated as function of volume, pressure, temperature and mean piston velocity, as suggested by HOHENBERG (1979). The conversion from time to crank position domain is made by dividing the heat transfer rate by the angular velocity of the shaft ω.

$$\frac{\mathrm{d}Q}{\mathrm{d}\theta} = \frac{h^{HT}A\left(T - T_w\right)}{\omega} \tag{4.7}$$

The two–zone model consists in applying the energy conservation law to the zones, one formed by reactants and the other formed by combustion products. The development of the model is based on the following assumptions:

- Both zones are at mechanical equilibrium, *i.e.*, the same pressure;
- Blow–by is neglected;
- Burned and unburned gases do not mixture;
- The zones are separated by the flame front;
- Flame is considered to be impermeable and adiabatic and it has an infinitesimal width;
- Heat transfer is modelled and considered to occur exclusively via convection. Radiation is neglected.
- In the equations, enthalpy is only a function of temperature. Energy released by the combustion is accounted in the variable H_{comb}.

The composition of combustion products was considered to be dependant on the air–fuel ratio. The model considered a fixed composition of combustion products. The complete combustion led to a mixture of carbon dioxide, water, argon, and nitrogen if the stoichiometric condition ($\lambda = 1$) was achieved. If excess air remained, *i.e.*, the lean condition ($\lambda > 1$), then oxygen was present in the combustion products. On the other hand, if air was insufficient, *i.e.*, the rich condition ($\lambda < 1$), then the combustion was incomplete, and a part of the carbon present in the fuel was converted to carbon monoxide, whereas a part of the hydrogen present in the fuel was converted to molecular hydrogen. It should be noted that the species balance did not provide the sufficient number of relationships to solve the stoichiometric balance. Thus, it was necessary to assume that a relationship existed between carbon monoxide and molecular hydrogen, based on an estimate of the chemical equilibrium between those substances (HOVAH *et al.*, 1971).

Applying the energy conservation law to reactants and using the relation between internal energy and enthalpy: $U = H - PV$, Eq. 4.8 can be established.

$$\frac{\mathrm{d}H_r}{\mathrm{d}\theta} = \frac{\mathrm{d}Q_r}{\mathrm{d}\theta} + V_r\frac{\mathrm{d}P}{\mathrm{d}\theta} - h_r m\frac{\mathrm{d}x_b}{\mathrm{d}\theta} \tag{4.8}$$

The reaction of combustion is modelled as a mass transfer phenomenon, in which a certain amount of mass leaves the reactants system and reacts when trespassing the flame front, before entering the products system. Thus, the effect of mass transfer is given by the term $h_r m\frac{\mathrm{d}x_b}{\mathrm{d}\theta}$, in which h_r is the intensive enthalpy of the reactants. The detailed process for calculating the terms is demonstrated in Appendix C.

By separating the effects of mass and temperature on the enthalpy H_r of the gas, indicated in Eq. 4.9, it is possible to isolate the temperature differential, yielding Eq. 4.10.

$$\frac{\mathrm{d}H_r}{\mathrm{d}\theta} = m\left(1 - x_b\right) c_{p,r} \frac{\mathrm{d}T_r}{\mathrm{d}\theta} + h_r m \frac{\mathrm{d}x_b}{\mathrm{d}\theta} \tag{4.9}$$

$$\frac{\mathrm{d}T_r}{\mathrm{d}\theta} = \frac{\frac{\mathrm{d}Q_r}{\mathrm{d}\theta} + V_r \frac{\mathrm{d}P}{\mathrm{d}\theta}}{\left(1 - x_b\right) m c_{p,r}} \tag{4.10}$$

The same procedure can be applied to the combustion products, leading to Eq. 4.11.

$$\frac{\mathrm{d}H_p}{\mathrm{d}\theta} = \frac{\mathrm{d}H_{comb}}{\mathrm{d}\theta} + \frac{\mathrm{d}Q_p}{\mathrm{d}\theta} + V_p \frac{\mathrm{d}P}{\mathrm{d}\theta} + m h_r \frac{\mathrm{d}x_b}{\mathrm{d}\theta} \tag{4.11}$$

The energy release by combustion is represented by $\frac{\mathrm{d}H_{comb}}{\mathrm{d}\theta}$, given by the heat release rate and it is related to the MFB, as indicated in Eq. 4.12.

$$\frac{\mathrm{d}H_{comb}}{\mathrm{d}\theta} = m_{fuel} h_{comb} \frac{\mathrm{d}x_b}{\mathrm{d}\theta} \tag{4.12}$$

The enthalpy variation between reactants and products is represented by h_{comb} (enthalpy of combustion) and the admitted mass of fuel m_{fuel}, calculated by the measured air–fuel ratio.

The temperature differential for combustion products can be isolated, providing Eq. 4.13.

$$\frac{\mathrm{d}T_p}{\mathrm{d}\theta} = \frac{\left[m_{fuel} h_{comb} + m\left(c_{p,r} T_r - c_{p,p} T_p\right)\right] \frac{\mathrm{d}x_b}{\mathrm{d}\theta} + \frac{\mathrm{d}Q_p}{\mathrm{d}\theta} + V_p \frac{\mathrm{d}P}{\mathrm{d}\theta}}{c_{p,p} x_b m} \tag{4.13}$$

The rate of volume dislocation is given by Eq. 4.14.

$$\frac{\mathrm{d}V}{\mathrm{d}\theta} = \frac{\mathrm{d}V_r}{\mathrm{d}\theta} + \frac{\mathrm{d}V_p}{\mathrm{d}\theta} \tag{4.14}$$

From the ideal gas law, Eq. 4.14 can be rewritten as Eq. 4.15.

$$\frac{\mathrm{d}V}{\mathrm{d}\theta} = V_r \left(\frac{1}{T_r}\frac{\mathrm{d}T_r}{\mathrm{d}\theta} + \frac{1}{m_r}\frac{\mathrm{d}m_r}{\mathrm{d}\theta} - \frac{1}{P}\frac{\mathrm{d}P}{\mathrm{d}\theta}\right) + V_p \left(\frac{1}{T_p}\frac{\mathrm{d}T_p}{\mathrm{d}\theta} + \frac{1}{m_p}\frac{\mathrm{d}m_p}{\mathrm{d}\theta} - \frac{1}{P}\frac{\mathrm{d}P}{\mathrm{d}\theta}\right) \tag{4.15}$$

By multiplying the relation in Eq. 4.15 by the pressure and considering that $m_r = -m\frac{\mathrm{d}x_b}{\mathrm{d}\theta}$ and $m_p = m\frac{\mathrm{d}x_b}{\mathrm{d}\theta}$ leads to Eq. 4.16.

$$P\frac{\mathrm{d}V}{\mathrm{d}\theta} + V\frac{\mathrm{d}P}{\mathrm{d}\theta} = \frac{PV_r}{T_r}\frac{\mathrm{d}T_r}{\theta} + \frac{PV_p}{T_p}\frac{\mathrm{d}T_p}{\mathrm{d}\theta} + mP\left(\frac{V_p}{m_p} - \frac{V_r}{m_r}\right)\frac{\mathrm{d}x_b}{\mathrm{d}\theta} \tag{4.16}$$

Applying the ideal gas law to Eq. 4.16 and re–arranging the terms, Eq. 4.17 can be

obtained.

$$m\left(1-x_b\right)\frac{\mathrm{d}x_b}{\mathrm{d}\theta}+mx_bR_p\frac{\mathrm{d}T_p}{\mathrm{d}\theta}=P\frac{\mathrm{d}V}{\mathrm{d}\theta}+V\frac{\mathrm{d}P}{\mathrm{d}\theta}-m\left(1-x_b\right)R_r\frac{\mathrm{d}T_r}{\mathrm{d}\theta} \tag{4.17}$$

As $\frac{\mathrm{d}T_p}{\mathrm{d}\theta}$ is dependant on $\frac{\mathrm{d}x_b}{\mathrm{d}\theta}$, it is necessary to substitute this term on Eq. 4.17, leading to Eq. 4.18.

$$\frac{\mathrm{d}x_b}{\mathrm{d}\theta}=\frac{P\frac{\mathrm{d}V}{\mathrm{d}\theta}+V\frac{\mathrm{d}P}{\mathrm{d}\theta}\frac{R_p}{c_{p,p}}\left(\frac{\mathrm{d}Q_p}{\mathrm{d}\theta}-V_p\frac{\mathrm{d}P}{\mathrm{d}\theta}\right)-m\left(1-x_b\right)\frac{\mathrm{d}T_r}{\mathrm{d}\theta}}{m\left\{R_pT_p-R_rT_r+\frac{R_p}{c_{p,p}}\left[\frac{m_{fuel}h_{comb}}{m}+c_{p,r}T_r-c_{p,p}T_p\right]\right\}} \tag{4.18}$$

With three differential equations, it was necessary to define an initial value to implement the Runge–Kutta method. The initial value of the MFB was null. The initial temperature value for reactants was determined by the ideal gas model applied at the instant of intake valve closing. At the start of combustion, the initial portion of burned gas has not interacted with its boundaries yet, and the entire energy released by combustion is converted into internal energy. Therefore, the initial temperature for the first portion of combustion products was considered to be the adiabatic flame temperature.

4.1.2 CA50

Once the profile of released heat was determined, the criteria for specifying the start and end of combustion must be chosen. It was selected the method based on identifying instants of 10, 50, and 90% of the MFB, also known as CA10, CA50, and CA90, respectively. These parameters were given by the integration of the heat release rate, *i.e.*, the heat released, which was smoother than the first because of the integration process.

Generally, the MFB was approximated by a function, which described the development of combustion . The researcher Ivan Wiebe developed a semi-empirical correlation that could reproduce the effect of a complicated chemical reaction chain with a simple expression (GHOJEL, 2010). Thus, this developed model could reproduce the behaviour of combustion by adjusting only a few parameters (MUELLER *et al.*, 1983) calibrated with experimental data. It was reported that each engine and condition would provide different parameters for this model. The function is given in Eq. 4.19, commonly referred to in literature as Wiebe's function.

$$x_b=1-\exp\left[\ln\left(1-\eta_r\right)\left(\frac{\theta-\theta_0}{\Delta\theta}\right)^{n+1}\right] \tag{4.19}$$

The term η_r is the maximum value of MFB and is actually dependent on the com-

bustion efficiency. In this work, the combustion efficiency was estimated rather than calculated. This parameter is usually replaced by another parameter, $a = -\ln(1-\eta_r)$. Many authors chose arbitrary values for this parameter, a, which varied from 4 to 6.908 (ABBASZADEHMOSAYEBI and GANIPPA, 2014). The latter value was the pioneering suggestion of Wiebe (GHOJEL, 2010) and reinforced by other authors (HEYWOOD, 1988; BONATESTA *et al.*, 2010). That value was adopted for this work, which led to a combustion efficiency of $\eta = 0.999$.

Moreover, the use of CA50 was important to estimate parameters $\Delta\theta$ and n, which were also used to indicate whether the engine was operating at the optimum condition of the combustion phase, *i.e.*, at the MBT.

4.1.3 Form Factor

In this study, the parameter n was named as form factor. The form parameter indicated the degree of asymmetry of the combustion profile. The effects of this parameter on the burning profile can be verified in the works of MUELLER *et al.* (1983) and GALLO (1990). The higher the value of n, the slower the combustion will be at its beginning. On the other hand, small values of n indicate that the combustion develops quickly, and the fast burning region occurs earlier.

By substituting the obtained crank angles of CA10 (θ_{10}), CA50 (θ_{50}), and CA90 (θ_{90}) in θ and 0.1, 0.5, and 0.9 in MFB (Eq. 4.19), respectively, it is possible to determine the start of combustion by the relation presented in Eq. 4.20.

$$\frac{\theta_{10}-\theta_0}{\theta_{90}-\theta_0} = \left(\frac{\theta_{50}-\theta_0}{\theta_{90}-\theta_0}\right)^L \tag{4.20}$$

The constant L is given by Eq. 4.21.

$$L = \frac{\ln\left(\frac{\ln 0.9}{\ln 0.1}\right)}{\ln\left(\frac{\ln 0.5}{\ln 0.1}\right)} \tag{4.21}$$

Multiple roots can be found when solving Eq. 4.20 for θ_0 (SOC). Hence, the bisection method of numerical solving was implemented for the interval between the ignition and CA10. In most cases, the start of the combustion was given as the same instant of the ignition. In other cases, it was observed that there was a brief delay between the ignition and start of combustion. This period of time is defined as the Ignition delay.

The n parameter can be determined by Eq. 4.22 (YELIANA *et al.*, 2008).

$$n = \frac{\ln\left(\frac{\ln 0.9}{\ln 0.1}\right)}{\ln\left(\frac{\theta_{10}-\theta_0}{\theta_{90}-\theta_0}\right)} \tag{4.22}$$

Table 4.1: Engine characteristics.

Cylinders	3 in–line
Compression ratio	12.28:1
Connecting rod length $[mm]$	145.6
Displacement $[cm^3]$	1200
Bore $[mm]$	75
Stroke $[mm]$	90.5

4.1.4 Combustion duration

One of the most fundamental parameters is the duration of combustion. This parameter is directly linked to the efficiency of the engine, and a faster combustion is preferred in most conditions. By using Eq. 4.23, the combustion duration can be determined (YELIANA *et al.*, 2008).

$$\Delta\theta = (\theta_{50} - \theta_0)\left(\frac{\ln 0.5}{1-\eta_r}\right)^{\frac{-1}{n+1}} \tag{4.23}$$

4.2 Experimental setup

Experimental tests were executed in the PSA's spark–ignition port fuel injection engine, three in–line cylinders with a nominal compression ratio of 12.5:1 (Tab. 4.1). Data were measured for all of the cylinders, whose measured compression ratios were 12.28:1, 12.25:1, and 12.23:1. Results from the three cylinders were averaged for the analysis. The tested engine was a multi–fuel engine, also known as flexfuel, widely used in light duty vehicles in Brazil. It was capable of operating fuelled with either gasoline or hydrous ethanol, or even with a blend of both fuels composed of any proportion between ethanol and gasoline. Bench tests were executed in the IMT (Instituto Mauá de Tecnologia) facilities. A development ECU ETAS was used in order to control the engine. In–cylinder pressure was acquired by using instrumented spark plugs AVL ZI31_Y5S, calibrated within the range of 0 to 80 bar with a sensitivity of 11.69 pC/bar, and a Phoenix AM Acquisition System. The tests were performed with a passive eddy current Positron Brown–Boveri dynamometer (ZABEU *et al.*, 2017).

The fuels used in the test were those currently available in the Brazilian market for spark-ignition engines: E95h and E27. E27, also known as gasohol, consists of a gasoline 86 MON/95 RON blended with 27% ethanol in volume. E95h, hydrous ethanol, consists of a blend of 95% ethanol and 5% water in a volume of liquid. In all conditions, the engine was running under normal operational conditions. The experiments were separated in three categories: Full load, Spark timing sweep and Lean Mixture. Operational parameters are given in Tab. 4.2. It was not possible to obtain a stable engine operation for the condition of $\lambda = 1.3$ for 50 Nm of

load. Thus, results are not provided for that specific condition.

Table 4.2: Test parameters.

	Full load	Spark timing sweep	Lean mixture
Engine speed	1000–6000	1500 & 3000	1000–4000
λ	<1	1	1–1.3
Load	Full	20% to 100% of Throttle	25Nm & 50 Nm of Torque
Fuel	E27&E95h	E95h	E27&E95h

Air–fuel ratio was uncontrolled for Full load test, being at rich condition during all the test. Spark timing was set either to MBT condition or knock limited for both Full load and Lean mixture tests. The load conditions of 25 Nm and 50 Nm are representative on the vehicle's engine operation and they represent a different percentage of the torque at full load for different engine speed conditions. Those values are indicated in Fig. 4.3. A total of 300 cycles were obtained for the Full load and Spark timing sweep tests. For the Lean Mixture test, a total of 150 cycles were obtained since this test was performed separately from the others. The spark timing sweep is schematically demonstrated in Fig. 4.2 for the condition of 3000 rpm of engine speed.

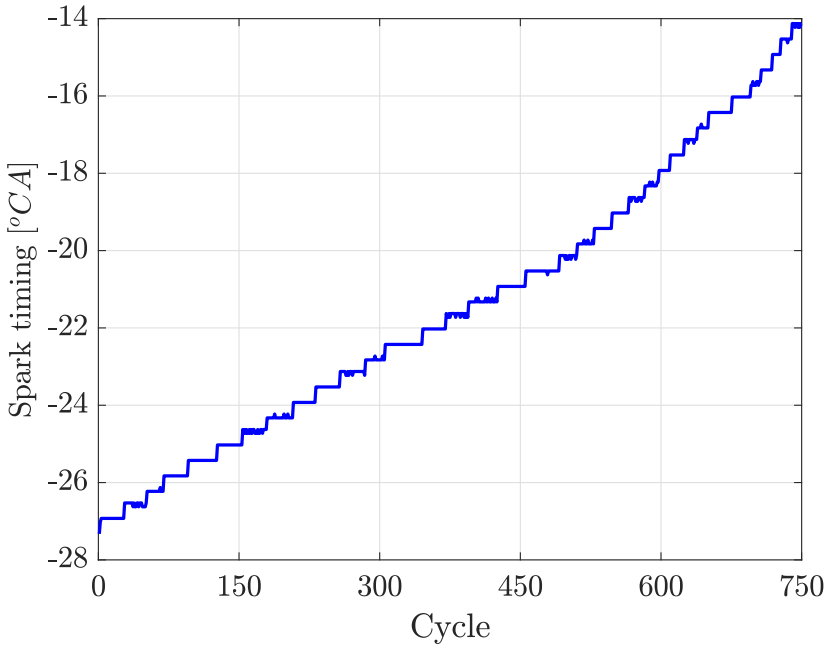

Figure 4.2: Spark timing sweep for 3000 rpm.

Before the evaluation, data processing (Fig. 4.1) consisted of averaging the obtained cycles and parameters used in the calculation of the released heat, such as the rate of fuel flow, ambient temperature, humidity, air–fuel ratio, and ambient pressure. After averaging, the pressure profile must be smoothed to eliminate fluctuations caused by phenomena that were not

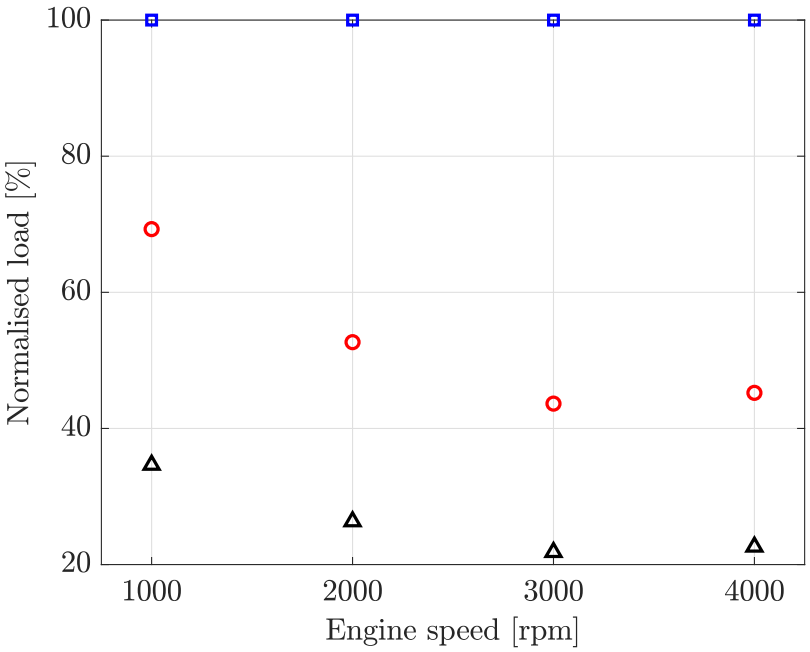

Figure 4.3: Percentage of load for partial loads conditions.

modelled in the heat release analysis, *e.g.*, charge motion and pressure waves caused by valve closing. In addition to those phenomena, noise can also influence the signal. When the signal was derived without signal processing for eliminating noise, those fluctuations were amplified, which decreased the reliability of the diagnosis. Although digital filters, such as Butterworth, or smoothing techniques, such as Savitsky–Golay, are commonly used to perform the signal processing of pressure data (PAYRI *et al.*, 2010), it was opted to implement a new technique based on the support vector machine (SMOLA and SCHÖLKOPF, 2004) because this method was proven to be more robust and reliable (Fig. 4.4). A numerical differentiation of fourth order was used to perform pressure differentiation (Fig. 4.5), which is detailed in Section C.2. Without the smoothing process, the noise is amplified by the differentiation process and the diagnosis equations.

One example was obtained by a simple single zone approach to illustrate the effects of noise in the profile of heat release rate (Fig. 4.6). It is verified that the SOC and the EOC are not easily identified in the profile obtained with raw data.

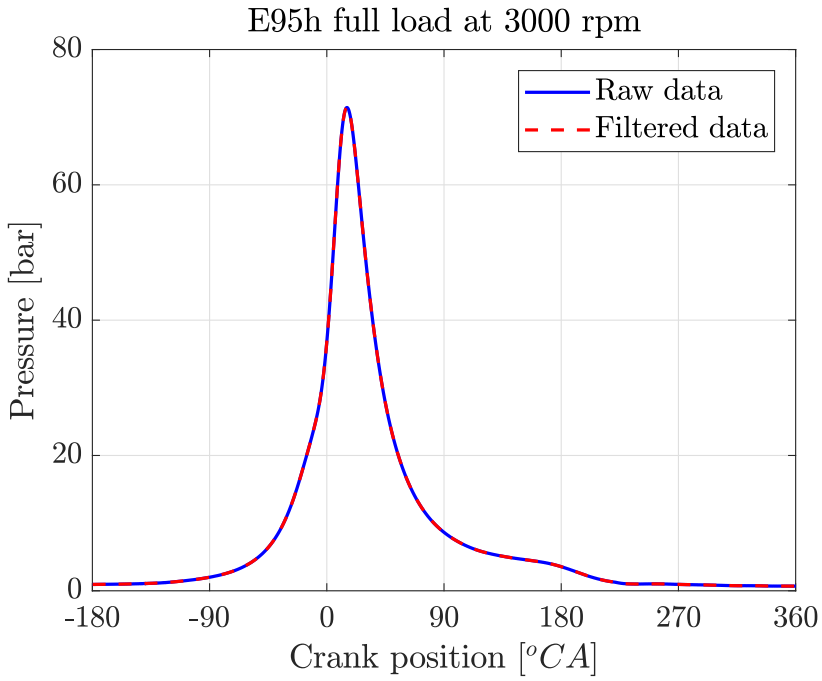

Figure 4.4: In–cylinder pressure raw and filtered.

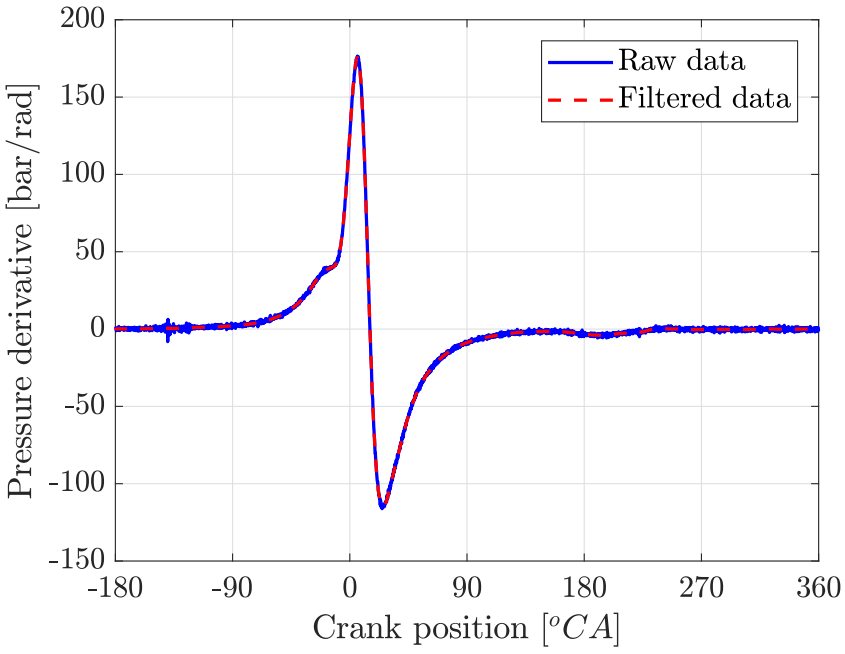

Figure 4.5: In–cylinder pressure derivative raw and filtered.

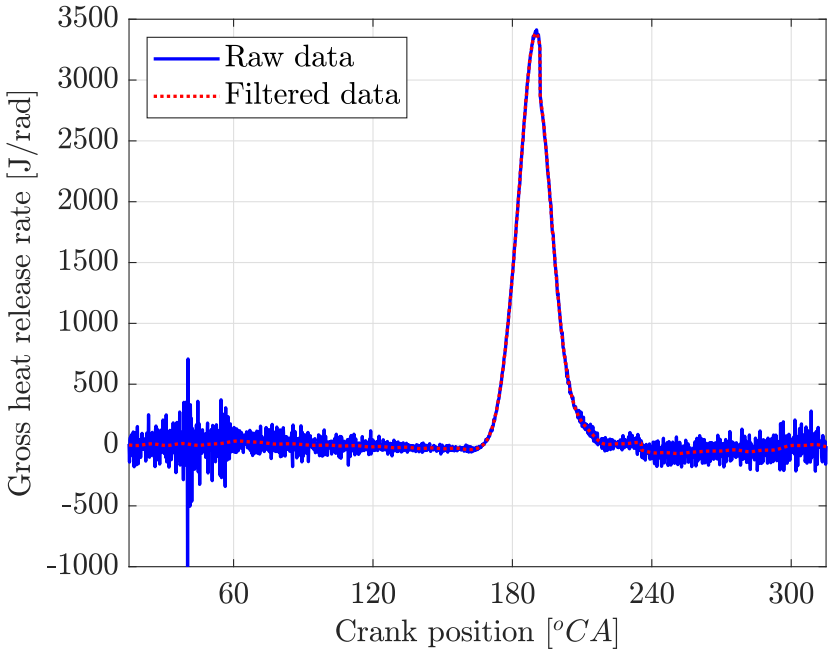

Figure 4.6: Gross heat release rate raw and filtered.

4.3 Results and Discussion

The heat released profiles were obtained for the aforementioned experimental conditions. Three profiles are presented in Fig. 4.7 for different engine speed conditions. Combustion duration, n and ignition delay are calculated based on the heat release profile according to the method through Eqs. 4.20 to 4.23.

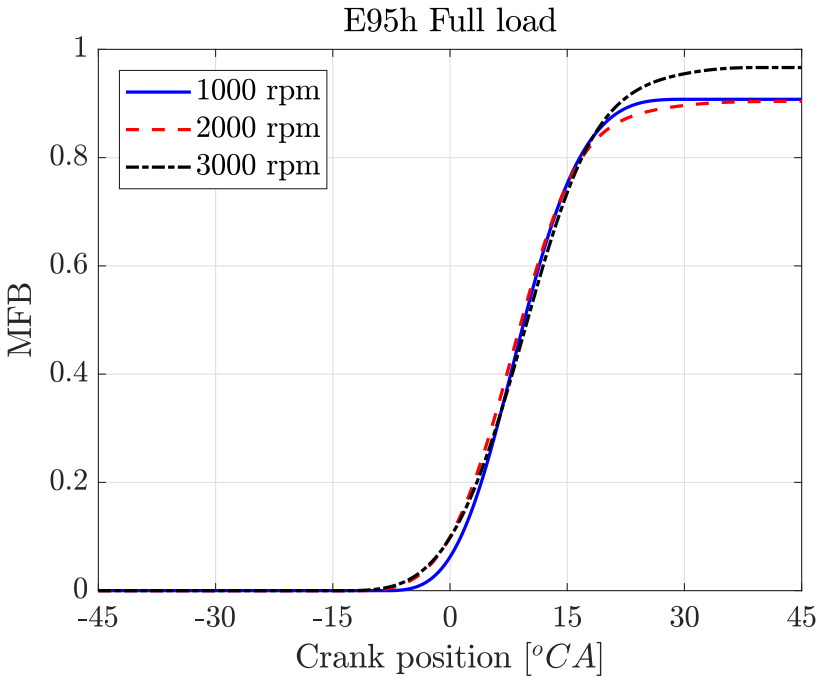

Figure 4.7: MFB profile for different engine speed.

4.3.1 A/F ratio and load effects.

Lean Mixture test has been carried out for both E95h and E27 fuels. However, results are herein presented only for E95h as the focus of this research is to analyse the operation of a VSE operating with ethanol. Results obtained in the Lean Mixture test for gasohol are presented in Appendix D.

Combustion duration in terms of crank angle angle is shown for Ethanol at 25 Nm of load (Fig. 4.8). Combustion duration presented an increase at high engine speeds. However, crank position is dependent of angular velocity. Therefore, combustion duration was actually decreasing with engine speed increasing (Fig. 4.9). Although most works in the literature perform combustion analysis for engines in the crank position domain, an analysis carried out in the time domain is more comprehensible to the understanding of the author. Thus, parameters are provided in ms rather than ^oCA in this analysis. Results in ^oCA are presented in Appendix D.

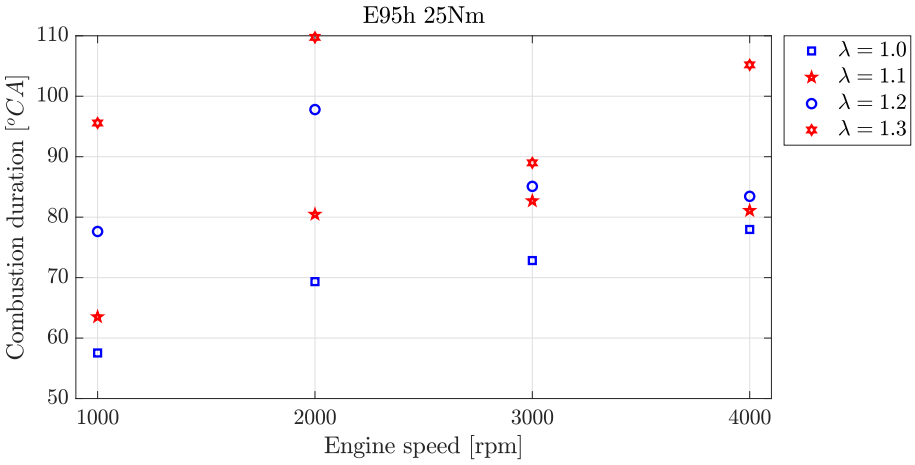

Figure 4.8: Combustion duration at different A/F ratios and engine speed in crank angle.

The major contribution to flame speed comes from turbulence (BAE and KIM, 2017). This trend was easily verified by the significant decrease in combustion duration with engine speed increasing (Figs. 4.9 and 4.10). However, laminar flame speed can indicate the effect of other parameters on combustion, such as: pressure, temperature, and A/F ratio (KONNOV *et al.*, 2011). EISAZADEH-FAR *et al.* (2011a) have shown that the concentration of diluent gases concentration also influences laminar flame speed, indicating that higher concentration of diluent gases induces a decrease on the adiabatic flame temperature, decreasing flame speed. VAREA *et al.* (2012) and GÜLDER (1984) have shown that flame velocity is maximised for slightly rich mixtures. Moreover, studies have shown that flame speed of ethanol is lower for lean mixture compared to that of stoichiometric condition (ALEIFERIS *et al.*, 2017). In the results obtained, combustion duration did not present a strong relation to A/F ratio, except for the condition of $\lambda = 1.3$, which presented a longer combustion duration than those of other A/F ratio conditions. This trend may be attributed to fact that the stochastic nature of the turbulent flame can overlap the effect of A/F ratio on laminar flame speed. As load reduction is performed by limiting the amount of trapped mass, the in–cylinder pressure was reduced for low loads. Therefore, a decrease in combustion duration was for 50 Nm compared to that of 25 Nm (Figs. 4.9 and 4.10), agreeing with results found in the literature for engines fuelled with gasoline (GUEZENNEC and HAMAMA, 1999; BONATESTA *et al.*, 2010) and gasohol (SCHIFTER *et al.*, 2011).

Ignition delay proved to reduce for load increasing (Figs. 4.11 and 4.12), indicating the relation between pressure and flame development. Moreover, ignition delay decreased with engine speed increasing. For low speed it was observed a higher level of sensibility to A/F ratio on the ignition delay. Leaner A/F ratios induced higher ignition delay, except for the conditions of 2000 and 4000 rpm at 50 Nm of load, in which slight leaner conditions presented the lower ignition delay. This trend can indicate a trade–off for the temperature at the beginning of combustion. Leaner mixtures presents a high temperature at the end of compression because

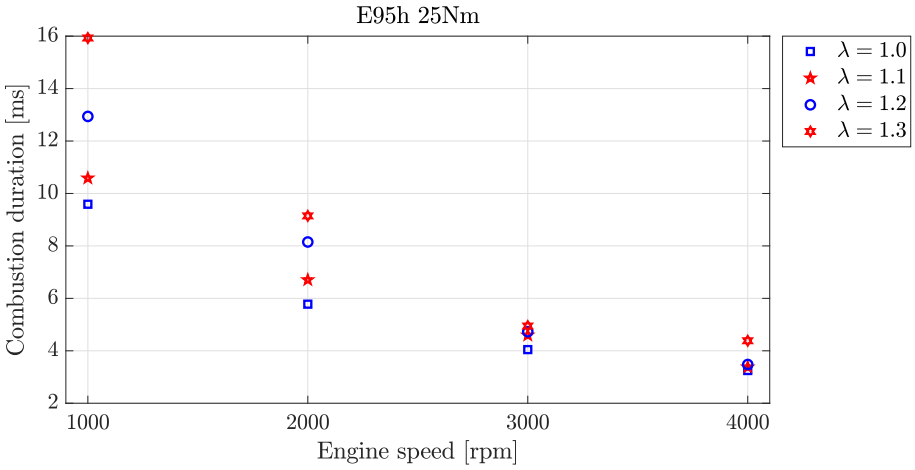

Figure 4.9: Combustion duration for different A/F ratios and engine speed at 25 Nm.

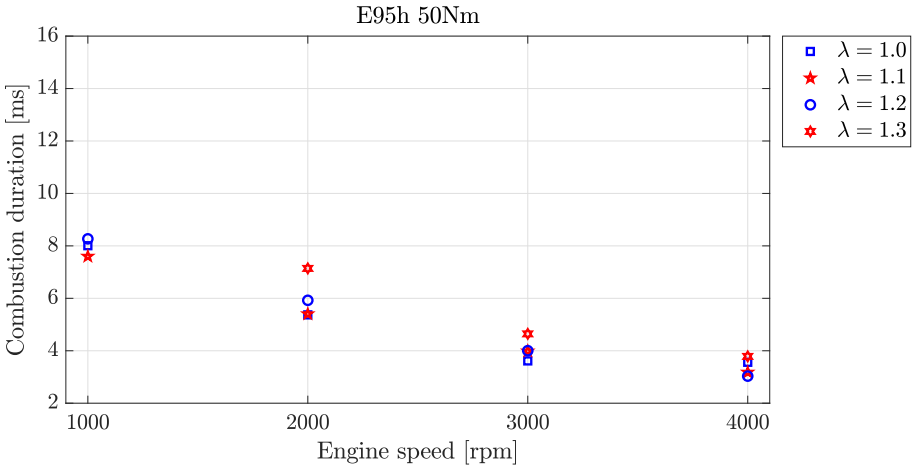

Figure 4.10: Combustion duration for different A/F ratios and engine speed at 50 Nm.

of the lower concentration of fuel, favouring combustion. However, leaner conditions also present a higher concentration of diluent gases and the temperature of combustion products is low.

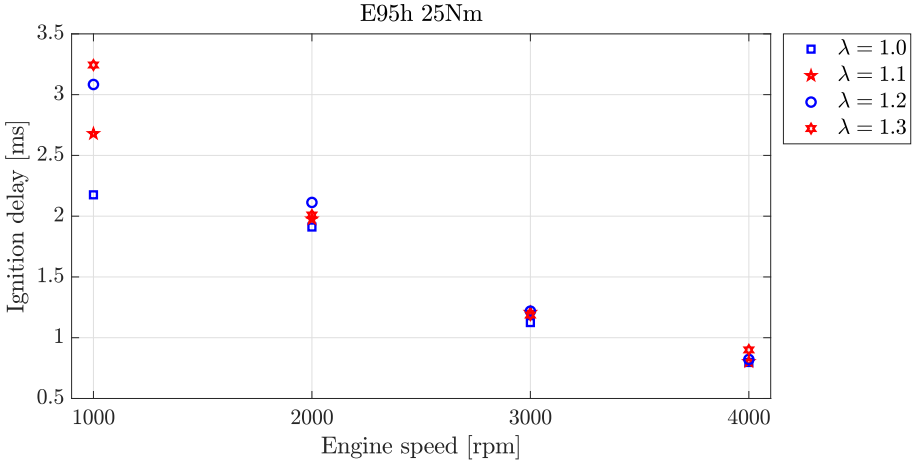

Figure 4.11: Ignition delay for different A/F ratios and engine speed at 25 Nm.

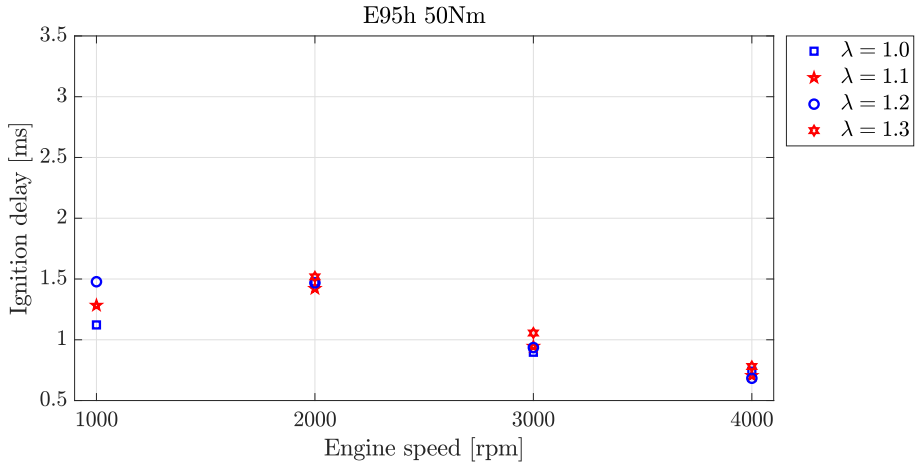

Figure 4.12: Ignition delay for different A/F ratios and engine speed at 50 Nm.

The parameter CA50 exhibited a shift from TDC for high values of λ as combustion duration was increased for leaner mixtures. No relation between CA50 and engine speed was observed (Figs. 4.13 and 4.14) once the values were constant aside minor fluctuations. The trend found for CA50 is explained by the fact that combustion duration decrease in terms of time was decreased with increased engine speed, the increased angular velocity led to a different trend for combustion duration in terms of crank position.

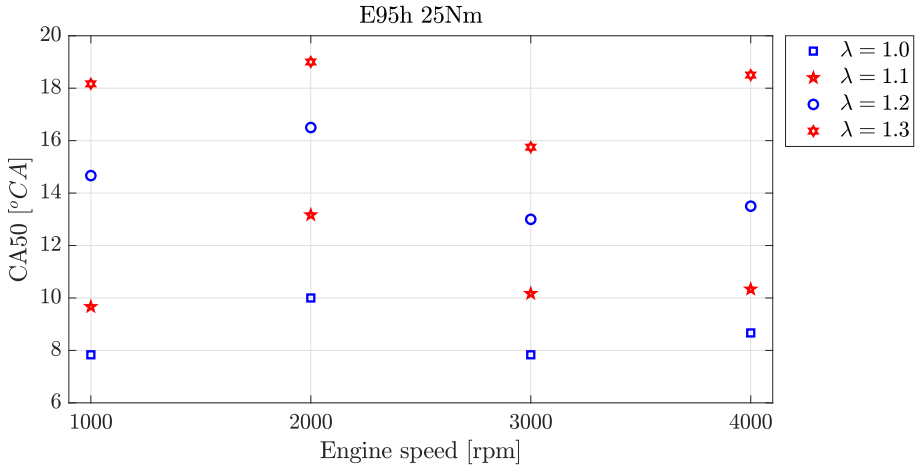

Figure 4.13: CA50 for different A/F ratios and engine speed at 25 Nm.

Combustion is divided in four main phases: the flame development phase, determined by the period between the SOC and CA10, the beginning of the fast burn phase, determined by the period between CA10 and CA50, the end of the fast burn phase, determined by the period between CA50 and CA90, and the final phase, determined by the period between CA90 and the EOC. The fast burn period comprises the period between CA10 and CA90. Absolute and normalised values are presented, *i.e.*, the ratio between each phase and the total combustion duration. Values are respectively provided for 25 Nm and 50 Nm in Tabs. 4.3 and 4.4.

Stoichiometric condition presented the longest flame development phase for 25 Nm,

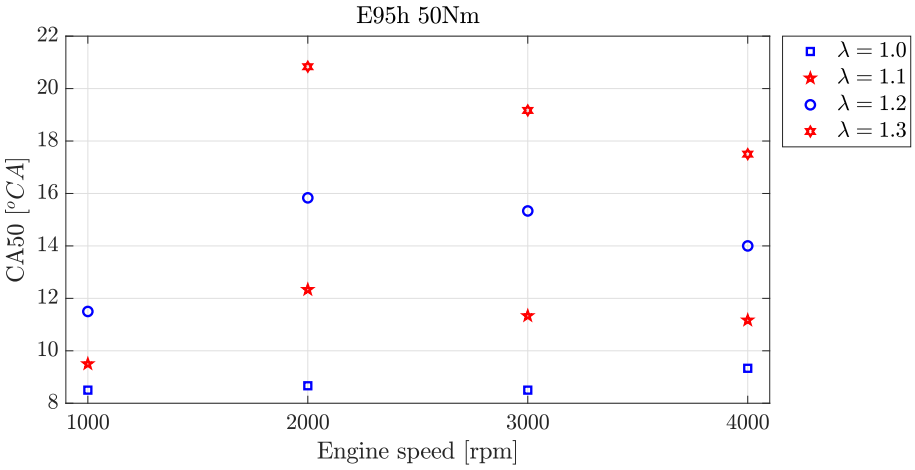

Figure 4.14: CA50 for different A/F ratios and engine speed at 50 Nm.

except for 4000 rpm, condition in which the turbulence effect overlapped the effect of A/F ratio, or the method requires more precision in order to evaluate this condition. For 50 Nm, the effect of load overlapped the effect of A/F ratio and no trend was observed. Engine speed evidently reduced the phase of flame development independently of the load condition. The decrease in the flame development phase was verified in absolute values only for 1000 rpm.

For the fast burn and the final phase of the combustion, increased A/F ratio induced a longer duration of each phase in terms of °CA. However, it was possible to verify some conditions for 50 Nm of load in which this trend was not confirmed.

The overall fast burn phase participation on combustion duration presented a reduction with engine speed increasing. The effect of A/F ratio on fast burn phase was not clearly observed for 25 Nm. For 50 Nm condition, stoichiometric condition exhibited the smaller share of fast burn on combustion. On the other hand, there was no direct relation between the duration of fast burn phase and A/F ratio as the condition $\lambda = 1.2$ presented the longer fast burn phase and $\lambda = 1.3$ presented the second longest duration for fast burn phase. For a stoichiometric mixture, the temperature at the end of compression is low because for the high concentration of fuel, resulting in a slower combustion at its beginning than those of lean mixtures. Whereas, the fast burn and the final phases of the combustion are faster for the stoichiometric condition, as the temperature of its combustion products and its concentration of radicals are higher compared to those of lean mixtures.

The final phase of combustion exhibited no relation to A/F ratio while it was increased with engine speed increasing for both 25 Nm and 50 Nm.

Table 4.3: Duration of each combustion phase for 25 Nm.

Engine speed [rpm]		1000				2000				3000				4000			
λ		1.0	1.1	1.2	1.3	1.0	1.1	1.2	1.3	1.0	1.1	1.2	1.3	1.0	1.1	1.2	1.3
SOC - CA10	Abs	9	7	7	6	6	6	6	6	5	4	5	6	3	4	5	5
	Norm	16	12	9	7	9	8	6	6	7	5	6	7	4	5	6	5
CA10 - CA50	Abs	10	12	14	15	12	14	15	16	11	12	13	14	10	11	12	15
	Norm	18	18	17	16	18	17	15	15	15	14	15	16	13	14	15	14
CA50 - CA90	Abs	14	16	20	25	18	21	26	29	19	22	22	24	20	21	22	28
	Norm	24	26	26	26	26	27	26	26	26	26	26	26	26	26	26	26
CA10 - CA90	Abs	24	28	34	40	30	35	41	46	30	33	35	38	31	32	34	42
	Norm	43	44	44	42	44	43	42	41	41	40	41	42	39	40	41	40
CA90 - EOC	Abs	24	28	37	49	33	39	51	58	38	45	45	46	44	45	44	58
	Norm	41	45	47	51	47	49	53	53	52	54	53	51	56	55	53	55

Table 4.4: Duration of each combustion phase for 50 Nm.

Engine speed [rpm]		1000				2000				3000				4000			
λ		1.0	1.1	1.2	1.3	1.0	1.1	1.2	1.3	1.0	1.1	1.2	1.3	1.0	1.1	1.2	1.3
SOC - CA10	Abs	10	9	9	-	6	7	7	8	4	5	6	7	3	5	6	6
	Norm	21	20	18	-	9	11	10	9	7	6	9	8	4	6	9	6
CA10 - CA50	Abs	9	9	10	-	11	12	13	15	10	11	12	14	10	11	12	14
	Norm	19	20	20	-	17	18	18	18	15	15	17	17	12	15	17	15
CA50 - CA90	Abs	11	11	12	-	17	17	19	23	17	19	19	22	22	20	19	24
	Norm	23	24	25	-	26	26	26	26	26	26	26	27	25	26	26	26
CA10 - CA90	Abs	21	20	22	-	27	29	32	38	27	30	32	36	32	31	31	38
	Norm	43	45	45	-	42	44	45	44	41	41	44	43	37	41	43	41
CA90 - EOC	Abs	17	16	18	-	31	29	32	40	34	38	34	41	50	41	35	48
	Norm	36	36	37	-	49	45	45	47	52	53	47	49	59	53	48	53

4.3.2 Effect of spark timing.

The effects of spark timing and load on combustion duration are shown for 1500 rpm and 3000 rpm (Figs. 4.15 and 4.16). A large variability on results was observed for low engine speed (Figs. 4.15 and 4.16). Combustion duration decreased as load increased for high loads owing to higher in–cylinder temperature. Moreover, late spark timing induced a higher combustion duration in an exponential relation, similar to results found by LIU *et al.* (2017) for engines fuelled with gasoline.

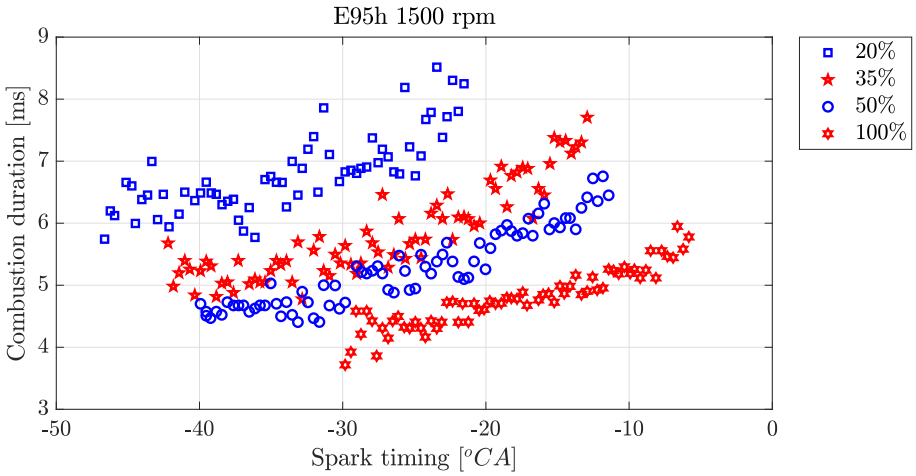

Figure 4.15: Combustion duration for different loads and spark timing at 1500 rpm.

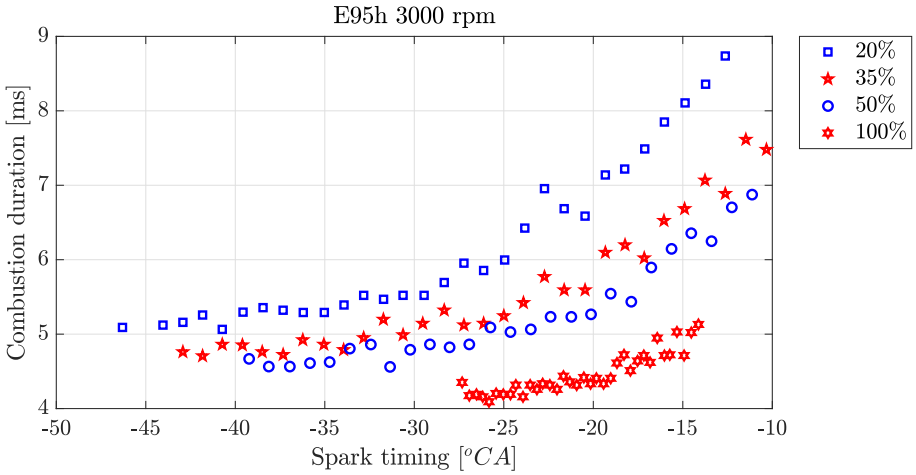

Figure 4.16: Combustion duration for different loads and spark timing at 3000 rpm.

Ignition delay presented a significant relation to spark timing and only a slight influence of load (Figs. 4.17 and 4.18). It was not possible the algorithm to identify ignition delay for 1500 rpm, full load and spark timing values above -20°aTDC (Fig. 4.17) because the ignition delay is very short and the resolution of the pressure profile is not sufficient to identify the ignition delay. As ignition was retarded, the pressure and temperature of the reactants were higher and, therefore, the period of flame kernel development was decreased in a linear relation.

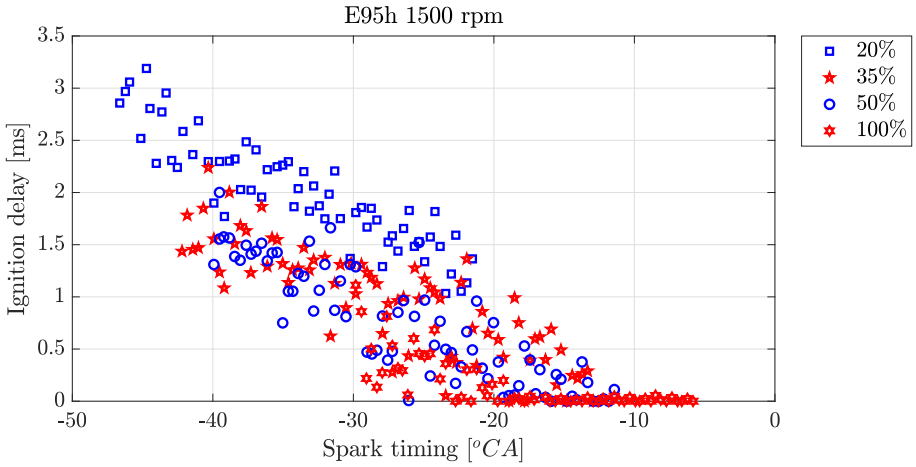

Figure 4.17: Ignition delay for different loads and spark timing at 1500 rpm.

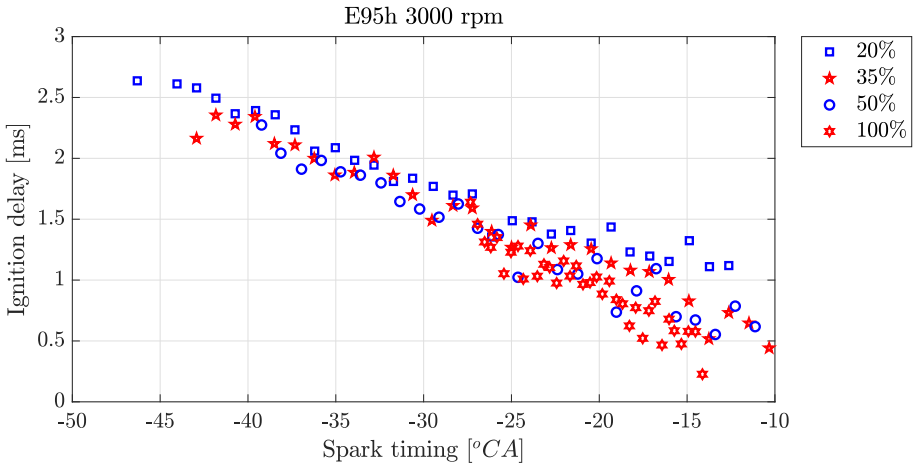

Figure 4.18: Ignition delay for different loads and spark timing at 3000 rpm.

CA50 presented an almost linear relation to spark timing (Figs. 4.19 and 4.20). This trend was result of the effect of a late SOC owing to late spark timing added to the fact that late spark timing increased combustion duration (Figs. 4.15 and 4.16). Therefore, it was possible to derive a relation between CA50 and combustion duration (Fig. 4.21).

ALEIFERIS *et al.* (2017) have indicated that the position of CA50 and the pressure peak location can be used as approximation for MBT. Although industries apply some empirical rules to determine the location of the optimum CA50 (SCHIFTER *et al.*, 2011), different values were found: around 6°CA aTDC for optimum CA50 against 10°CA aTDC provided by the literature and the pressure peak located at 12°CA against 16°CA aTDC provided by the literature (Figs. 4.22 and 4.23, respectively). Those results corroborate with the conclusions of CARVALHO *et al.* (2012). The relation for CA50, imep and combustion duration can be observed for all tested loads conditions in Appendix D.

The relation between spark timing and imep is well established in the literature. There is an optimum value for spark timing as late combustion is longer, decreasing the rate of heat release while the early combustion increases the pressure during the compression stroke,

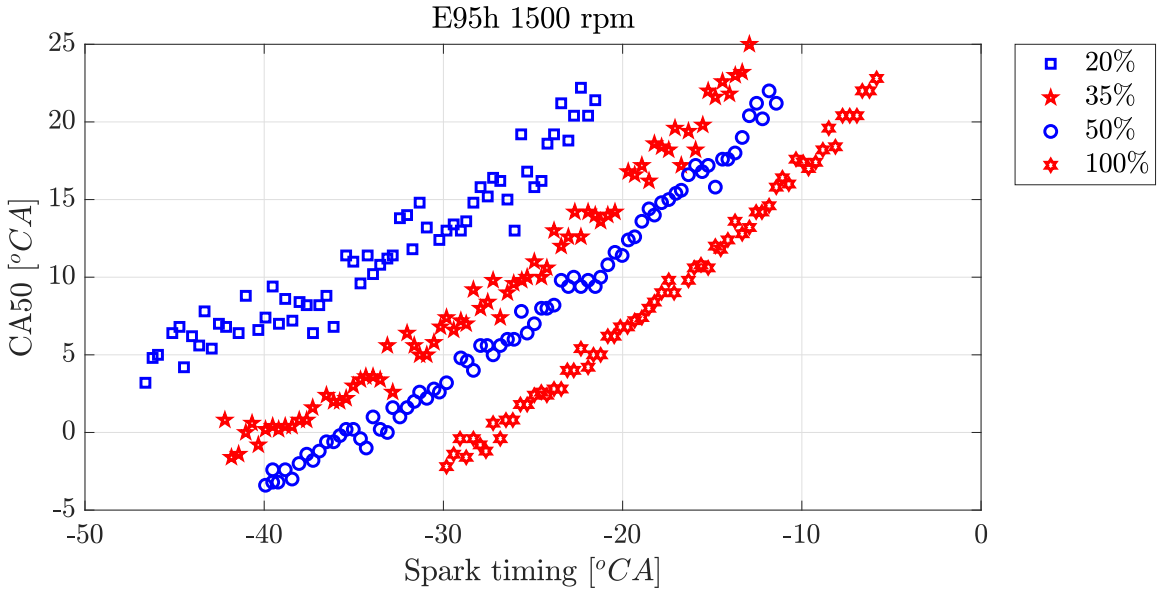

Figure 4.19: CA50 for different loads and spark timing at 1500 rpm.

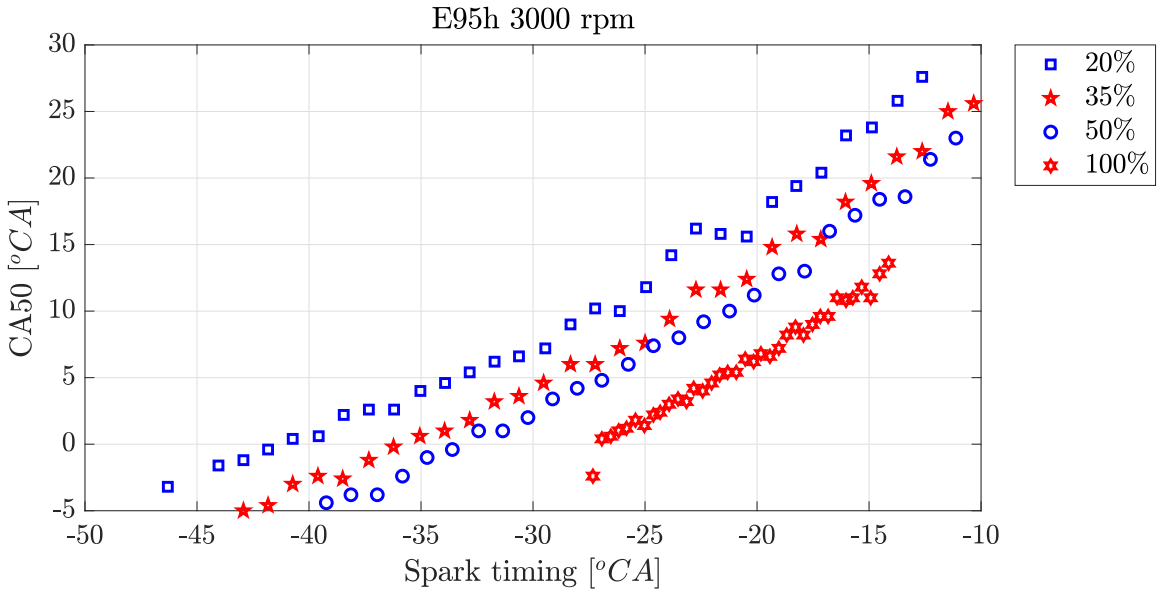

Figure 4.20: CA50 for different loads and spark timing at 3000 rpm.

generating negative power (HEYWOOD, 1988) (Fig. 4.24). It was verified that imep was reduced for faster combustion as the ignition time was too advanced, indicating that imep was not only function of combustion duration but also of combustion phasing.

Results of combustion phases were obtained for 3000 rpm as these values presented a lower level of variability compared to those of 1500 rpm. Load presented a negligible influence on the flame development in terms of °CA (Fig. 4.26). A similar trend was observed for the normalised values (Fig. 4.25), mainly for high load conditions (50% and 100%).

The beginning of the fast burning phase exhibited a relation to spark timing whereas it exhibited no relation to load (Fig. 4.28). However, in terms of percentage, it was not verified a relation between the beginning of the fast burning phase and spark timing. The final part of

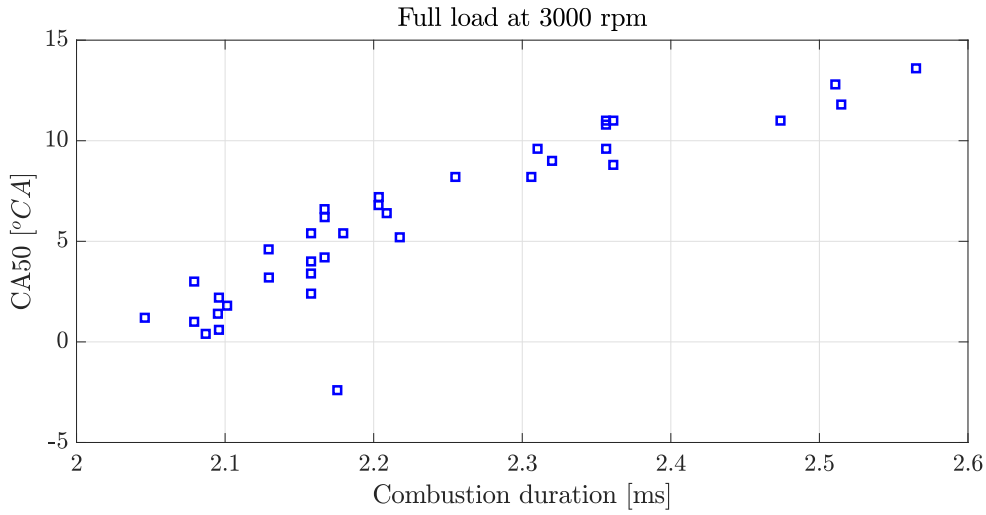

Figure 4.21: Relation between CA50 and combustion duration.

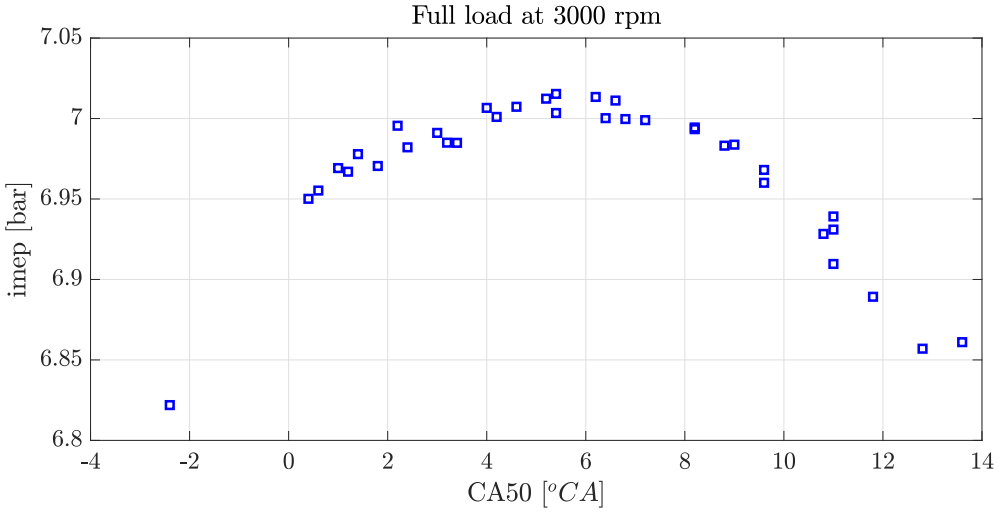

Figure 4.22: Relation between imep and CA50.

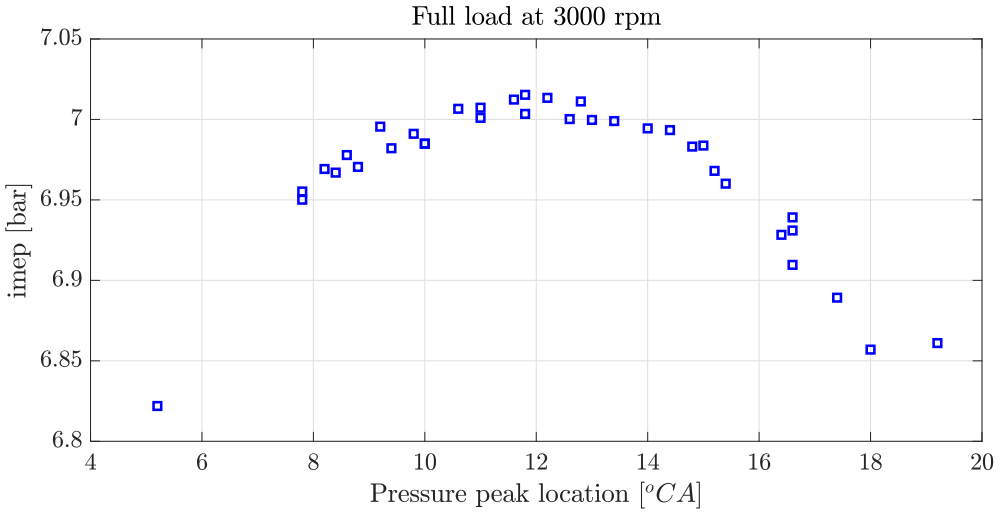

Figure 4.23: Relation between pressure peak and CA50.

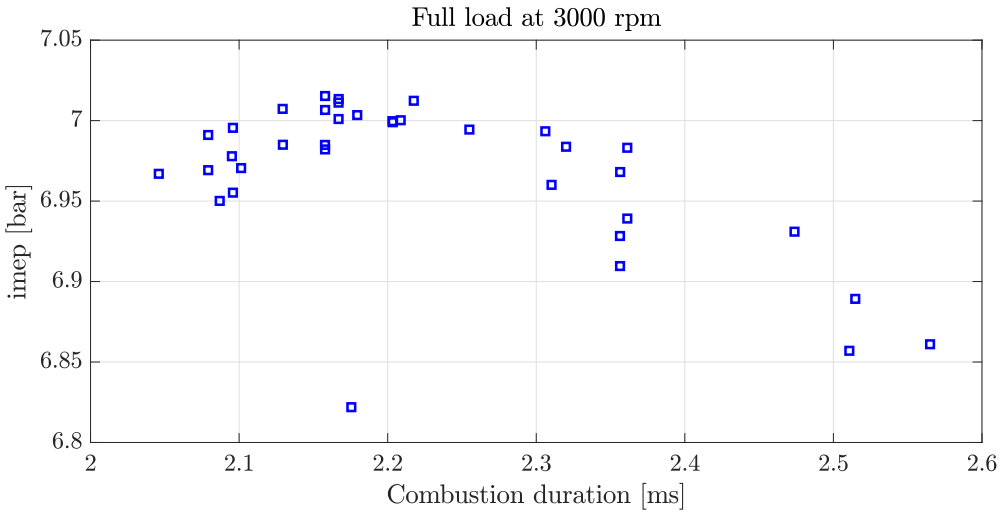

Figure 4.24: Relation between imep and combustion duration.

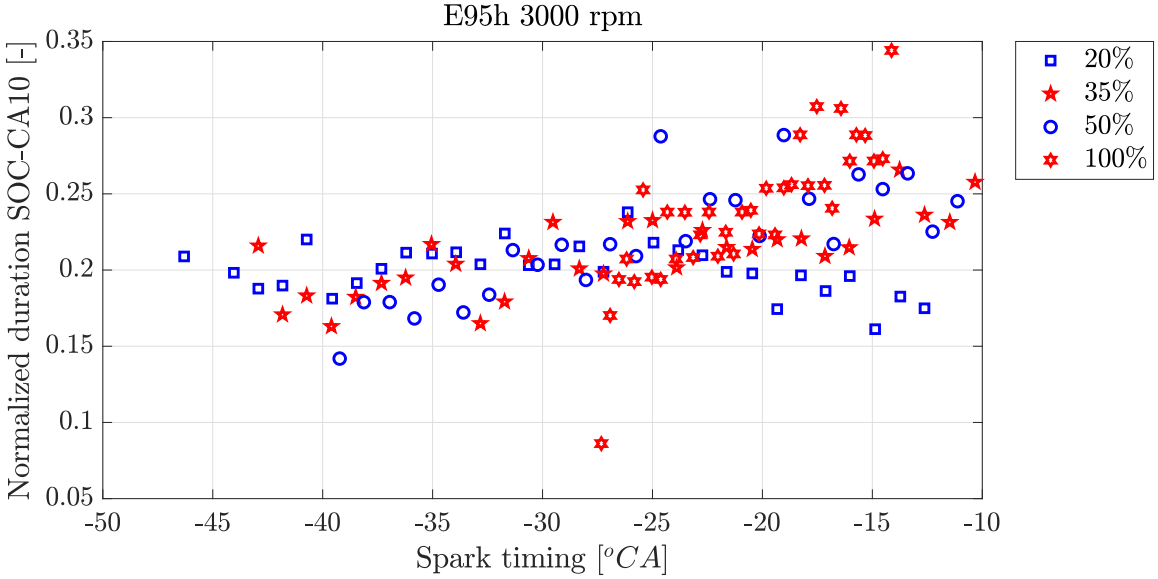

Figure 4.25: Normalised initial phase of combustion for 3000 rpm.

the fast burning presented no relation to spark timing only for full load condition (Fig. 4.30). Consequently, final part of the fast burn phase was decreased in means of percentage (Fig. 4.29). The overall fast burn phase presented a decrease in the participation of the combustion duration with spark timing advancing (Fig. 4.31), although this phase was being increased with respect to spark timing in absolute values (Fig. 4.32).

The final phase of the combustion also presented a decrease in its share on the combustion duration (Fig. 4.33) whereas this phase was being increased in means of °CA (Fig. 4.34). Results indicated that the effect of retarding induced a greater initial phase of combustion. The found results were not expected as flame development phase should be shortened by ignition retarding owing to increased pressure and temperature at the SOC (SERRAS-PEREIRA *et al.*, 2013), similarly to the trend observed for ignition delay. One hypothesis is that the imple-

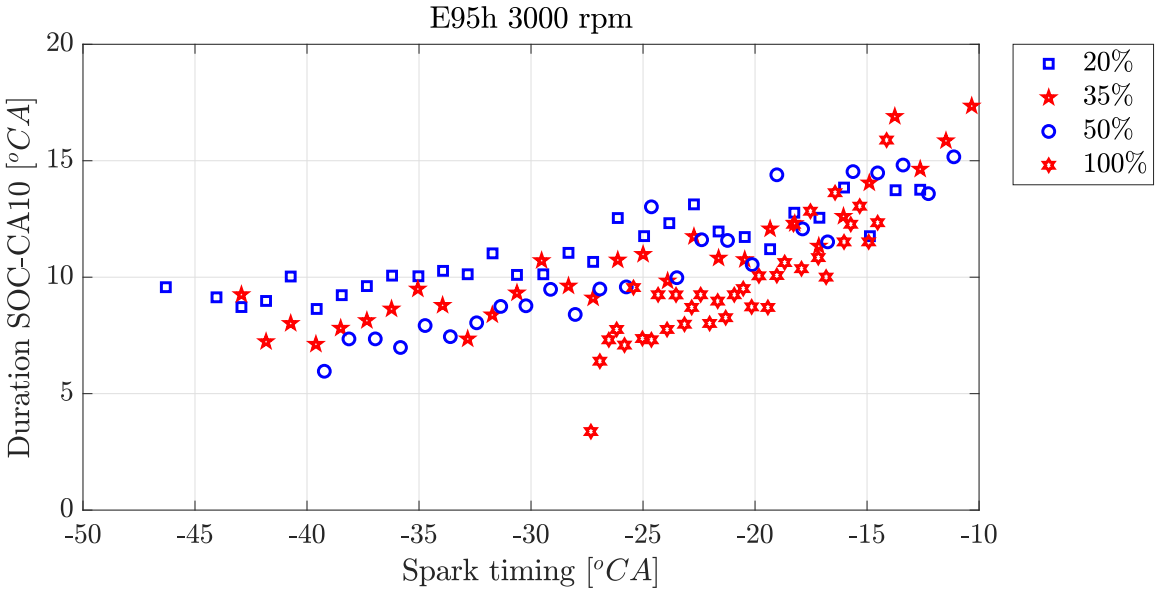

Figure 4.26: Absolute initial phase of combustion for 3000 rpm.

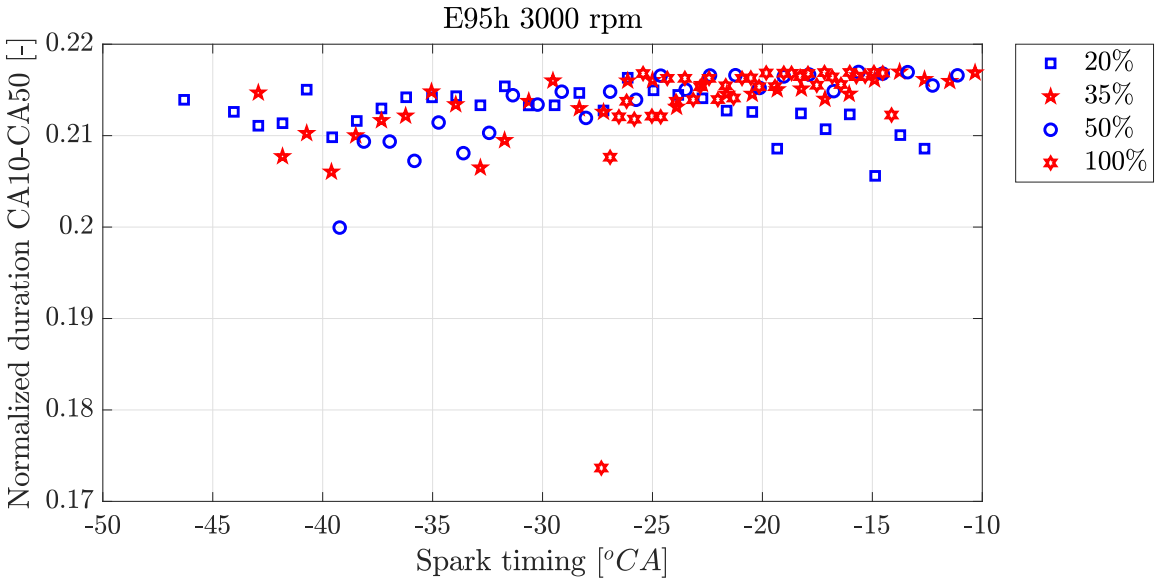

Figure 4.27: Normalised beginning of fast burn phase of combustion for 3000 rpm.

mented algorithm cannot identify SOC precisely and, thus, part of the flame development was accounted for ignition delay.

4.3.3 Comparison between ethanol and gasohol for full load condition.

As expected, ethanol presents a shorter combustion duration than gasohol, confirming remarks in the literature (Fig. 4.35). The heat of vaporisation of ethanol is higher than that of gasohol, leading to a lower temperature for ethanol–air mixture. Although low temperatures causes a decrease on flame speed, the effect of ethanol combustion chemistry prevails over the temperature effects and, therefore, ethanol presents faster flame speed than gasohol (SZYBIST

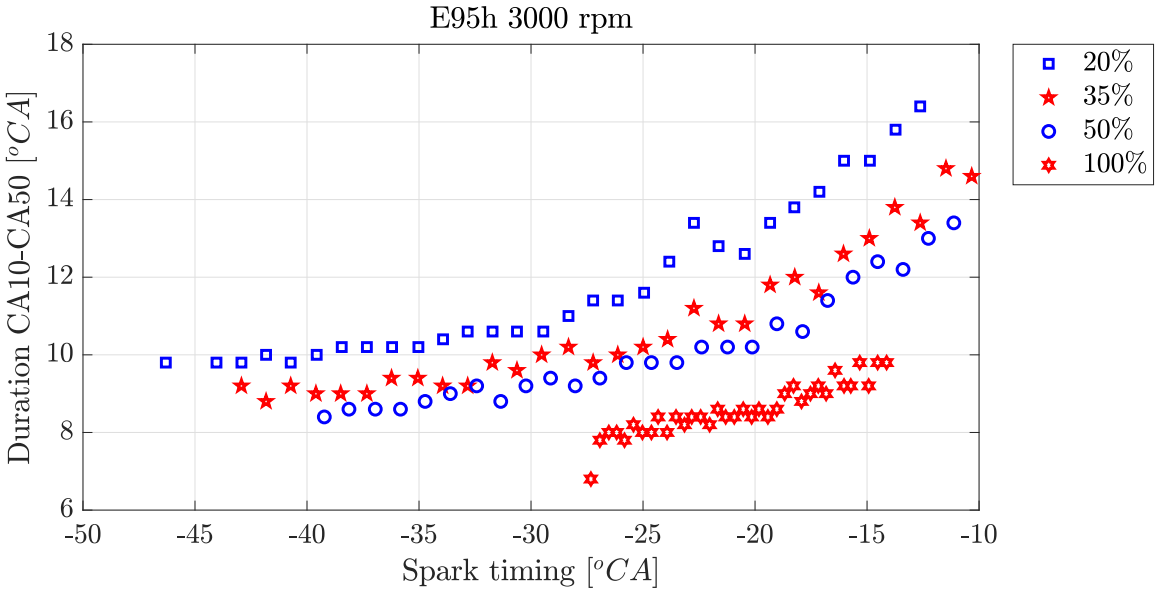

Figure 4.28: Absolute beginning of fast burn phase of combustion for 3000 rpm.

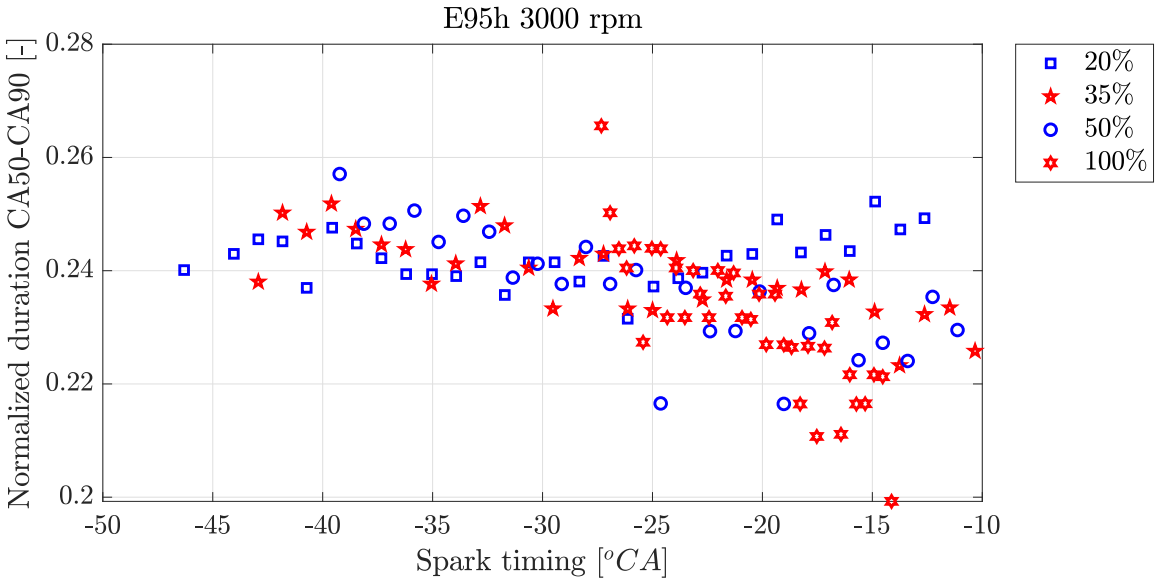

Figure 4.29: Normalised end of fast burn phase of combustion for 3000 rpm.

and SPLITTER, 2016).

Effects of charge cooling owing to fuel vaporisation can be verified even in port fuel injection (PFI) engines, in which the air–fuel mixture is formed outside the cylinder. Adding the effects of charge cooling and a fast flame speed result in a high resistance to knock onset for ethanol (STEIN *et al.*, 2012). Consequently, the difference between combustion duration of ethanol and gasohol was more pronounced for engines speeds lower than 1750 rpm because of ignition retarding for gasohol in order to avoid knock onset (Fig. 4.36).

Moreover, ECU calibration strategy predicted a late spark timing for gasohol even for conditions in which the knock onset was not critical (Fig. 4.36), *i.e.*, for values of engine speed higher than 2000 rpm. By combining the late spark timing and the longer combustion

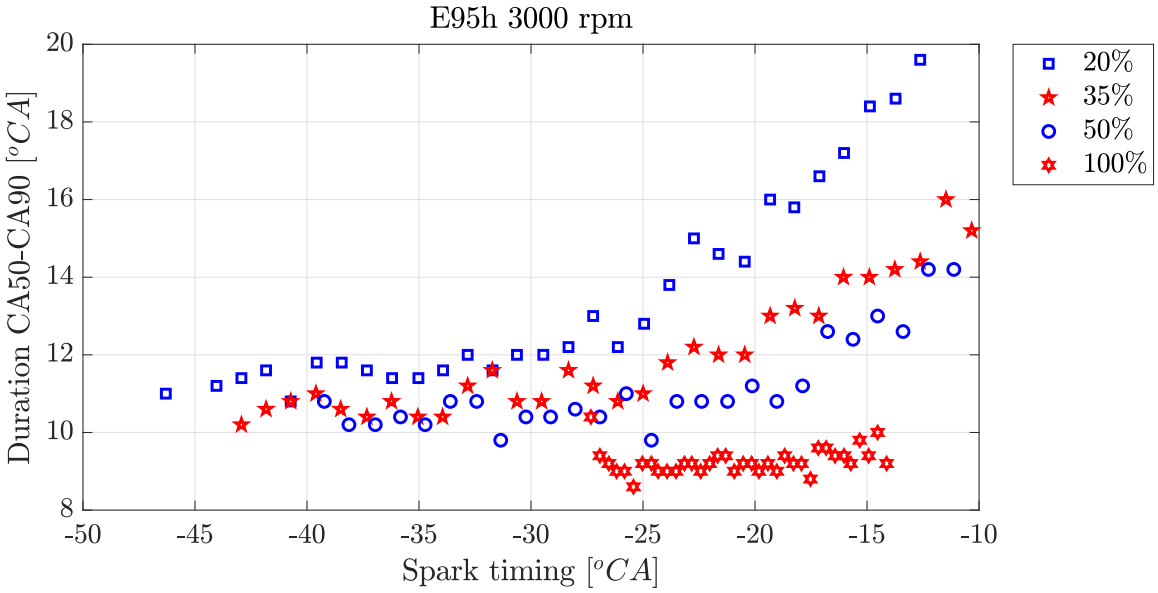

Figure 4.30: Absolute end of fast burn phase of combustion for 3000 rpm.

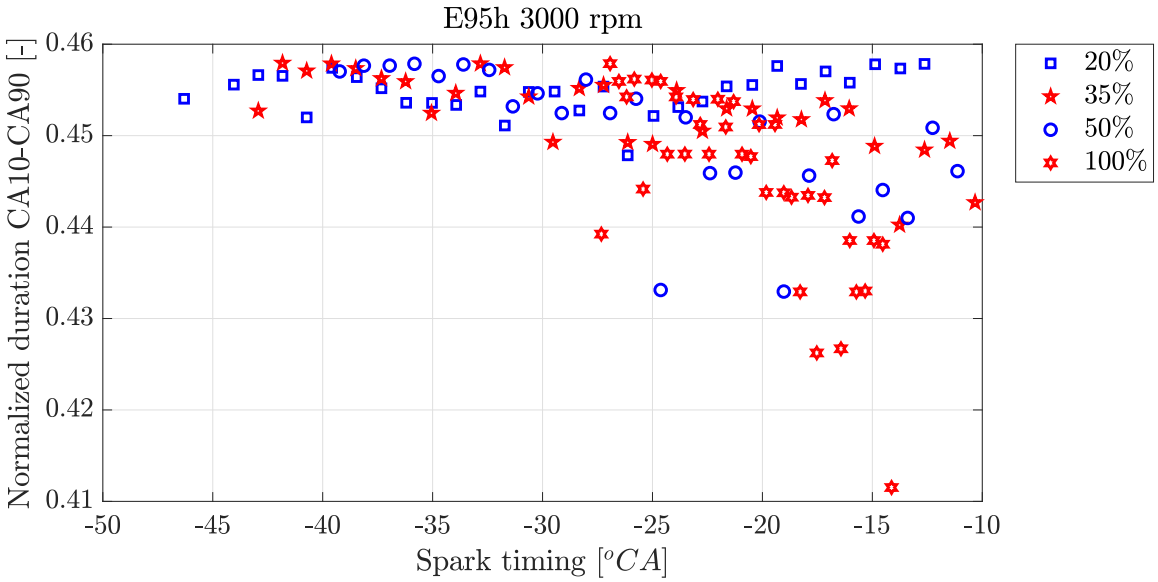

Figure 4.31: Normalised fast burn phase of combustion for 3000 rpm.

duration, the CA50 parameter occured late for gasohol (Fig. 4.37).

Ignition delay presented lower values for gasohol than for ethanol (Fig. 4.38). This result can be attributed to the low temperature of ethanol–air mixture.

Results for each phase of the combustion are provided for ethanol and gasohol respectively in Tabs. 4.5 and 4.6.

Ethanol exhibited a faster combustion in all of its phases in absolute terms. Although the ignition delay was longer for ethanol, the flame development presents a larger share in the combustion duration for gasohol.

The initial part of the fast burn was shorter for ethanol whereas the final part of the fast burn was shorter for gasohol.

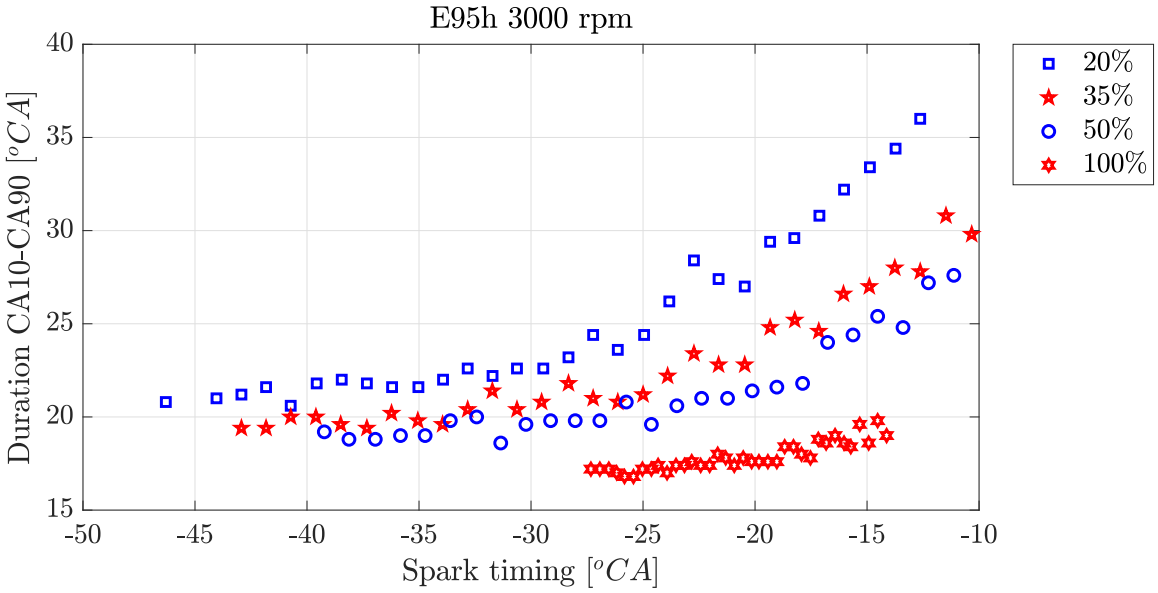

Figure 4.32: Absolute fast burn phase of combustion for 3000 rpm.

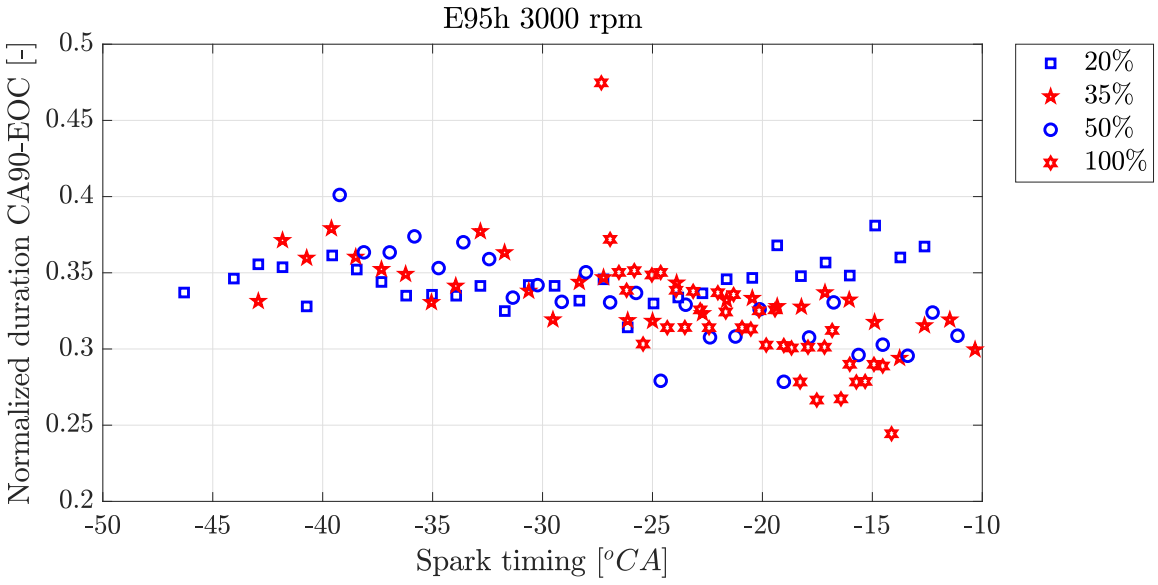

Figure 4.33: Normalised final phase of combustion for 3000 rpm.

The overall fast burn phase was relatively longer for ethanol and it was slightly influenced by engine speed while the fast burn phase for gasohol presented a significant sensibility to engine speed.

The final phase of the combustion of gasohol presented a lower share in combustion duration for engine speed above 2000 rpm. This results was due to the late spark timing for gasohol at low speed, increasing combustion duration. Consequently, the EOC occurred late in the expansion stroke, when pressure and temperature were reduced owing to the increasing of combustion chamber volume.

COONEY *et al.* (2009) have found a similar trend for gasohols with different compositions, indicating that the increase of ethanol concentration decreases the flame development

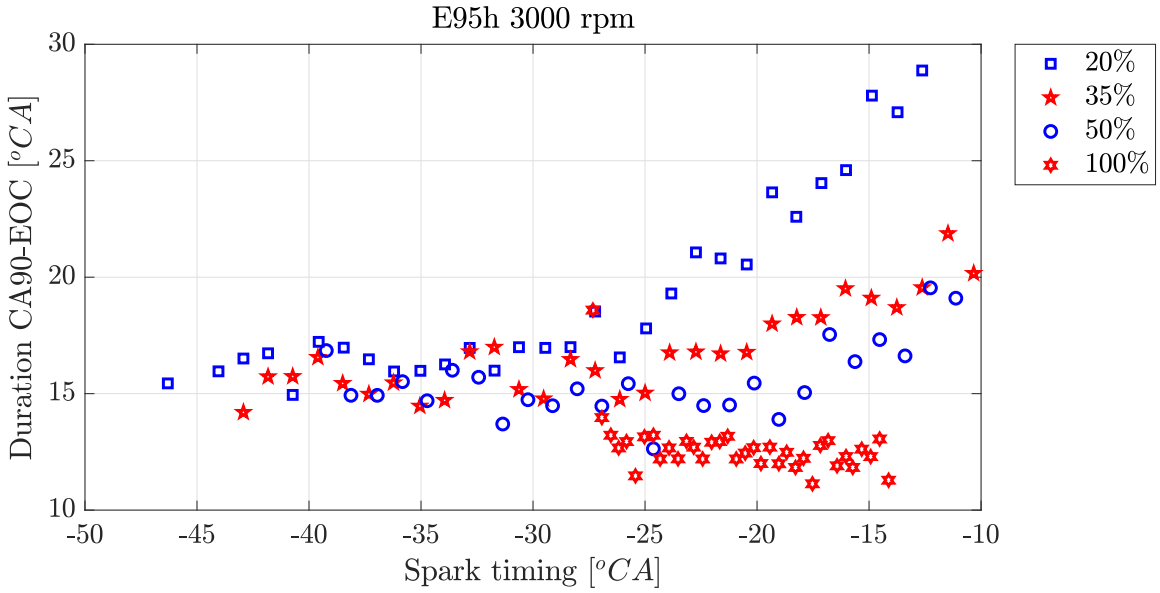

Figure 4.34: Absolute final phase of combustion for 3000 rpm.

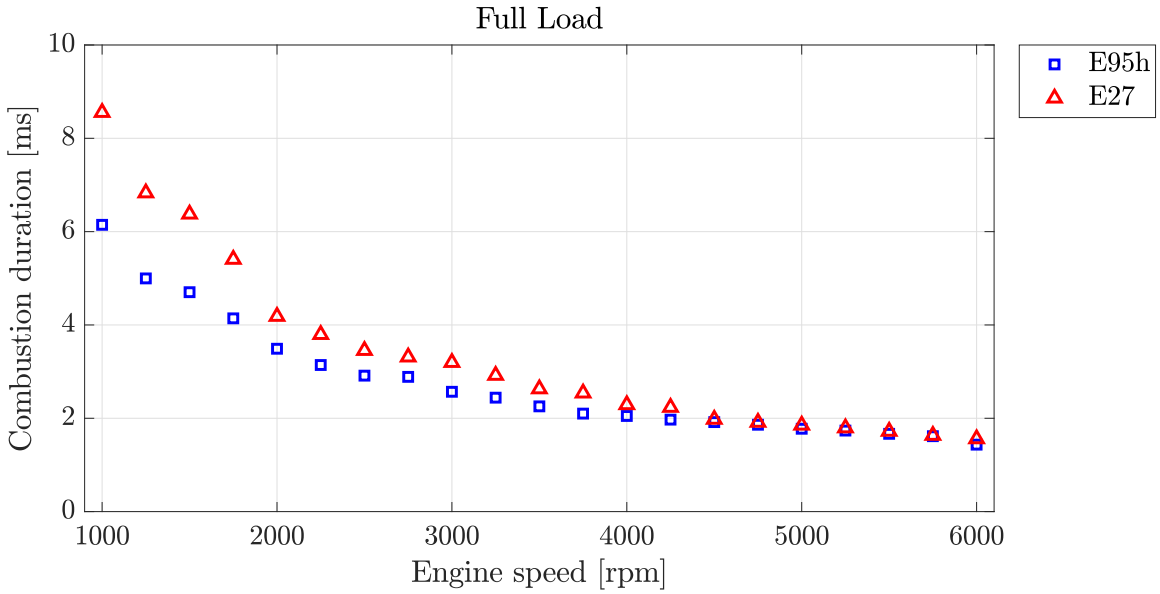

Figure 4.35: Comparison between combustion duration of ethanol and gasohol for different speed at full load.

phase. MELO *et al.* (2012a) have tested various blends of hydrous ethanol and gasoline in an engine operating at 3875 rpm and two conditions of load: 60 Nm and 105 Nm, demonstrating that higher concentration of ethanol leads to an earlier peak of heat release rate. Results on the contribution of each combustion phase found in this work corroborate the remarks of the literature. This result is due to the difference of flame speed between both fuels. By fitting the Wiebe function using the method described in section 4.1, it was possible to verify the effect of combustion profile on the form factor n (Fig. 4.39), which was constant for gasohol for low engine speed below 4250 rpm at 2.5 and decreasing at high engine speed, reaching values around 2, which is considered as a "standard" value for all types fuels in commercial software simu-

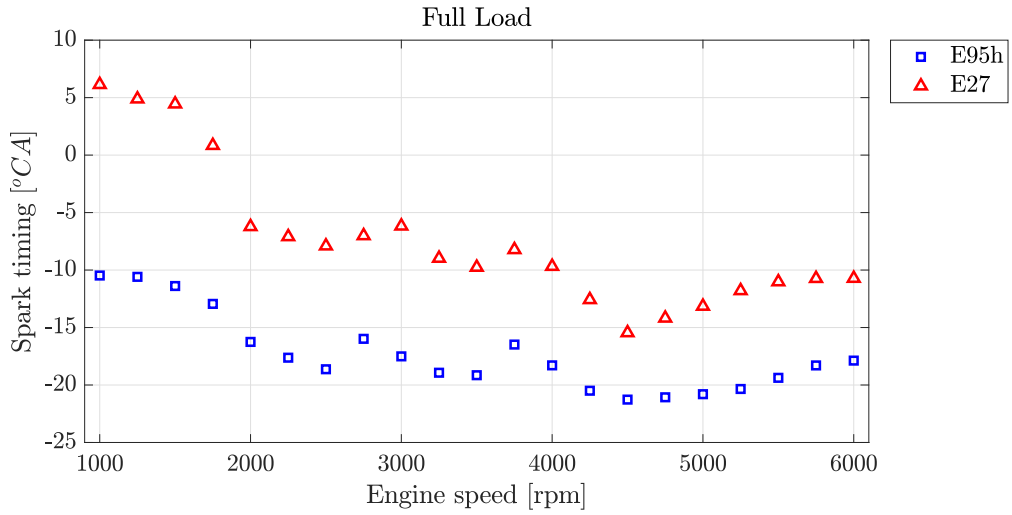

Figure 4.36: Spark timing for ethanol and gasohol at full load.

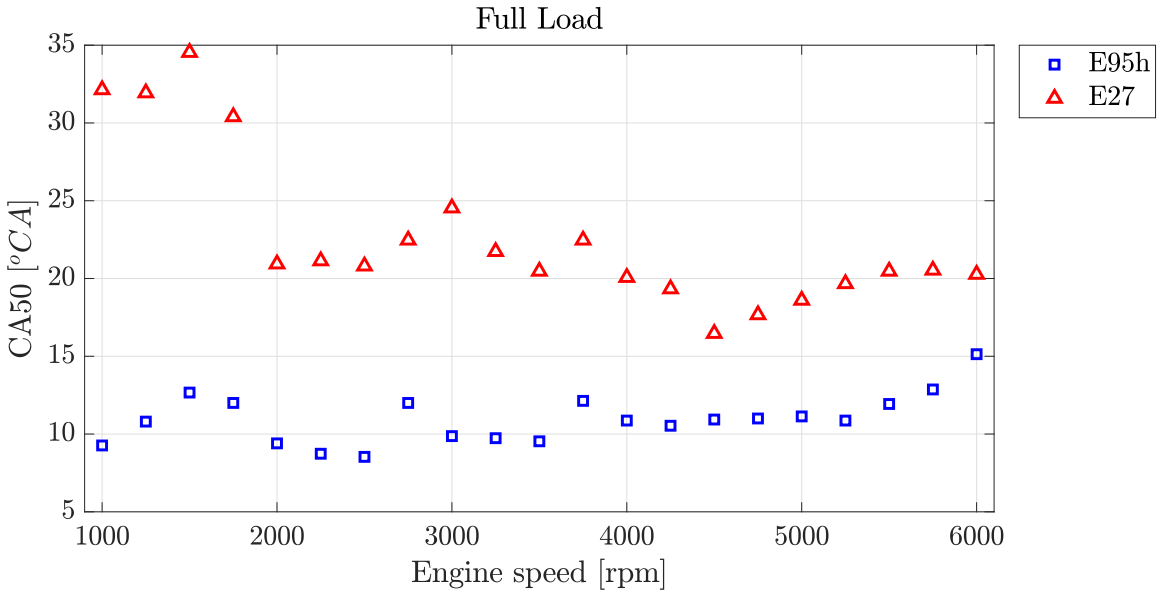

Figure 4.37: Comparison between CA50 of ethanol and gasohol for different speed at full load.

Table 4.5: Duration of each combustion phase for ethanol at full load condition.

Engine speed [rpm]		1000	2000	3000	4000	5000	6000
SOC - CA10	Abs	7	10	9	9	8	12
	Norm	19	23	20	18	16	23
CA10 - CA50	Abs	8	9	10	10	11	11
	Norm	21	21	21	21	20	21
CA50 - CA90	Abs	9	10	11	12	13	12
	Norm	24	23	24	25	25	23
CA10 - CA90	Abs	17	19	21	22	24	23
	Norm	46	45	45	46	45	45
CA90 - EOC	Abs	13	14	16	18	21	17
	Norm	35	32	35	37	39	33

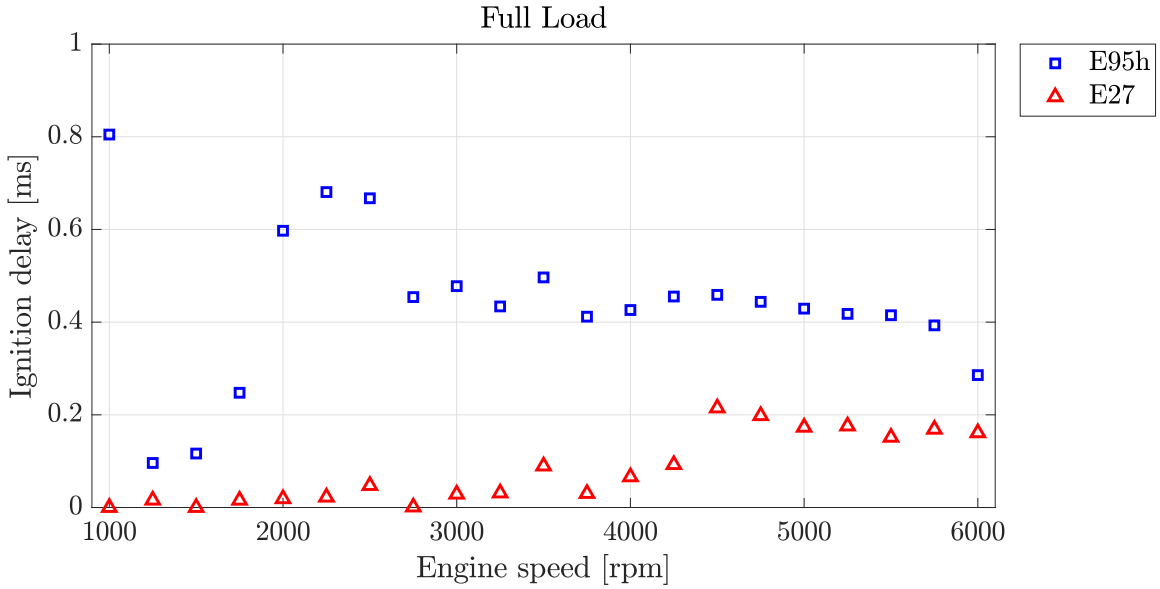

Figure 4.38: Comparison between ignition delay of ethanol and gasohol for different speed at full load.

Table 4.6: Duration of each combustion phase for gasohol at full load condition.

Engine speed [rpm]		1000	2000	3000	4000	5000	6000
SOC - CA10	Abs	15	16	18	16	15	13
	Norm	29	32	31	30	26	23
CA10 - CA50	Abs	11	11	13	12	12	12
	Norm	22	22	22	22	22	21
CA50 - CA90	Abs	10	10	12	12	12	13
	Norm	20	20	20	21	22	23
CA10 - CA90	Abs	22	21	24	24	24	25
	Norm	42	41	42	43	44	45
CA90 - EOC	Abs	15	13	16	15	17	18
	Norm	29	27	27	27	30	32

lation (Gam, 2004). Additionally, this result agreed with values provided by MUELLER *et al.* (1983), who has found values between 2 and 2.7. A value around 1.5 was observed for ethanol, decreasing to 1 for high engine speed. The characteristic of an early heat release profile for ethanol was also verified by comparing the values found for gasohol to those found for ethanol. The form factor was also calculated for the Lean Mixture and Spark timing sweep tests, results are presented in Appendix D.

The verified influences of the engine's parameters on E95h combustion are summarised below:

- Engine speed had the most significant influence through turbulence, whose increase led to a faster combustion, influencing mainly the initial phases of combustion;
- Leaner mixtures increased combustion duration. However, A/F ratio had only a slight

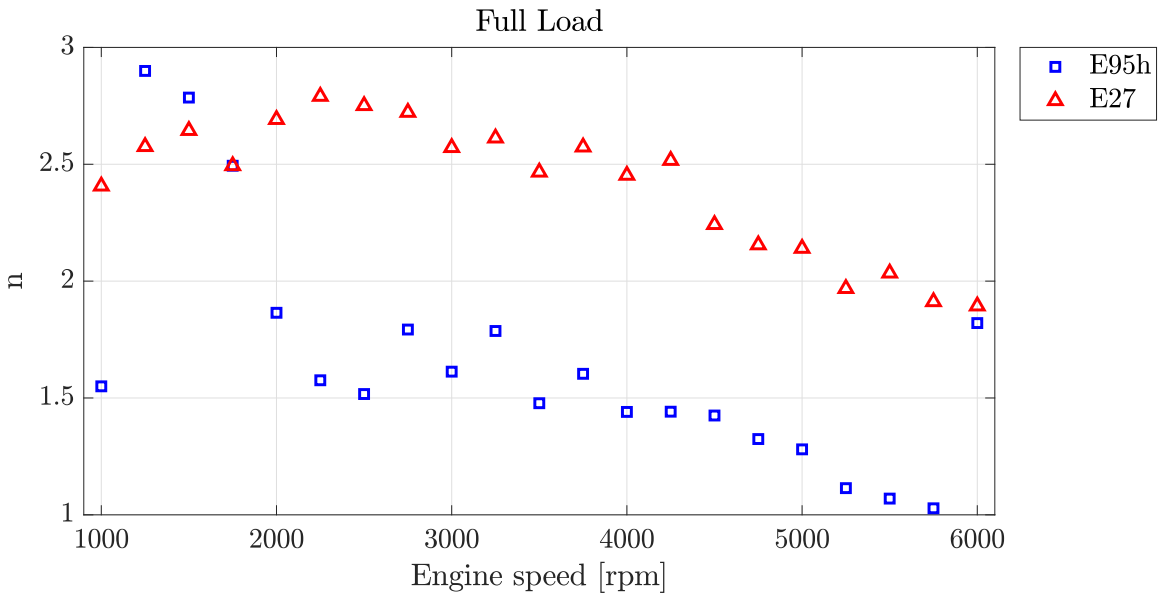

Figure 4.39: Comparison between form factor of ethanol and gasohol for different speed at full load.

influence on combustion and it was overlapped by the stochastic nature of combustion, mainly for high engine speed conditions;

- Spark timing increased combustion duration as it was retarded, although the ignition delay was reduced;

- CA50 parameter was related to MBT. However, its optimum value was not fixed for different types of fuel. Whereas, engine speed had a negligible effect on optimum CA50 as combustion duration presented a small variation in terms of crank angle.

The comparison between the combustion of E95h and that of E27 showed that the former followed the same trend as the latter. The most evident difference between those fuels was that E95h presented faster combustions with faster phases of flame development and the beginning of the fast burn phase, resulting in lower values of form factor of the Wiebe function, n. This difference among combustion durations was more significant at low speeds because the engine had to retard spark timing in order to avoid knock when running with E27.

The predictive simulation requires a model for combustion rate. This model can be implemented by using the data and trends obtained from the study presented in this chapter. More details of the implementation of the combustion model are given in Chapter 6.

5. Predictive model

The phenomenological model used in the predictive algorithm is described in this chapter. The development of the algorithm was carried out with the purpose of creating a model for engine simulation, which would be used by all researchers of the Laboratory of Biofuel Engines. Thus, besides performing the technological investigations related to the research by using the algorithm, each researcher would contribute to the engine simulation model by implementing submodels to the algorithm. The author of this work was responsible for the development of the mathematical model for the thermodynamic relations of a two–zone simulation for a SI engine, described in details in Section 5.3. Although two–zone models are well known in the literature, being described by many authors, the development of the mathematical relations is detailed here and in the Appendix B to assist graduate and undergraduate students whoever may use this specific simulation model or develop their own model in the future.

5.1 Phenomenological model

A Thermodynamic two zone model was chosen to predict performance and phenomenological submodels for combustion and knock onset were implemented in order to define a calibration strategy for the proposed engine and then to estimate the improvements in efficiency of the proposed engine compared to that of a conventional engine.

The model is capable of predicting the thermodynamic properties of the gases in the cylinder along the engine cycle. Pressure, temperature of burned and unburned mixtures, mass flow through valves, residual mass are the properties calculated by the model. Once the thermodynamic properties of the gases are calculated for a given operational condition, it is possible to calculate performance parameters of the engine.

5.2 Properties of substances

The composition of the in–cylinder gases is a fundamental information for the thermodynamic processes simulation. For the air–fuel mixture, the following species are considered:

- Nitrogen;
- Oxygen;
- Argon;
- Water steam (because of air humidity);
- Fuel (hydrous ethanol).

And the following species are considered for combustion products:

- Nitrogen;
- Argon;
- Oxygen (only for lean mixtures);
- Carbon dioxide;
- Water steam;
- Carbon monoxide (only for rich mixtures);
- Hydrogen (only for rich mixtures).

The proportion of each specie is calculated based on the combustion stoichiometry.

The specific heat at constant pressure $\bar{c_{p,i}}$ for each specie i can be determined in molar basis by a 6th order polynomial function of temperature (Eq. 5.1), which was fitted using data from JANAF tables (MATTOS, 2018). The coefficients $a_{i,j}$ can be found on Appendix A.

$$\bar{c_{p,i}} = \sum_{j=0}^{6} a_{i,j} T^j \tag{5.1}$$

The conversion from molar basis to mass basis is performed by dividing the thermodynamic property in molar basis by the molecular weight indicated in Eq. 5.2.

$$c_{p,i} = \frac{\bar{c_{p,i}}}{M_i} \tag{5.2}$$

Other thermodynamic properties can be derived from specific heat at constant pressure, such as the specific heat at constant volume $c_v = c_p - R$, in which the specific gas constant R is given as a function of molecular weight M and the universal constant of gases $\bar{R} = 8.3143 J/(mol.K)$, as indicated in Eq. 5.3.

$$R_i = \frac{\bar{R}}{M_i} \tag{5.3}$$

The specific heat ratio is given by Eq. 5.4.

$$k = \frac{c_p}{c_v} \tag{5.4}$$

To determine the property of a mixture, it is performed a weighted mean on molecular fraction $f_{m,i}$ in Eq. 5.5.

$$\bar{c_p} = \sum f_{m,i} \bar{c_{p,i}} \tag{5.5}$$

5.2.1 Fuel

Hydrous ethanol is considered as fuel in the simulations as it is provided in Brazilian market from renewable sources. It is represented by the code E95h as it is formed by 95% of anhydrous ethanol (C_2H_5OH) in volume, while the rest is water. The specific heat at constant pressure of pure ethanol $c_{p,et}$ is given as function of temperature by Eq. 5.6.

$$c_{p,et} = \sum_{j=0}^{3} a_{et,j} T^j \tag{5.6}$$

The content of water in the hydrous ethanol can be calculated in mass basis y_{H_2O} from the volumetric fraction of water x_{H_2O} by 5.7, in which ρ_{et} is the pure ethanol density while ρ_{H_2O} is the density of water. The molar fraction of water f_{m,H_2O} in hydrous ethanol is given by Eq. 5.8, in which M_{et} is the pure ethanol molecular weight while ρ_{H_2O} is the molecular weight of water.

$$y_{H_2O} = \frac{1}{1 - \frac{\rho_{et}}{\rho_{H_2O}} \frac{1 - x_{H_2O}}{x_{H_2O}}} \tag{5.7}$$

$$f_{m,H_2O} = \frac{1}{1 - \frac{M_{et}}{M_{H_2O}} \frac{1 - y_{H_2O}}{y_{H_2O}}} \tag{5.8}$$

The A/F mixture quality is given as a function of the stoichiometric condition and the relative A/F ratio λ being:

- $\lambda = 1$: Stoichiometric condition;

- $\lambda < 1$: Rich condition, excess of fuel;
- $\lambda > 1$: Lean condition, excess of air.

The properties of pure ethanol are given in Table 5.1

Table 5.1: Properties of pure ethanol.

Specific gravity	Combustion enthalpy $[J/kg]$	Octane number (RON)
0.785	2.75918165e7	108.6

It is noted that the given properties are related to the anhydrous ethanol. It is necessary to correct to the hydrous ethanol according to the weight content of anhydrous ethanol of the fuel. The octane number of the hydrous ethanol was considered to be the same as the anhydrous ethanol.

5.2.2 Humid air

Relative humidity is provided as input for the simulation. The partial pressure of water steam is the relative humidity multiplied by the saturated vapour pressure P_{sat}. For a given atmospheric temperature T_{atm} in Celsius degrees, the saturation pressure can be calculated in kPa from the equation of Antoine (BOUBLÍK *et al.*, 1984) with coefficients suggested by MATTOS (2018), presented in Eq. 5.9.

$$P_{sat} = 10^{5.11564 - \frac{1687.53}{T_{atm} + 230.17}} \tag{5.9}$$

The molar fraction of water vapour in the humid air is given by the ratio between vapour pressure and the atmospheric pressure. Other components of air are considered to be: nitrogen, argon, carbon dioxide and oxygen. The molar fractions of each component in the dry air are provided in Tab. 5.2.

Table 5.2: Composition of dry air.

Substance	Molar fraction
Argon	0.00937
Carbon dioxide	0.00033
Oxygen	0.20946
Nitrogen	0.78084

5.3 Mathematical model

The in–cylinder thermodynamic process is divided in two phases, the closed phase comprising compression, combustion and expansion of gases, in which the valves are closed.

A diagram is shown in Fig. 5.1 to illustrate the engine cycle. The inner segment represents the closed phases. The compression stroke begins after the Intake Valve Closing (IVC), represented by the blue arc in the diagram. Before the piston reaching the Top Dead Centre (TDC), the spark is set and the combustion begins at the event called Start of Combustion (SOC), represented by the red arc in the diagram. After the TDC, combustion ends at the End of Combustion event (EOC), initiating the expansion stroke, represented by the yellow arc in the diagram.

The expansion stroke ends at the instant in which the exhaust valve opens, the Exhaust Valve Opening (EVO) event. The EVO occurs before the BDC in order to improve the efficacy of the gases exhaust process, as valve lifting occurs progressively. Then, the closed phases end and the open phases begin with the exhaust stroke, represented by the orange arc in the diagram. Note that Intake Valve Opening (IVO) occurs before Exhaust Valve Closing (EVC), and the intake and exhaust processes overlap during a period called valve overlapping. In the diagram, valve overlapping is verified by the superposition of the orange and green arcs. Intake, represented by the green arc, ends at the IVC event, completing the engine cycle.

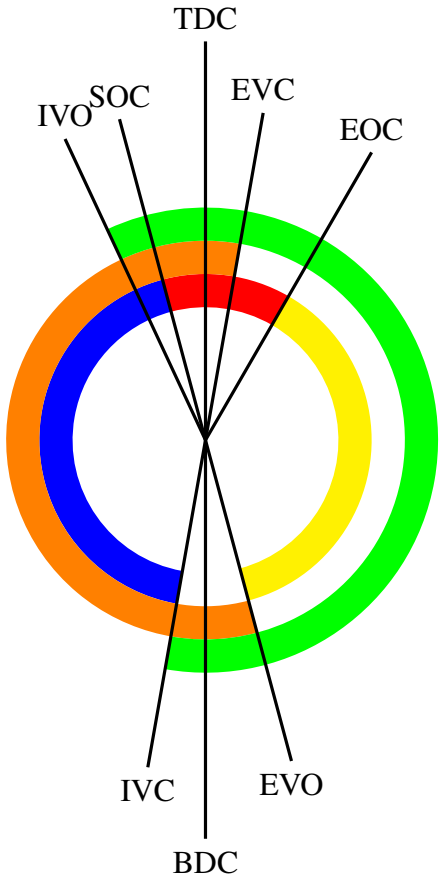

Figure 5.1: Engine processes.

Two zones are considered for the closed phases. The hypothesis adopted to implement the phenomenological model are the following:

- Both zones are at mechanical equilibrium, *i.e.*, the same pressure;

- Blow–by is neglected;
- Burned and unburned gases do not mixture;
- The zones are separated by the flame front;
- Flame is considered to be impermeable and adiabatic and it has an infinitesimal width;
- Area of heat transfer is proportional to volume;
- Heat transfer from cylinder walls to cooling water is not modelled. Cylinder walls are considered to be at constant temperature;
- Heat transfer is considered to occur exclusively via convection. Radiation is neglected.
- In the equations, enthalpy is only a function of temperature. Energy released by the combustion is considered by the variable H_{comb}.

As temperature of gases is considerably high, the hypothesis of ideal gas behaviour is reasonable, as proven by ZACHARIAS (1967).

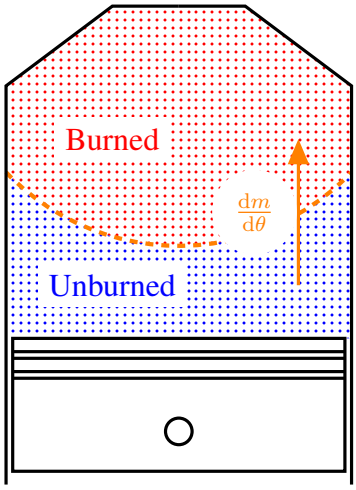

Figure 5.2: System considered for the two zone model.

A scheme of the model is presented in Fig. 5.2. As combustion occurs, mass is transferred from the unburned mixture to the burned gases, releasing energy. Because of the assumption of adiabatic flame, the energy released by combustion is absorbed by the combustion products. The differential equations for temperature of burned gases T_b, temperature of unburned bases T_u and Pressure P are respectively indicated in Eqs. 5.10, 5.11 and 5.12. The whole development of the equations is provided in Appendix B.

$$\frac{\mathrm{d}T_b}{\mathrm{d}\theta} = \frac{\frac{\mathrm{d}H_{comb}}{\mathrm{d}\theta} + \frac{\mathrm{d}Q_b}{\mathrm{d}\theta} + \frac{\mathrm{d}m_b}{\mathrm{d}\theta}\left(c_{p,u}T_u - c_{p,b}T_b\right) + V_b\frac{\mathrm{d}P}{\mathrm{d}\theta}}{m_b c_{p,b}} \tag{5.10}$$

$$\frac{\mathrm{d}T_u}{\mathrm{d}\theta} = \frac{\frac{\mathrm{d}Q_u}{\mathrm{d}\theta} + V_u \frac{\mathrm{d}P}{\mathrm{d}\theta}}{m_u c_{p,u}} \tag{5.11}$$

$$\frac{\mathrm{d}P}{\mathrm{d}\theta} = \frac{P\frac{\mathrm{d}V}{\mathrm{d}\theta} - R_u T_u \frac{\mathrm{d}m_u}{\mathrm{d}\theta} - R_b T_b \frac{\mathrm{d}m_b}{\mathrm{d}\theta} - \frac{R_u \frac{\mathrm{d}Q_u}{\mathrm{d}\theta}}{c_{p,u}} - \frac{R_b\left[\frac{\mathrm{d}H_{comb}}{\mathrm{d}\theta} + \frac{\mathrm{d}Q_b}{\mathrm{d}\theta} + \frac{\mathrm{d}m_b}{\mathrm{d}\theta}\left(c_{p,u}T_u - c_{p,b}T_b\right)\right]}{c_{p,b}}}{\frac{V_b R_b}{c_{p,b}} + \frac{V_u R_u}{c_{p,u}} - V} \tag{5.12}$$

Only unburned mixture exists prior to combustion, including the fresh air–fuel mixture and the residual gases from the previous cycles, which are considered to behave as a diluent in the air–fuel mixture. Therefore, there is only one zone during the compression stroke. After the combustion, all of the air–fuel mixture has been consumed by the flame and only combustion products exist in the cylinder, also comprehended by only one zone during the expansion stroke. Consequently, two zones are observed only during the combustion. However, Eqs. 5.10, 5.11 and 5.12 can be implemented for the whole closed phases, including compression, combustion and expansion. Whenever one zone does not exists, its differential of temperature can be set zero. In the pressure differential, the gas constant can be set for zero to eliminate the effect of one non–existent zone. It is noted that for compression, the volume occupied by the unburned gases is the total volume of the combustion chamber, whilst burned gases occupy the total volume of combustion chamber during the expansion stroke.

Heat transfer rate, represented by the term $\frac{\mathrm{d}Q}{\mathrm{d}\theta}$, is assumed to occur mainly owing to convection between gases and cylinder walls (Eq. 5.13) as the main source of radiation is the particulate matter, which is negligible in spark–ignition engines (ANNAND, 1963). Thus, its estimation is based on the instantaneous area of heat transfer A and the estimated temperature of cylinder walls T_w. The heat transfer coefficient h^{HT} is given by Hohenberg correlation (HOHENBERG, 1979) as function of pressure, temperature, volume and piston velocity v_m, as demonstrated in Eq. 5.14.

$$\frac{\mathrm{d}Q}{\mathrm{d}\theta} = -\frac{h^{HT} A \left(T - T_w\right)}{\omega} \tag{5.13}$$

$$h^{HT} = 130 V^{-0,06} P^{0,8} T^{-0,4} (v_m + 1,4)^{0,8} \tag{5.14}$$

Rate of energy released by the combustion process is proportional to burn rate $\frac{\mathrm{d}x_b}{\mathrm{d}\theta}$ and it can be calculated as function of admitted mass of fuel m_{fuel} and h_{comb} as indicated in Eq. 5.15.

$$\frac{\mathrm{d}H_{comb}}{\mathrm{d}\theta} = \eta_{comb} m_{fuel} h_{comb} \frac{\mathrm{d}x_b}{\mathrm{d}\theta} \tag{5.15}$$

An efficiency for combustion η_{comb} can be defined as function of A/F ratio. This efficiency is related to the amount of energy converted to thermal energy in the combustion process (BLAIR, 1999) and it is given by Eq. 5.16.

$$\eta_{comb} = \eta_{comb,max} \left(-1,6082 + 4,6509\lambda - 2,0764\lambda^2\right) \tag{5.16}$$

Mass fraction burn is provided by Wiebe function. Eq. 5.17 presents Wiebe function as defined by LANZAFAME (1999), in which an asymptotic limit is defined by η_r. Combustion duration and form factor are calculated from data based models obtained from a combustion diagnosis, described in chapter 4.

$$x_b(\theta) = 1 - \exp\left[\ln\left(1-\eta_r\right)\left(\frac{\theta-\theta_o}{\Delta\theta_b}\right)^{n+1}\right] \tag{5.17}$$

The rate of mass burning is derived from the differentiation of Eq. 5.17, which leads to Eq. 5.18.

$$\frac{\mathrm{d}x_b}{\mathrm{d}\theta} = -\frac{\ln\left(1-\eta_r\right)}{\Delta\theta_b}\left(n+1\right)\left(\frac{\theta-\theta_o}{\Delta\theta_b}\right)^{n} \exp\left[\ln\left(1-\eta_r\right)\left(\frac{\theta-\theta_o}{\Delta\theta_b}\right)^{n+1}\right] \tag{5.18}$$

For the open phases, only one zone is considered. Hence, the hypothesis of a perfect mixing is considered, *i.e.*, when the fresh air–fuel mixture is admitted in the cylinder, it mixes with the residual gas, forming a homogeneous mixture. A scheme is presented in Fig. 5.3.

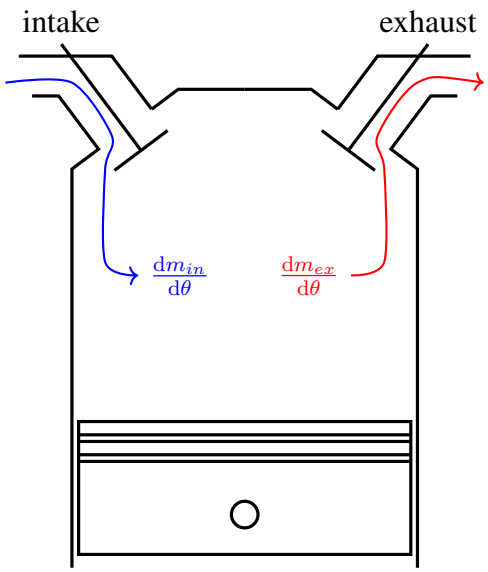

Figure 5.3: System considered for the gas exchange processes.

Subscripts in and ex represent respectively intake and exhaust. It is highlighted that flow always goes from the higher to the lower pressure. Thus, the algorithm always verifies the ratio of pressure between cylinder and ports, defining which system consists of the upstream us and downstream ds.

A positive flow is considered to be a flow entering the cylinder, independent of the valve being analysed. The gases flow from the intake port to the cylinder during most part of the intake process, *i.e.*, positive flow (see blue arrow in Fig. 5.3). However, an inverse flow can occur depending on the conditions in the cylinder and in the intake port. This negative flow is known as backflow. Whenever backflow occurs, a certain amount of gases flow from the cylinder to the intake port. Then, it is assumed that this amount can be re–admitted if the flow becomes positive. The same phenomenon can occur in the exhaust port (see red arrow in Fig. 5.3), but backflow is considered to be positive in the exhaust, *i.e.*, exhaust backflow occurs when gases flow from the exhaust port to the cylinder.

The differential equations for temperature for this phase of the cycle are given in Eq. 5.19. Pressure can be calculated in the integral form of the ideal gases law. Further details on the development of the equations are provided in Appendix B.

$$\frac{\mathrm{d}T}{\mathrm{d}\theta} = \frac{\frac{\mathrm{d}Q}{\mathrm{d}\theta} - P\frac{\mathrm{d}V}{\mathrm{d}\theta} + (c_{v,in}T_{in} - c_vT)\frac{\mathrm{d}m_{in}}{\mathrm{d}\theta} + (c_{v,ex}T_{ex} - c_vT)\frac{\mathrm{d}m_{ex}}{\mathrm{d}\theta}}{mc_v} \tag{5.19}$$

$$\frac{\mathrm{d}P}{\mathrm{d}\theta} = P\left(\frac{1}{T}\frac{\mathrm{d}T}{\mathrm{d}\theta} + \frac{1}{m}\frac{\mathrm{d}m}{\mathrm{d}\theta} - \frac{1}{V}\frac{\mathrm{d}V}{\mathrm{d}\theta}\right) \tag{5.20}$$

For the open phases, the heat transfer coefficient is calculated according to the model proposed by NISHIWAKI *et al.* (1979) as function of cylinder diameter D_c, Pressure, Temperature and piston's mean velocity. For the exhaust, the heat transfer coefficient is given by Eq. 5.21 whilst it is given by Eq. 5.22 for intake process.

$$h^{HT} = 82,3D_c^{-0.193}(v_mP)^{0.807}T^{-0.534} \tag{5.21}$$

$$h^{HT} = 679D_c^{-0.422}(v_mP)^{0.578}T^{-0.199} \tag{5.22}$$

It is highlighted that exhaust and intake overlaps around the TDC (see Fig. 5.1). Moreover, the effects of mass intake and exhausted are minimized as valves close at the beginning and the end of each mass transfer process. Thus, the heat transfer coefficients were calculated according to the three models *i.e.*, Hohenberg and both Nishiwaki. The resultant heat transfer coefficient was calculated by a mean value, weighted by the area of flow in each valve.

The isentropic flow through an orifice hypothesis is assumed to calculate the isentropic mass flow. Real mass flow is given by multiplying the isentropic mass flow by a coefficient of discharge C_D, experimentally calculated as function of valve lifting (Fig. 5.4). In the diagram, a flow from the port to the cylinder is exemplified. In that case, the port is considered as upstream and the cylinder is considered the downstream. Thus, cylinder pressure must be lower than the port pressure.

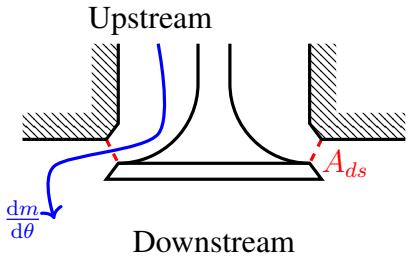

Figure 5.4: Mass flow through valve.

Firstly, the algorithm has to determine whether the flow is subsonic or choked, *i.e.*, sonic flow at the minimum area. This condition is demonstrated in Eq. 5.23.

$$\frac{P_{ds}}{P_{us}} \leq \left(\frac{2}{k+1}\right)^{\frac{k}{k-1}} \tag{5.23}$$

If the condition presented in Eq. 5.23 is satisfied, the flow is choked and the mass flow depends only on the upstream conditions, being calculated by the expression in Eq. 5.24. Downstream area A_{ds} represents the minimum area for the flow. This area represents the frustum of a cone formed by the distance between valve and seat for small lifts (Fig. 5.4). For major lifts, the area of the port limits the flow. The relations used to calculate A_{ds} are presented in Appendix B.

$$\dot{m} = C_D \frac{A_{ds} P_{us}}{\sqrt{R T_{us}}} \sqrt{k \left(\frac{2}{k+1}\right)^{\frac{k+1}{k-1}}} \tag{5.24}$$

Otherwise, the mass flow also depends on the downstream conditions, being calculated by the expression in Eq. 5.25.

$$\dot{m} = C_D \frac{A_{ds} P_{us}}{R T_{us}} \sqrt{2 \left(\frac{k}{k-1}\right) \left[\left(\frac{P_{ds}}{P_{us}}\right)^{\frac{2}{k}} - \left(\frac{P_{ds}}{P_{us}}\right)^{\frac{k+1}{k}}\right]} \tag{5.25}$$

It is highlighted that the area A_{ds} presented in the equations is the minimum area of flow, *i.e.*, the area in the valve. More details on the calculation of mass flow, valve lifting, valve area and calculation of coefficient of discharge are available in Appendix B.

The presented equations characterise a set of differential equations, which can be

solved by numerical integration methods. For the described model, it was implemented a 5th order Runge–Kutta method, also known as Butcher method, as suggested by LOPES (2014). The steps of the integration are provided in Eq. 5.32, in which ϕ represents an arbitrary thermodynamic property.

$$\phi_{j+1} = \phi_j + \frac{1}{90}\Delta\theta\left(7a_1 + 32a_3 + 12a_4 + 32a_5 + 7a_6\right) \tag{5.26}$$

$$a_1 = f(\theta_j, \phi_j) \tag{5.27}$$

$$a_2 = f\left(\theta_j + \frac{\Delta\theta}{4}, \phi_j + \frac{a_1\Delta\theta}{4}\right) \tag{5.28}$$

$$a_3 = f\left(\theta_j + \frac{\Delta\theta}{4}, \phi_j + \frac{a_1\Delta\theta}{8} + \frac{a_2\Delta\theta}{8}\right) \tag{5.29}$$

$$a_4 = f\left(\theta_j + \frac{\Delta\theta}{2}, \phi_j - \frac{a_2\Delta\theta}{2} + a_3\Delta\theta\right) \tag{5.30}$$

$$a_5 = f\left(\theta_j + \frac{3\Delta\theta}{4}, \phi_j + \frac{3a_1\Delta\theta}{16} + \frac{9a_4\Delta\theta}{16}\right) \tag{5.31}$$

$$a_6 = f\left(\theta_j + \Delta\theta, \phi_j - \frac{3a_1\Delta\theta}{7} + \frac{2a_2\Delta\theta}{7} + \frac{12a_3\Delta\theta}{7} - \frac{12a_4\Delta\theta}{7} + \frac{8a_5\Delta\theta}{7}\right) \tag{5.32}$$

For initial values, the model considers ambient conditions at IVC in the first iteration. For the burned gases, adiabatic flame temperature is considered as initial condition. After each iteration, the values at IVC are updated until a difference smaller than 0.1 % is observed between the values found in the previous iteration and the values found in the current iteration for trapped mass, pressure and temperature.

5.4 Model for knock onset prediction

The knock phenomenon consists of the detonation of the end gas. It is induced by the auto ignition of the end gas during the combustion. The shock of flames propagates acoustic waves which can damage the engine in a long term operation (HEYWOOD, 1988). THerefore, this phenomenon is avoided in operation of commercial engines, in which the durability is an important factor. According to LIVENGOOD and WU (1955), an air–fuel mixture achieves auto ignition after a period of time exposed to an elevated level of pressure and temperature. This period of time is known as auto ignition delay τ. This delay can be determined as function of pressure and temperature, and as pressure and temperature are varying along the combustion process, it is necessary to integrate this delay as respect with time, as indicated in Eq. 5.33. This method for knock onset prediction is known as Knock Integral Method (KIM), being the result of the integral as the Knock Index K_I

$$K_I = \int_{IVC}^{EOC} \frac{1}{\tau} dt \tag{5.33}$$

It is assumed that knock occurs when $K_I \geq 1$. It has been proposed by LIVENGOOD and WU (1955) that the delay can be calculated by the Arrhenius relation, shown in Eq. 5.34.

$$\tau = A_K P^{-n_K} \exp\left[\frac{B_K}{T}\right] \tag{5.34}$$

The work of DOUAUD and EYZAT (1978) is one of the pioneers to provide values for the constants A_K, n_K and B_K as function of the research octane number (ON) of the fuel:

$$A_K = 0.01869 \left(\frac{ON}{100}\right)^{3,4017} \tag{5.35}$$

$$n_K = 1,7 \tag{5.36}$$

$$B_K = 3800 \tag{5.37}$$

5.5 Performance parameters

Once the engine processes are simulated, the profiles of pressure, temperature, in–cylinder trapped mass can be used to calculated parameters for performance evaluation of the engine. The chosen parameter to perform the analysis are the following:

- Indicated power $\dot{W}$;
- Indicated torque T;
- Thermal efficiency η_t;
- Volumetric efficiency η_v;
- Indicated mean effective pressure $imep$.

The indicated power $\dot{W}$ consists of the amount of work performed by the in cylinder gases W_{cycle} in a certain period of time. The work can be calculated as presented in Eq. 5.38. As a cycle of pressure is performed at every two rotations of the engine because the engine operates with four strokes, the power is given by multiplying the work performed in a cycle by half the angular velocity of the engine, as shown in Eq. 5.39.

$$W_{cycle} = \oint P \, \mathrm{d}V \tag{5.38}$$

$$\dot{W} = \frac{W_{cycle}\omega}{2} \tag{5.39}$$

Thermal efficiency is given by the ratio between power and energy flow input to the engine. The energy flow can be calculated as the fuel flow $\dot{m}_{fuel}$ multiplied by the combustion enthalpy of the fuel h_{comb}, as presented in Eq. 5.40.

$$\eta_t = \frac{\dot{W}}{\dot{m}_{fuel} h_{comb}} \tag{5.40}$$

It is highlighted that the thermal efficiency is inversely proportional to the specific fuel consumption, as the last is defined as the ratio between fuel consumption and power.

Volumetric efficiency is an index for evaluating the exhaust and intake processes. It is defined as the ratio of admitted mass m_{adm} and the ideal capacity of the cylinder, *i.e.*, the amount of mass which can be contained in the cylinder in the ambient conditions given by $\frac{P_0 V_{max}}{RT_0}$, as shown in Eq. 5.41.

$$\eta_V = \frac{m_{adm}}{\frac{P_{atm} V_{max}}{RT_{atm}}} \tag{5.41}$$

Indicated mean effective pressure is an index representing the "density of power" of the engine. As work consists of the integral of pressure for a variation of volume, the mean pressure can be calculated by the ratio between the work performed by the gases in a cycle of pressure and the variation of volume, as indicated in Eq. 5.42.

$$imep = \frac{W_{cycle}}{\Delta V} \tag{5.42}$$

It is highlighted that only indicated parameters are considered for the analysis as friction is not being estimated in this work. Models estimating friction in engines are based on empirical studies performed on conventional engines, such as the standard ISO 1585:1992, being inaccurate for different types of mechanism, such as the proposed VSE.

5.6 Validation

The algorithm was implemented in FORTAN 95 and MATLAB computing languages. Thereafter, the algorithms were used to reproduce a case from the experiments performed on a conventional engine, described in chapter 4. The case of 50 Nm and 2000 rpm was selected for the algorithm validation (Fig. 5.5).

It is verified a difference of 2% in the value for pressure peak and a deviation of 0,85 °CA in pressure peak location.

Another case was simulated in order to illustrate the features of the developed algo-

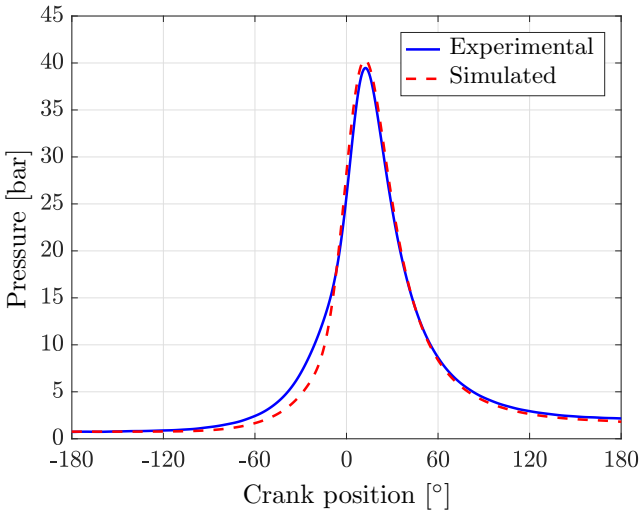

Figure 5.5: Comparison between experimental and simulated pressure.

rithm. The VSE was simulated for 400 cm^3 of cubic capacity, 12:1 of compression ratio, spark timing for -20 °CA, 3000 rpm of engine speed and full load. A simple comparison of processing time have indicated 4.00 s of simulation for the algorithm implemented in MATLAB and 0.42 s of simulation for the algorithm implemented in FORTRAN. Indicated performance of the engine for the simulated case is presented in Tab. 5.3.

Table 5.3: Indicated performance for the demonstrative simulation.

Parameter	Value
Power [kW]	9.98
Torque [Nm]	31.8
Fuel consumption [kg/h]	3.92
Specific fuel consumption [g/kWh]	393.63
Thermal efficiency [%]	35.37
Volumetric efficiency [%]	94.24
Pressure peak [bar]	53.07
Knock index [-]	0.72
imep [bar]	10.00

In–cylinder pressure profile for the simulated case is presented (Fig. 5.6). This is a fundamental parameter as power and imep are calculated from this profile (Eqs. 5.42 and 5.39). Two temperatures lines are seen, one for unburned gases and the other for burned gases (Fig. 5.7). The temperature for unburned gases ends when the unburned gases are completely consumed by the flame. The temperature for the burned gases begins with combustion at the adiabatic flame temperature of the air–fuel mixture.

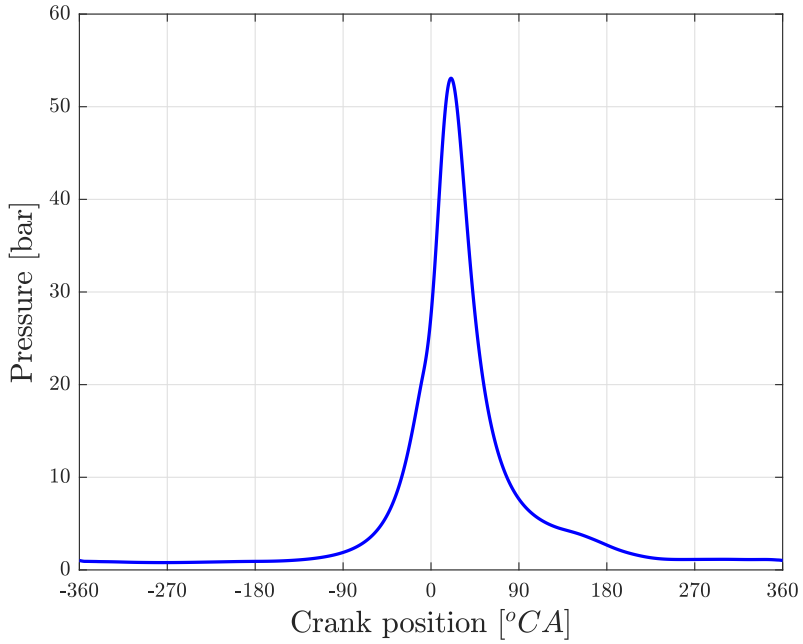

Figure 5.6: Pressure for the simulated case.

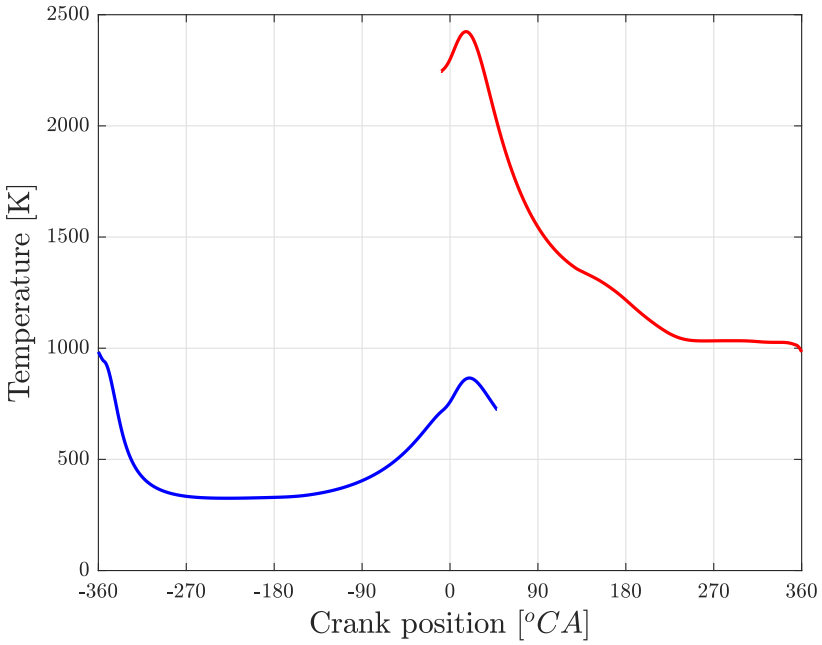

Figure 5.7: Temperatures for the simulated case.

In-cylinder mass is presented in Fig. 5.8. The closed and open phases can be distinguished in this profile. The closed phase is comprised by the part of the cycle in which the mass is constant while the open phase is comprised by the part in which the mass is changing. Backflow phenomenon can be observed by a small peak of mass prior to IVC (around -180 °CA).

The mass flow profile is verified in Fig. 5.9. As this profile presents the liquid flow,

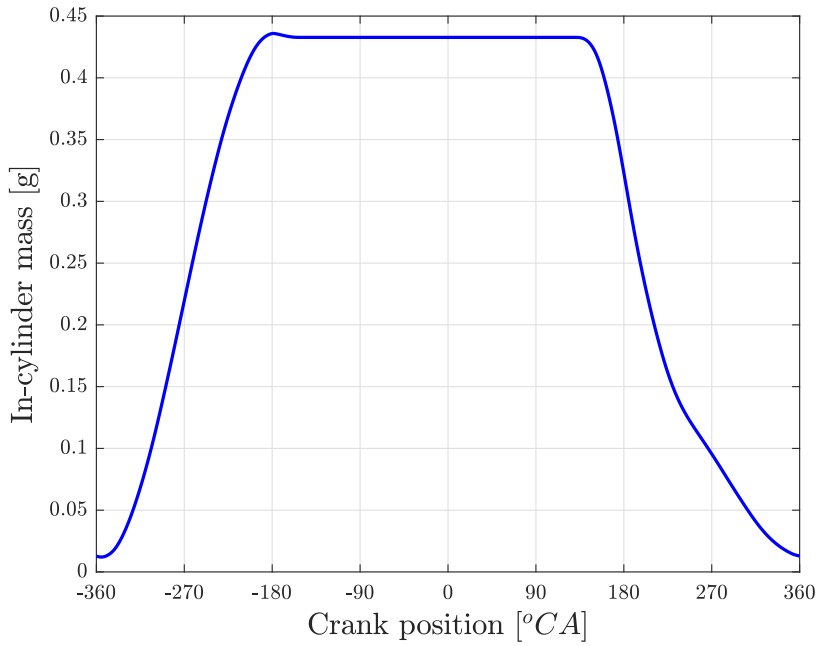

Figure 5.8: In–cylinder mass for the simulated case.

it is not possible to separate the flow through intake and exhaust valves during the period of valve overlap. However, most part of each process can be analysed from the flow profile. The exhaust is comprised by the two negative peaks on the right side of the graph. The first peak occurs before BTC and it is caused by the elevated pressure in the cylinder, consisting in the blow-off process. The second peak is caused by the movement of the cylinder, which is going from the BDC to the TDC in that moment. Intake process is represented by the positive peak in the left side of the graph. The backflow can also be noticed in this profile by looking at the small negative peak at the end of the intake process. By neglecting the blow-by phenomenon, flow is kept at null values for the closed phase of the engine cycle.

The same algorithm was used to carry out studies on a predictive second law analysis. RUFINO *et al.* (2018b) presented a comparative analysis indicating the effect of choosing the adequate hypothesis for combustion products composition on an exergetic analysis, which was carried out on thermodynamic data provided by the same model presented in this work.

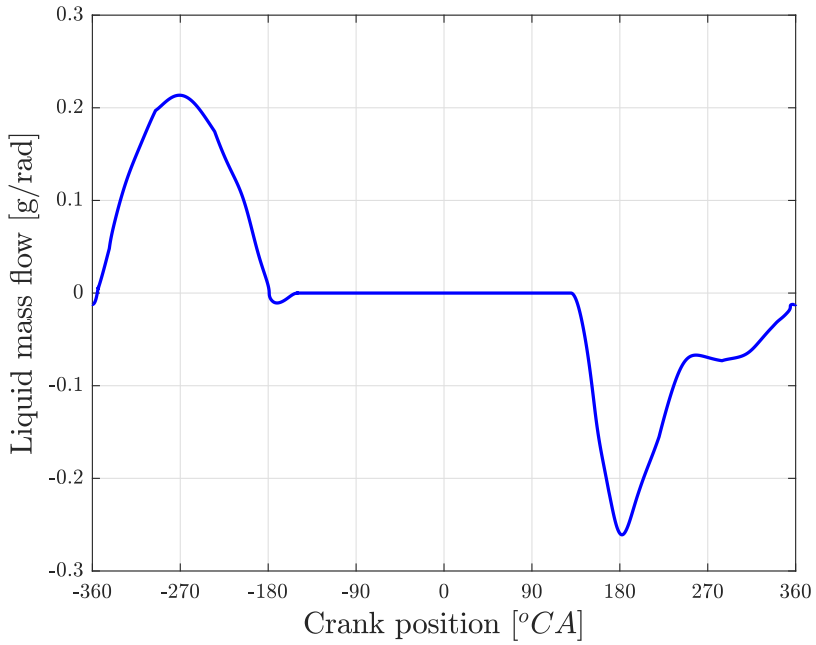

Figure 5.9: Mass flow for the simulated case.

6. Simulations

This chapter is divided in two parts. The first one consists of the description of the simulation performed, the set-up of the simulated engine and the strategy for optimizing thermal efficiency. The second part consists of the presentation of the results obtained from the optimisation and the performance of the engine operating in those conditions. Moreover, a comparison is made with a fixed compression ratio engine (FCR), a variable compression ratio engine (VCR) and the proposed variable stroke engine (VSE). A compression ratio of 10:1 was chosen for the FCR as that was the highest compression ratio in which knock onset could be avoided in the range of spark timing used in the simulation.

6.1 Simulation set-up

Initially, the simulation algorithm was developed in MATLAB. However, as several simulation cases were carried out to obtain a calibration map, it became necessary to develop an algorithm in FORTRAN for better computational performance (see Section 5.6).

The prototype simulations were performed for a single–cylinder engine fuelled with hydrous ethanol (5% of water in volume) at stoichiometric conditions. The parameters used as variables in the calibrations were: spark timing, percentage of maximum manifold absolute pressure (MAP), cubic capacity and compression ratio. The simulations were carried out for different engine speed conditions. The range and steps used in the simulation are given in Tab. 6.1. TDM FORTRAN 95 was used for generating the simulation algorithm.

Table 6.1: Range of variables.

Variable	Minimum	Maximum	Step
Engine speed [rpm]	1000	5000	250
MAP [% of maximum]	50	100	1
Cubic capacity [cm^3]	315	400	2.5
Compression ratio	10:1	18:1	0.25:1
Spark timing [°CA]	-40	0	0.5

The spark timing is referenced with the top dead centre (TDC) of the closed phase, being negative values occurring before TDC. The physical position of the throttle has a non–linear relation with load. Thus, it was opted to work with the percentage of MAP since it is a consequence of the throttle action.

Manifold conditions were obtained from the Full load test performed on a conventional engine (see Section 4.2). The conditions include pressure in both intake and exhaust manifold temperature in the exhaust manifold as function of engine speed at full load operation. Temperature in the intake manifold was considered to be the same as environment. A non–dimensional pressure P^* is defined as the ratio between actual pressure and the atmospheric pressure (Fig. 6.1). The non–dimensional pressure in intake manifold P^*_{im} at full load condition is related to engine speed N (in [rpm]) according to the expression indicated in Eq. 6.1.

$$P^*_{im} = {}_0a_{im,P} + {}_1a_{im,P}N + {}_2a_{im,P}N^2 + {}_3a_{im,P}N^3 + {}_4a_{im,P}N^4 + {}_5a_{im,P}N^5 + {}_6a_{im,P}N^6 \quad (6.1)$$

The coefficients in Eq. 6.1 are given in Tab. 6.2.

Table 6.2: Coefficients for intake manifold pressure.

Coefficient	Value
${}_0a_{im,P}$	1.066132e00
${}_1a_{im,P}$	-2.188493e-04
${}_2a_{im,P}$	2.322634e-07
${}_3a_{im,P}$	-1.191250e-10
${}_4a_{im,P}$	3.070731e-14
${}_5a_{im,P}$	-3.846635e-18
${}_6a_{im,P}$	1.860873e-22

A non–dimensional pressure for the exhaust manifold used in the prototype simulation was also fitted for the conventional engine. However, the pressure in the exhaust manifold was considered to be dependent only of the engine speed, without being affect by throttle actuation. The function used to estimate the non–dimensional pressure in the exhaust manifold P^*_{em} is given by Eq. 6.2 (Fig. 6.2).

$$P^*_{em} = {}_0a_{em,P} + {}_1a_{em,P}N + {}_2a_{em,P}N^2 \quad (6.2)$$

The values of the coefficients are given in Tab. 6.3.

Temperature in the exhaust manifold was considered to present a linear relation to the engine speed as obtained in the conventional engine. The function is given by Eq. 6.3 (Fig. 6.3).

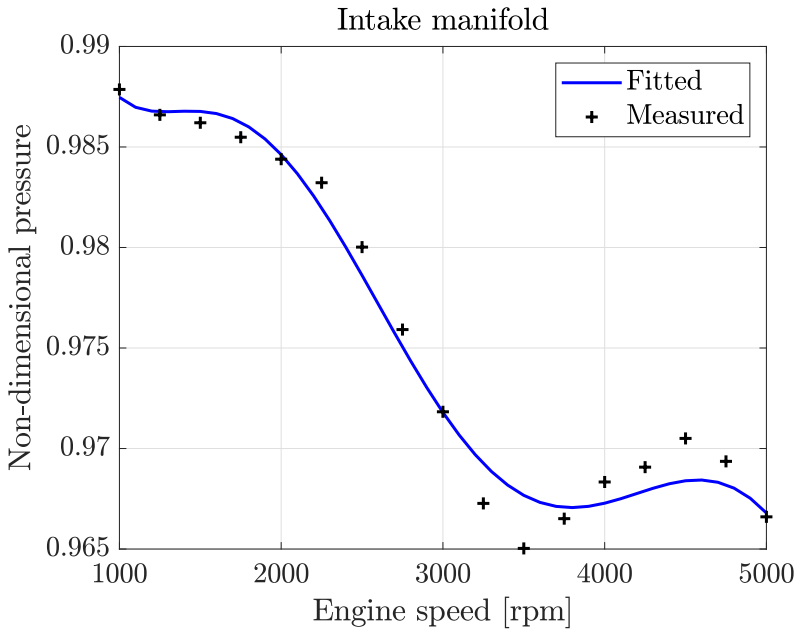

Figure 6.1: Function for non-dimensional pressure in intake manifold.

Table 6.3: Coefficients for exhaust manifold pressure.

Coefficient	Value
${}_0a_{em,P}$	9.757461e-01
${}_1a_{em,P}$	3.642364e-05
${}_2a_{em,P}$	4.837319e-09

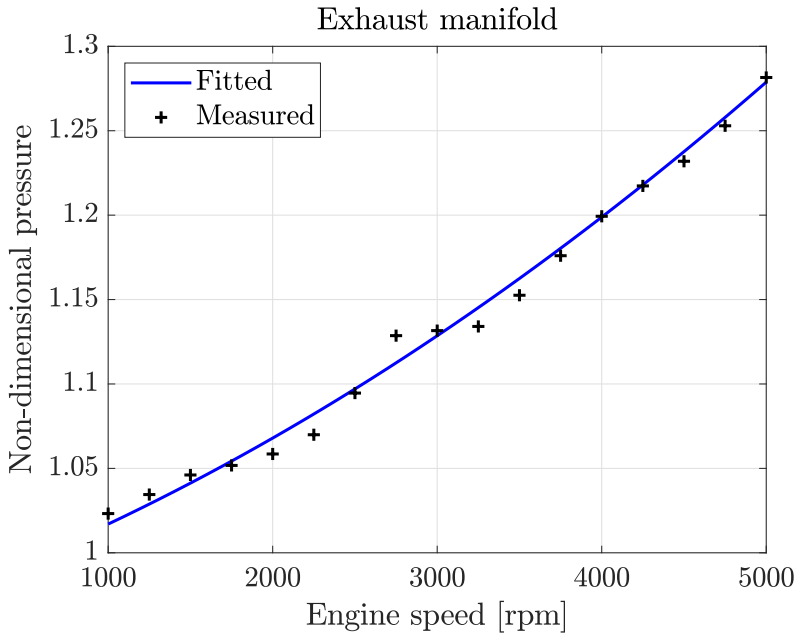

Figure 6.2: Function for non-dimensional pressure in exhaust manifold.

$$T_{em} = {}_0a_{em,T} + {}_1a_{em,T}N \tag{6.3}$$

The temperature in the exhaust manifold T_{em} is given in K and its coefficients are presented in Tab. 6.4.

Table 6.4: Coefficients for exhaust manifold temperature.

Coefficient	Value
${}_0a_{em,T}$	3.352479540552874e02
${}_1a_{em,T}$	9.034073500671359e-02

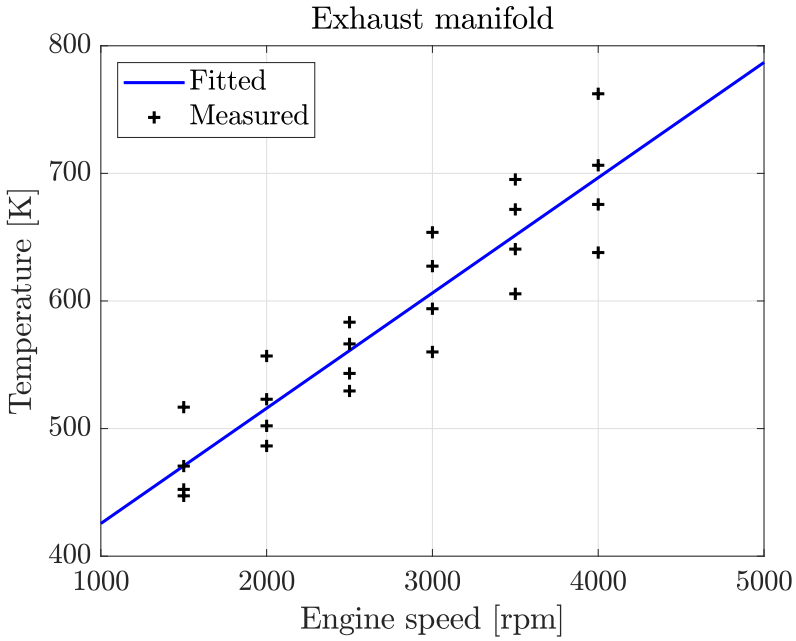

Figure 6.3: Function for temperature in exhaust manifold.

Whenever backflow phenomena occurred, the gases were assumed to return to the cylinder at the same temperature as cylinder walls, which was assumed as 520 K. Ambient conditions were assumed to be 295 K of temperature, 95 kPa of pressure and 50% of relative humidity.

The valve train used has its properties listed in Tab. 6.5.

Table 6.5: Valves characteristics.

Parameter	Value
Number of valves	2
Intake valve opening [^oCA]	-20
Exhaust valve opening [^oCA]	-230
Intake duration [^oCA]	230
Exhaust duration [^oCA]	245
Intake valve diameter [mm]	30.93
Exhaust valve diameter [mm]	28.27

Values provided in °CA in Tab. 6.5 are referenced with TDC of the open phase. A lift/diameter ratio of 0.3 was considered for both valves.

Many conditions can affect combustion duration, such as charge density, compression ratio, spark timing and air–fuel ratio (see Chapter 4). However, engine speed has the most significant influence in combustion. Data for air–fuel ratio influence was only obtained in the lean mixture conditions and the simulations were carried out with the engine running at stoichiometric conditions. Thus, effects of air–fuel ratio in the combustion have been neglected. Effects of spark timing on combustion were only studied for 1500 and 3000 rpm conditions. It was considered more convenient to neglect effect of spark timing instead of extrapolating the combustion behaviour for other engine speed conditions. Therefore, combustion was considered to be influenced only by engine speed.

By using the results presented in Chapter 4 (Fig. 4.35), a function was fitted to obtain combustion duration for ethanol with respect to engine speed to be used in the prototype simulation (Fig. 6.4). The relation presented in Eq. 6.4 provides the combustion duration $\Delta\theta_c$ in milliseconds. Its coefficients are given in Tab. 6.6.

$$\Delta\theta_c = {}_0a_{CD} + \frac{{}_1a_{CD}}{N} \tag{6.4}$$

Table 6.6: Coefficients for combustion duration.

Coefficient	Value
${}_0a_{CD}$	5.717577730101888e-01
${}_1a_{CD}$	5.419497901334530e+03

Although the form factor has been observed to change with engine speed (Fig. 4.39), it was adopted a more conservative assumption of $n = 2$. Ignition delay was assumed to constant with a duration of 0.4 ms for all conditions.

6.1.1 Optimisation method

A simple search method was implemented for FCR and VCR engines. Maximum efficiency was searched in the region in which knock onset was not observed.

The algorithm in FORTRAN simulated the VSE operation by adjusting spark timing and compression ratio in order to maximise efficiency. The output consisted of a set of data, comprising results of engine performance for the whole range of cubic capacity and MAP in each engine speed.

After carrying out the simulations in FORTRAN, the optimisation algorithm was implemented in MATLAB. A data fitting procedure was performed by using the least squares method providing efficiency, torque, optimum spark timing and optimum compression ratio as

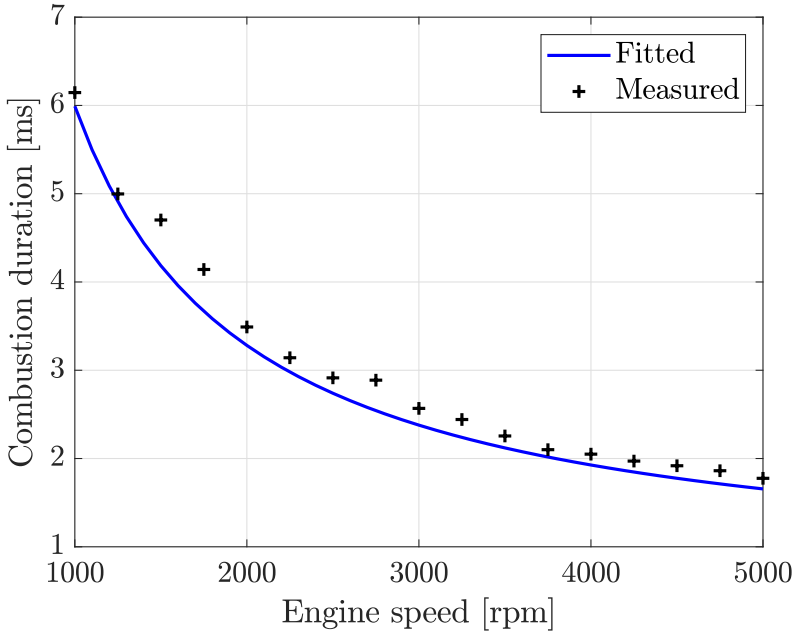

Figure 6.4: Model for combustion duration.

functions of cubic capacity and MAP for each engine speed condition. Therefore, the optimisation consisted of:

$$\max \eta \left(\mathcal{X}, \mathcal{Y} \right) , \tag{6.5}$$

subjected to:

$$\mathcal{T} \left(\mathcal{X}, \mathcal{Y} \right) = constant \tag{6.6}$$

$$\mathcal{X}_{min} < \mathcal{X} < \mathcal{X}_{max} \tag{6.7}$$

$$\mathcal{Y}_{min} < \mathcal{Y} < \mathcal{Y}_{max} \tag{6.8}$$

in which $\mathcal{X}$ and $\mathcal{Y}$ represent cubic capacity and MAP, while $\mathcal{T}$ represents torque and η represents efficiency. The optimum combinations of cubic capacity and MAP were determined by the direct search method along each level of torque.

6.2 Results

The calibration process is herein described for FCR, VCR and VSE. The procedure for each simulated engine is detailed. Then the base calibration for optimum efficiency is presented. Afterwards, the performance for each engine in the optimum operation is given and, finally, a comparison of the performance of the engines is presented.

6.2.1 FCR and VCR

Although flame speed is maximised for slightly rich mixtures, the maximum efficiency for the engine occurs for slightly lean mixtures. However, due to the operation of the three–way–catalyst, lean mixtures can increase the emission of NOx gases (BAE and KIM, 2017). Therefore, air–fuel ratio is kept constant at stoichiometric condition.

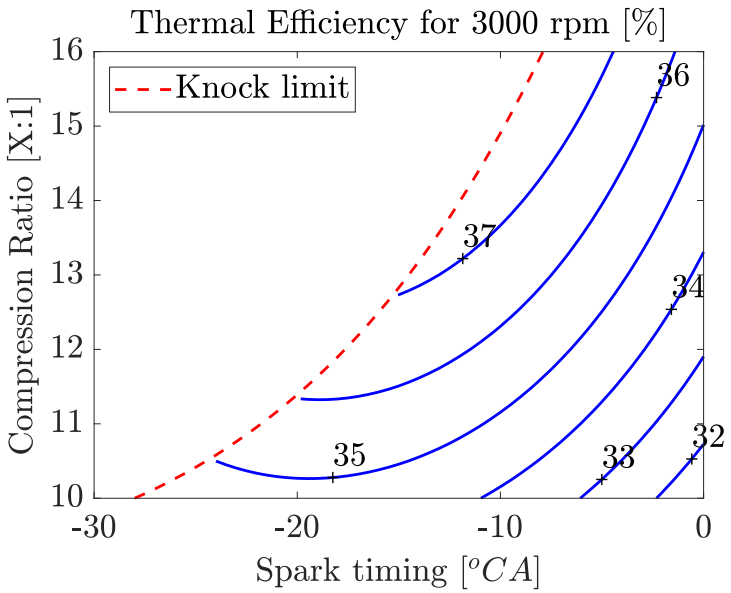

Figure 6.5: Effect of compression ratio and spark timing on efficiency.

Knock suppression is usually performed by delaying spark timing in a FCR. Compression ratio can also be reduced in order to avoid knock onset in a VCR (Fig. 6.5). Efficiency was used as criterion for the decision of which parameter to control in order to suppress knock onset.

The MBT position can be found for medium speed (3000 rpm) and a compression ratio of 11:1 (Fig. 6.6). However, as compression ratio is increased, the spark timing becomes limited by knock. For low engine speed, the air–fuel mixture is exposed to high levels of pressure and temperature for a longer period of time, favouring the conditions for knock onset (Fig. 6.7). No MBT can be achieved in this condition of engine speed and no compression ratio above 12.5:1 can be achieved without knock occurrence.

Load presents strong effect on knock onset. For the condition of 1500 rpm and 70% of maximum MAP, it is possible to reach 17:1 of compression ratio and a MBT condition can be attained for 11:1 of compression ratio (Fig. 6.8).

The relation of spark timing, compression ratio, efficiency and knock is summarized in Fig. 6.9. A FCR engine with a low compression ratio can easily operate at MBT, represented by point 1 in the figure. However, there are conditions in which it is preferable to operate at a knock limited condition and, thus, obtaining more efficiency. Modern flexfuel engines operates

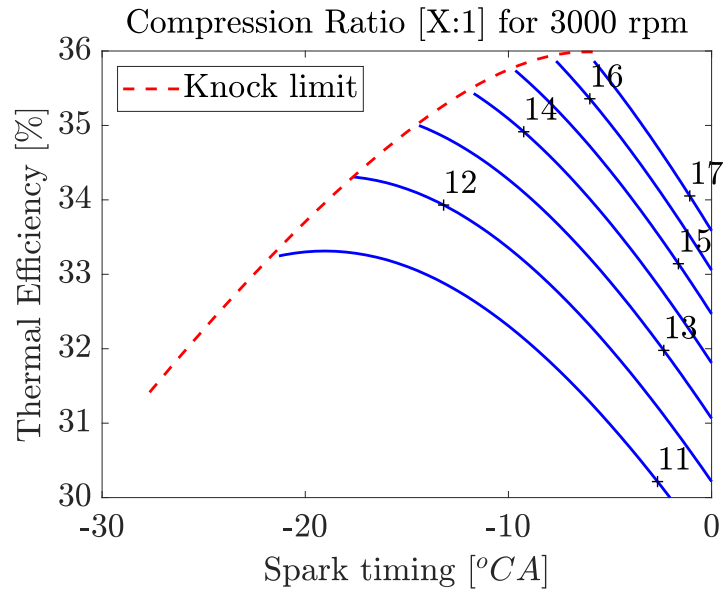

Figure 6.6: Efficiency as function of spark timing and compression ratio for medium engine speed and full load.

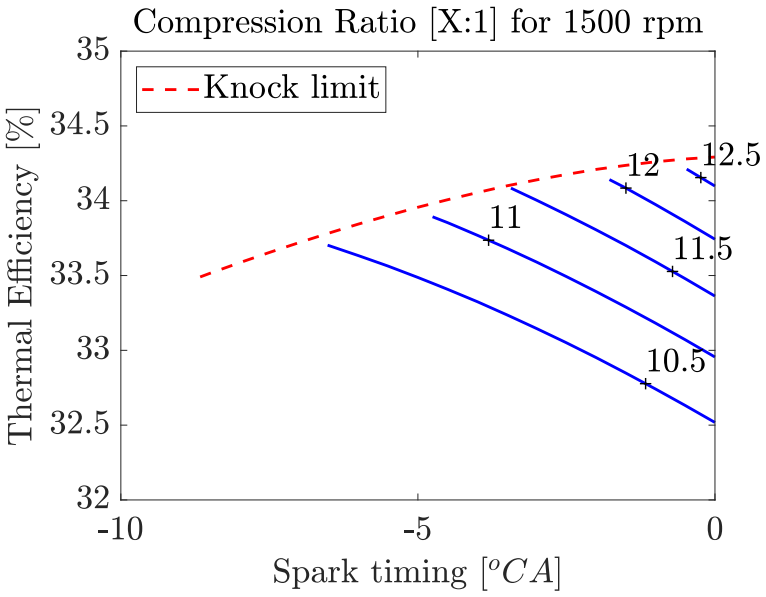

Figure 6.7: Efficiency as function of spark timing and compression ratio for low engine speed.

according to this strategy, represented by point 2 in the figure.

A VCR can increase its compression ratio at significantly higher levels, represented by point 3. However, there is a limit for compression ratio, in which the spark timing is too delayed, and the gain provided by compression ratio increasing is compensated by the late spark timing. Moreover, different types of fuel exhibit different limits for knock due to octane number and heat of vaporisation.

The base calibration process for the FCR engine consisted of searching for the MBT in the level of 10:1 of compression ratio (Fig. 6.7). Whenever it was not possible to achieve the

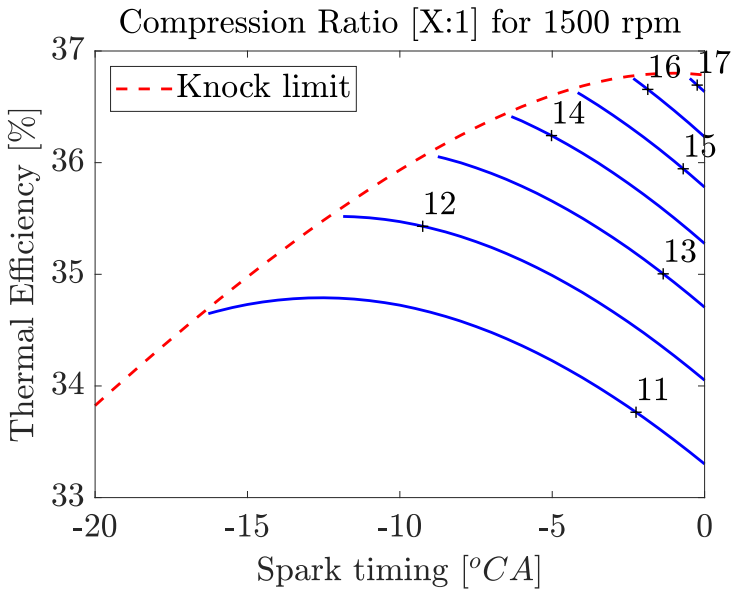

Figure 6.8: Efficiency as function of spark timing and compression ratio for low engine speed and partial load.

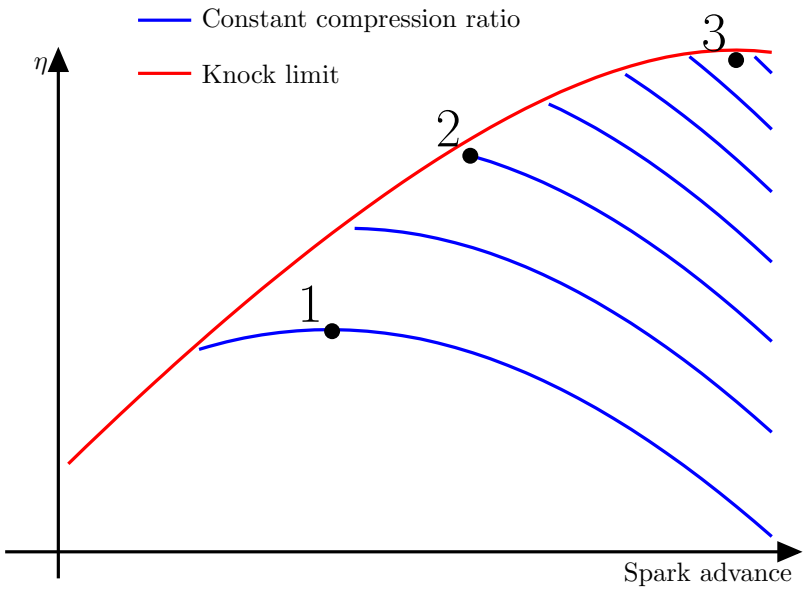

Figure 6.9: Calibration procedure for FCR and VCR engines.

MBT due to knock onset, the lower value of limited spark timing was chosen. This procedure was performed for each combination of engine speed and MAP (Fig. 6.10).

The result for base spark timing agrees with the well–established knowledge that high loads and low engine speed is critical for knock onset. As engine speed was increased for a constant level of torque, the spark timing could be increased (Fig. 6.11).

For the VCR engine, the procedure of calibration consisted of searching for the best combination of compression ratio and spark timing (Figs. 6.12 and 6.13).

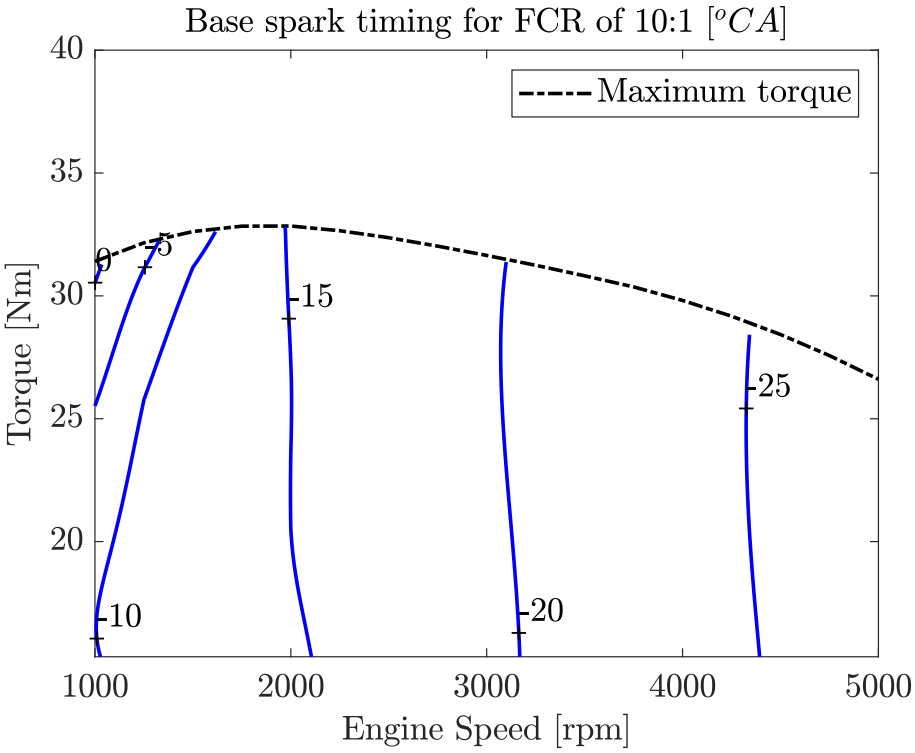

Figure 6.10: Complete map of base spark timing for the FCR engine.

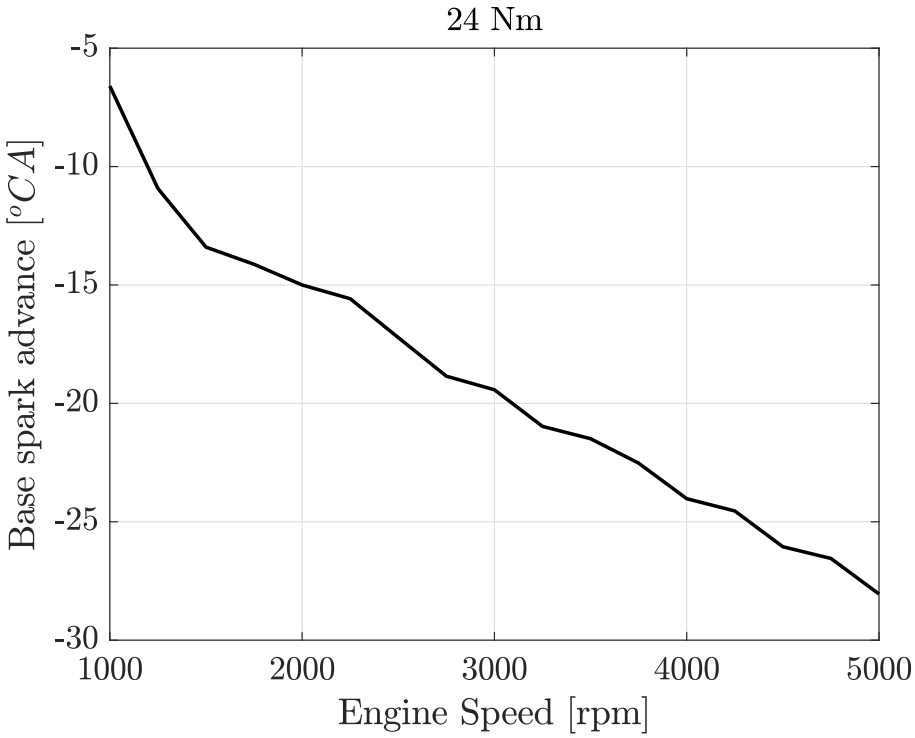

Figure 6.11: Base spark timing for the FCR engine for 24 Nm.

The region in which a late spark timing was observed was greater for the VCR engine than that for the FCR engine (Figs. 6.10 and 6.12). The spark timing occurred earlier than -15°CA for the FCR engine at higher engine speed levels beyond 2000 rpm. For the VCR

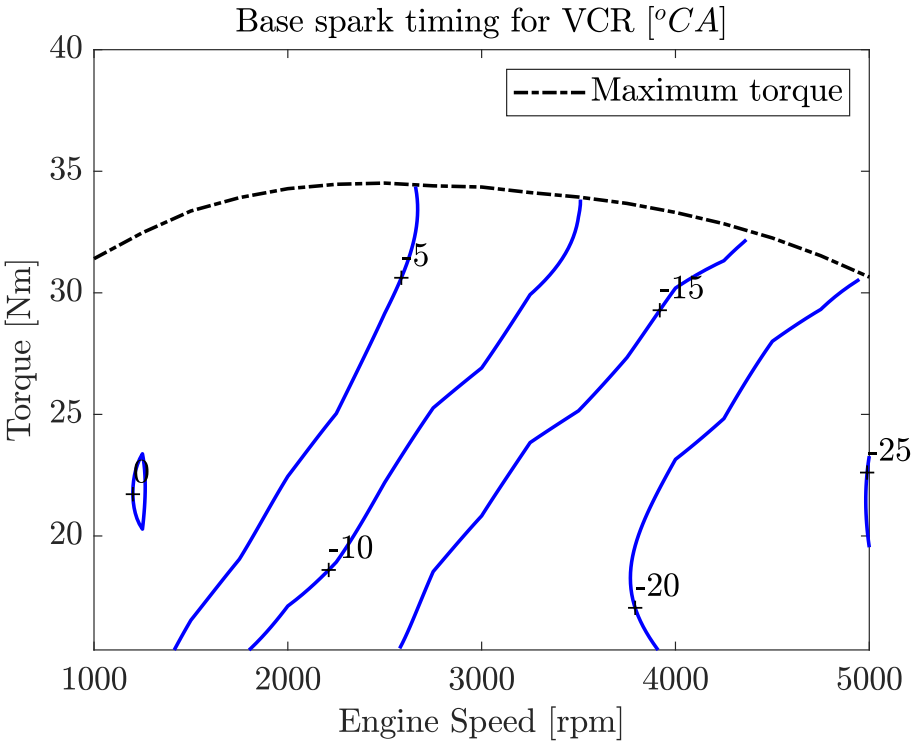

Figure 6.12: Complete map of base spark timing for the VCR engine.

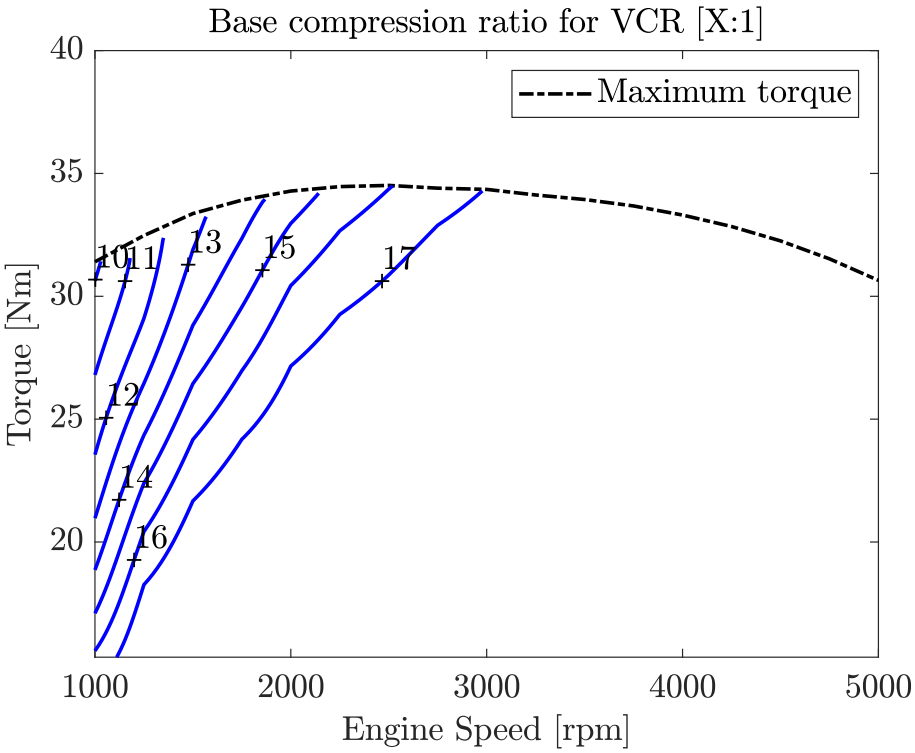

Figure 6.13: Complete map of base compression ratio for the VCR engine.

engine, spark timing was kept later than -5°CA for most of the engine speed conditions lower than 2000 rpm while knock onset was being controlled by the adjustment on the compression ratio (Fig. 6.13).

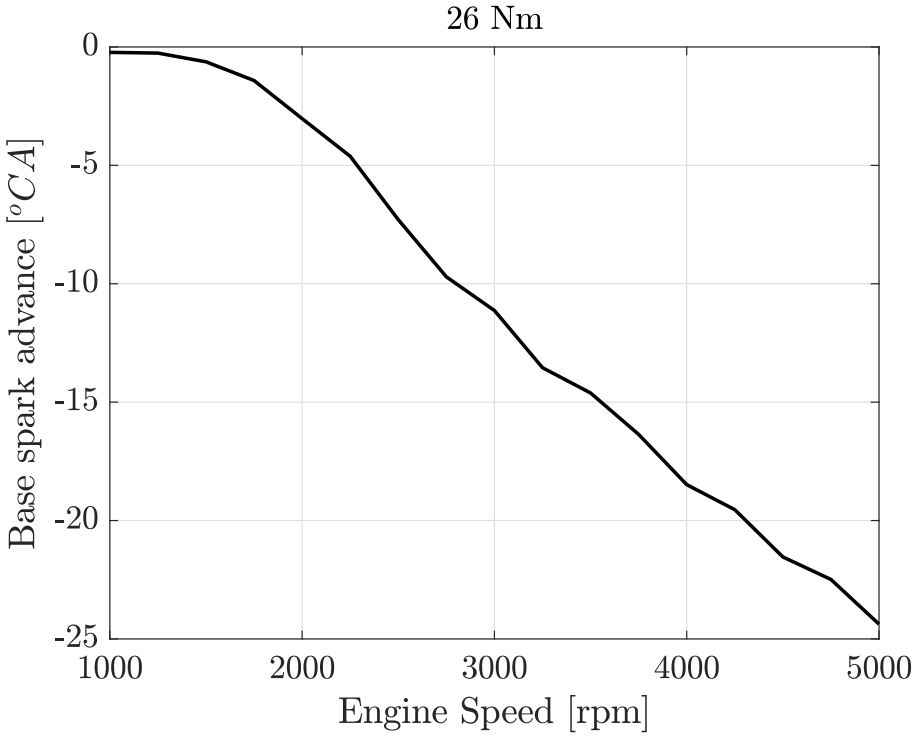

Figure 6.14: Base spark timing for the VCR engine for 26 Nm.

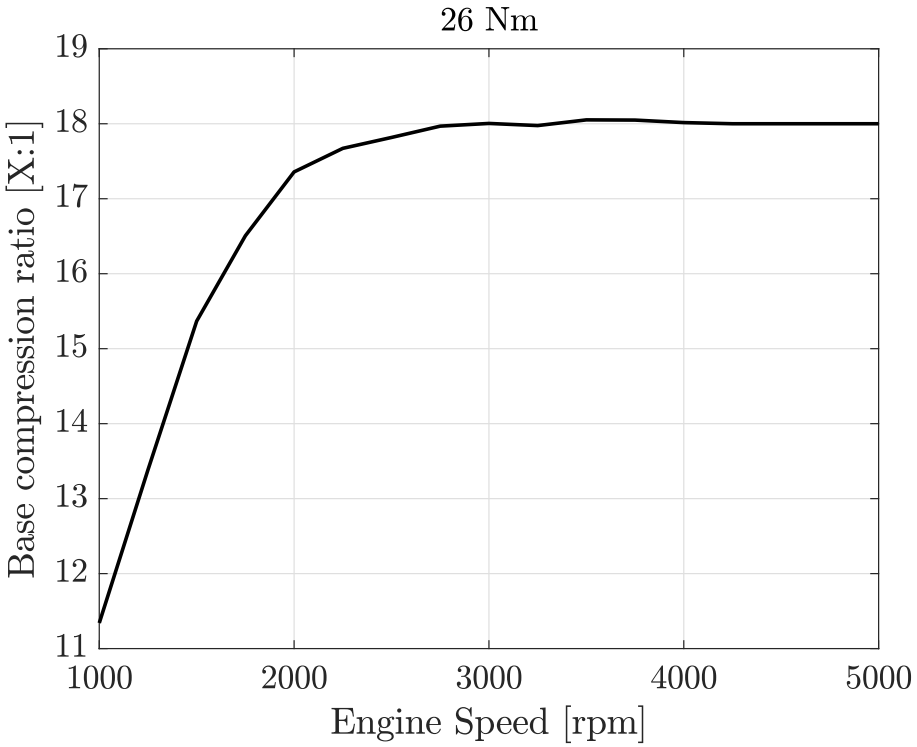

Figure 6.15: Base compression ratio for the VCR engine for 26 Nm.

The VCR operated with the compression ratio around 10:1 in the region wherein knock onset is critical, while it operated in the maximum compression ratio of 18:1 in most part of its operational range. Beyond 3000 rpm condition, it was possible to keep the compression ratio at 18:1 (Fig. 6.15). If engine speed continued to increase, the spark timing was verified to

occurs early (Fig. 6.14). For 1000 rpm, knock onset is critical and, thus, spark timing was near from the TDC and compression ratio was reduced.

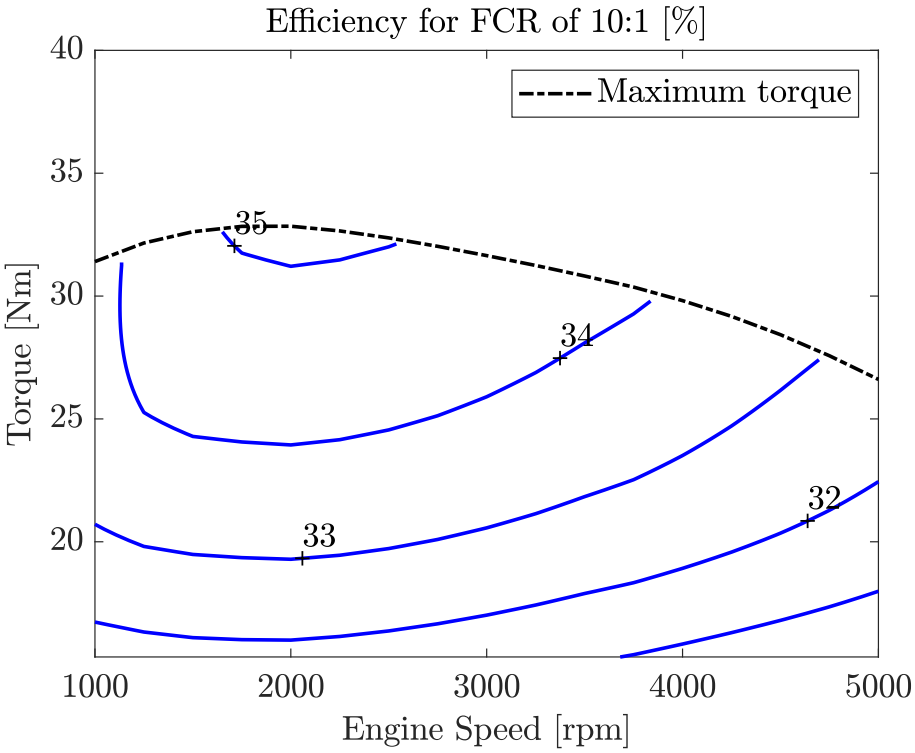

Figure 6.16: Complete efficiency map for the FCR engine.

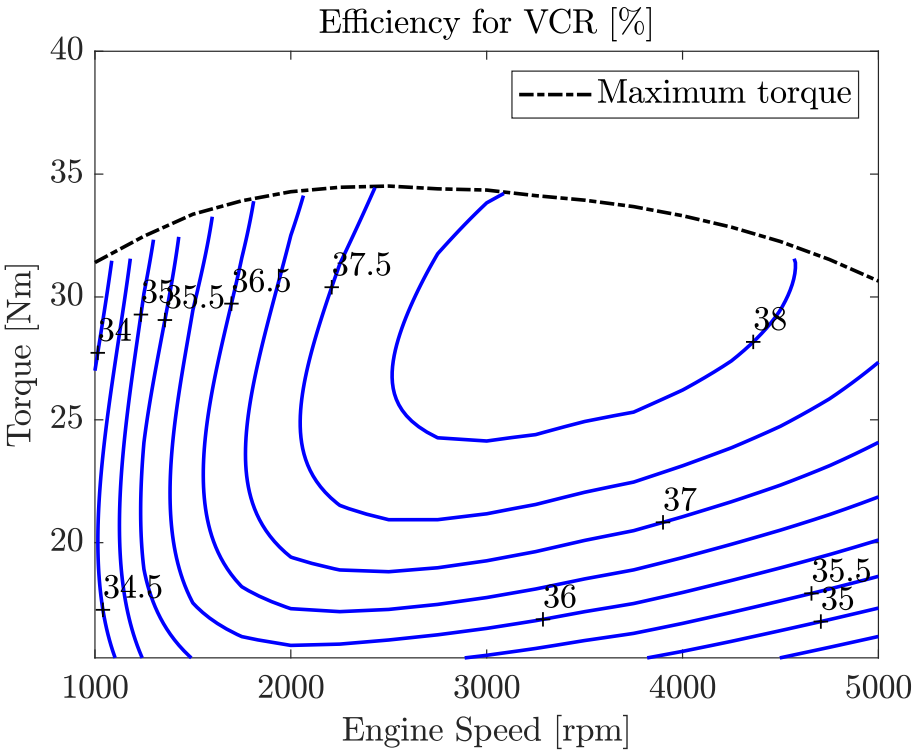

Figure 6.17: Complete efficiency map for the VCR engine.

Efficiency maps of commercial engines presents a maximum efficiency region for

mid–load at medium engine speed due to the enrichment of the air–fuel mixture for full load conditions. This result was not observed in this work as air–fuel mixture was stoichiometric for all conditions of load. A dislocation of the maximum efficiency region was observed when comparing the FCR and the VCR engines (Figs. 6.16 and 6.17). The FCR engine exhibited a maximum efficiency for middle engine speed while the VCR engine exhibited a maximum efficiency for high speed as compression ratio was being increased as knock becomes less critical for higher engine speed. Moreover, the FCR engine presented a maximum efficiency around 36%, while the VCR engine could reach larger region in which the efficiency reached up to 38 %. The gradient of efficiency was highly dependent on engine load for the FCR engine, except for very low engine speed because of knock occurrence. For the VCR engine, the gradient of efficiency was more related to engine speed up to 2500 rpm, becoming load dependent for higher engine speed.

6.2.2 VSE

The procedure adopted for calibrating the FCR and the VCR engines was performed for all combinations of engine speed and MAP at a constant cubic capacity of 400 cm^3. A similar procedure was adopted for all combinations of engine speed, MAP and cubic capacity, being the last being varied between 315 cm^3 and 400 cm^3 (Tab. 6.1). Results for optimum spark timing and compression ratio were then used to determine the strategy for load control by adjusting MAP and cubic capacity simultaneously.

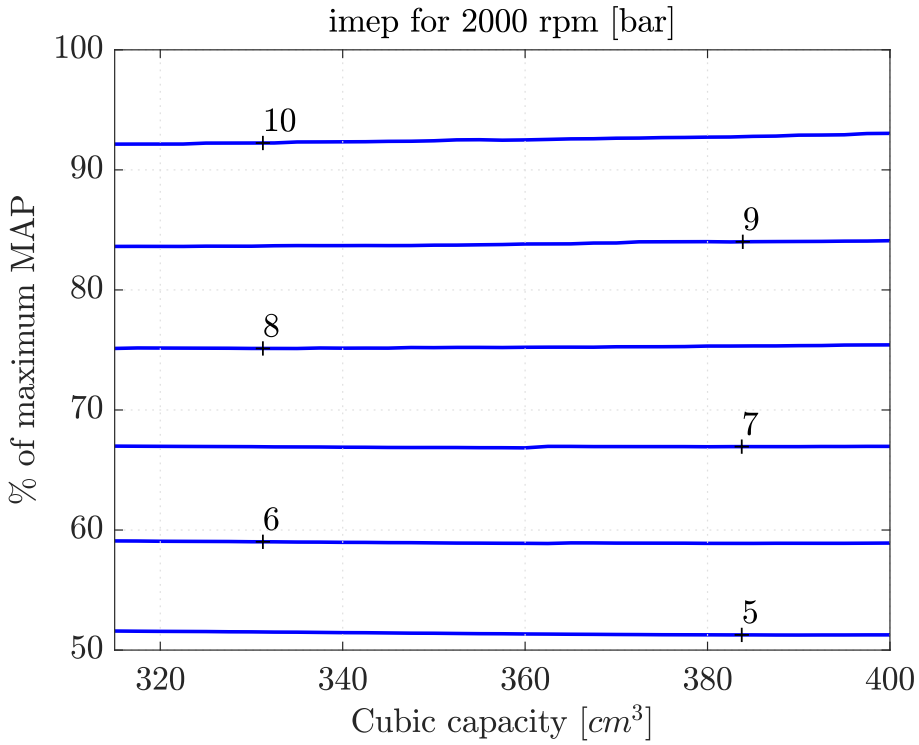

Figure 6.18: Imep as function of MAP and cubic capacity.

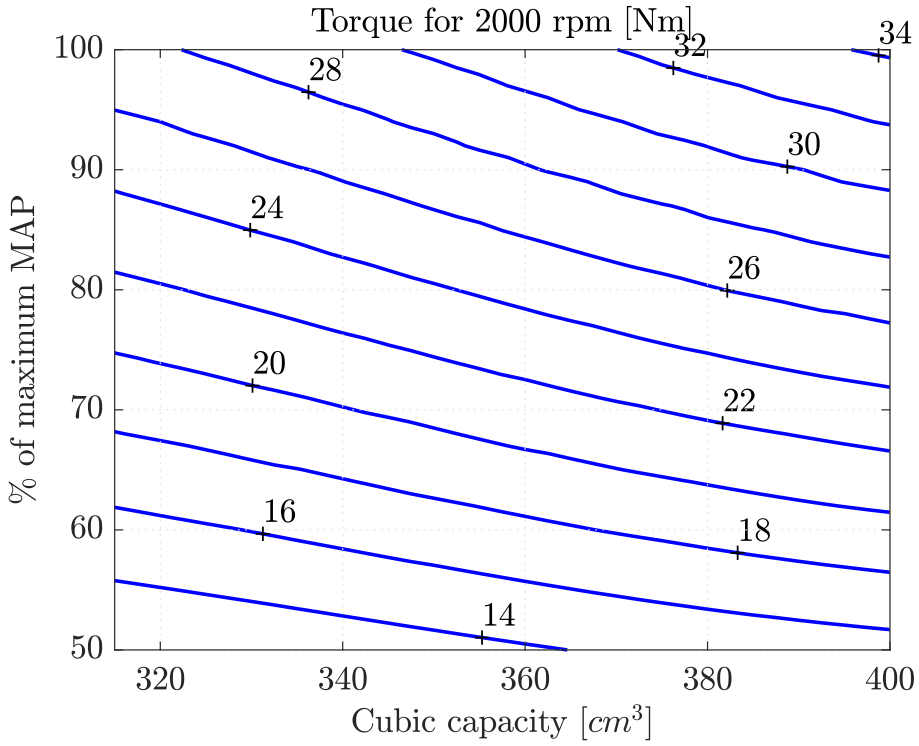

Figure 6.19: Lines of constant torque as function of MAP and cubic capacity.

For a non–fixed cubic capacity engine, imep is not a convenient parameter to indicate load as it is possible to reduce torque output of the engine by reducing cubic capacity and maintaining imep constant (Figs. 6.18 and 6.19). Therefore, load is always represented by torque in this study. It was verified the possibility of obtaining the same level of load for different combinations of MAP and cubic capacity (Fig. 6.19). Thus, the calibration process consisted of identifying the levels of load, fitting the efficiency along the iso–torque lines and finding the optimum combination of cubic capacity and MAP for a maximised efficiency, as mentioned in the Methods section.

As torque was increased, the possible combinations of MAP and cubic capacity were reduced. Consequently, the maximum level of torque could only be achieved when the VSE engine was operating at both maximum MAP and cubic capacity. Moreover, cubic capacity presented a higher effect on load control for low engine speed than that for high speed (Figs. 6.20 to 6.22).

The maximum compression ratio of 18:1 could not be attained even for low levels of load at 1000 rpm (Fig. 6.23). As a decrease in cubic capacity requires an increase in the intake manifold pressure, higher levels for compression ratio were verified for higher cubic capacity. The maximum compression ratio could be achieved for medium and high engine speed.

The base calibration for spark timing in each iso–torque line are respectively presented for medium and high engine speed in Figs. 6.24 and 6.25. For low engine speed, the spark timing was always kept near the TDC, and knock onset was suppressed by compression

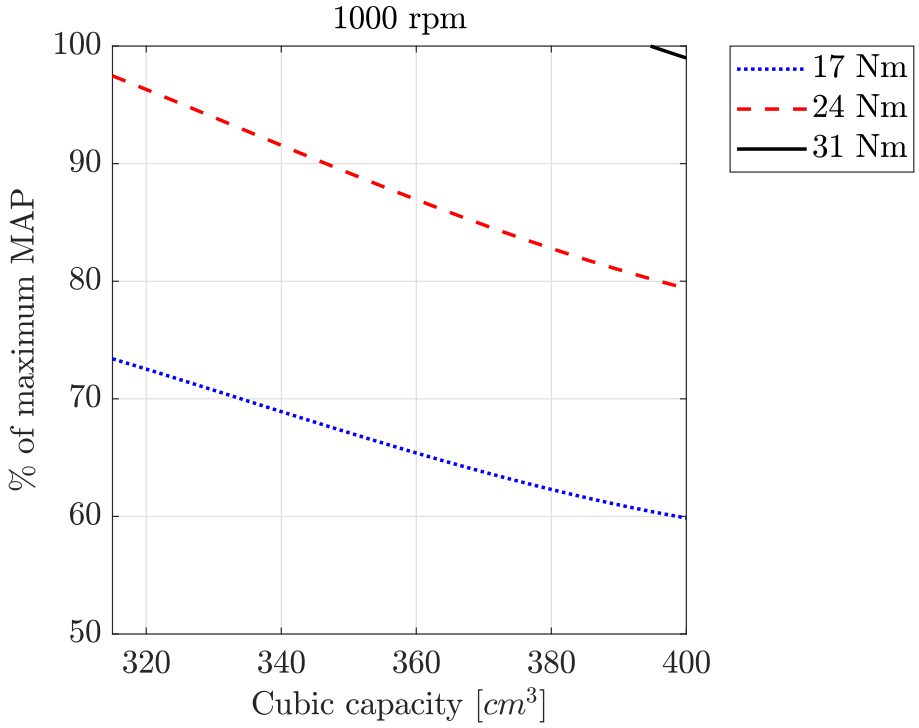

Figure 6.20: MAP along iso–torque lines for 1000 rpm.

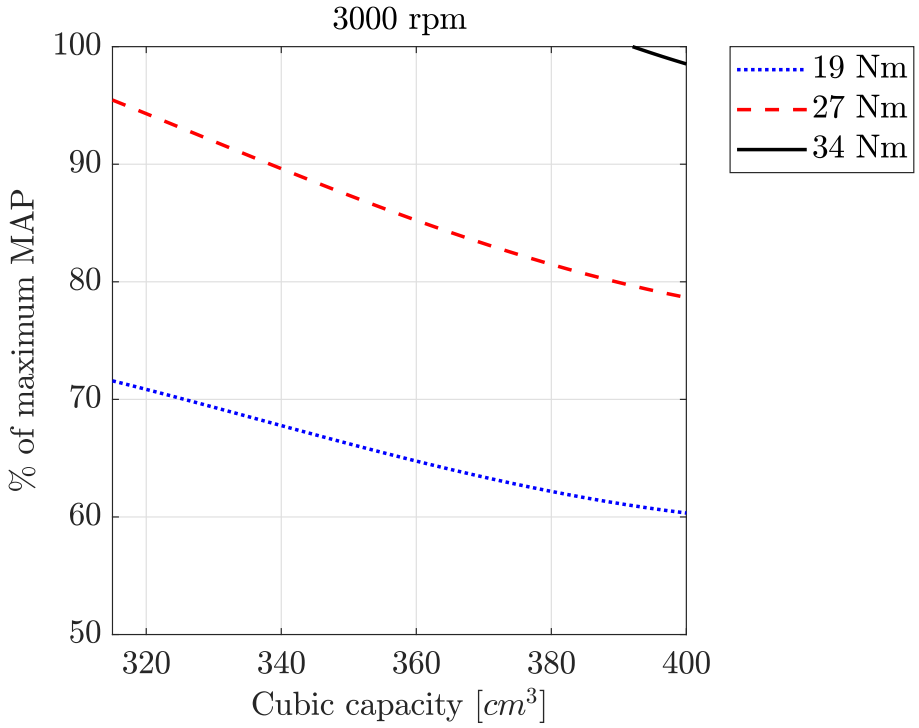

Figure 6.21: MAP along iso–torque lines for 3000 rpm.

ratio reduction (Fig. 6.23).

Knock was not verified for partial loads at high engine speed. Therefore, the spark timing was set to MBT for all cubic capacity levels. For higher loads and for medium speed, the spark timing was retarded in order to suppress knock.

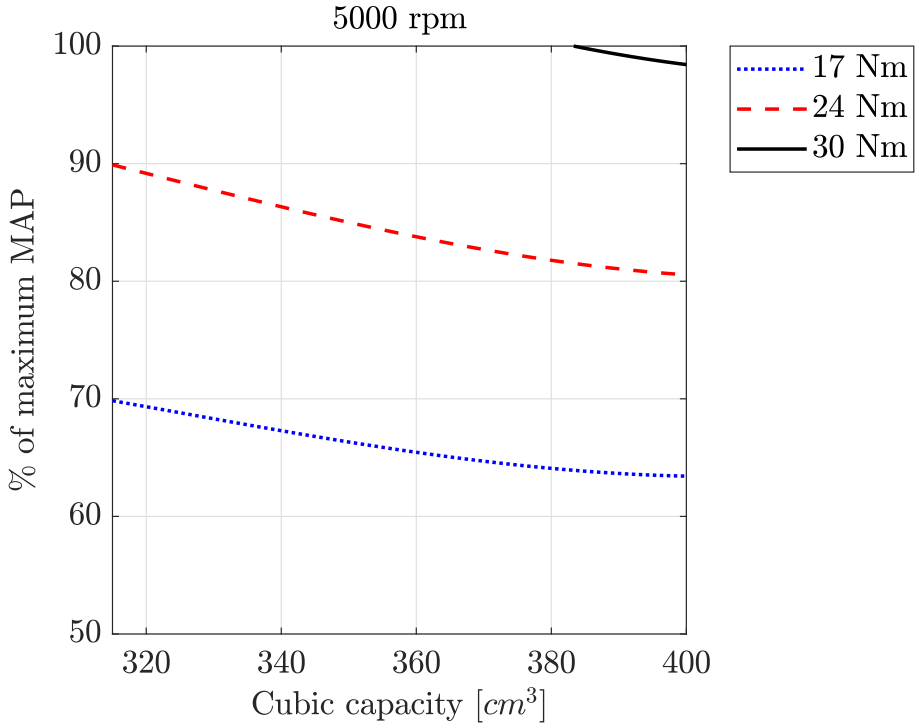

Figure 6.22: MAP along iso–torque lines for 5000 rpm.

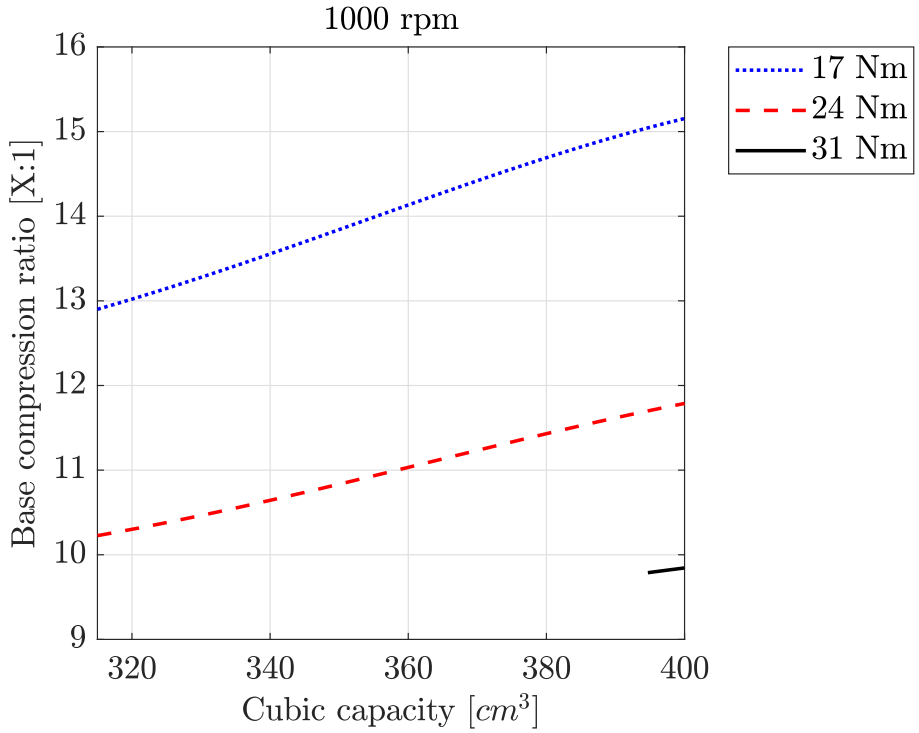

Figure 6.23: Optimum compression ratio along iso–torque lines for 1000 rpm.

For low engine speed, it is convenient to keep in–cylinder pressure as low as possible due to knock onset (Fig. 6.26). Therefore, the optimum efficiency can be found for the engine operating at maximum cubic capacity. An optimum combination between cubic capacity can be found for low load. For medium and high engine speed, the lowest cubic capacity level

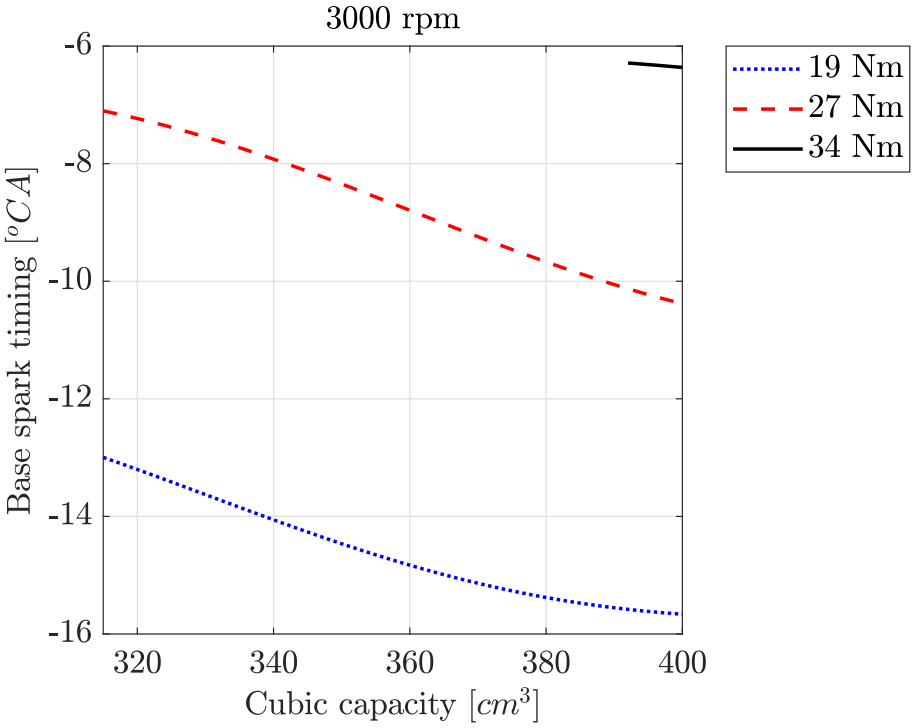

Figure 6.24: Optimum spark timing along iso–torque lines for 3000 rpm.

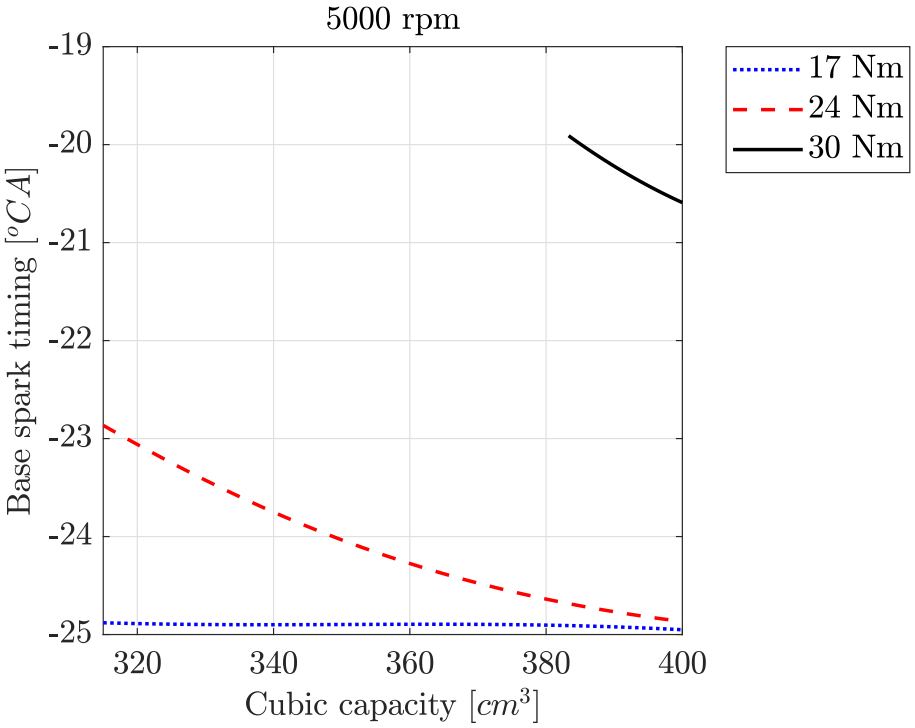

Figure 6.25: Optimum spark timing along iso–torque lines for 5000 rpm.

presented the highest efficiency (Figs. 6.27 and 6.28).

The verified trends can be partially explained by the effect of load control on volumetric efficiency. Low volumetric efficiency was related to high pump losses. Therefore, the load control by cubic capacity adjusting promises the mitigation of pump losses. This hy-

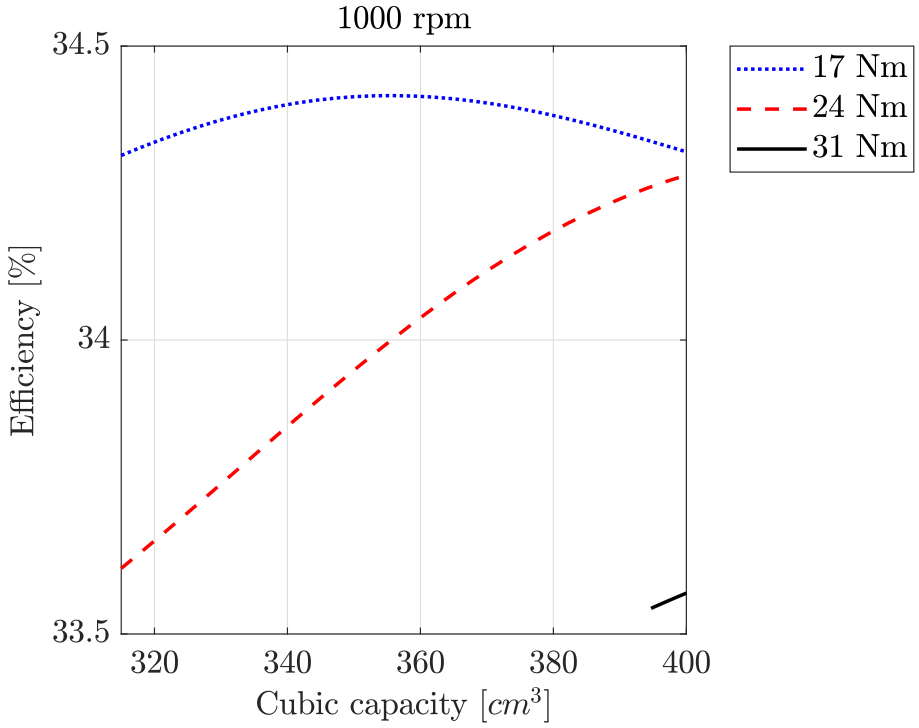

Figure 6.26: Efficiency along iso–torque lines for 1000 rpm.

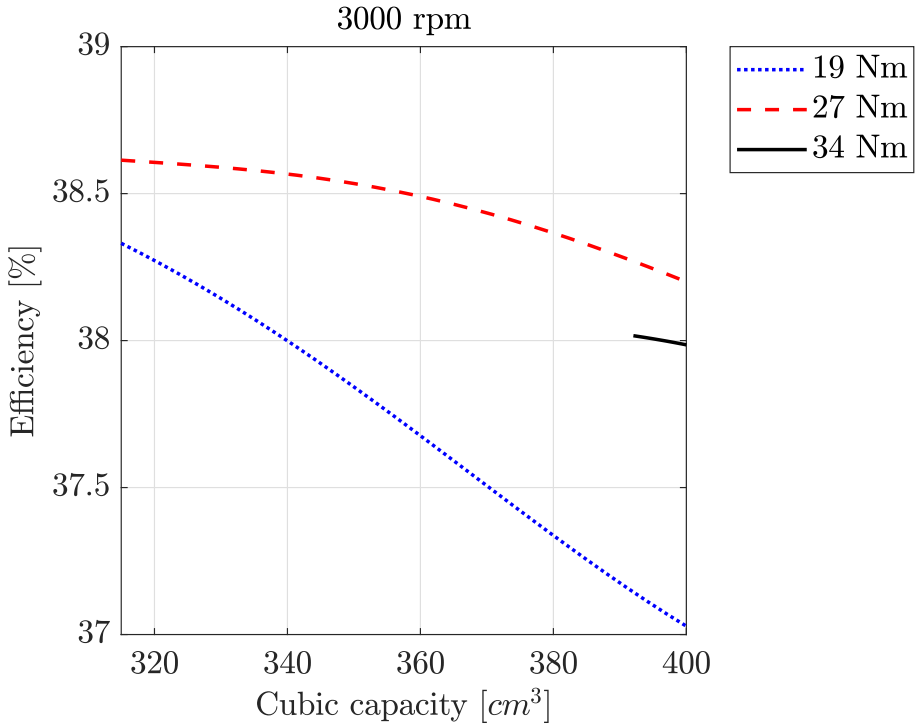

Figure 6.27: Efficiency along iso–torque lines for 3000 rpm.

pothesis was corroborated by the results of volumetric efficiency (Fig. 6.32). The volumetric efficiency is verified to increase with MAP increasing and cubic capacity decreasing (Figs. 6.29 to 6.31).

Both cubic capacity and MAP present a linear relation to load (Figs. 6.33 and

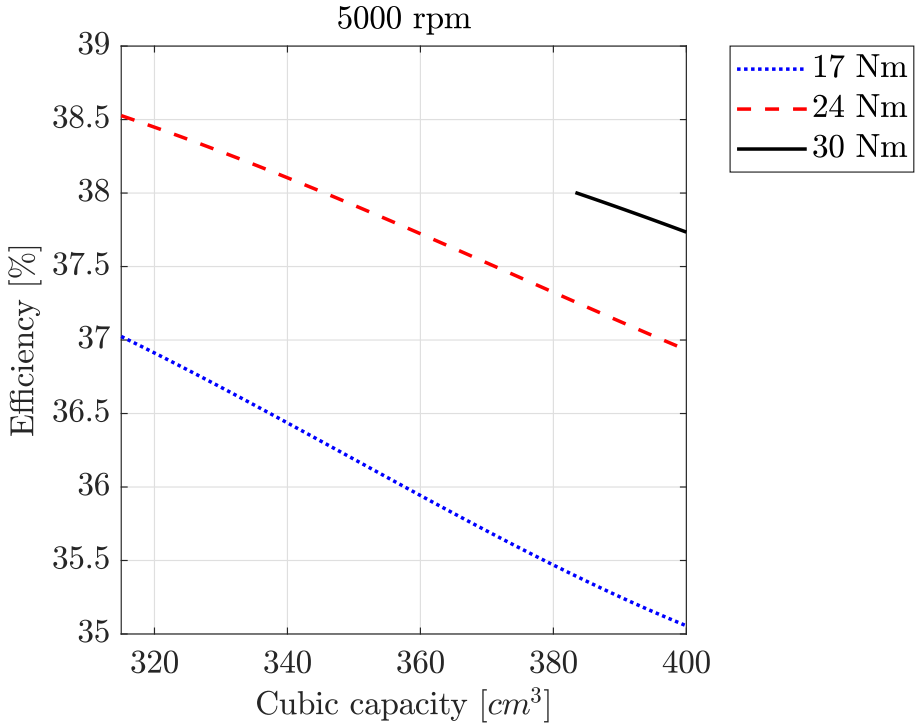

Figure 6.28: Efficiency along iso–torque lines for 5000 rpm.

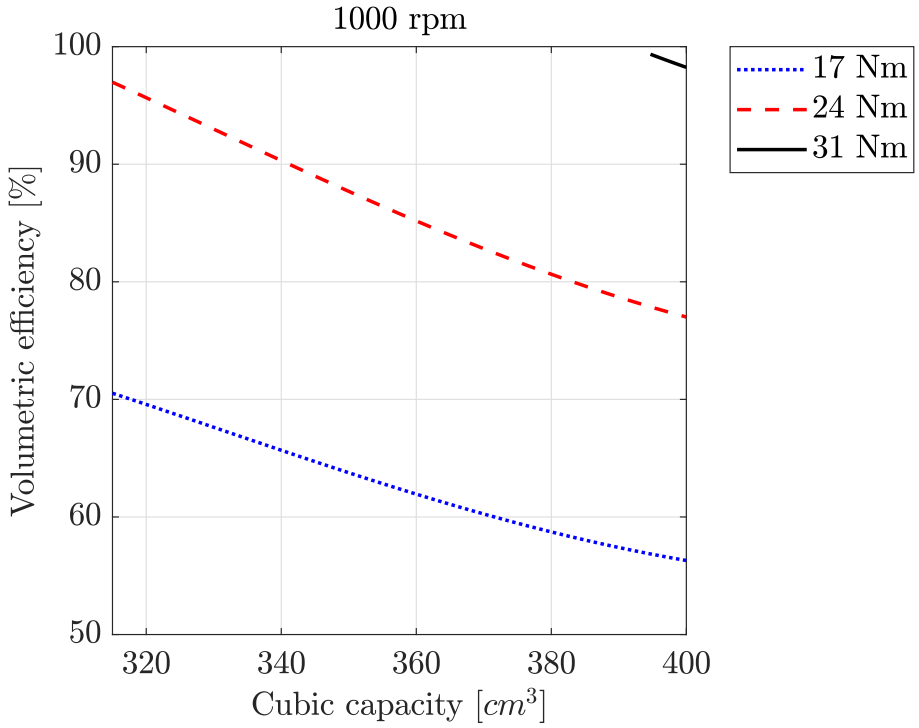

Figure 6.29: Volumetric efficiency along iso–torque lines for 1000 rpm.

6.34). Load decreasing from full load to partial load conditions can be separated in two regions. Firstly, the reduction of cubic capacity is performed it reaches its minimum value (Fig. 6.33). Thereafter, it is necessary to exclusively close the throttle, reducing MAP (Fig. 6.34), producing a secondary regions of load control.

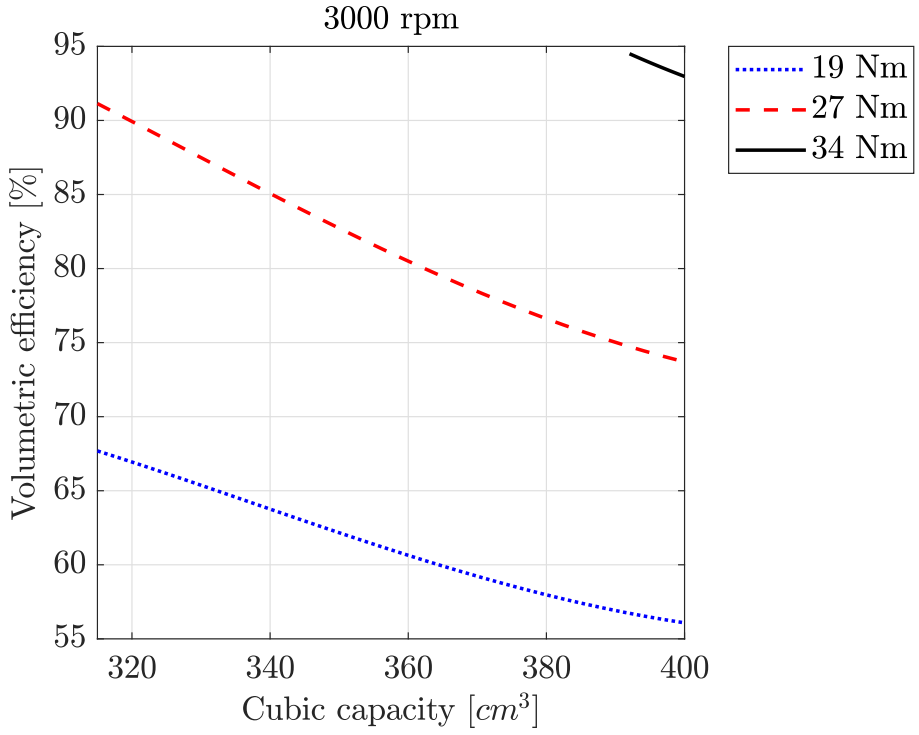

Figure 6.30: Volumetric efficiency along iso–torque lines for 3000 rpm.

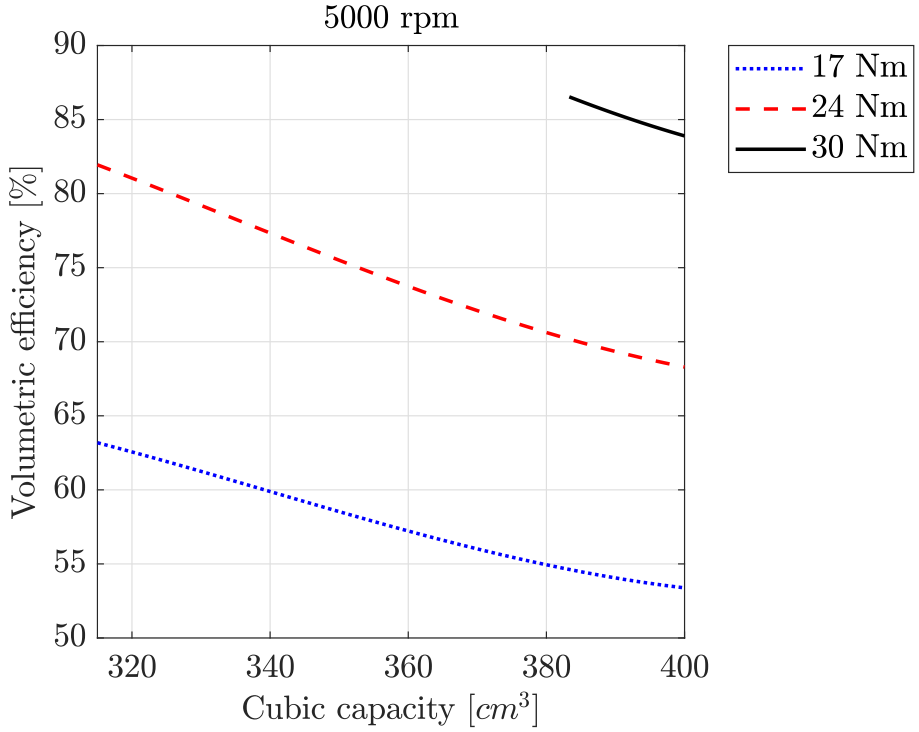

Figure 6.31: Volumetric efficiency along iso–torque lines for 5000 rpm.

Spark was delayed for low engine speed (Fig. 6.35), as it was preferable to increase compression ratio to obtain a higher efficiency (Fig. 6.36). For medium and high engine speeds, the spark timing was delayed during the cubic capacity control region, being increased as MAP was reduced in the throttle closing region. Compression ratio was maintained in its maximum

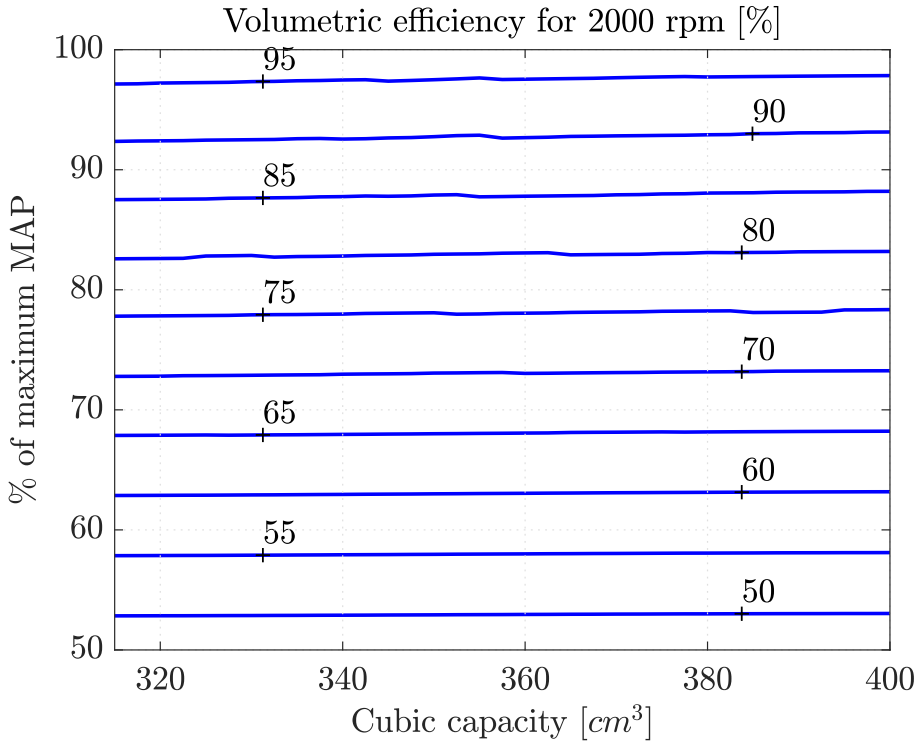

Figure 6.32: Volumetric efficiency as function of MAP and cubic capacity.

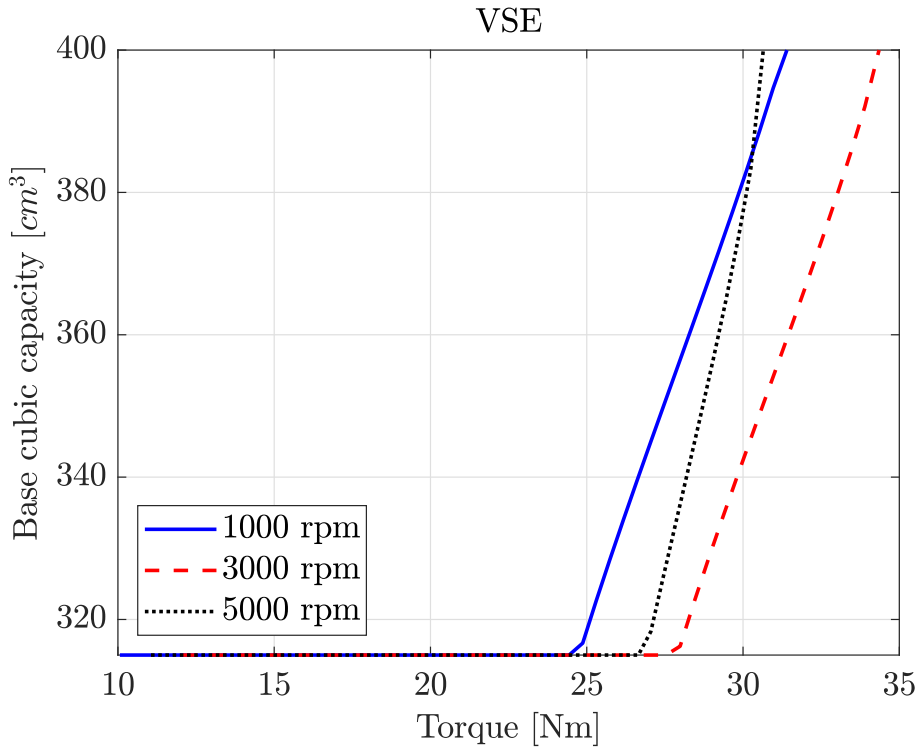

Figure 6.33: Base cubic capacity on different engine speed for the VSE engine.

value for high engine speed. For medium engine speed, the compression ratio was kept constant around 17.5:1 in the region of cubic capacity control, being increased to its maximum value in the region of throttle control. The same behaviour was verified for low engine speed, although

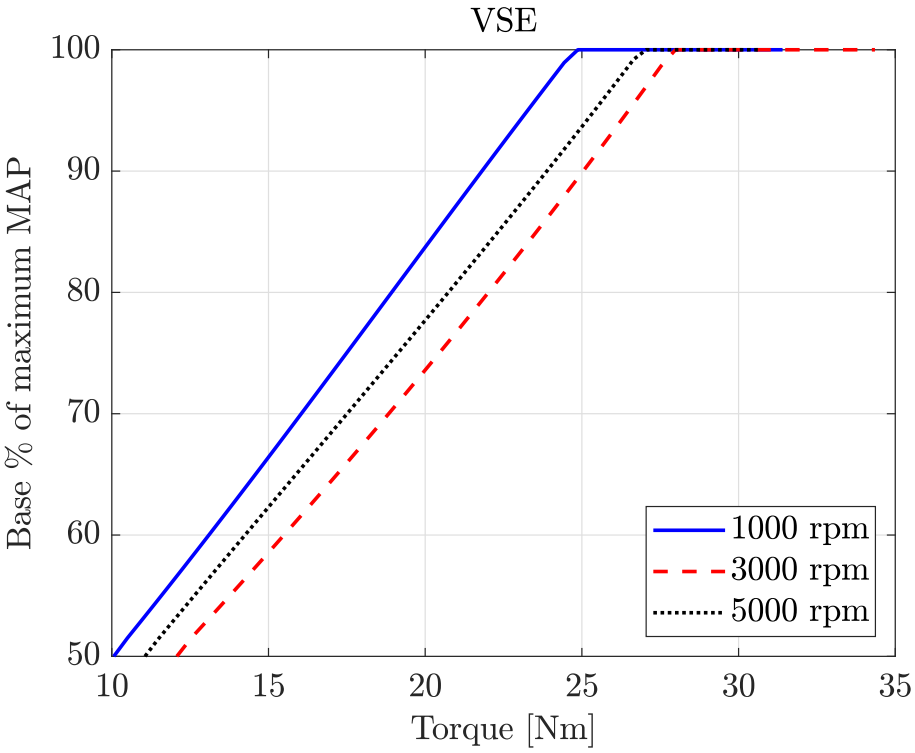

Figure 6.34: Base MAP on different engine speed for the VSE engine.

it was not possible to attain the maximum value for compression ratio.

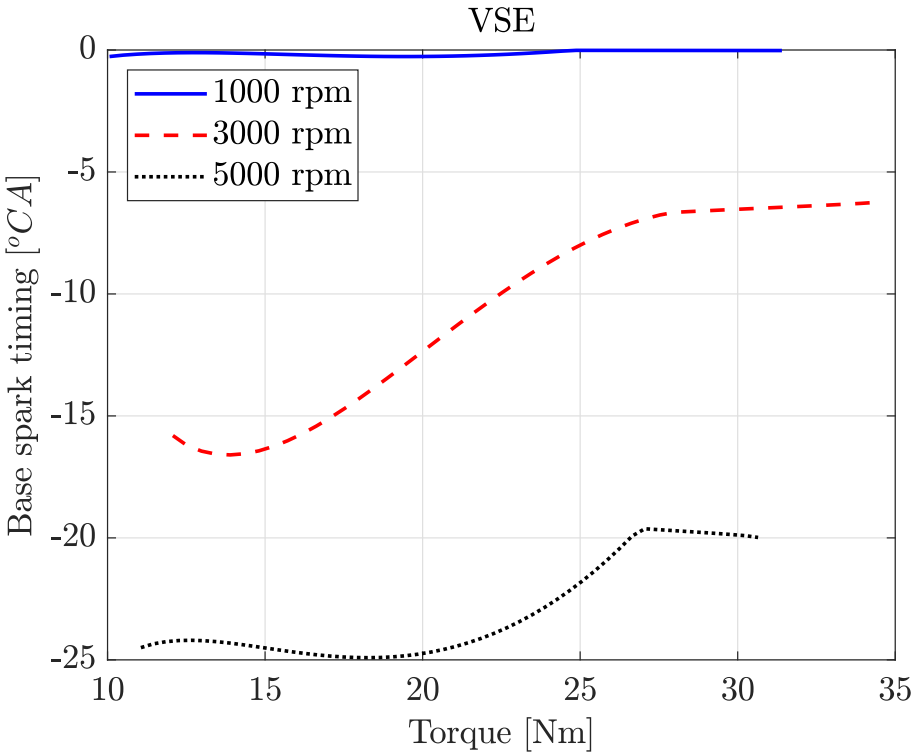

Figure 6.35: Base spark timing on different engine speed for the VSE engine.

VSE and VCR engines presented a very similar strategy for spark timing and compression ratio (Fig. 6.37 to Fig. 6.14 and Fig. 6.38 to Fig. 6.15).

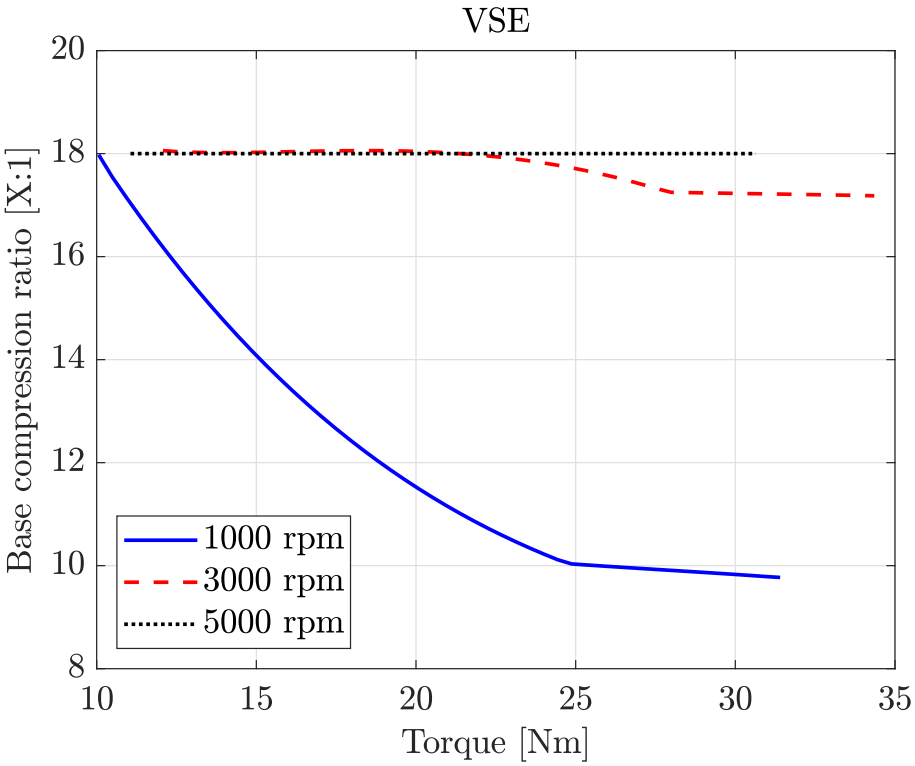

Figure 6.36: Base compression ratio on different engine speed for the VSE engine.

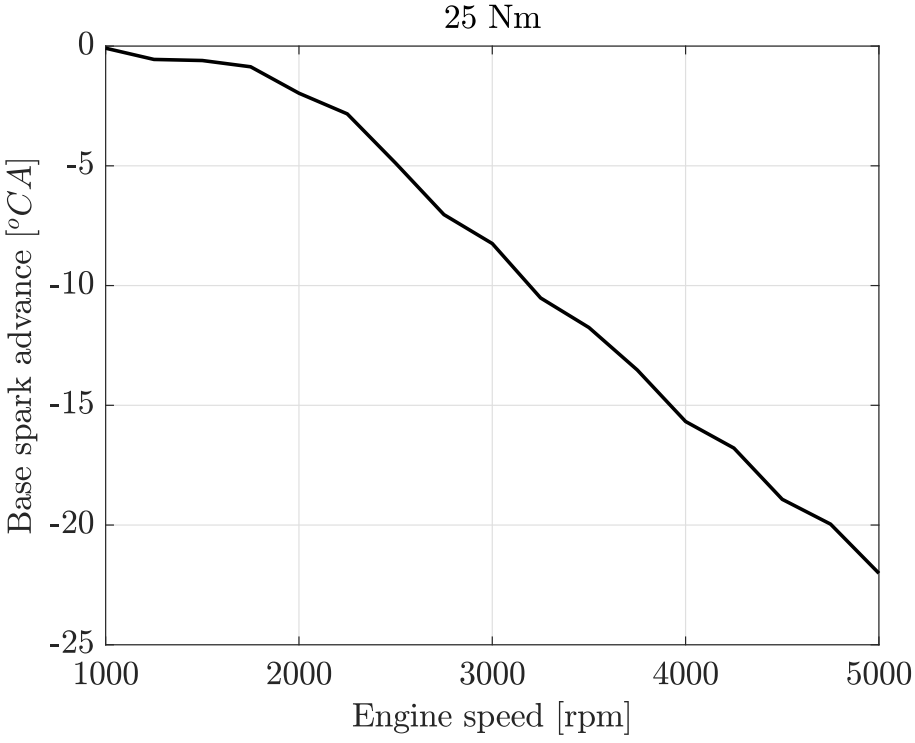

Figure 6.37: Base spark timing of the VSE engine for 25 Nm.

Both base calibration calibration MAP and cubic capacity (Figs. 6.39 and 6.40) presented constant values almost parallel to the lines of minimum and maximum torque owing to the linear relation between both parameters and load. The regions of throttle control can be

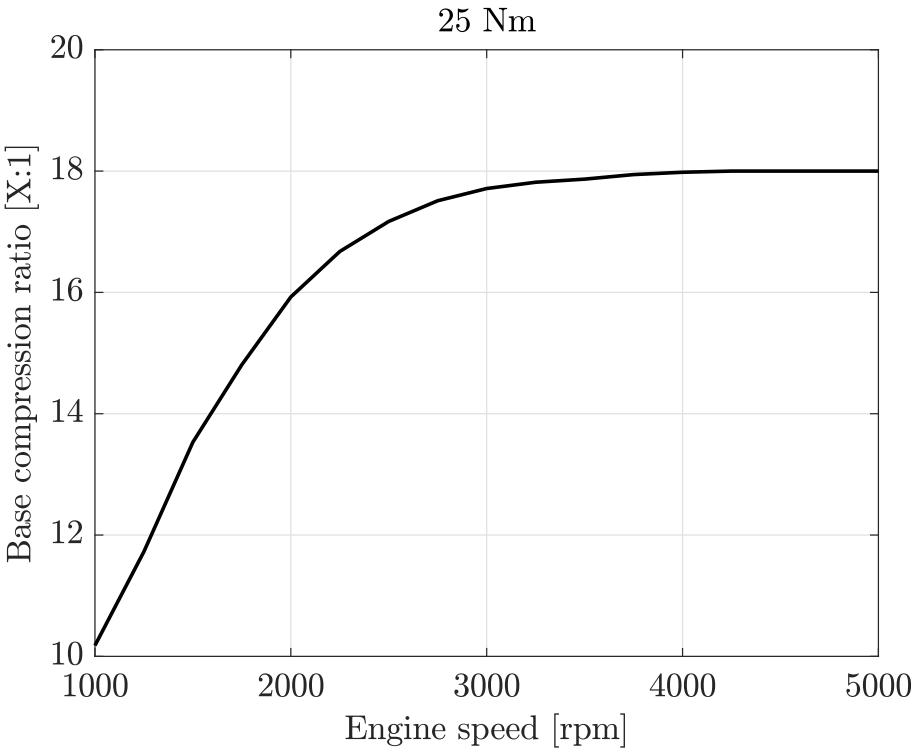

Figure 6.38: Base compression ratio of the VSE engine for 25 Nm.

identified in Fig. 6.39, while the region of cubic capacity control can be identified in Fig. 6.40.

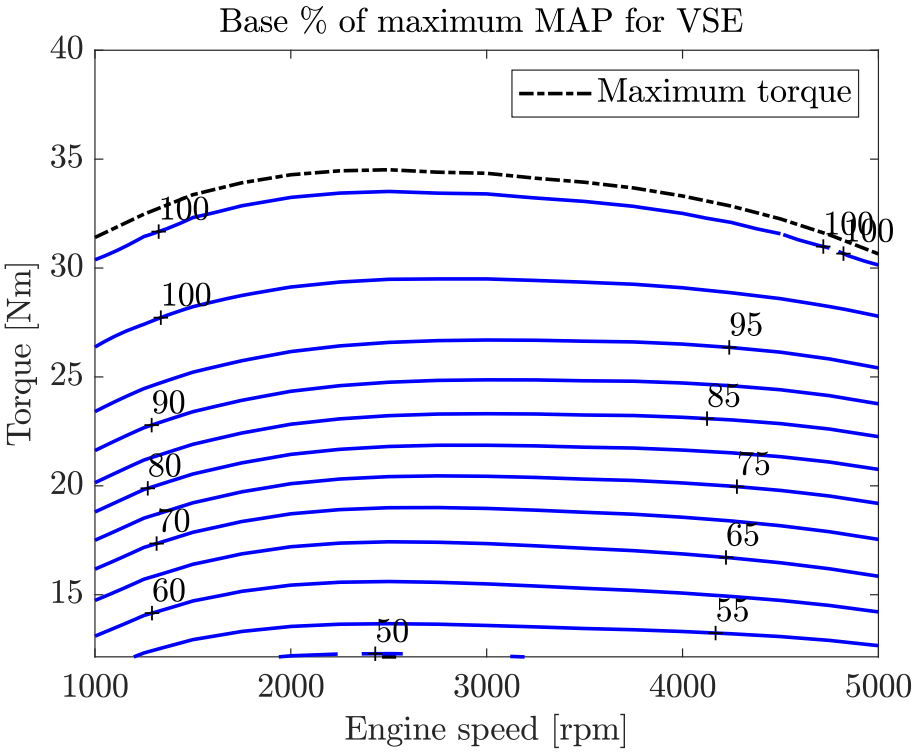

Figure 6.39: Complete map of base MAP for the VSE.

The base calibration for spark timing and compression ratio (Figs. 6.41 and 6.42) presented a similar behaviour to that for the VCR engine (See Figs. 6.12 and 6.13). Spark

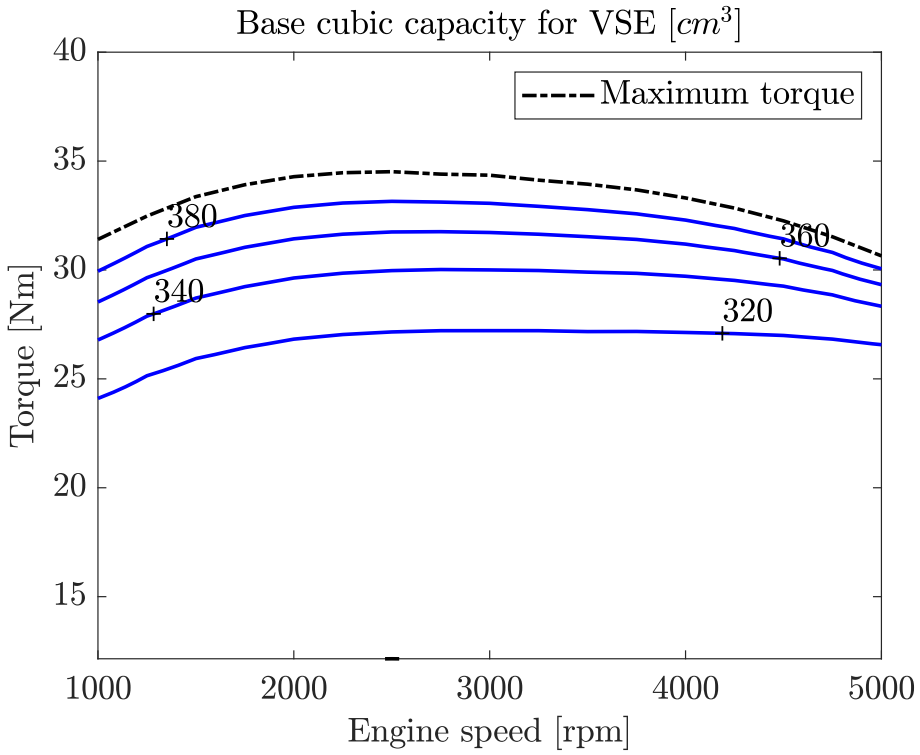

Figure 6.40: Complete map of base cubic capacity for the VSE.

timing was kept delayed, being increased with engine speed increasing. Compression ratio was held at maximum value for most part of engine operation even though the MAP was increased compared that of the VCR engine.

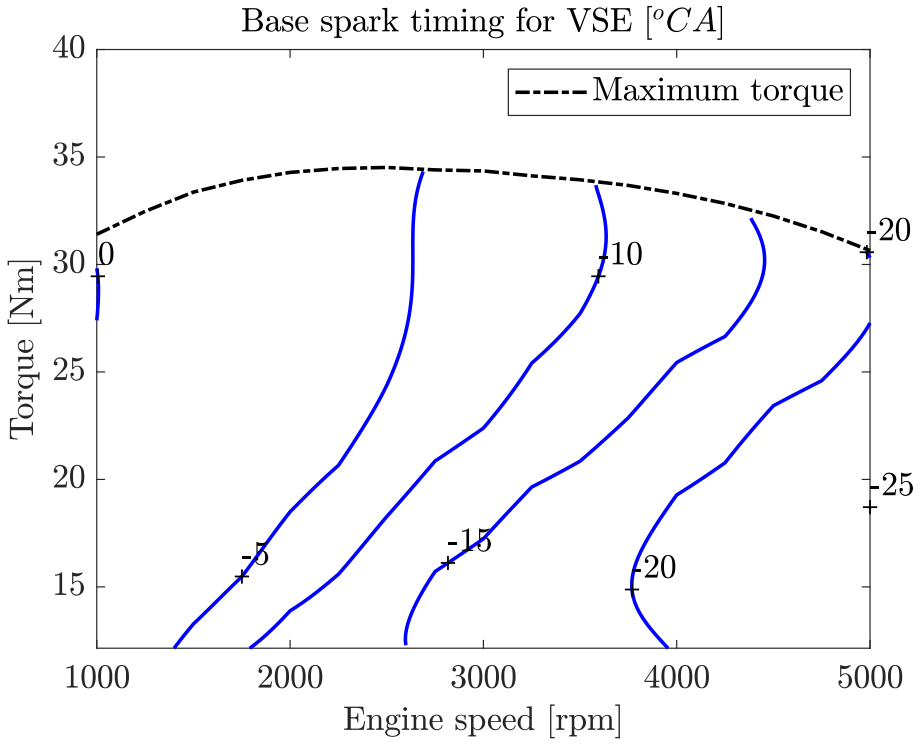

Figure 6.41: Complete map of base spark timing for the VSE.

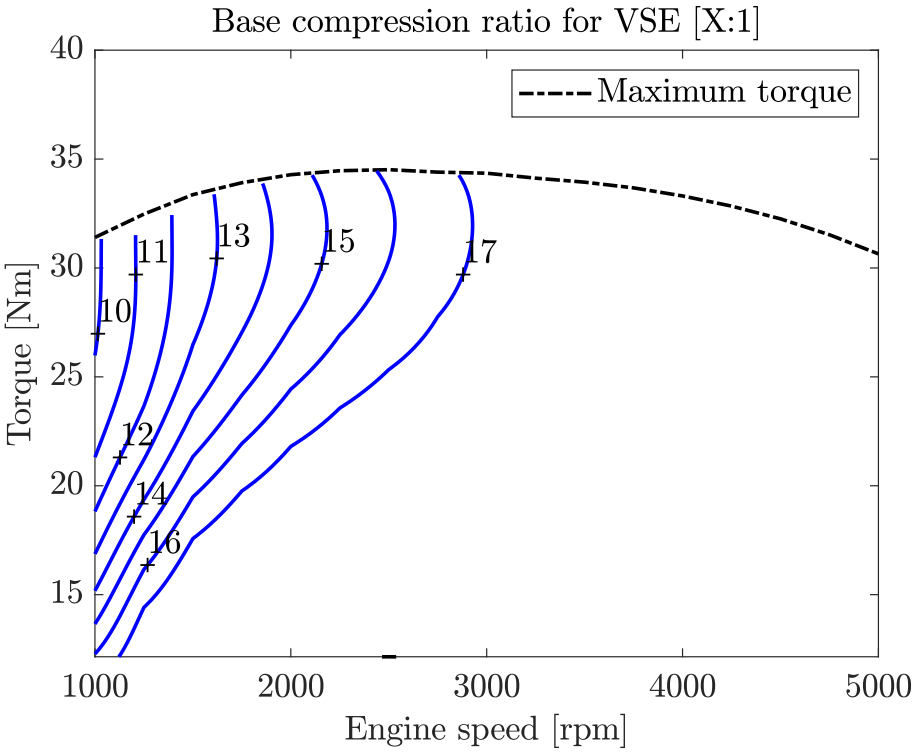

Figure 6.42: Complete map of base compression ratio for the VSE.

A constant efficiency of 38.5% was verified for a significant range of operation. For low engine speed, load had only a slight influence on efficiency (Fig. 6.43).

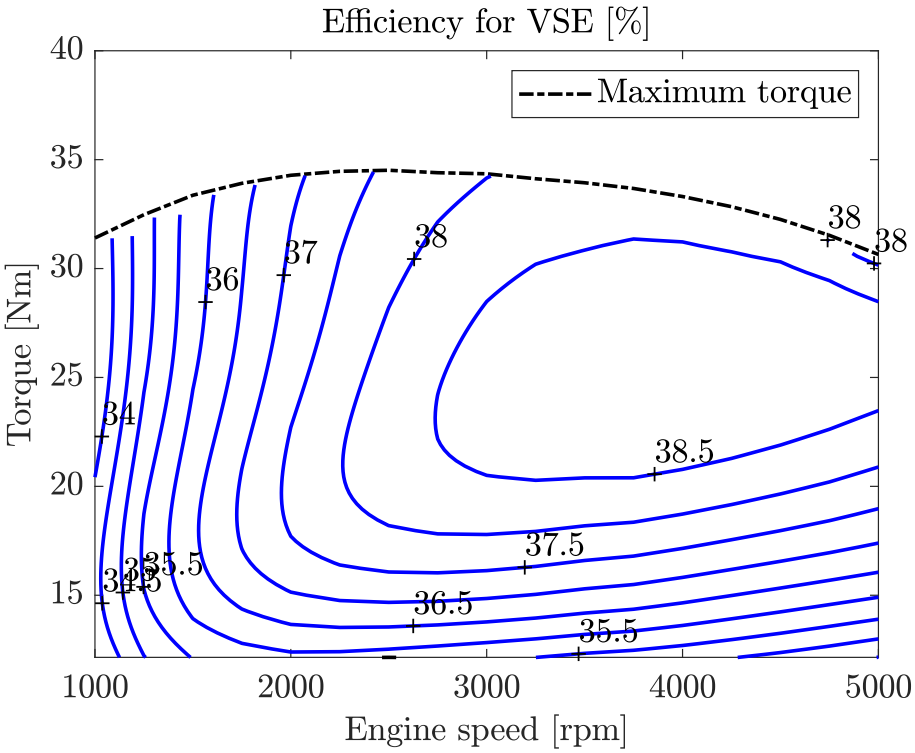

Figure 6.43: Complete efficiency map for the VSE.

6.2.3 Comparison of technologies

After obtaining results on efficiency for the three simulated engines, a comparison is presented for the engine speeds of 2500 rpm, 3000 rpm and 3500 rpm (Figs 6.44, 6.45 and 6.46).

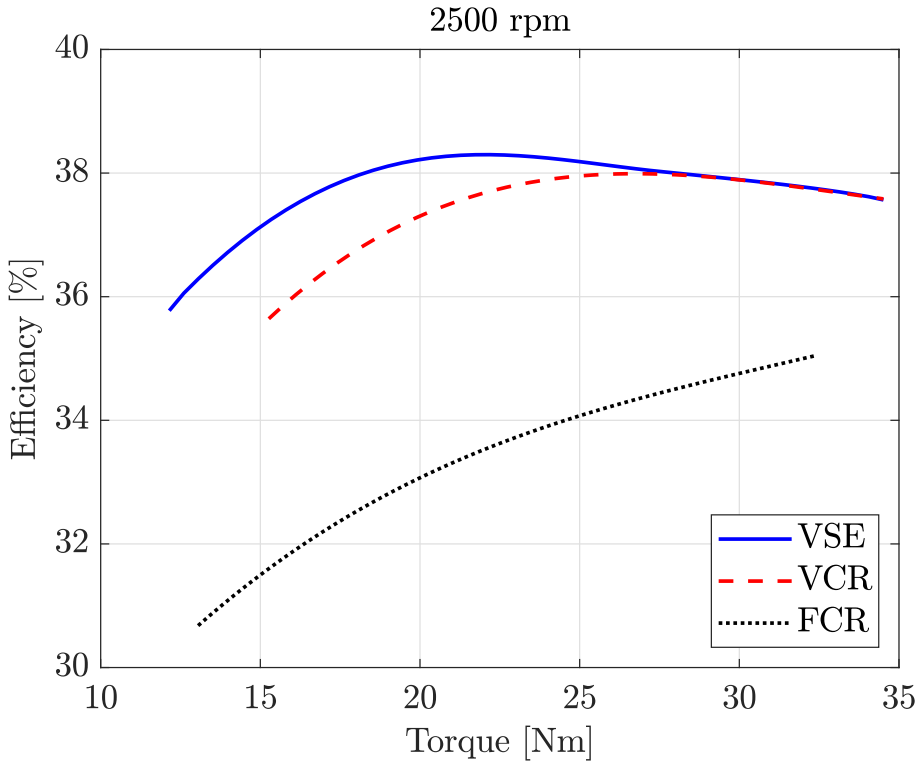

Figure 6.44: Comparison of efficiency for 2500 rpm.

For 2500 rpm, the decrease in volumetric efficiency owing to MAP reduction was compensated by the increase in compression ratio for the VCR engine. Therefore, the VCR engine presented an efficiency almost as high as the VSE engine for high load condition. The advantage of VSE engine was more evident for partial loads conditions.

For 3000 rpm and 3500 rpm, the VSE engine increased its compression ratio as knock onset is not critical, resulting in a higher efficiency compared to that of VCR engine. It is highlighted that the condition of maximum load is equivalent for both VSE and VCR engines as cubic capacity and MAP are at their maximum value for both engines.

The effect of controlling compression ratio was verified when comparing both VSE and VCR engines to the FCR engine, which presented a significantly lower efficiency compared to those of VCR and VSE engines. Moreover, increase in compression ratio also leads to a gain in maximum torque (Fig. 6.47). For low engine speed conditions, the torque was the same owing to knock onset. However, as engine speed is increased and knock onset becomes less critical, the compression ratio increased, leading to a gain of almost 8% in maximum torque for 5000 rpm.

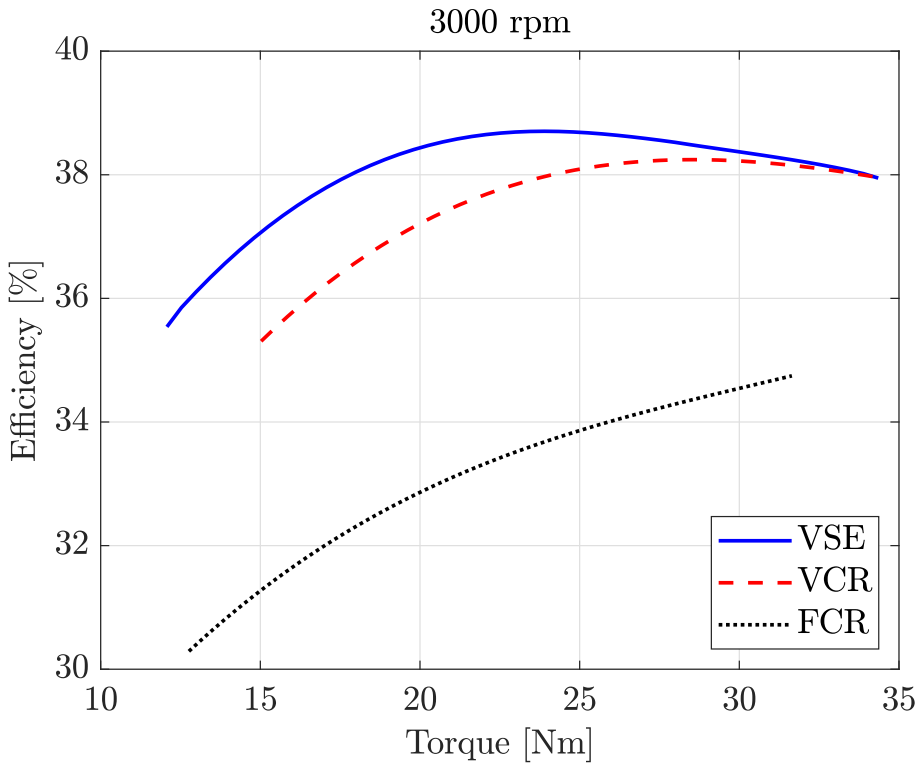

Figure 6.45: Comparison of efficiency for 3000 rpm.

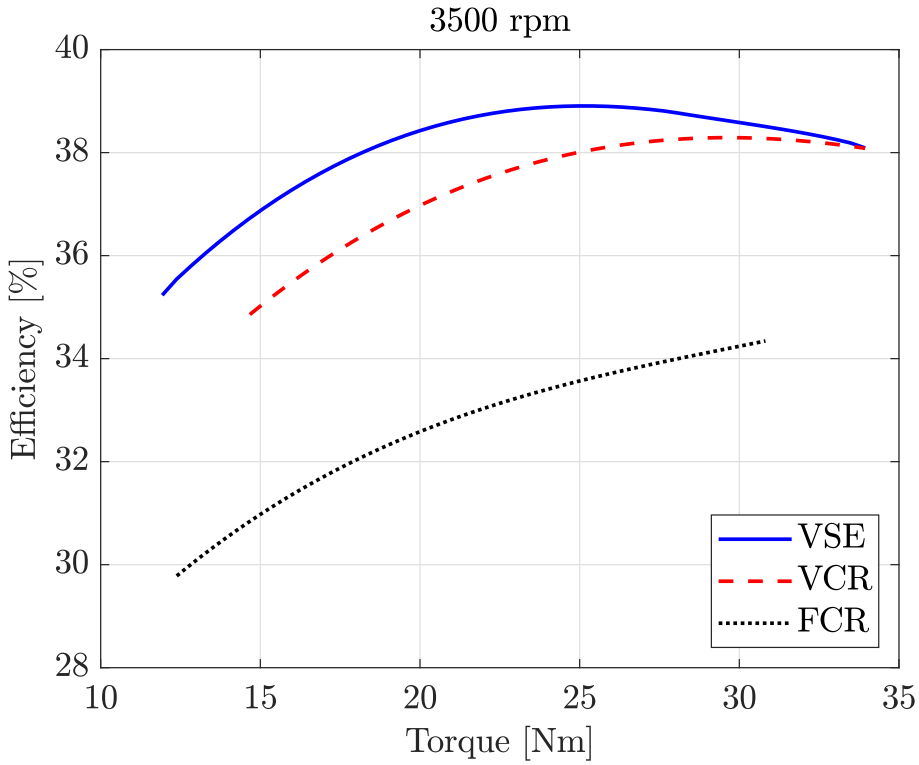

Figure 6.46: Comparison of efficiency for 3500 rpm.

The advantages of the VSE engine were more evident for high engine speed at high loads and partial loads for the entire rage of speed, providing a gain in efficiency between 5% and 15% (Fig. 6.48).

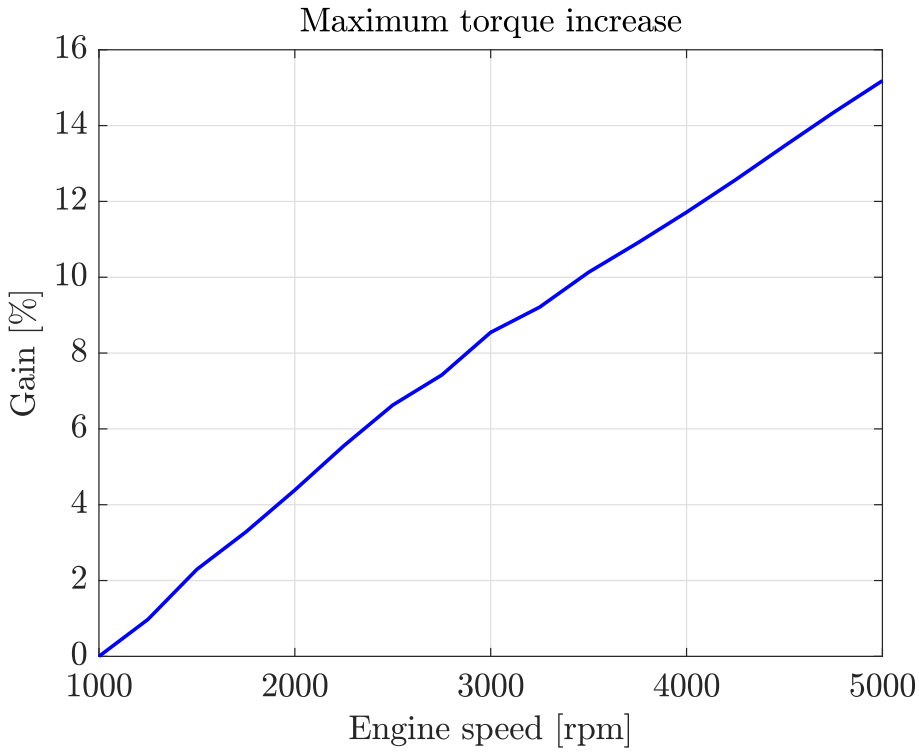

Figure 6.47: Comparison of maximum torque between FCR and VSE.

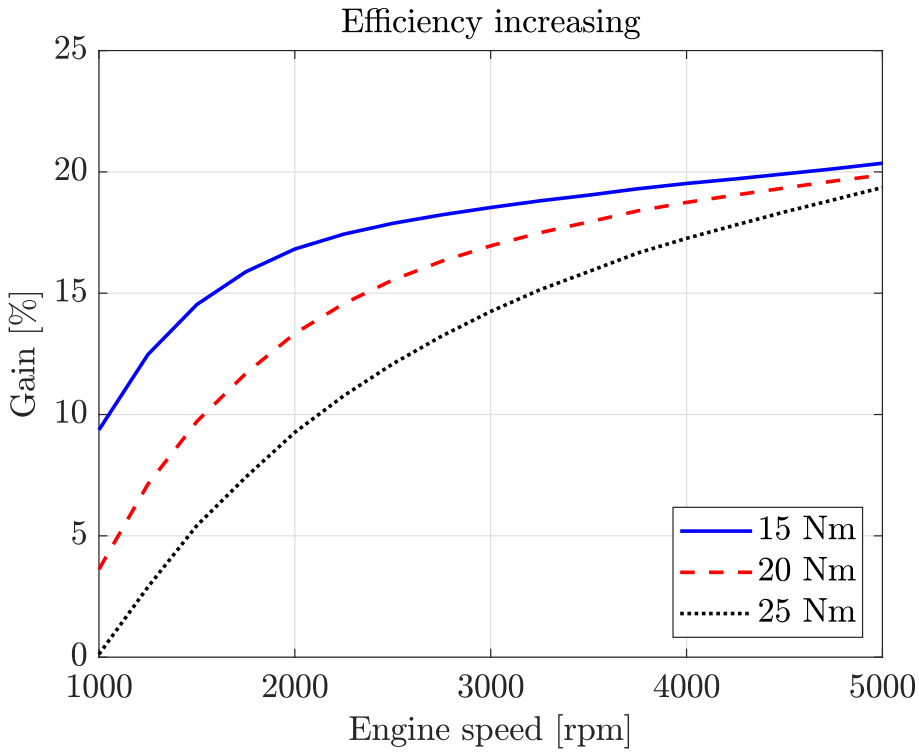

Figure 6.48: Comparison of efficiency between FCR and VSE.

The fact that the simulation model was calibrated by using data from a specific engine is highlighted. Results obtained from a functional prototype of the VSE engine in the future may differ from the results found on the simulations owing to different engine characteristics.

Parameters provided by the data from the tested engine are:

1. Exhaust manifold temperature;
2. Exhaust manifold pressure;
3. Intake manifold pressure;
4. Combustion duration.

Exhaust manifold conditions have little influence in the engine cycle. The fluid properties downstream from the cylinder during the exhaust process impacts in the residual gas trapped in the cylinder. The exhaust manifold temperature will only affect residual gas fraction when backflow occurs, *i.e.*, at specific conditions of very low engine speed, occurring between the EVO and the BDC. This condition is rarely achieved in spark ignition engines. The lower the pressure in the exhaust manifold, the lower the amount of residual gas. However, the pressure profile for the exhaust manifold is not expected to present a significant variation from one engine to another.

Intake manifold pressure is expected to present more influence in the engine cycle than the exhaust manifold pressure. As manifold pressure has direct relation to the intake process, it directly affects the volumetric efficiency. The pressure profile obtained from the tested engine is typical for a multi–cylinder engine. The pressure variation observed in Fig. 6.1 is due to acoustic interactions between cylinders. Mono–cylindrical engines usually exhibit a monotonic relation between pressure and engine speed. Consequently, volumetric efficiency of a VSE prototype is expected to diverge from the results obtained by the simulation.

Combustion duration is expected to be significantly affected by modifications in the engine. Combustion is influenced by: combustion chamber geometry, varying bore–stroke ratio, charge temperature, and fuel atomisation among others factors. The flame velocity is directly related to turbulence, therefore, the engine design must favour turbulence increase, resulting in a shorter combustion time.

6.3 Considerations on the impact of implementing the technology

Usually, improvement in efficiency for engines is evaluated as means of fuel consumption. As the engine can undergo through a variety of operational condition involving acceleration, deceleration, full load, and partial load, absolute consumption is not a convenient parameter for the analysis. Specific fuel consumption (sfc) is therefore used in order to compare different conditions for different engines. The definition of sfc is demonstrated in Eq. 6.9.

$$sfc = \frac{\dot{m}_{fuel}}{\dot{W}} = \frac{1}{h_{comb}\eta_t} \tag{6.9}$$

As one can observe, sfc is inversely proportional to thermal efficiency. Consequently, the observed improvement from 5% to 15% in efficiency for the VSE engine results in a reduction from 4.8% to 13% in the indicated sfc.

6.3.1 Comparison with other technologies

Other studies on VSE engines performance were conducted by SIEGLA and SIEWERT (1978) and ALSTERFALK *et al.* (1997). SIEGLA and SIEWERT (1978) tested the engine produced in the Sandia Laboratories under the conditions of an EPA driving cycle 55% Urban and 45% Highway for two different vehicles, finding a reduction in fuel consumption of 19.7% for a light vehicle and 16.7% for a heavy vehicle using an optimized combustion chamber. ALSTERFALK *et al.* (1997) simulated a VSE engine with fixed compression ratio, expectedly obtaining the same result for VSE and conventional engines at full load. For partial loads, the authors found a brake sfc (bsfc) reduction of 18% for 1500 rpm and 21% for 3000 rpm. The mechanisms studied by those studies allowed a significant variation of cubic capacity.

Other technologies compete with the proposed engine by combining the VCR technology with other means for load control. One of these technologies is the variable valve timing (VVT) as means for load control. RABHI *et al.* (2004) predicted that the combination of the VCR, VVT, and fuel direct injection technologies would provide a gain in fuel consumption between 15% and 45%. SUGIYAMA *et al.* (2007) found a reduction of 16.2% in fuel consumption for a partial load condition of 2.5 bar bmep with early IVC combined to VCR. The authors found that the early IVC reduces the effective compression ratio, resulting in a low temperature at the beginning of the combustion, delaying flame propagation. LI *et al.* (2018) conducted an experimental on an Otto-Atkinson engine, obtaining a gain of 11% in bsfc at 3200 rpm and 5.5 Nm.

Charge dilution is another possibility for load control. When increasing the EGR rate, it is necessary to increase compression ratio and advance spark timing to obtain a stable combustion. XIE *et al.* (2013) found a reduction of 5% in bsfc for an engine fuelled with methanol.

FUKUI *et al.* (1983) tested the strategy of turning off cylinders for load control. An economy of 20% was obtained for stable operation whilst an economy of 11% was obtained for the EPA Urban cycle. Other similar strategy consists in skipping cycles instead of turning cylinders off. YÜKSEK *et al.* (2012) found a gain of 4.3% in bsfc for all partial loads conditions. However, this strategy presented an increase in emissions, which can be reduced by using the VVT actuation (DOGRU *et al.*, 2018).

6.4 Considerations for other applications

This study focused on the implementation of the proposed mechanism for a spark–ignition engine fuelled with ethanol, aiming the automotive application. There are other forms of utilisation in which the mechanism can be used. A brief discussion is presented in this section, commenting the possible advantages of adopting the VSE mechanism for: other types of fuels, compression ignition engines, and for stationary engines.

6.4.1 Operation with gasoline and other fuels

One of the indicated advantages of the proposed engine is the capability of operating with multiple types of fuels. Although this study was only conducted for hydrous ethanol, its main motivation is the application on flexfuel engines. As the fuel properties considered for the simulation model are: elements composition, stoichiometry, enthalpy of combustion h_{comb}, and octane number. Results are therefore predicted for the operation with the engine fuelled with other types of fuel by comparing those properties for the different fuels (Tab. 6.7). Those properties are: composition, stoichiometric air–fuel ratio (AFRs), specific enthalpy of combustion for a stoichiometric mixture (in means of mixture mass), motoring and research octane numbers (MON and RON, respectively), and combustion products composition considering a complete oxidation of the reactants. Fuels considered for the comparison are: liquid natural gas (LNG), liquefied petroleum gas (LPG), gasoline, and alcohols. For the LNG and the LPG, the pure components were analysed individually. For the gasoline, there are several surrogates, *i.e.*, substances present in the gasoline that can represent its thermochemical behaviour. For this analysis, two surrogates were chosen, which are used in the primary fuel research (PRF) for octane number references: n–heptane and iso–octane. The alcohols were analysed in their anhydrous composition, comprising: methanol, ethanol and n–butanol.

Usually, the literature provides the values for lower heating value (LHV), as means of kJ for each kg of fuel. However, the AFRs is different for each fuel owing to their different composition. When the enthalpy of combustion is calculated for a mixture, the values are similar. Acetylene and Ethylene presented higher values for enthalpy of combustion. However, they represent only a small fraction in the composition of LPG.

The combustion products composition indicates the behaviour of gases during the expansion and exhaust processes, in which the heat capacity and the high temperature of the mixture influence the in–cylinder pressure and temperature profiles. As the simulation model does not include a chemical kinetic model for emission formation, it is not possible to compare fuels in means of pollutant emissions. Moreover, the concentrations of nitric oxides, carbon monoxide, and hydrocarbons are much lower than those of carbon dioxide, nitrogen, and water, thus presenting low relevance in the thermodynamic properties of the mixture. Combustion of

alcohols leads to a lower fraction of nitrogen and a higher concentration of water in the combustion products compared to those for hydrocarbons. Additionally, methane combustion leads to a higher concentration of water and a lower concentration of carbon dioxide compared to those for others hydrocarbons. In addition to the results found, the variations in the combustion products are not expected to affect combustion gas behaviour.

Consequently, the only fuel parameter to present a relevant variation is the octane number, which can significantly affect the results. As the compression ratio and spark timing are strongly dependent on the knock onset, each fuel would require a different calibration for those parameters. This strategy is already adopted for flexfuel engines, which not only are calibrated for operation with hydrous ethanol or gasohol, as also their ECU's have meanings for identifying when the engine is fuelled with a blend. By identifying a fuel blend, the ECU can apply strategies for calibrating spark timing.

Table 6.7: Comparison for properties of many fuels components[1].

Fuel type	Component	Composition	AFRs	h_{comb} [MJ/kg of mixture]	MON	RON	$\%\ CO_2$	$\%\ H_2O$	$\%\ N_2$ and others
LNG[2]	Methane	CH_4	17.2	2.7	120	120	9.51	19.01	71.48
LPG[3]	Ethane	C_2H_6	16.1	2.8	99	115	11.01	16.52	72.47
	Ethylene	C_2H_4	14.7	3	-	-	13.09	13.09	73.82
	Acetylene	C_2H_2	13.2	3.4	50	50	16.13	8.06	75.81
	Propane	C_3H_8	15.7	2.8	97	112	11.63	15.50	72.87
	n-Butane	C_4H_{10}	15.5	2.8	90	94	11.96	14.95	73.09
	iso-Butane	C_4H_{10}	15.5	2.8	98	102	11.96	14.95	73.09
Gasoline[4]	n-Heptane	C_7H_{16}	15.2	2.8	0	0	12.42	14.19	73.39
	iso-Octane	C_8H_{18}	15.1	2.8	100	100	12.50	14.06	73.44
Alcohol	Methanol	CH_3OH	6.5	2.7	92	106	11.57	23.15	65.28
	Ethanol	C_2H_5OH	9.0	2.7	89	109	12.29	18.43	69.29
	n-Butanol[5]	C_4H_9OH	11.2	2.7	85	98	12.67	15.84	71.48

[1] Source: MCALLISTER *et al.* (2011), except when indicated

[2] According to the composition described by CHO and HE (2007)

[3] According to the composition described by DAGAUT and ALI (2003)

[4] Surrogates used in PRF

[5] Source: TRINDADE and SANTOS (2017)

Combustion duration is another parameter that could affect the results. Each combustion profile, exhibited by different fuels, requires a specific calibration, as combustion duration can present influence on knock sensibility, and the position of optimum spark timing and optimum compression ratio for maximum torque. However, experimental data is required for an appropriate calibration for the simulation model, according to the process described in this study. Moreover, enthalpy of vaporisation is another parameter that can affect the combustion behaviour. Fuels with higher enthalpy of vaporisation can present issues for cold start and idle operation, as the vaporisation process decreses in–cylinder temperature. These issues can be avoided by increasing compression ratio, leading to higher in–cylinder temperature. Therefore, for multifuel application, the control of compression ratio not only aims towards higher efficiency, as it also enables a more steady operation for different types of fuels at different operational conditions.

6.4.2 Compression ignition engines

The control over compression ratio for CI engines does not have the same attention as that for SI engines. CI engines have a higher compression ratio as it is necessary to ensure autoignition. Consequently, knock is not a limiting factor for CI engines. However, as the indicated thermal efficiency increases with increased compression ratio, the mechanical efficiency decreases because of the higher level of friction caused by the increased pressure in the cylinder. Therefore, there is an optimum value for compression ratio in which the global efficiency for the engine, *i.e.* the brake efficiency, is maximum (PEŠIĆ *et al.*, 2010). As the engine load is variable on its operation, the optimum compression ratio is not fixed. Moreover, compression ratio can be adjusted in order to reduce emission for specific operational conditions and to guaratee a more stable combustion at cold start and idle operation. The proper implementation of biodiesel blends as fuels also requires the VCR technology. Studies have shown that the origin of the biodiesel and the composition of the blend result in different characteristics for the fuel (MURALIDHARAN and VASUDEVAN, 2011).

In CI engines, load control is mainly performed by controlling air–fuel ratio, which is always kept at the lean condition. For a given level of load at a lower cubic capacity than that for a conventional engine, the imep has to be increased. In that case, the air–fuel ratio decreases. There are some advantages expected when air–fuel ratio decreases, such as reduced carbon monoxide emission and better combustion stability. However, there are some drawbacks associated with the increased air–fuel such as increase of nitric oxides and even increase of fuel consumption. A more detailed analysis is required for a better comprehension on the advantages and disadvantages of using the VSE mechanism for a CI engine.

6.4.3 Stationary engines

Stationary engines are usually used for electricity production or combined heat and power (CHP) utilisation in plants, involving the generation of a great amount of power compared to that required by the transportation sector. Consequently, the application of a VSE mechanism for stationary engines is not subjected to restrictions of engine weight and volume. Therefore, the VSE engine can be a promising alternative for improving the flexibility and efficiency of this type of engine.

Generally, CI engines are used as stationary engines. In this case, the use of a VSE CI engine for stationary application is subjected to the paradigms described in Section 6.4.2. However, LNG are presented as an alternative for decreasing emissions for stationary engines. Hence, the ultra lean condition is achieved to reduce NOx emissions. For low loads conditions, the air–fuel ratio is increased and the combustion becomes unstable, whereas at high loads conditions, the high compression ratio can lead to knock onset despite the high octane number of the LNG (CHO and HE, 2007). Therefore, the VSE mechanism would allow a better control on combustion stability and knock onset by adjusting compression ratio and avoiding ultra lean conditions for partial loads by decreasing cubic capacity. Moreover, the composition of the LNG can present other components aside from methane (SAIKALY *et al.*, 2008). The concept of methane number (MN) was developed for LNG fuelled SI engines. Similar to the ON, the MN indicates the knock sensibility of a LNG fuel. A MN of 100 corresponds to the knock sensibility of pure methane whilst a MN of 0 corresponds to the knock sensibility of molecular hydrogen. Expectedly, a variable compression ratio can optimise the operation of a LNG fuelled engine by adjusting compression ratio according to the MN of the LNG available in the region in which the engine is operating.

7. Conclusions

The first task of this research was the analysis of the proposed mechanism. A Kinematic model was developed to evaluate the effects of implementing the multi–link mechanism in the piston motion, and to provide a mathematical model for calculating instantaneous volume, area, and volume differential for the combustion chamber. After the model development, a configuration of the mechanism was suggested. For the proposed configuration, the cubic capacity can be adjusted between 315 and 400 cm^3 for each cylinder and a compression ratio of 18:1 could be achieved. The stroke to bore ratio of the engine was kept between 1.3 and 1.6.

A phase shift for TDC and BDC was observed when comparing the VSE mechanism to the conventional crank–rod mechanism. The phase shift in TDC was observed to be more dependent on compression ratio, presenting values between 3 and 5.2 °CA. It is highlighted that the VSE mechanism was compared to a symmetrical crank–rod. The phase shift in TDC is also observed for eccentric crank–rod mechanisms. The phase shift in BDC was more dependent of cubic capacity, being approximately symmetrical, varying between -1.5 and 1.5 °CA.

The modification in the piston kinematics presented an increase in maximum velocity of piston up to 8% for the VSE mechanism compared to that of the conventional crank–rod mechanism. A maximum deviation of 18% was found for piston acceleration in the VSE engine compared to that of the conventional crank–rod mechanism.

The second task of the research was the diagnosis of ethanol combustion. This task has the objective of providing information for the predictive model to simulate combustion. Data from a commercial engine was obtained and processed in the diagnosis model, providing information regarding effects of engine parameters in the combustion duration, being those parameter: spark timing, engine speed, load, and air–fuel ratio. Besides quantitative information, some conclusions with respect to the combustion behaviour were drawn, supporting trends well known in the literature as well as new insights.

The CA50 parameter presented a good correlation to the MBT as indicated in the literature. However, the position for CA50 was not fixed for all engine conditions, contradicting the “thumb rule”, which states that the MBT is achieved whenever it is fixed at 10 °CA. New

fuels present different profiles for flame propagation, thus leading to different conditions for optimum operation, and insights from the literature are not valid anymore as they were drawn from gasoline fuelled engines. Expectedly, combustion was chiefly influenced by engine speed, as combustion is strongly dependent on turbulence, which intensity is directly proportional to the engine speed. spark timing was observed to increase combustion time when it was delayed. However, the development of the combustion can be accelerated with a delayed spark timing owing to a higher temperature at prior to ignition, although the combustion is longer on the overall for this case. Leaner mixtures presented a slight increase in the combustion duration, although the stochastic nature of the combustion surpassed the effect of leaner mixture in some conditions. The ignition delay was roughly constant in means of time. Similar trends were found when comparing ethanol and gasohol. Ethanol presented both faster development of flame and overall combustion duration compared to those of gasohol, whereas the ignition delay was higher for ethanol, trend explained by the higher heat of vaporisation, which leads to a colder charge at the instant of spark. Wiebe exponent exhibited lower values for ethanol owing to the faster flame development phase.

For the predictive model, a model for combustion duration was implemented considering engine speed as variable, with a constant ignition time. The simulation model is capable of predicting knock onset and performance of an engine. Comparisons with experimental data have indicated the accuracy of the model, by calculating an in–cylinder pressure profile that presented a deviation less than 2% from the profile measured in bench. Although the model has been used for predicting performance of a VSE engine, the same algorithm has been used for other application, by combining other modules to the algorithm, such as: pollutant formation, gas flow through manifolds, water injection, and exergetic analysis. This type of simulation model presents a good reliability as it has been used for 40 years. Although the model is well–known in the literature, it was minutely detailed in this work in order to provide an useful tool for other researchers.

Thereafter, a simple approach for simulation based calibration was implemented. The optimum combination of compression ratio and spark timing were found in parallel to the simulations for all combinations of % MAP, cubic capacity and engine speed. For the optimisation, the direct search technique on all combinations was only possible because of the assumption of a fixed timing for the valves and a stoichiometric air–fuel for all conditions. More degrees of freedom for the optimisation would prohibit the use of the technique. Further investigations and combinations of more parameters in the engine analysis would require Design of Experiments (DoE) techniques coupled with more robust methods for optimisation. A very straightforward strategy for calibration was used, considering that the objective is maximising efficiency.

Results were obtained for the VSE, VCR and FCR engines. The first remark is

related to the position of the optimum efficiency. Results agreed with the literature, indicating that a high compression ratio induces knock onset more easily. Consequently, there is a trade off since it is necessary to delay spark timing for high compression ratio, decreasing efficiency. However, an improvement for efficiency was observed by operating the engine at a knock limited condition and medium compression ratio levels, in which the spark timing is not significantly delayed. In those conditions, the engine presented higher efficiency than those in which the spark timing was set to MBT and the compression ratio was reduced. These results indicated that compression ratio plays a more important role on engine efficiency than spark timing when assuming that combustion duration is only dependent of engine speed.

The consequences of assuming engine speed as the only parameter affecting combustion were observed on the calibration maps obtained for the FCR engine. spark timing exhibited no influence from load, except at low engine speeds conditions. For other conditions, MBT was achieved, being only influenced by engine speed.

For the VCR engine, compression ratio was kept in the maximum value for high speed, being decreased in low engine speed and high loads. Owing to the increase in compression ratio, load presented more influence on spark timing for the VCR engine, which was delayed for high loads conditions.

The use of a stoichiometric mixture affected the efficiency maps of both VCR and FCR engines. The highest efficiency was observed for full load conditions. In commercial engines, the maximum efficiency is observed for partial loads since the engine operates with a rich air–fuel ratio for full load conditions, in order to generate a higher level of torque.

Expectedly, the VCR engine presented a higher efficiency than that of FCR engine. Furthermore, the highest efficiency level for VCR was found for higher speeds that those for the FCR engine. This result corroborates with the hypothesis that the efficiency of the FCR engine is limited by the critical conditions for knock, which occurs only at low engine speed.

After the VCR and the FCR engines, the VSE engine was simulated. Results reinforced the meaning of the parameter imep. The mean pressure can be interpreted as a “power density” of the engine. Imep was observed to vary linearly with the % of maximum MAP, whereas it was almost independent on cubic capacity. Therefore, imep is not a convenient parameter for the VSE engine analysis, as it is possible to reduce load without changing imep.

Cubic capacity was proved as a good alternative for controlling load. One could assume that the adjustment of cubic capacity is always preferable to throttle actuation. However, this hypothesis was not assumed in this work because of the hypothesis in which the combined actuation on throttle and stroke length could lead to a higher efficiency. There are infinite combinations of cubic capacity and % of maximum MAP that lead to the same level of torque. Hence the proposal of calibration for the VSE was to search for the maximum efficiency along a constant torque line, providing the optimum combination of cubic capacity and % of maximum

MAP.

The effect of cubic capacity on load was observed to be more evident for low engine speed. One hypothesis behind this trend is that the intake process is harmed for long strokes and high engine speed. This hypothesis was verified by comparing the obtained values of volumetric efficiency for different engine speeds. However, the maximum cubic capacity always presented higher volumetric efficiency for a constant level of load. Compression ratio has to be reduced for low cubic capacity at low engine speed because the higher % of maximum MAP lead to a higher in–cylinder pressure, inducing knock. The same trend was observed for spark timing retarding.

By analysing efficiency for constant levels of torque, the minimum cubic capacity lead to the highest efficiency for most cases. For medium and high engine speed, knock onset was not critical and the compression ratio was consequently kept at higher levels, even for higher in–cylinder pressure, favouring the actuation on stroke length instead of throttle opening. However, whenever the knock onset was critical, the reduction of pressure in the cylinder allowed a higher compression ratio than that required for higher levels of pressure. Consequently, a trade–off between cubic capacity and % of maximum MAP was observed for low engine speed.

After selecting the optimum combinations, the base calibration for cubic capacity was found to present different trends for different engine speeds, corroborating the hypothesis that the combined actuation on stroke length and throttle position yields to the maximum efficiency.

The base spark timing was always knock limited for low engine speed. For medium and high engine speed, the base spark timing was only knock limited during the actuation on cubic capacity. After cubic capacity reaches its minimum condition, an inflection was observed for the spark timing. As % of maximum MAP was decreased, spark timing was set towards the MBT position.

Compression ratio was kept at its maximum value in the entire range of torque for high engine speed. For medium engine speed, compression ratio was reduced with the reduction of cubic capacity. For the condition of minimum cubic capacity, an inflection was also observed for compression ratio, which increased towards its maximum values as the % of maximum MAP was decreased. The compression ratio is slightly increased as load is decreased until the value of minimum cubic capacity for low engine speeds condition, in which the stroke length and throttle position are both adjusted simultaneously. For the conditions of minimum capacity, the base calibration for compression ratio at low engine speed followed the same trend of the base calibration for compression ratio at other levels of engine speed.

Distinctly from the VCR and the FCR engines, the maximum efficiency for the VSE engine occurred at high engine speed and partial loads, proving the effectiveness of controlling

cubic capacity for load control. Moreover, the efficiency was approximately constant for a great part of the engine map.

A comparison between the technologies VSE, VCR and FCR engines indicated that both VCR and VSE engines present a significant improvement on efficiency owing to the compression ratio control, approximatelly increasing efficiency from 35% to 38% for full load condition between 2500 and 3500 rpm. For the condition of maximum load, the VSE and the VCR engines were expectedly equivalent, as both engines were operating at the same condition, *i.e.*, wide open throttle and maximum cubic capacity. The VSE engine presented higher efficiency for partial load conditions, being this advantage more evident for higher engine speed. More advantages of controlling compression ratio are expected to become evident when operating the engine with multiple fuel, such as more stable operation at idle and cold start conditions for liquid fuels with high enthalpy of vaporisation and high efficiency for fuels with high octane number.

Although compression ratio influences directly on efficiency, maximum torque was also improved owing to compression ratio increasing. A comparison of maximum torque between FCR and VSE engines indicates that the latter can produce up to 15% more torque compared to the earlier.

A final comparison indicates the gains in substituting the FCR engine by the VSE engine. At high loads, the gain is more evident only for higher engine speed. However, the efficiency improvement is significant for all conditions of engine speed at partial loads. Results indicate that it is possible an improvement of 20% in efficiency for the VSE engine compared to that of the FCR engine. The proposed engine was proven to be competitive to others technologies, as the gain in efficiency was equivalent to other technological solutions such as: skipping cycle strategy, VVT, and EGR. To obtain a better performance, the mechanism can be redesigned in order to allow a wider range of cubic capacity, reducing the need for throttling.

In conclusion, the VSE engine does have the capacity for improving engine efficiency, as indicated by simulations. More comprehensive investigations are required as some simplified hypotheses were assumed to perform the simulations owing to the lack of information regarding the effects of compression ratio and bore–stroke ratio in combustion behaviour. Next steps of the investigation on the VSE engine should focus on the technological aspects of the implementation of the solution in the market, as well as conduct evaluation on emissions and other application of the mechanism, which is further explained in the following section.

7.1 Suggestions for future work

The present study has indicated advantages of implementing the proposed mechanism for spark–ignition engines. This work focused on the application of such engines in

the transportation sector. Therefore, the first suggestion is the expansion of the analysis to other application of internal combustion engines. This technology could also be implemented in compression ignition engines, being used in both transportation and energy sectors, each presenting its own challenges due to the unique characteristics found in each type of operation. Moreover, the transportation sector could be divided in heavy duty vehicles and trains.

Other fuels and blends could be used in the VSE. The adjustment on compression ratio provides to the engine the necessary flexibility to operate with several types of different fuels and blends. Therefore, investigating other types of fuels for a VSE engine will indicate the feasibility of implementing the technology in flexfuel, stationary, and CI engines.

A more specific suggestion for future work include the comparison of the technology with its competitors. Many technologies also propose the load control by avoiding losses originated from throttling. A VCR engine with VVT technology can control the load by combining different compression and expansion ratios. A comparison can present the technical and the consequences of implementing each VSE or VVT. In order to obtain more information on the gas exchange processes, a second law analysis is suggested as the most suitable for this comparison.

This study was carried out by keeping the air–fuel mixture at the stoichiometric condition. Future work will comprehend also rich mixtures, condition used in high loads or transient conditions, and also lean mixtures, which have been avoided so far due to NOx formation. However, with improvements in the catalyst system, lean mixture operation has been explored for low loads conditions, strategy that could be adopted together with the VSE.

More analyses could be performed on the combination of technologies. The VSE engine can be implemented with turbocharging, direct injection and VVT technologies. Although it is expected the increase in costs for producing a complex engine, the improvement in efficiency can compensate this increase and only a strict analysis on performance could indicate whether a combination of technologies is feasible.

An improvement on this study can be performed by optimising the valve timing taking into account the phase shift on the BDC in order to improve volumetric efficiency for each condition of cubic capacity.

About the investigations on the VSE implementation for SI engines, experimental experiments are suggested. The construction of a prototype will first indicate the effects of compression ratio on combustion development. Data for those effects are missing since there are only few studies on the literature regarding effects of compression ratio, which provide the evaluation of effects of varying compression ratio for limited conditions.

The unfavourable argument against this technology can be the increase in complexity and size of the engine. However, the current configuration analysed in this study is not expected to be the final configuration. More studies regarding the mechanism construction are

suggested in order to perform the cubic capacity and compression ratio by using less moving parts, or by constructing a more compact mechanism whilst obtaining a larger range for cubic capacity. One example is found in FERREIRA *et al.* (2017). Additionally, the construction and tests of a prototype will indicate the technological issues regarding the commercial production, *e.g.*, the modifications in the production lines, which will require further investigations.

Secondly, the prototype can indicate the gains in adjusting cubic capacity against the throttle operation. It is predicted that even for a fixed compression ratio it will be possible to verify an improvement in efficiency. Then, a test comparing the operation for low compression ratio and optimum spark timing against the operation with high compression ratio with a knock limited spark timing can validate the trends found in the simulation performed in this study.

Suggestions regarding the mechanism are given so far. Other suggestions are provided regarding the tools developed in this work. The focus of this thesis is the operation of the VSE engine. Details on other features developed on the simulation algorithms by the research group can be found: turbocharging simulation (MATTOS, 2018), water injection (BERNAL and FERREIRA, 2019), pollutant formation (LIMA, 2017) and characteristics method for manifolds phenomena (GOMES, 2019). Exergetic analysis was herein mentioned (see section 5.6). Future work includes the expansion of the exergetic analysis to the gas exchange processes, the implementation of a multi–dimensional simulation for specific phenomena such as fuel vaporisation for direct injection application and soot formation, and the structuring of the algorithm in a code oriented for objects, unifying all of the modules and creating an interface for users. A new model for knock onset prediction can be developed by calibrating the knock integral method with results obtained from chemical kinetics evaluation. In this approach, the autoignition delay is calculated based on the reaction involved in the combustion of a specific fuel for each condition of stoichiometry, pressure, and temperature. Then, the term for autoignition delay used in the knock integral method is adjusted with the obtained results.

The model based calibration algorithm can be improved by including pollutant reduction as objective and different calibration strategies, such as fuel enrichment at full load condition, and boundary conditions aiming safety and engine durability such as maximum temperature in the exhaust and maximum pressure peak. Thus, the pollutant formation can be included in the simulations. However, the implementation of such algorithm can induce a long processing time. Therefore, other techniques should be implemented, such as Design of Experiments for the simulations and other strategies for optimisation. For extreme cases of combining several technologies, creating a wide range of parameters included in the optimisation process, stochastic methods are suggested, such as neural network and other artificial intelligence schemes.

Bibliography

ABBASZADEHMOSAYEBI, G. and GANIPPA, L. Characterising wiebe equation for heat release analysis based on combustion burn factor (ci). **Fuel**, 119:301–307, 2014.

ADAMS, W. H., HINRICHS, H. G., PISCHINGER, F. F., ADAMIS, P., SCHUMACHER, V., and WALZER, P. Analysis of the combustion process of a spark ignition engine with a variable compression ratio. **SAE Technical Paper No. 870610**, 1987.

AKERLIND, I. B., BASTANI, P., BERRY, I., BHATT, K., CHAO, A., E., CHOW, KARPLUS, V., KEITH, D., KHUSID, M., NISHIMURA, E., and ZOEPF, S. On the road toward 2050. Technical report, MIT, 2015.

ALEGRE, J. A. A. V. **Simulação de processos e Análise Exergética do Motor de Ciclo Diesel**. PhD thesis, Faculdade de Engenharia Mecânica, Unicamp, 1993.

ALEIFERIS, P. G. and BEHRINGER, M. K. Flame front analysis of ethanol, butanol, iso-octane and gasoline in a spark-ignition engine using laser tomography and integral length scale measurements. **Combustion and Flame**, 162(12):4533–4552, 2015.

ALEIFERIS, P. G., SERRAS-PEREIRA, J., and RICHARDSON, D. Characterisation of flame development with ethanol, butanol, iso-octane, gasoline and methane in a direct-injection spark-ignition engine. **Fuel**, 109:256–278, 2013.

ALEIFERIS, P. G., BEHRINGER, M. K., OUDENIJEWEME, D., and FREELAND, P. Insights into stoichiometric and lean combustion phenomena of gasoline–butanol, gasoline–ethanol, iso-octane–butanol, and iso-octane–ethanol blends in an optical spark-ignition engine. **Combustion Science and Technology**, 189(6):1013–1060, 2017.

ALLA, G. H. A. Computer simulation of a four stroke spark ignition engine. **Energy conversion and Management**, 43(8):1043–1061, 2002.

ALSTERFALK, M., FILIPI, Z. S., and ASSANIS, N. The potential of the variable stroke spark-ignition engine. **SAE Technical Paper No. 970067**, 1997.

ANNAND, W. J. D. Heat transfer in the cylinders of reciprocating internal combustion engines. **Proceedings of the Institution of Mechanical Engineers**, 177(1):973–996, 1963.

ARSIE, I., PIANESE, C., and RIZZO, G. Models for the prediction of performance and emissions in a spark ignition engine-a sequentially structured approach. **SAE transactions No. 980779**, pages 1065–1079, 1998.

ASSANIS, D. N., FILIPI, Z., FIVELAND, S. B., and SYRIMIS, M. A methodology for cycle-by-cycle transient heat release analysis in a turbocharged direct injection diesel engine. **SAE Technical Paper Nr 2000-01-1185**, 2000.

ASTHANA, S., BANSAL, S., JAGGI, S., and KUMAR, N. A comparative study of recent advancements in the field of variable compression ratio engine technology. **SAE Technical Paper No. 2016-01-0669**, 2016.

ATASHKARI, K., NARIMAN-ZADEH, N., GÖLCÜ, M., KHALKHALI, A., and JAMALI, A. J. E. C. Modelling and multi-objective optimization of a variable valve-timing spark-ignition engine using polynomial neural networks and evolutionary algorithms. **Energy Conversion and Management**, 48(3):1029–1041, 2007.

ATKINSON, C. and MOTT, G. Dynamic model-based calibration optimization: An introduction and application to diesel engines. **SAE Technical Paper No. 2005-01-0026**, 2005.

AUGOYE, A. and ALEIFERIS, P. Characterization of flame development with hydrous and anhydrous ethanol fuels in a spark-ignition engine with direct injection and port injection systems. **SAE Technical Paper Nr 2014-01-2623**, 2014.

BAE, C. and KIM, J. Alternative fuels for internal combustion engines. **Proceedings of the Combustion Institute**, 36(3):3389–3413, 2017.

BALAT, M. and BALAT, H. Recent trends in global production and utilization of bio-ethanol fuel. **Applied energy**, 86(11):2273–2282, 2009.

BALL, J. K., RAINE, R. R., and STONE, C. R. Combustion analysis and cycle-by-cycle variations in spark ignition engine combustion part 1: an evaluation of combustion analysis routines by reference to model data. **Proceedings of the Institution of Mechanical Engineers, Part D: Journal of Automobile Engineering**, 212(5):381–399, 1998.

BARROS, J. E. M. **Estudo de Motores de Combustão Interna Aplicando Análise Orientada a Objetos**. PhD thesis, Escola de Engenharia, UFMG, 2003.

BAYRAKTAR, H. Mathematical modeling of spark-ignition engine cycles. **Energy sources**, 25(7):651–666, 2003.

BECCARI, S., PIPITONE, E., and GENCHI, G. Knock onset prediction of propane, gasoline and their mixtures in spark ignition engines. **Journal of the Energy Institute**, 89(1):101–114, 2016.

BENSON, R. S. The solution of non-steady flow equations by the method of characteristics. **The thermodynamics and gas dynamics of internal combustion engines**, 1:73–97, 1982.

BENSON, R. S., ANNAND, W. J. D., and BARUAH, P. C. A simulation model including intake and exhaust systems for a single cylinder four-stroke cycle spark ignition engine. **International Journal of Mechanical Sciences**, 17(2):97–124, 1975.

BERNAL, J. L. L. and FERREIRA, J. V. Model of water injection process during closed phase of spark ignition engine. **Energy**, 174:1121–1132, 2019.

BEROFF, J. Moteur à combustion interne, à rapport volumétrique et à cylindrée variables, 2000. Patent European Patent Office No. EP 1 143 127.

BIERMANN, A. E. Variable stroke piston engines, 1955. Patent USPTO No. US 2.909.163.

BLAIR, G. P. **Design and simulation of four-stroke engines**. SAE International, 1999.

BLUMBERG, P. N., LAVOIE, G. A., and TABACZYNKKI, R. J. Phenomenological models for reciprocating internal combustion engines. **Progress in Energy and Combustion Science**, 5(2):123–167, 1979.

BOGGS, D. L. Variable capacity reciprocating engine, 2001. Patent USPTO No. US 6.289.857.

BONATESTA, F., WATERS, B., and SHAYLER, P. J. Burn angles and form factors for wiebe function fits to mass fraction burned curves of a spark ignition engine with variable valve timing. **International Journal of Engine Research**, 11(2):177–186, 2010.

BORETTI, A., MASUDI, H., and SCALZO, J. Alternative crankshaft mechanisms and kinetic energy recovery systems for improved fuel economy of light duty vehicles. **SAE Technical Paper No. 2011-01-2191**, 2011.

BORMAN, G. and NISHIWAKI, K. Internal-combustion engine heat transfer. **Progress in energy and combustion science**, 13(1):1–46, 1987.

BOUBLÍK, T., FRIED, V., and HáLA, E. **The vapour pressures of pure substances**. Elsevier Science Pub. Co., Inc., New York, NY, 1984.

BOZZA, F., DE BELLIS, V., and TEODOSIO, L. A numerical procedure for the calibration of a turbocharged spark-ignition variable valve actuation engine at part load. **International Journal of Engine Research**, 18(8):810–823, 2017.

BRADLEY, D., MORLEY, C., and WALMSLEY, H. L. Relevance of research and motor octane numbers to the prediction of engine autoignition. **SAE Technical Paper No. 2004-01-1970**, 2004.

BRINKMAN, M. L. J., DA CUNHA, M. P., HEIJNEN, S., WICKE, B., GUILHOTO, J. J. M., WALTER, A., FAAIJI, A. P. C., and VAN DER HILST, F. Interregional assessment of socio-economic effects of sugarcane ethanol production in brazil. **Renewable and sustainable energy reviews**, 88:347–362, 2018.

BRUNT, M. F. J. and EMTAGE, A. L. Evaluation of burn rate routines and analysis errors. **SAE Technical Paper Nr 970037**, 1997.

BRUNT, M. F. J., RAI, H., and EMTAGE, A. L. The calculation of heat release energy from engine cylinder pressure data. **SAE Technical Paper Nr 981052**, 1998.

BUENO, A. V., ALEGRE, J. A. A. V., and MILANEZ, L. F. Exergy based diagnosis of in-cylinder diesel engine processes. **SAE paper Nr 2004-01-3258**, page 3258, 2004.

BURK, R., JACQUELIN, F., and WAKEMAN, R. A contribution to predictive engine calibration based on vehicle drive cycle performance. **SAE Technical Paper No. 2003-01-0225**, 2003.

BURLUKA, A. A., LIU, K., SHEPPARD, C. G. W., SMALLBONE, A. J., and WOOLLEY, R. The influence of simulated residual and no concentrations on knock onset for prfs and gasolines. **SAE transactions No. 2004-01-2998**, pages 1873–1889, 2004.

BUTLER, T. D., CLOUTMAN, L. D., DUKOWICZ, J. K., and RAMSHAW, J. D. Multidimensional numerical simulation of reactive flow in internal combustion engines. **Progress in Energy and Combustion Science**, 7(4):293–315, 1981.

CARVALHO, L. O., MELO, T. C. C., and CRUZ NETO, R. M A. Investigation on the fuel and engine parameters that affect the half mass fraction burned (ca50) optimum crank angle. **SAE Technical Paper Nr 2012-36-0498**, 2012.

CASSIANI, M. B., BITTENCOURT, M. L., GALLI, L. A., and VILLALVA, S. G. Variable compression ratio engines. **SAE Technical Paper No. 2009-36-0245**, 2009.

CASTAÑEDA, E. H., ROMERO, C. A., and QUINTERO, H. F. Synthesis of a variable stroke slider crank mechanism for a reciprocating internal combustion engine. **Contemporary Engineering Sciences**, 11(104), 2018.

CATANIA, A. E., MISUL, D., MITTICA, A., and SPESSA, E. A refined two-zone heat release model for combustion analysis in si engines. **JSME International Journal Series B Fluids and Thermal Engineering**, 46(1):75–85, 2003.

CHAKRABORTY, N., MASTORAKOS, E., and CANT, R. S. Effects of turbulence on spark ignition in inhomogeneous mixtures: a direct numerical simulation (dns) study. **Combustion science and technology**, 179(1-2):293–317, 2007.

CHEN, L., LI, T., YIN, T., and ZHENG, B. A predictive model for knock onset in spark-ignition engines with cooled egr. **Energy Conversion and management**, 87:946–955, 2014.

CHEUNG, H. M. and HEYWOOD, J. B. Evaluation of a one-zone burn-rate analysis procedure using production si engine pressure data. **SAE Technical Paper Nr 932749**, 1993.

CHO, H. M. and HE, B. Q. Spark ignition natural gas engines – a review. **Energy conversion and management**, 48(2):608–618, 2007.

COONEY, C. P., WORM, J. J., and NABER, J. D. Combustion characterization in an internal combustion engine with ethanol- gasoline blended fuels varying compression ratios and ignition timing. **Energy & Fuels**, 23(5):2319–2324, 2009.

COSTA, R. C. and SODRÉ, J. R. Hydrous ethanol vs. gasoline–ethanol blend: Engine performance and emissions. **Fuel**, 89(2):287–293, 2010.

COSTA, R. C. and SODRÉ, J. R. Compression ratio effects on an ethanol/gasoline fuelled engine performance. **Applied Thermal Engineering**, 31(2-3):278–283, 2011.

CRISE, G. W. Variable displacement internal combustion engine having automatic piston stroke control, 1978. Patent USPTO No. US 4.131.094.

CRUZ NETO, R. M. A. **Simulação computacional e análise exergética de um motor de motocicleta de baixa cilindrada com misturas de gasolina e etanol**. PhD thesis, COPPE, UFRJ, 2013.

D'ADAMO, A., BREDA, S., FONTANESI, S., IRIMESCU, A., MEROLA, S. S., and TORNATORE, C. A rans knock model to predict the statistical occurrence of engine knock. **Applied energy**, 191:251–263, 2017.

DAGAUT, P. and ALI, K. H. Kinetics of oxidation of a lpg blend mixture in a jsr: experimental and modeling study. **Fuel**, 82(5):475–480, 2003.

D'AMBROSIO, S., FERRARI, A., and GALLEANI, L. In-cylinder pressure-based direct techniques and time frequency analysis for combustion diagnostics in ic engines. **Energy Conversion and Management**, 99:299–312, 2015.

DAMJI, N., DRESSER, D., BELLAVOINE, J., and SWAMINATHAN, M. Automated model-based calibration for drivability using a virtual engine test cell. **SAE Technical Paper No. 2015-01-1628**, 2015.

DANIELS, C. F. The comparison of mass fraction burned obtained from the cylinder pressure signal and spark plug ion signal. **SAE Technical Paper Nr 980140**, 1998.

DE BELLIS, V., BOZZA, F., SIANO, D., and GIMELLI, A. Fuel consumption optimization and noise reduction in a spark-ignition turbocharged vva engine. **SAE International Journal of Engines No. 2013-01-1625**, 6(2):1262–1274, 2013.

DEPCIK, C., JACOBS, T., HAGENA, J., and ASSANIS, D. Instructional use of a single-zone, premixed charge, spark-ignition engine heat release simulation. **International Journal of Mechanical Engineering Education**, 35(1):1–31, 2007.

D'ERRICO, G., CERRI, T., and PERTUSI, G. Multi-objective optimization of internal combustion engine by means of 1d fluid-dynamic models. **Applied Energy**, 88(3):767–777, 2011.

DOGRU, B., LOT, R., and DINESH, K. K. J. R. Valve timing optimisation of a spark ignition engine with skip cycle strategy. **Energy conversion and management**, 173:95–112, 2018.

DORIĆ, J. Ž. and KLINAR, I. J. Efficiency of a new internal combustion engine concept with variable piston motion. **Thermal Science**, 18(1), 2014.

DOUAUD, A. M. and EYZAT, P. Four-octane-number method for predicting the anti-knock behavior of fuels and engines. **SAE Technical Paper No. 780080**, 1978.

DRANGEL, H., OLOFSSON, E., and REINMANN, R. The variable compression (svc) and the combustion control (scc)-two ways to improve fuel economy and still comply with world-wide emission requirements. **SAE Technical paper No. 2002-01-0996**, 2002.

EISAZADEH-FAR, K., MOGHADDAS, A., AL-MULKI, J., and METGHALCHI, H. Laminar burning speeds of ethanol/air/diluent mixtures. **Proceedings of the Combustion Institute**, 33(1):1021–1027, 2011a.

EISAZADEH-FAR, K., MOGHADDAS, A., AL-MULKI, J., and METGHALCHI, H. Laminar burning speeds of ethanol/air/diluent mixtures. **Proceedings of the Combustion Institute**, 33(1):1021–1027, 2011b.

EL-FAROUG, M. O., YAN, F., LUO, M., and TURKSON, R. F. Spark ignition engine combustion, performance and emission products from hydrous ethanol and its blends with gasoline. **Energies**, 9(12):984, 2016.

ELMQVIST, C., LINDSTRÖM, F., ÅNGSTRÖM, H. E., GRANDIN, B., and KALGHATKI, G. Optimizing engine concepts by using a simple model for knock prediction. **SAE Technical Paper No. 2003-01-3123**, 2003.

FAN, L. and REITZ, R. D. Development of an ignition and combustion model for spark-ignition engines. **SAE transactions No. 2000-01-2809**, pages 1977–1989, 2000.

FANDAKOV, A., GRILL, M., BARGENDE, M., and KULZER, A. C. A two-stage knock model for the development of future si engine concepts. **SAE Technical Paper No. 2018-01-0855**, 2018.

FERGUSON, C. R. and KIRKPATRICK, A. T. **Internal combustion engines: applied thermosciences**. John Wiley & Sons, 2015.

FERREIRA, J. V. and RUFINO, C. H. Motor de combustão interna com mecanismo que permite controle instantâneo sobre a taxa de compressão e a capacidade volumétrica de cada cilindro individualmente e seus usos, 2014. Patent INPI BR 10 2014 026240 7.

FERREIRA, J. V., ZAMBON, G., and RUFINO, C. H. Motor de combustão interna, 2017. Patent INPI BR 10 2017 027318 0.

FINOL, C. A. and ROBINSON, K. Thermal modelling of modern engines: a review of empirical correlations to estimate the in-cylinder heat transfer coefficient. **Proceedings of the institution of mechanical engineers, part D: journal of automobile engineering**, 220(12): 1765–1781, 2006.

FREUNDENSTEIN, F. and MAKI, E. R. Variable displacement piston engine, 1981. Patent USPTO No. US 4.270.495.

FUIORESCU, D. and RADU, B. A proposed relation for knock auto-ignition induction period evaluation in a lpg fueled si engine. **SAE Technical Paper No. 2010-01-1455**, 2010.

FUJIMOTO, H. and MOTEKI, K. Internal combustion engine with variable compression ratio mechanism, 2003. Patent USPTO No. US 6.510.821.

FUKUI, T., NAKAGAMI, T., ENDO, H., KATSUMOTO, T., and DANNO, Y. Mitsubishi orion-md - a new variable displacement engine. **SAE Technical Paper No. 831007**, 1983.

GALLO, W. L. R. Avaliação de coeficientes de película para estudos de transmissão de calor instantânea em motores de combustão interna. **Anais do II Encontro Nacional de Ciências Térmicas**, pages 57–60, 1988.

GALLO, W. L. R. **Análise exergética de motores a gasolina e a álcool**. PhD thesis, Faculdade de Engenharia Mecânica, Unicamp, 1990.

GT-Suite Version 7.1 Manual. Gamma Technologies, 2004.

GATOWSKI, J. A., BALLES, E. N., CHUN, K. M., NELSON, F. E., EKCHIAN, J. A., and HEYWOOD, J. B. Heat release analysis of engine pressure data. **SAE Technical Paper Nr 841359**, 1984.

GHOJEL, J. I. Review of the development and applications of the wiebe function: a tribute to the contribution of ivan wiebe to engine research. **International Journal of Engine Research**, 11(4):297–312, 2010.

GOMES, F. A. F. Numerical simulation of unsteady flow inside single-cylinder engine's intake and exhaust manifolds. Master thesis, Faculdade de Engenharia Mecânica, Unicamp, 2019.

GONZALEZ, L. M. Variable stroke mechanism for internal combustion engine, 1999. Patent USPTO No. US 5.927.236.

GRASREINER, S., NEUMANN, J., WENSING, M., and HASSE, C. Model-based virtual engine calibration with the help of phenomenological methods for spark-ignited engines. **Applied Thermal Engineering**, 121:190–199, 2017.

GRIFFITHS, J. F. Reduced kinetic models and their application to practical combustion systems. **Progress in energy and combustion science**, 21(1):25–107, 1995.

GUERRIER, M. and CAWSEY, P. The development of model based methodologies for gasoline ic engine calibration. **SAE Technical paper No. 2004-01-1466**, 2004.

GUEZENNEC, Y. G. and HAMAMA, W. Two-zone heat release analysis of combustion data and calibration of heat transfer correlation in an ic engine. **SAE Technical Paper Nr 1999-01-0218**, 1999.

GÜLDER, Ö. L. Burning velocities of ethanol-isooctane blends. **Combustion and flame**, 56 (3):261–268, 1984.

HALSTEAD, M. P., KIRSCH, L. J., PROTHERO, A., and QUINN, C. P. A mathematical model for hydrocarbon autoignition at high pressures. **Proceedings of the Royal Society of London. A. Mathematical and Physical Sciences**, 346(1647):515–538, 1975.

HALSTEAD, M. P., KIRSCH, L. J., and QUINN, C. P. The autoignition of hydrocarbon fuels at high temperatures and pressures-fitting of a mathematical model. **Combustion and flame**, 30:45–60, 1977.

HENIGES, W. B. Scotch yoke engine with variable stroke and compression ratio, 1984. Patent USPTO No. US 4.485.768.

HEYWOOD, J. B. **Internal Combustion Engine Fundamentals**. McGraw-Hill, 1988.

HOEPKE, B., JANNSEN, S., KASSERIS, E., and CHENG, W. K. Egr effects on boosted si engine operation and knock integral correlation. **SAE International Journal of Engines No. 2012-01-0707**, 5(2):547–559, 2012.

HOHENBERG, G. F. Advanced approaches for heat transfer calculations. **SAE Technical Paper No. 790825**, 1979.

HOVAH, M. S., TROICKIJ, A., and LEIB, G. V. **Motor vehicle engines**. Mir Publishers, 1971.

JANEWAY, R. N. Quantitative analysis of heat transfer in engines. **SAE Transactions**, pages 371–380, 1938.

JIANG, S. and SMITH, M. H. Geometric parameter design of a multiple-link mechanism for advantageous compression ratio and displacement characteristics. **SAE Technical Paper No. 2014-01-1627**, 2014.

KAMIMOTO, T., MINAGAWA, T., and KOBORI, S. A two-zone model analysis of heat release rate in diesel engines. **SAE Technical Paper Nr 972959**, 1997.

KASTNER, L. J., WILLIAMS, T. J., and WHITE, J. B. Poppet inlet valve characteristics and their influence on the induction process. **Proceedings of the Institution of Mechanical Engineers**, 178(1):955–975, 1963.

KONNOV, A. A., MEUWISSEN, R. J., and DE GOEY, L. P. H. The temperature dependence of the laminar burning velocity of ethanol flames. **Proceedings of the Combustion Institute**, 33(1):1011–1019, 2011.

LANZAFAME, R. Water injection effects in a single-cylinder cfr engine. **SAE Technical Paper No. 1999-01-0568**, 1999.

LANZANOVA, T. D. M., NORA, M. D., and ZHAO, H. Performance and economic analysis of a direct injection spark ignition engine fueled with wet ethanol. **Applied Energy**, 169: 230–239, 2016.

LEI, M., CHUNNIAN, Z., HONG, L., JIE, L., WEN, L., and XIANGHUA, L. Research on modeling and simulation of si engine for afr control application. **Open Automation and Control Systems Journal**, 6:803–812, 2014.

LI, M., ZHANG, Q., LI, G., and SHAO, S. Experimental investigation on performance and heat release analysis of a pilot ignited direct injection natural gas engine. **Energy**, 90:1251–1260, 2015.

LI, Y., KHAJEPOUR, A., and DEVAUD, C. Realization of variable otto-atkinson cycle using variable timing hydraulic actuated valve train for performance and efficiency improvements in unthrottled gasoline engines. **Applied energy**, 222:199–215, 2018.

LIMA, A. J. T. B. Pollutant formation simulation models (co, nox and uhc) for ethanol-fueled engines. Master thesis, Faculdade de Engenharia Mecânica, Unicamp, 2017.

LIU, J., ZHU, G., FU, J., XU, Z., YAO, J., and ZHAN, Z. Quantitative study on in-cylinder combustion and heat release characteristic parameters of gasoline engine based on single variable sweeping tests. **Applied Thermal Engineering**, 117:487–500, 2017.

LIVENGOOD, J. C. and WU, P. C. Correlation of autoignition phenomena in internal combustion engines and rapid compression machines. In **Symposium (International) on Combustion**, volume 5, pages 347–356. Elsevier, 1955.

LOMAX, H., PULLIAM, T. H., and ZINGG, D. W. **Fundamentals of computational fluid dynamics**. Springer Science & Business Media, 2013.

LOPES, A. V. B. **Simulação Fenomenológica de Motores Diesel**. PhD thesis, Faculdade de Engenharia Mecânica, Unicamp, 2014.

LOPES, G. S. and FERREIRA, J. V. Análise termodinâmica, cinemática e dinâmica de um motor com taxa de compressão variável'. **Blucher Engineering Proceedings**, 1(2):275–287, 2014.

MACHADO, G. B. **Metodologias para desenvolvimento de combustíveis e determinação da velocidade de propagação de chama em motores de ignição por centelha**. PhD thesis, Pontifícia Universidade Católica do Rio de Janeiro, 2012.

MACLEAN, H. L. and LAVE, L. B. Evaluating automobile fuel/propulsion system technologies. **Progress in energy and combustion science**, 29(1):1–69, 2003.

MALIKOPOULOS, A. A., ASSANIS, D. N., and PAPALAMBROS, P. Y. Real-time self-learning optimization of diesel engine calibration. **Journal of Engineering for Gas Turbines and Power**, 131(2), 2009.

MATTOS, A. P. **Estudo do desempenho de um motor turbo-alimentado a etanol empregando EGR para redução de emissões de NOx e controle de detonação.** PhD thesis, Faculdade de Engenharia Mecânica, Unicamp, 2018.

MCALLISTER, S., CHEN, J. Y., and FERNANDEZ-PELLO, A. C. **Fundamentals of combustion processes**, volume 302. Springer, 2011.

MEDINA, A., CURTO-RISSO, P. L., HERNÁNDEZ, A. C., GUZMÁN-VARGAS, L., ANGULO-BROWN, F., and SEN, A. K. **Quasi-dimensional simulation of spark ignition engines**. Springer, 2014.

MELO, T. C. C. **Modelagem termodinâmica de um motor do ciclo Otto tipo flex–fuel, funcionando com gasolina, álcool e gás natural**. PhD thesis, COPPE,UFRJ, 2007.

MELO, T. C. C., MACHADO, G. B., DE OLIVEIRA, E. J., BELCHIOR, C. R. P., COLAÇO, M. J., and DE OLIVEIRA, D. G. Different hydrous ethanol-gasoline blends-ftir emissions of a flex-fuel engine and chemical properties of the fuels. **SAE Technical Paper Nr 2011-36-0080**, 2011.

MELO, T. C. C., MACHADO, G. B., BELCHIOR, C. R. P., COLAÇO, M. J., BARROS, J. E. M., DE OLIVEIRA, E. J., and DE OLIVEIRA, D. G. Hydrous ethanol–gasoline blends–combustion and emission investigations on a flex-fuel engine. **Fuel**, 97:796–804, 2012a.

MELO, T. C. C., MACHADO, G. B., CARVALHO, L. O., BELCHIOR, C. R. P., COLAÇO, M. J., BARROS, J. E. M., and PAIVA, C. E. F. In cylinder pressure curve and combustion parameters variability with ethanol addition. **SAE Technical Paper Nr 2012-36-0486**, 2012b.

MILLO, F., PERAZZO, A., and PAUTASSO, E. Optimizing the calibration of a turbocharged gdi engine through numerical simulation and direct optimization. **SAE International Journal of Engines No. 2010-01-0780**, 3(1):556–570, 2010.

MITTAL, M., ZHU, G., and SCHOCK, H. Fast mass-fraction-burned calculation using the net pressure method for real-time applications. **Proceedings of the Institution of Mechanical Engineers, Part D: Journal of Automobile Engineering**, 223(3):389–394, 2009.

MOREL, T. and KERIBAR, R. A model for predicting spatially and time resolved convective heat transfer in bowl-in-piston combustion chambers. **SAE Technical Paper No. 850204**, 1985.

MOTEKI, K., AOYAMA, S., USHIJIMA, K., HIYOSHI, R., TAKEMURA, S., FUKIMOTO, H., and ARAI, T. A study of a variable compression ratio system with a multi-link mechanism. **SAE Technical paper No. 2003-01-0921**, 2003.

MUELLER, R. P., LI, C., and TSAO, K. C. Modeling for mass burning rate and combustion duration in spark ignition engines using gasohol fuels. **SAE Technical Paper Nr 831677**, 1983.

MURALIDHARAN, K. and VASUDEVAN, D. Performance, emission and combustion characteristics of a variable compression ratio engine using methyl esters of waste cooking oil and diesel blends. **Applied energy**, 88(11):3959–3968, 2011.

MYERS, P. The art of choosing a model. **SAE Technical Paper No. 850341**, 1985.

NELSON, C. D. Variable stroke engine, 1985. Patent USPTO No. US 4.517.931.

NISHIWAKI, K., SHIMAMOTO, Y., and MIYAKE, K. Average heat transfer coefficients on a cylinder wall in the intake and exhaust processes of motoring test. **Bulletin of JSME**, 22(174):1796–1809, 1979.

NUNES, P. G. K. **Simulação Termodinâmica para Motores Diesel**. PhD thesis, Faculdade de Engenharia Mecânica, Unicamp, 2017.

OH, S., MIN, K., and SUNWOO, M. Real-time start of a combustion detection algorithm using initial heat release for direct injection diesel engines. **Applied Thermal Engineering**, 89: 332–345, 2015.

ORTIZ-SOTO, E. A., LAVOIE, G. A., MARTZ, J. B., WOOLDRIDGE, M. S., and ASSANIS, D. N. Enhanced heat release analysis for advanced multi-mode combustion engine experiments. **Applied Energy**, 136:465–479, 2014.

PAL, L. J. G. and PAL, L. L. Internal combustion engine variable stroke mechanism, 1990. Patent USPTO No. US 4.938.186.

PATTAKOS, M., SANNIOU-PATTAKOU, V., and PATTAKOS, E. Rack gear variable compression ratio engines, 2012. Patent USPTO No. US 8.220.422.

PAYRI, F., LUJÁN, J. M., MARTÍN, J., and ABBAD, A. Digital signal processing of in-cylinder pressure for combustion diagnosis of internal combustion engines. **Mechanical Systems and Signal Processing**, 24(6):1767–1784, 2010.

PEŠIĆ, R. B., MILOJEVIĆ, S. T., and VEINIVIĆ, S. P. Benefits and challenges of variable compression ratio at diesel engines. **Thermal Science**, 14(4), 2010.

PHILLIPPS, R. A. and ORMAN, P. L. Simulation of combustion in a gasoline engine using a digital computer. In **Cranfield Int. Symp. Series**, volume 8, 1966.

PIERCE, J. Variable stroke mechanism, 1914. Patent USPTO No. US 1.112.832.

POULIOT, H. N., DELAMETER, W. R., and ROBINSON, C. W. A variable displacement spark ignition engine. **SAE Technical Paper No. 770114**, 1977.

RABHI, V., BEROFF, J., and DIONNET, F. Study of a gear-based variable compression ratio engine. **SAE Technical Paper No. 2004-01-2931**, 2004.

RAKOPOULOS, D. C., RAKOPOULOS, C. D., PAPAGIANNAKIS, R. G., and KYRITSIS, D. C. Combustion heat release analysis of ethanol or n-butanol diesel fuel blends in heavy-duty di diesel engine. **Fuel**, 90(5):1855–1867, 2011.

RAMOS, J. I. Comparisons between thermodynamic and one-dimensional combustion models of spark-ignition engines. **Applied mathematical modelling**, 10(6):409–422, 1986.

RAO, V. D. N., IMAI, Y. A., M., ZAITZ, SASHIDHARAN, P., and BARASZU, D. J. Connecting rod for a variable compression ratio engine, 2002. Patent USPTO No. US 6.394.047.

RASK, E. and SELLNAU, M. Simulation-based engine calibration: tools, techniques, and applications. **SAE transactions No. 2004-01-1264**, pages 821–832, 2004.

REITZ, R. D. Directions in internal combustion engine research. **Combustion and Flame**, 1 (160):1–8, 2013.

RICHARD, S., COLIN, O., VERMOREL, O., BENKENIDA, A., ANGELBERGER, C., and VEYNANTE, D. Towards large eddy simulation of combustion in spark ignition engines. **Proceedings of the combustion institute**, 31(2):3059–3066, 2007.

RIES, J. D. Variable-displacement piston-cylinder device, 2010. Patent USPTO No. US 7.779.627.

RIETTI, G. Combustion engine, 1914. Patent USPTO No. US 1.095.675.

ROBERT, A., RICHARD, S., COLIN, O., MARTINEZ, L., and DE FRANCQUEVILLE, L. Les prediction and analysis of knocking combustion in a spark ignition engine. **Proceedings of the Combustion Institute**, 35(3):2941–2948, 2015.

ROBERTS, M. Benefits and challenges of variable compression ratio (vcr). **SAE Technical Paper No. 2003-01-0398**, 2003.

ROMERO, C. A. and CASTAÑEDA, E. J. H. Developing small variable compression ratio engines for teaching purposes in an undergraduate program. **SAE Technical Paper No. 2019-01-0331**, 2019.

ROSSO, P. A., BEARD, J., and BLOUGH, J. R. A variable displacement engine with independently controllable stroke length and compression ratio. **SAE Technical Paper No. 2006-01-0741**, 2006.

RUFINO, C. H. and FERREIRA, J. V. Kinematics of a variable stroke and compression ratio mechanism of an internal combustion engine. **Journal of the Brazilian Society of Mechanical Sciences and Engineering**, 40(9):476, 2018.

RUFINO, C. H., LIMA, A. J. T. B., MATTOS, A. P., ALLAH, F. U. M., BERNAL, J. L. L., FERREIRA, J. V., and GALLO, W. L. R. Exergetic diagnosis of a spark ignition engine fuelled with ethanol. In Wojciech Stanek, Wojciech Kostowski and Gładysz, Paweł, editors, **Proceedings of the 5th International Conference on Contemporary Problems of Thermal Engineering**, pages 1003–1010. Institute of Thermal Technology, sep 2018a. ISBN 978-83-61506-46-1.

RUFINO, C. H., LIMA, A. J. T. B., MATTOS, A. P., ALLAH, F. U. M., FERREIRA, J. V., and GALLO, W. L. R. Effects of combustion products composition models on the exergetic analysis of spark–ignition engine fuelled with ethanol. In Wojciech Stanek, Wojciech Kostowski and Gładysz, Paweł, editors, **Proceedings of the 5th International Conference on Contemporary Problems of Thermal Engineering**, pages 1011–1020. Institute of Thermal Technology, sep 2018b. ISBN 978-83-61506-46-1.

RUFINO, C. H., LIMA, A. J. T. B., MATTOS, A. P., ALLAH, F. U. M., BERNAL, J. L. L., FERREIRA, J. V., and GALLO, W. L. R. Exergetic analysis of a spark ignition engine fuelled with ethanol. **Energy Conversion and Management**, 192:20–29, 2019.

RUTLAND, C. J. Large-eddy simulations for internal combustion engines–a review. **International Journal of Engine Research**, 12(5):421–451, 2011.

SAIKALY, K., ROUSSEAU, S., RAHMOUNI, C., LE CORRE, O., and TRUFFET, L. Safe operating conditions determination for stationary si gas engines. **Fuel Processing Technology**, 89(11):1169–1179, 2008.

SANTOS, D. **Desenvolvimento de um modelo termodinâmico de duas zonas de combustão para a simulação computacional de motores de ignição por centelha**. PhD thesis, Pontifícia Universidade Católica do Paraná, 2009.

SCHIEHLEN, W. and EBERHARD, P. **Technische dynamik**. Springer, 1986.

SCHIFTER, I., DIAZ, L., RODRIGUEZ, R., GÓMEZ, J. P., and GONZALEZ, U. Combustion and emissions behavior for ethanol–gasoline blends in a single cylinder engine. **Fuel**, 90(12): 3586–3592, 2011.

SCHREIBER, M., SAKAK, A. S., LINGENS, A., and GRIFFITHS, J. F. A reduced thermokinetic model for the autoignition of fuels with variable octane ratings. In **Symposium (International) on Combustion**, volume 25, pages 933–940. Elsevier, 1994.

SERRAS-PEREIRA, J., ALEIFERIS, P. G., and RICHARDSON, D. An analysis of the combustion behavior of ethanol, butanol, iso-octane, gasoline, and methane in a direct-injection spark-ignition research engine. **Combustion Science and Technology**, 185(3):484–513, 2013.

SHAIK, A., MOORTHI, N. V., and RUNDRAMOORTHY, R. Variable compression ratio engine: a future power plant for automobiles - an overview. **Proc. IMechE Part D: Automobile Engineering**, 221, 2007.

SHERMAN, R. H. and BLUMBERG, P. N. The influence of induction and exhaust processes on emissions and fuel consumption in the spark ignited engine. **SAE Technical Paper No. 770880**, 1977.

SIEGLA, D. C. and SIEWERT, R. M. The variable stroke engine - problems and promisses. **SAE Technical Paper No. 780700**, 1978.

SIEWERT, R. C. Engine combustion at large bore-to-stroke ratios. **SAE Technical Paper No. 780968**, 1978.

SILEGHEM, L., WALLNER, T., and VERHELST, S. A quasi-dimensional model for si engines fueled with gasoline–alcohol blends: Knock modeling. **Fuel**, 140:217–226, 2015.

SITKEI, G. and RAMANAIAH, G. V. A rational approach for calculation of heat transfer in diesel engines. **SAE Technical Paper No. 720027**, 1972.

SMOLA, A. J. and SCHÖLKOPF, B. A tutorial on support vector regression. **Statistics and computing**, 14(3):199–222, 2004.

SOYLU, S. Prediction of knock limited operating conditions of a natural gas engine. **Energy conversion and management**, 46(1):121–138, 2005.

STEIN, R. A., POLOVINA, D., ROTH, K., FOSTER, M., LYNSKEY, M., WHITING, T., ANDERSON, J. E., SHELBY, M. H., LEONE, T. G., and VAN DER GRIEND, S. Effect of heat of vaporization, chemical octane, and sensitivity on knock limit for ethanol-gasoline blends. **SAE International Journal of Fuels and Lubricants**, 5(2):823–843, 2012.

STEURS, K., BLOMBERG, C., and BOULOUCHOS, K. Formulation of a knock model for ethanol and iso-octane under specific consideration of the thermal boundary layer within the end-gas. **SAE International Journal of Engines No. 2014-01-2607**, 7(4):1752–1772, 2014.

STOECKER, W. F. **Design of thermal systems**. McGraw Hill Book Company, 1980.

STONE, C. R. and GREEN-ARMYTAGE, D. I. Comparison of methods for the calculation of mass fraction burnt from engine pressure-time diagrams. **Proceedings of the Institution of Mechanical Engineers, Part D: Transport Engineering**, 201(1):61–67, 1987.

STONE, R. **Introduction to internal combustion engines**. Springer, 1999.

SUGIYAMA, T., HIYOSHI, R., TAKEMURA, S., and AOYAMA, S. Technology for improving engine performance using variable mechanisms. **SAE Technical Paper No. 2007-01-1290**, 2007.

SYED, I. Z., MUKHERJEE, A., and NABER, J. Numerical simulation of autoignition of gasoline-ethanol/air mixtures under different conditions of pressure, temperature, dilution, and equivalence ratio. **SAE Technical Paper No. 2011-01-0341**, 2011.

SZYBIST, J. P. and SPLITTER, D. Effects of fuel composition on egr dilution tolerance in spark ignited engines. **SAE International Journal of Engines**, 9(2):819–831, 2016.

TAVARES, F., JOHRI, R., and FILIPI, Z. Simulation study of advanced variable displacement engine coupled to power-split hydraulic hybrid powertrain. **Journal of Engineering for Gas Turbines and Power**, 133(12):122803, 2011.

TEODOSIO, L., DE BELLIS, V., BOZZA, F., and TUFANO, D. Numerical study of the potential of a variable compression ratio concept applied to a downsized turbocharged vva spark ignition engine. **SAE Technical Paper No. 2017-24-0015**, 2017a.

TEODOSIO, L., TUFANO, D., and BOZZA, F. Development of a virtual calibration methodology for a downsized si engine by using advanced valve strategies. **Energy Procedia**, 126: 923–930, 2017b.

TOUGRI, I., COLAÇO, M. J., LEIROZ, A. J. K., and MELO, T. C. C. Knocking prediction in internal combustion engines via thermodynamic modeling: preliminary results and comparison with experimental data. **Journal of the Brazilian Society of Mechanical Sciences and Engineering**, 39(1):321–327, 2017.

TRINDADE, W. R. S. and SANTOS, R. G. Review on the characteristics of butanol, its production and use as fuel in internal combustion engines. **Renewable and Sustainable Energy Reviews**, 69:642–651, 2017.

TSUCHIDA, H., HIRAYA, K., TANAKA, D., SHIGEMOTO, S., AOYAMA, S., TOMITA, M., SUGIYAMA, T., and HIYOSHI, R. The effect of a longer stroke on improving fuel economy of a multiple-link vcr engine. **SAE Technical Paper No. 2007-01-4004**, 2007.

VANCOILLIE, J., SILEGHEM, L., and VERHELST, S. Development and validation of a quasi-dimensional model for methanol and ethanol fueled si engines. **Applied energy**, 132: 412–425, 2014.

VAREA, E., MODICA, V., VANDEL, A., and RENOU, B. Measurement of laminar burning velocity and markstein length relative to fresh gases using a new postprocessing procedure: Application to laminar spherical flames for methane, ethanol and isooctane/air mixtures. **Combustion and Flame**, 159(2):577–590, 2012.

VERHELST, S. and SHEPPARD, C. G. W. Multi-zone thermodynamic modelling of spark-ignition engine combustion–an overview. **Energy Conversion and management**, 50(5): 1326–1335, 2009.

VERMOREL, O., RICHARD, S., COLIN, O., ANGELBERGER, C., BENKENIDA, A., and VEYNANTE, D. Towards the understanding of cyclic variability in a spark ignited engine using multi-cycle les. **Combustion and flame**, 156(8):1525–1541, 2009.

VILJOEN, C. L., YATES, A. D. B., SWARTS, A., BALFOUR, G., and MÓLLER, K. An investigation of the ignition delay character of different fuel components and an assessment of various autoignition modelling approaches. **SAE transactions No. 2005-01-2084**, pages 748–764, 2005.

WANG, Z., LIU, H., and REITZ, R. D. Knocking combustion in spark-ignition engines. **Progress in Energy and Combustion Science**, 61:78–112, 2017.

WELSH, H. W. and RILEY, C. T. The variable displacement engine: An advanced concept power plant. **SAE Technical Paper No. 710830**, 1971.

WILDHABER, E. Variable stroke engine, 1951. Patent USPTO No. US 2.539.880.

WILLIAMS, F. A. **Combustion theory**. CRC Press, 1994.

WIRBELEIT, F. G., BINDER, K., and GWINNER, D. Development of pistons with variable compression height for increasing efficiency and specific power output of combustion engines. **SAE Technical Paper No. 900229**, 1990.

WITTEK, K., TIEMANN, C., and PISCHINGER, S. Two-stage variable compression ratio with eccentric piston pin and exploitation of crank forces. **SAE Technical Paper No. 2009-01-1457**, 2009.

WOS, P., BALAWENDER, K., JAKUBOWSKI, M., KUSZEWSKI, H., LEJDA, K., and USTRZYCKI, A. Design of affordable multi-cylinder variable compression ratio (vcr) engine for advanced combustion research purposes. **SAE Technical Paper No. 2012-01-0414**, 2012.

WOSCHNI, G. A universally applicable equation for the instantaneous heat transfer coefficient in the internal combustion engine. Technical report, SAE Technical paper No. 670931, 1967.

WU, H. and KNAPP, R. A. Heat transfer analysis of automotive internal combustion gasoline engines. **Numerical methods in heat transfer**, 1981.

XIAO, B., WANG, S., and PRUCKA, R. G. Virtual combustion phasing target correction in the knock region for model-based control of multi-fuel si engines. **SAE International Journal of Engines No. 2013-01-0307**, 6(1):228–236, 2013.

XIE, F., LI, X., WANG, X., SU, Y., and HONG, W. Research on using egr and ignition timing to control load of a spark–ignition engine fueled with methanol. **Applied Thermal Engineering**, 50(1):1084–1091, 2013.

YAMADA, Y. and SATO, Y. Variable stroke engine, 2004. Patent USPTO No. US 6.814.034.

YAMIN, J. A. A. and DADO, M. H. Performance simulation of a four-stroke engine with variable stroke-length and compression ratio. **Applied energy**, 77(4):447–463, 2004.

YATES, A., BELL, A., and SWARTS, A. Insights relating to the autoignition characteristics of alcohol fuels. **Fuel**, 89(1):83–93, 2010.

YELIANA, Y., COONEY, C., WORM, J., MICHALEK, D., and NABER, J. Wiebe function parameter determination for mass fraction burn calculation in an ethanol-gasoline fuelled si engine. **Journal of KONES**, 15:567–574, 2008.

YELIANA, Y., COONEY, C., WORM, J., MICHALEK, D. J., and NABER, J. D. Estimation of double-wiebe function parameters using least square method for burn durations of ethanol-gasoline blends in spark ignition engine over variable compression ratios and egr levels. **Applied Thermal Engineering**, 31(14):2213–2220, 2011.

YÜKSEK, L., ÖZENER, O., and SANDALCI, T. Cycle-skipping strategies for pumping loss reduction in spark ignition engines: An experimental approach. **Energy conversion and management**, 64:320–327, 2012.

ZABEU, C. B., CAMARGOS, L. C., MARINSEK, L. R., BERTI, R. C. R., NICOLA, R. L., and SERRALVO NETO, R. Influence of injection timing on the engine efficiency and emissions in a si pfi engine using ethanol-gasoline blends with several water content levels. **SAE Technical Paper Nr 2017-36-0147**, 2017.

ZACHARIAS, F. Analytical representation of the thermodynamic properties of combustion gases. **SAE Technical Paper No. 670930**, 1967.

A. Coefficients for specific heat determination

A.1 Molecular weight

Molecular weight are given in Tab. A.1.

Table A.1: Molecular weight of species

Specie	M [kg/kmol]
Nitrogen	28.01
Argon	39.94
Oxygen	32
Carbon dioxide	44.01
Water steam	18
Carbon monoxide	28.01
Hydrogen	2.016
Ethanol	46

A.2 Coefficients for polynomial interpolation

For the ethanol, the polynomial function of 3rd order was fitted only on the first range of temperature since ethanol is considered to be present only in the unburned gases. Coefficients are given in Tab. A.2.

Table A.2: Coefficients for specific heat of ethanol.

Coefficient	Value
a_0	0.0014
a_1	-8.1208e-1
a_2	21.237
a_3	9.2838

The coefficients were used to calculate specific heat at contant pressure as a function of $T/100$. MATTOS (2018) fitted polynomials functions from data provided by NIST thermophysical tables. The temperature range was separated in two ranges of temperature in order to achieve a better precision. Cofficients for the first range are given in Tab. A.3 and those for the second range are given in Tab. A.4.

Table A.3: Coefficients for $300K < T < 1000K$.

Specie	a_0	a_1	a_2	a_3	a_4	a_5	a_6
Nitrogen	27.979	1.5673	-8.0587e-1	1.8732e-1	-1.9484e-2	9.4082e-4	-1.6935e-5
Argon	20.786	-3.3678e-15	0.0	0.0	0.0	0.0	0.0
Oxygen	29.525	1.4506e-1	-5.8615e-1	2.9268e-1	-4.9720e-2	3.7162e-3	-1.0460e-4
Carbon dioxide	19.418	7.6637	-0.65488	2.8209e-2	-4.4603e-4	0.0	0.0
Water steam	34.086	-5.0867e-1	-1.2026e-1	1.3914e-1	-2.5728e-2	2.0144e-3	-5.9005e-5
Carbon monoxide	29.934	-0.69261	0.14397	2.2257e-4	-4.4540e-4	0.0	0.0
Hydrogen	13.576	14.077	-5.2082	1.0129	-1.0924e-1	6.2203e-3	-1.4586e-4

Table A.4: Coefficients for $1000K < T < 3000K$.

Specie	a_0	a_1	a_2	a_3	a_4	a_5	a_6
Nitrogen	21.270	1.9239	-1.0444e-1	3.0703e-3	-4.6826e-5	2.9116e-7	0.0
Argon	20.786	-3.3678e-15	0.0	0.0	0.0	0.0	0.0
Oxygen	21.478	2.9462	-2.5971e-1	1.2996e-2	-3.5703e-4	5.0826e-6	-2.9433e-8
Carbon dioxide	29.042	4.5286	-0.27556	8.9390e-3	-1.4825e-4	9.9035e-7	0.0
Water steam	30.484	0.12508	1.9997e-1	-1.4392e-2	4.5866e-4	-7.1527e-6	4.4391e-8
Carbon monoxide	26.216	0.52016	7.3447e-2	-8.4653e-3	3.5024e-4	-6.6045e-6	4.7523e-8
Hydrogen	33.793	-1.7771	2.375e-1	-1.2592e-2	3.4892e-4	-4.9735e-6	2.889e-8

B. Development of the Predictive model

B.1 Two zone model

There are three unknown varibles in the two zone model: T_u, T_b e P. Volume of each zone is given by the equation of ideal gases, respectively presented for unburned and burned zones in Eqs. B.1 and B.2.

$$V_u = \frac{m_u R_u T_u}{P} \tag{B.1}$$

$$V_b = \frac{m_b R_b T_b}{P} \tag{B.2}$$

The mass of each burned and unburned zones are given by the Wiebe function in Eqs. B.3 and B.4, respectively.

$$m_b = m x_b \tag{B.3}$$

$$m_u = m\left(1 - x_b\right) \tag{B.4}$$

The equations employed in this model in order to solve the unknown variables are:

1. Energy balance on the burned zone, in order to obtain T_b;
2. Energy balance on the unburned zone, in order to obtain T_u;
3. Volume balance, in order to obtain P.

1. Energy balance on the burned zone:

Eq. B.5 is obtained by applying the energy conservation law to the burned gases.

$$\frac{\mathrm{d}U_b}{\mathrm{d}\theta} = \frac{\mathrm{d}H_{comb}}{\mathrm{d}\theta} + \frac{\mathrm{d}Q_b}{\mathrm{d}\theta} - \frac{\mathrm{d}W_b}{\mathrm{d}\theta} + h_u \frac{\mathrm{d}m_b}{\mathrm{d}\theta} \tag{B.5}$$

The energy released by the combustion ir represented by $\frac{\mathrm{d}H_{comb}}{\mathrm{d}\theta}$ and $\frac{\mathrm{d}Q}{\mathrm{d}\theta}$ is the rate of heat transfer whilst $\frac{\mathrm{d}W}{\mathrm{d}\theta}$ is the rate of work.

The terms in Eq. B.5 can be re-writen as:

1. Differential of internal energy $\frac{\mathrm{d}U_b}{\mathrm{d}\theta} = \frac{\mathrm{d}\left(m_b c_{v,b} T_b\right)}{\mathrm{d}\theta}$;
2. Rate of work $\frac{\mathrm{d}W_b}{\mathrm{d}\theta} = P\frac{\mathrm{d}V_b}{\mathrm{d}\theta}$;
3. Enthalpy of mass crossing boundaries: $h_u = c_{p,u}T_u$.

Being the rate of heat transfer given by Eq. B.6.

$$\frac{\mathrm{d}Q}{\mathrm{d}\theta} = \frac{\partial t}{\partial \theta}\frac{\mathrm{d}Q}{\mathrm{d}t} = \frac{1}{\omega}\frac{\mathrm{d}Q}{\mathrm{d}t} = -\frac{h^{HT}A\left(T - T_w\right)}{\omega} \tag{B.6}$$

The angular velocity of the engine is represented by ω, h^{HT} is the coefficient of heat transfer, A is the area of the zone and T_w is the temperature of cylinder walls.

The energy released by combustion can be calculated as indicated in Eq. B.7, wherein x_b is the mass fraction burn, calculated by Wiebe function. The term h_{comb} represents the enthalpy of combustion. The efficiency of combustion is given by η_{comb} and the amount of fuel trapped in the cylinder is given by m_{fuel}.

$$\frac{\mathrm{d}H_{comb}}{\mathrm{d}\theta} = \eta_{comb} m_{fuel} h_{comb}\frac{\mathrm{d}x_b}{\mathrm{d}\theta} \tag{B.7}$$

Eq. B.8 is obtained by expanding the terms of internal energy differential.

$$\frac{\mathrm{d}(m_b c_{v,b} T_b)}{\mathrm{d}\theta} = m_b c_{v,b}\frac{\mathrm{d}T_b}{\mathrm{d}\theta} + c_{v,b}T_b\frac{\mathrm{d}m_b}{\mathrm{d}\theta} \tag{B.8}$$

By substituting the presented relations in Eq. B.5, the balance of energy can be written as indicated in Eq. B.9.

$$m_b c_{v,b}\frac{\mathrm{d}T_b}{\mathrm{d}\theta} + c_{v,b}T_b\frac{\mathrm{d}m_b}{\mathrm{d}\theta} = \frac{\mathrm{d}H_{comb}}{\mathrm{d}\theta} + \frac{\mathrm{d}Q_b}{\mathrm{d}\theta} - P\frac{\mathrm{d}V_b}{\mathrm{d}\theta} + c_{p,u}T_u\frac{\mathrm{d}m_b}{\mathrm{d}\theta} \tag{B.9}$$

The rate of volume change in the unburned zone $\frac{\mathrm{d}V_b}{\mathrm{d}\theta}$ is unknown, thus it is substituted by the ideal gas equation indicated in Eq. B.10.

$$\frac{\mathrm{d}V_b}{\mathrm{d}\theta} = V_b\left(\frac{1}{m_b}\frac{\mathrm{d}m_b}{\mathrm{d}\theta} + \frac{1}{T_b}\frac{\mathrm{d}T_b}{\mathrm{d}\theta} - \frac{1}{P}\frac{\mathrm{d}P}{\mathrm{d}\theta}\right) \tag{B.10}$$

By substituting Eq. B.10 in Eq. B.9 and re-organising the terms in the left hand of the equation, Eq. B.11 is obtained.

$$m_b c_{v,b}\frac{\mathrm{d}T_b}{\mathrm{d}\theta} + c_{v,b}T_b\frac{\mathrm{d}m_b}{\mathrm{d}\theta} = \\ = \frac{\mathrm{d}H_{comb}}{\mathrm{d}\theta} + \frac{\mathrm{d}Q_b}{\mathrm{d}\theta} - PV_b\left(\frac{1}{m_b}\frac{\mathrm{d}m_b}{\mathrm{d}\theta} + \frac{1}{T_b}\frac{\mathrm{d}T_b}{\mathrm{d}\theta} - \frac{1}{P}\frac{\mathrm{d}P}{\mathrm{d}\theta}\right) + c_{p,u}T_u\frac{\mathrm{d}m_b}{\mathrm{d}\theta} \quad \text{(B.11)}$$

Substituting the relations

1. $\frac{PV_b}{m_b} = R_b T_b$;
2. $\frac{PV_b}{T_b} = R_b m_b$;

in Eq. B.11 leads to Eq. B.12.

$$m_b c_{v,b}\frac{\mathrm{d}T_b}{\mathrm{d}\theta} = \frac{\mathrm{d}H_{comb}}{\mathrm{d}\theta} + \frac{\mathrm{d}Q_b}{\mathrm{d}\theta} + c_{p,u}T_u\frac{\mathrm{d}m_b}{\mathrm{d}\theta} - c_{v,b}T_b\frac{\mathrm{d}m_b}{\mathrm{d}\theta} - R_b T_b\frac{\mathrm{d}m_b}{\mathrm{d}\theta} - m_b R_b\frac{\mathrm{d}T_b}{\mathrm{d}\theta} + V_b\frac{\mathrm{d}P}{\mathrm{d}\theta} \quad \text{(B.12)}$$

Re-arranging the terms in Eq. B.12 yields to Eq. B.13.

$$m_b\left(c_{v,b} + R_b\right)\frac{\mathrm{d}T_b}{\mathrm{d}\theta} = \frac{\mathrm{d}H_{comb}}{\mathrm{d}\theta} + \frac{\mathrm{d}Q_b}{\mathrm{d}\theta} + \frac{\mathrm{d}m_b}{\mathrm{d}\theta}\left(c_{p,u}T_u - c_{v,b}T_b - R_b T_b\right) + V_b\frac{\mathrm{d}P}{\mathrm{d}\theta} \quad \text{(B.13)}$$

Since $c_{p,b} = c_{v,b} + R_b$, Eq. B.13 can re-written as Eq. B.14.

$$m_b c_{p,b}\frac{\mathrm{d}T_b}{\mathrm{d}\theta} = \frac{\mathrm{d}H_{comb}}{\mathrm{d}\theta} + \frac{\mathrm{d}Q_b}{\mathrm{d}\theta} + \frac{\mathrm{d}m_b}{\mathrm{d}\theta}\left(c_{p,u}T_u - c_{p,b}T_b\right) + V_b\frac{\mathrm{d}P}{\mathrm{d}\theta} \quad \text{(B.14)}$$

Eq. B.15 is obtained by isolating $\frac{\mathrm{d}T_b}{\mathrm{d}\theta}$.

$$\frac{\mathrm{d}T_b}{\mathrm{d}\theta} = \frac{\frac{\mathrm{d}H_{comb}}{\mathrm{d}\theta} + \frac{\mathrm{d}Q_b}{\mathrm{d}\theta} + \frac{\mathrm{d}m_b}{\mathrm{d}\theta}\left(c_{p,u}T_u - c_{p,b}T_b\right) + V_b\frac{\mathrm{d}P}{\mathrm{d}\theta}}{m_b c_{p,b}} \quad \text{(B.15)}$$

2. Energy balance on the unburned zone:

The procedure adopted for the unburned gases is similar to that applied to the burned gases. However, it is assumed that the energy released by the combustion is integrally absorved by the burned gases, as indicated in Eq. B.16.

$$\frac{\mathrm{d}U_u}{\mathrm{d}\theta} = \frac{\mathrm{d}Q_u}{\mathrm{d}\theta} - \frac{\mathrm{d}W_u}{\mathrm{d}\theta} + h_u\frac{\mathrm{d}m_u}{\mathrm{d}\theta} \quad \text{(B.16)}$$

Expading the terms of the differential of internal energy in Eq. B.16 yields to Eq. B.17.

$$\frac{\mathrm{d}(m_u c_{v,u} T_u)}{\mathrm{d}\theta} = m_u c_{v,u} \frac{\mathrm{d}T_u}{\mathrm{d}\theta} + c_{v,u} T_u \frac{\mathrm{d}m_u}{\mathrm{d}\theta} \tag{B.17}$$

Substituting Eq. B.17 in Eq. B.16 leads to Eq. B.18.

$$m_u c_{v,u} \frac{\mathrm{d}T_u}{\mathrm{d}\theta} + c_{v,u} T_u \frac{\mathrm{d}m_u}{\mathrm{d}\theta} = \frac{\mathrm{d}Q_u}{\mathrm{d}\theta} - P\frac{\mathrm{d}V_u}{\mathrm{d}\theta} + c_{p,u} T_u \frac{\mathrm{d}m_u}{\mathrm{d}\theta} \tag{B.18}$$

The ideal gas equation in its differential form is indicated in Eq. B.19.

$$\frac{\mathrm{d}V_u}{\mathrm{d}\theta} = V_u \left(\frac{1}{m_u}\frac{\mathrm{d}m_u}{\mathrm{d}\theta} + \frac{1}{T_u}\frac{\mathrm{d}T_u}{\mathrm{d}\theta} - \frac{1}{P}\frac{\mathrm{d}P}{\mathrm{d}\theta} \right) \tag{B.19}$$

It is possible to eliminate the volume differential in Eq. B.18 by implementing Eq. B.19, leading to Eq. B.20.

$$m_u c_{v,u} \frac{\mathrm{d}T_u}{\mathrm{d}\theta} + c_{v,u} T_u \frac{\mathrm{d}m_u}{\mathrm{d}\theta} = \frac{\mathrm{d}Q_u}{\mathrm{d}\theta} - PV_u \left(\frac{1}{m_u}\frac{\mathrm{d}m_u}{\mathrm{d}\theta} + \frac{1}{T_u}\frac{\mathrm{d}T_u}{\mathrm{d}\theta} - \frac{1}{P}\frac{\mathrm{d}P}{\mathrm{d}\theta} \right) + c_{p,u} T_u \frac{\mathrm{d}m_u}{\mathrm{d}\theta} \tag{B.20}$$

Eq. B.21 is obtained by re-arranging the terms in Eq. B.20.

$$m_u c_{v,u} \frac{\mathrm{d}T_u}{\mathrm{d}\theta} + c_{v,u} T_u \frac{\mathrm{d}m_u}{\mathrm{d}\theta} = \frac{\mathrm{d}Q_u}{\mathrm{d}\theta} - \left(\frac{PV_u}{m_u}\frac{\mathrm{d}m_u}{\mathrm{d}\theta} + \frac{PV_u}{T_u}\frac{\mathrm{d}T_u}{\mathrm{d}\theta} - V_u\frac{\mathrm{d}P}{\mathrm{d}\theta} \right) + c_{p,u} T_u \frac{\mathrm{d}m_u}{\mathrm{d}\theta} \tag{B.21}$$

Substituting the relations:

1. $\frac{PV_u}{m_u} = R_u T_u$ and
2. $\frac{PV_u}{T_u} = R_u m_u$

in Eq. B.21 yields to Eq. B.22.

$$m_u c_{v,u} \frac{\mathrm{d}T_u}{\mathrm{d}\theta} = \frac{\mathrm{d}Q_u}{\mathrm{d}\theta} - R_u T_u \frac{\mathrm{d}m_u}{\mathrm{d}\theta} - c_{v,u} T_u \frac{\mathrm{d}m_u}{\mathrm{d}\theta} + c_{p,u} T_u \frac{\mathrm{d}m_u}{\mathrm{d}\theta} - R_u m_u \frac{\mathrm{d}T_u}{\mathrm{d}\theta} + V_u \frac{\mathrm{d}P}{\mathrm{d}\theta} \tag{B.22}$$

Since $c_{p,u} - c_{v,u} - R_u = 0$, Eq. B.22 can be written as Eq. B.23.

$$m_u \left(c_{v,u} + R_u\right) \frac{\mathrm{d}T_u}{\mathrm{d}\theta} = \frac{\mathrm{d}Q_u}{\mathrm{d}\theta} + V_u \frac{\mathrm{d}P}{\mathrm{d}\theta} \tag{B.23}$$

Substituting $c_{v,u} + R_u = c_{p,u}$ and isolating $\frac{\mathrm{d}T_u}{\mathrm{d}\theta}$ in Eq. B.23 yields to Eq. B.24.

$$\frac{\mathrm{d}T_u}{\mathrm{d}\theta} = \frac{\frac{\mathrm{d}Q_u}{\mathrm{d}\theta} + V_u \frac{\mathrm{d}P}{\mathrm{d}\theta}}{m_u c_{p,u}} \tag{B.24}$$

3. Balance of volume differentials:

The balance of volume is provided in Eq. B.25.

$$V = V_u + V_b \tag{B.25}$$

Eq. B.25 can be written in its differential form, as indicated in Eq. B.26.

$$\frac{\mathrm{d}V}{\mathrm{d}\theta} = \frac{\mathrm{d}V_u}{\mathrm{d}\theta} + \frac{\mathrm{d}V_b}{\mathrm{d}\theta} \tag{B.26}$$

By substituting the differentials of each zone by the ideal gas equation in its differential form in the balance of volume differential (Eq. B.26), Eq. B.27 is obtained.

$$\frac{\mathrm{d}V}{\mathrm{d}\theta} = V_u \left(\frac{1}{m_u}\frac{\mathrm{d}m_u}{\mathrm{d}\theta} + \frac{1}{T_u}\frac{\mathrm{d}T_u}{\mathrm{d}\theta} - \frac{1}{P}\frac{\mathrm{d}P}{\mathrm{d}\theta} \right) + V_b \left(\frac{1}{m_b}\frac{\mathrm{d}m_b}{\mathrm{d}\theta} + \frac{1}{T_b}\frac{\mathrm{d}T_b}{\mathrm{d}\theta} - \frac{1}{P}\frac{\mathrm{d}P}{\mathrm{d}\theta} \right) \tag{B.27}$$

Expanding the terms in Eq. B.27 leads to Eq. B.28.

$$\frac{\mathrm{d}V}{\mathrm{d}\theta} = \frac{V_u}{m_u}\frac{\mathrm{d}m_u}{\mathrm{d}\theta} + \frac{V_u}{T_u}\frac{\mathrm{d}T_u}{\mathrm{d}\theta} + \frac{V_b}{m_b}\frac{\mathrm{d}m_b}{\mathrm{d}\theta} + \frac{V_b}{T_b}\frac{\mathrm{d}T_b}{\mathrm{d}\theta} - \frac{1}{P}\frac{\mathrm{d}P}{\mathrm{d}\theta}\left(V_u + V_b\right) \tag{B.28}$$

Isolating the term $\frac{\mathrm{d}P}{\mathrm{d}\theta}$ in Eq. B.28 yields to Eq. B.29.

$$\frac{\mathrm{d}P}{\mathrm{d}\theta} = -\frac{P}{V}\left(\frac{\mathrm{d}V}{\mathrm{d}\theta} - \frac{V_u}{m_u}\frac{\mathrm{d}m_u}{\mathrm{d}\theta} + \frac{V_u}{T_u}\frac{\mathrm{d}T_u}{\mathrm{d}\theta} + \frac{V_b}{m_b}\frac{\mathrm{d}m_b}{\mathrm{d}\theta} + \frac{V_b}{T_b}\frac{\mathrm{d}T_b}{\mathrm{d}\theta} \right) \tag{B.29}$$

Implementing the identities:

1. $\frac{PV_u}{m_u} = R_u T_u$,
2. $\frac{PV_b}{m_b} = R_b T_b$,
3. $\frac{PV_u}{T_u} = R_u m_u$ and
4. $\frac{PV_b}{T_b} = R_b m_b$:

in Eq. B.29 leads to Eq. B.30.

$$\frac{\mathrm{d}P}{\mathrm{d}\theta} = -\frac{1}{V}\left(P\frac{\mathrm{d}V}{\mathrm{d}\theta} - R_u T_u \frac{\mathrm{d}m_u}{\mathrm{d}\theta} - R_u m_u \frac{\mathrm{d}T_u}{\mathrm{d}\theta} - R_b T_b \frac{\mathrm{d}m_b}{\mathrm{d}\theta} - R_b m_b \frac{\mathrm{d}T_b}{\mathrm{d}\theta} \right) \tag{B.30}$$

Eq. B.31 can be obtained by substituting Eqs. B.15 and B.24 in Eq. B.30.

$$\frac{\mathrm{d}P}{\mathrm{d}\theta} = -\frac{1}{V}\left\{P\frac{\mathrm{d}V}{\mathrm{d}\theta} - R_u T_u \frac{\mathrm{d}m_u}{\mathrm{d}\theta} - R_b T_b \frac{\mathrm{d}m_b}{\mathrm{d}\theta} - \frac{R_u m_u \left(\frac{\mathrm{d}Q_u}{\mathrm{d}\theta} + V_u \frac{\mathrm{d}P}{\mathrm{d}\theta}\right)}{m_u c_{p,u}} - \right.$$
$$\left. - \frac{R_b m_b \left[\frac{\mathrm{d}H_{comb}}{\mathrm{d}\theta} + \frac{\mathrm{d}Q_b}{\mathrm{d}\theta} + V_b \frac{\mathrm{d}P}{\mathrm{d}\theta} + \frac{\mathrm{d}m_b}{\mathrm{d}\theta}\left(c_{p,u}T_u - c_{p,b}T_b\right)\right]}{m_b c_{p,b}}\right\} \quad \text{(B.31)}$$

By isolating $\frac{\mathrm{d}P}{\mathrm{d}\theta}$ in Eq. B.31, Eq. B.32 is obtained.

$$\frac{\mathrm{d}P}{\mathrm{d}\theta} = \frac{P\frac{\mathrm{d}V}{\mathrm{d}\theta} - R_u T_u \frac{\mathrm{d}m_u}{\mathrm{d}\theta} - R_b T_b \frac{\mathrm{d}m_b}{\mathrm{d}\theta} - \frac{R_u \frac{\mathrm{d}Q_u}{\mathrm{d}\theta}}{c_{p,u}} - \frac{R_b\left[\frac{\mathrm{d}H_{comb}}{\mathrm{d}\theta} + \frac{\mathrm{d}Q_b}{\mathrm{d}\theta} + \frac{\mathrm{d}m_b}{\mathrm{d}\theta}\left(c_{p,u}T_u - c_{p,b}T_b\right)\right]}{c_{p,b}}}{\frac{V_b R_b}{c_{p,b}} + \frac{V_u R_u}{c_{p,u}} - V} \quad \text{(B.32)}$$

B.2 Deduction of the single zone model for open phases

An energy balance is performed for a system in which mass changes along the processes of intake and exhaust in order to calculate in–cylinder mass, pressure and temperature. A homogeneous charge is considered. The energy balance is presented in Eq. B.33.

$$\frac{\mathrm{d}U}{\mathrm{d}\theta} = \frac{\mathrm{d}Q}{\mathrm{d}\theta} - \frac{\mathrm{d}W}{\mathrm{d}\theta} + h_{in}\frac{\mathrm{d}m_{in}}{\mathrm{d}\theta} + h_{ex}\frac{\mathrm{d}m_{ex}}{\mathrm{d}\theta} \quad \text{(B.33)}$$

Intake is represented by the subscript in whilst exhaust is represented by the subscript ex. It is highlighted that the properties of the flow are related to upstream conditions.

The internal energy can be written as function of mass, specific heat at constant volume and temperature, $U = mc_vT$. Also, the inexact differential of work can be written $\frac{\mathrm{d}W}{\mathrm{d}\theta} = P\frac{\mathrm{d}V}{\mathrm{d}\theta}$, leading to Eq. B.34.

$$\frac{\mathrm{d}(mc_vT)}{\mathrm{d}\theta} = \frac{\mathrm{d}Q}{\mathrm{d}\theta} - P\frac{\mathrm{d}V}{\mathrm{d}\theta} + h_{in}\frac{\mathrm{d}m_{in}}{\mathrm{d}\theta} + h_{ex}\frac{\mathrm{d}m_{ex}}{\mathrm{d}\theta} \quad \text{(B.34)}$$

Eq. B.35 is obtained by expanding the differential of internal energy.

$$mc_v\frac{\mathrm{d}T}{\mathrm{d}\theta} + c_vT\frac{\mathrm{d}m}{\mathrm{d}\theta} = \frac{\mathrm{d}Q}{\mathrm{d}\theta} - P\frac{\mathrm{d}V}{\mathrm{d}\theta} + h_{in}\frac{\mathrm{d}m_{in}}{\mathrm{d}\theta} + h_{ex}\frac{\mathrm{d}m_{ex}}{\mathrm{d}\theta} \quad \text{(B.35)}$$

The entalphy of the mass flow crossing intake and exhaust valves can be written as function of temperature $c_{v,in}T_{in}$ and $c_{v,ex}T_{ex}$, respectively. Moreover, the mass variation in the cylinder consists of the sum of the mass flow through each valve: $\frac{\mathrm{d}m}{\mathrm{d}\theta} = \frac{\mathrm{d}m_{in}}{\mathrm{d}\theta} + \frac{\mathrm{d}m_{ex}}{\mathrm{d}\theta}$

By applying the consideration and isolating the temperature differential, Eq. B.36 is obtained.

$$\frac{\mathrm{d}T}{\mathrm{d}\theta} = \frac{\frac{\mathrm{d}Q}{\mathrm{d}\theta} - P\frac{\mathrm{d}V}{\mathrm{d}\theta} + (c_{v,in}T_{in} - c_vT)\frac{\mathrm{d}m_{in}}{\mathrm{d}\theta} + (c_{v,ex}T_{ex} - c_vT)\frac{\mathrm{d}m_{ex}}{\mathrm{d}\theta}}{mc_v} \tag{B.36}$$

The pressure can be directly obtained from the ideal gas equation, indicated in Eq. B.37.

$$P = \frac{mRT}{V} \tag{B.37}$$

The gas constant R is calculated based on the gases composition, being updated at each step of the algorithm. Although the composition is changing during the gases exchange processes, the differential effects of this variation can be neglected.

B.3 Quasi–steady flow model

In order to calculate the mass flow through valves during the gases exchange process, a quasi-steady flow model was implemented. In the demonstration herein presented, the subscript us indicates condition upstream from valves whilst ds indicates condition downstream from the valve. SHERMAN and BLUMBERG (1977), GALLO (1990) and LOPES (2014) are cited among works which provide the demonstration of the equations used to determine valve flow. The following hypothesis are adopted to perform the analysis:

- Flowing gases behave as perfect gases (constant c_p);
- The flow is isentropic;
- Properties upstream of valve are considered to be at stagnation.

The mass conservation is applied for a uni-dimensional flow through an orifice, as indicated in Eq. B.38.

$$\dot{m}_{us} = \dot{m}_{ds} = \dot{m} = \rho_{ds}A_{ds}\nu_{ds} \tag{B.38}$$

Because of the ideal gases hypothesis, Eqs. B.39 and B.40 are merged together to B.41, which can be substituted into Eq. B.38 in order to obtain Eq. B.42.

$$\frac{\rho_{ds}}{\rho_{us}} = \frac{P_{ds}T_{us}}{P_{us}T_{ds}} \tag{B.39}$$

$$\rho_{us} = \frac{P_{us}}{RT_{us}} \tag{B.40}$$

$$\rho_{ds} = \frac{P_{ds}T_{us}}{P_{us}T_{ds}}\frac{P_{us}}{RT_{us}} \tag{B.41}$$

$$\dot{m} = \frac{P_{ds}T_{us}}{P_{us}T_{ds}}\frac{P_{us}}{RT_{us}}A_{ds}\nu_{ds} \tag{B.42}$$

The downstream velocity ν_{ds} can be determined by the energy balance presented in Eq. B.43.

$$h_{ds} + \frac{\nu_{ds}^2}{2} = h_{us} \tag{B.43}$$

By adopting the perfect gas hypothesis, *i.e.*, c_p and c_v are independent from temperature, the energy balance can be re-written as in Eq. B.44.

$$\nu_{ds} = \sqrt{2c_p\left(T_{us} - T_{ds}\right)} \tag{B.44}$$

Hence, the balance of mass can be written in the form indicated in Eq. B.45.

$$\dot{m} = \frac{A_{ds}P_{us}}{RT_{us}}\frac{P_{ds}}{P_{us}}\frac{T_{us}}{T_{ds}}\sqrt{2c_p\left(T_{us} - T_{ds}\right)} \tag{B.45}$$

Since the flow is assumed to be isentropic, the fundamental relations of thermodynamics, Eq. B.46, can be used to establish a relation between pressure and temperature.

$$T\,\mathrm{d}s = \mathrm{d}h - v\,\mathrm{d}P \Rightarrow ds = c_p\frac{\mathrm{d}T}{T} - R\frac{\mathrm{d}P}{P} = 0 \tag{B.46}$$

Integrating Eq. B.46 leads to Eq. B.47.

$$\left(\frac{T_{ds}}{T_{us}}\right)^{c_p} = \left(\frac{P_{ds}}{P_{us}}\right)^{R} \tag{B.47}$$

Eq. B.50 can be obtained by implementing the relations indicated in Eqs. B.48 and B.49 in Eq. B.47.

$$R = c_p - c_v \tag{B.48}$$

$$\frac{c_p}{c_v} = k \tag{B.49}$$

$$\left(\frac{T_{ds}}{T_{us}}\right) = \left(\frac{P_{ds}}{P_{us}}\right)^{\frac{k-1}{k}} \tag{B.50}$$

Substituting Eq. B.50 to the mass balance in Eq. Eq. B.46 yields to Eq. B.51.

$$\dot{m} = \frac{A_{ds} P_{us}}{R T_{us}} \sqrt{2 \left(\frac{k}{k-1} \right) \left[\left(\frac{P_{ds}}{P_{us}} \right)^{\frac{2}{k}} - \left(\frac{P_{ds}}{P_{us}} \right)^{\frac{k+1}{k}} \right]} \tag{B.51}$$

Eq. B.51 is only valid for subsonic flow. Whenever the flow achieves the critical condition, downstream pressure ceases to affect the mass flow, which is considered to be choked.

For a sonic flow, the velocity of the gas can be determined by the relation indicated in Eq. B.52.

$$\nu_{ds} = \sqrt{k R T_{ds}} \tag{B.52}$$

Eq. B.52 can be substituted in Eq. B.46, yielding to Eq. B.53.

$$\frac{T_{us}}{T_{ds}} = \frac{k+1}{2} \tag{B.53}$$

The condition for choked flow, indicated in Eq. B.54, can be established by adopting the hypothesis of isentropic flow.

$$\frac{P_{ds}}{P_{us}} \leq \left(\frac{2}{k+1} \right)^{\frac{k}{k-1}} \tag{B.54}$$

The mass flow can be determined for the chocked condition by the relation indicated in Eq. B.55.

$$\dot{m} = \rho_{ds} \nu_{ds} A_{ds} = A_{ds} \frac{P_{ds}}{R T_{ds}} \sqrt{k R T_{ds}} \tag{B.55}$$

Eq. B.55 can be manipulated into Eq. B.56.

$$\dot{m} = \frac{A_{ds} P_{us}}{\sqrt{R T_{us}}} \sqrt{k \left(\frac{2}{k+1} \right)^{\frac{k+1}{k-1}}} \tag{B.56}$$

A correction must be performed since the isentropic hypothesis does not account for effects of friction and heat transfer on the flow. The corection is made by multypling the isentropic flow by a coefficient of discharge C_D, as defined in Eq. B.57.

$$C_D = \frac{\dot{m}_{real}}{\dot{m}_{iso}} \tag{B.57}$$

GALLO (1990) has proposed a correlation for C_D as a function of valve lifting Y and valve diameter D_v, based on data provided by KASTNER *et al.* (1963), obtaining the relation presented in Eq. B.58.

$$C_D = \sum_{i=0}^{10} a_i \left(Y/D_v\right)^i \tag{B.58}$$

The coefficients for C_D are given in Tab. B.1.

Table B.1: Coefficients for C_D calculation.

Coefficient	Value
a_0	0,9999876
a_1	7,633573e-1
a_2	-4,089484e2
a_3	1,885862e4
a_4	-4,016319e5
a_5	4,720187e6
a_6	-3,295265e7
a_7	1,401485e8
a_8	-3,567916e8
a_9	5,004000e8
a_{10}	-2,977371e8

B.4 Determination of valve flow area

Firstly, it is necessary to determine the elevation profile of the valve. Although harmonic a cycloidal profiles are more realistic, a parabolic profile for valve elevation was adopted for this work, since it is fairly accurate for simulations purposes, according to SHERMAN and BLUMBERG (1977).

The method for elevation calculation presented here is based on the work of GALLO (1990). Area of flow consists of the minimum area in the ports. For small elevations, this area is given by Eq. B.59 and it corresponds to the area of a cone frustrum with an inclination of 45 $^\circ$.

$$A_v = \pi Y \cos 45^\circ \left(D_v + Y \cos^2 45^\circ\right) \tag{B.59}$$

When the elevation achieves the condition $\frac{Y}{D_v} = 0.125$, the inclination of the cone is changed and the area is given by Eq. B.60.

$$A_v = \pi \left(\frac{17 D_v}{16}\right) \sqrt{\left(Y - \frac{D_v}{16}\right)^2 + \left(\frac{D_v}{16}\right)^2} \tag{B.60}$$

When the opening area of the valve equals to the area of the port, the flow becomes limitted by the port area, given by Eq. B.61.

$$A_v = \pi \frac{7D_v^2}{64} \tag{B.61}$$

C. Development of the Diagnosis model

C.1 Two zone diagnosis model

In–cylinder pressure P and the pressure derivative $\frac{\mathrm{d}P}{\mathrm{d}\theta}$ are measured in bench. Total volume of the combustion chamber V and its derivative $\frac{\mathrm{d}V}{\mathrm{d}\theta}$ are calculated from engine geometry. The two zone approach consists in separating the in–cylinder gases in reactants and combustion products, represented by the subscripts r and p, respectively. Note that a different nomenclature is adopted for the predictive model. The two zones in the predictive model are unburned and burned, since residual gases are considered in the phenomenological model. For the diagnosis model, residual gases are neglected since no analysis is carried out on the gas exchange phases.

From the ideal gas hypothesis, the volume of each zone is respectively given in Eqs. C.1 and C.2.

$$V_r = \frac{m_r R_r T_r}{P} \tag{C.1}$$

$$V_p = \frac{m_p R_p T_p}{P} \tag{C.2}$$

The mass of each zone is calculated from the mass fraction burn x_b and the trapped mass m, indicated in Eqs. C.3 and C.4.

$$m_r = (1 - x_b)\, m \tag{C.3}$$

$$m_p = x_b m \tag{C.4}$$

The trapped mass can be determined from the fuel mass flow, measured in bench, and the A/F ratio, measured by the oxygen sensor.

There are three unknown variables: T_r, T_p and x_b. Thus, it is necessary three differential equations and three initials conditions. The initial MFB is zero. The initial temperature

of burned gases is assumed to be the abiabatic flame temperature of the A/F mixture. To calculate the initial temperature of the unburned mixture, the equation of state C.5 is applied for the intake valve closing event.

$$T_r = \frac{PV}{mR_r} \tag{C.5}$$

Applying the energy conservation law to the unburned gases leads to Eq. C.6.

$$\frac{\mathrm{d}U_r}{\mathrm{d}\theta} = \frac{\mathrm{d}Q_r}{\mathrm{d}\theta} - \frac{\mathrm{d}W_r}{\mathrm{d}\theta} + \frac{\mathrm{d}m_r}{\mathrm{d}\theta}h_r \tag{C.6}$$

The heat transfer differential $\frac{\mathrm{d}Q_r}{\mathrm{d}\theta}$ is estimated from the Newton law, indicated in Eq. C.7.

$$\frac{\mathrm{d}Q_r}{\mathrm{d}\theta} = \frac{\partial t}{\partial \theta}\frac{\mathrm{d}Q_r}{\mathrm{d}t} = \frac{1}{\omega}\frac{\mathrm{d}Q_r}{\mathrm{d}t} = -\frac{h_r^{HT}A_r\left(T_r - T_w\right)}{\omega} \tag{C.7}$$

The cylinder walls temperature is represented by T_w and A_r is the area of the unburned region, assumed to be proportional to the volume of that zone. The conversion from time domain to crank angle domain is performed by diving the heat transfer in time domain by the angular velocity of the engine ω. Work differential $\frac{\mathrm{d}W_r}{\mathrm{d}\theta}$ is given by the boundary dislocation, leading to Eq. C.8.

$$\frac{\mathrm{d}W_r}{\mathrm{d}\theta} = P\frac{\mathrm{d}V_r}{\mathrm{d}\theta} \tag{C.8}$$

The specific enthalpy of mass crossing the boundaries h_r is given as a function of specific heat, as indicated by Eq. C.9.

$$h_r = c_{p,r}T_r \tag{C.9}$$

It is possible to re–write internal energy U_r as a function of enthalpy, pressure and volume $U = H - PV$, yielding to Eq. C.10.

$$\frac{\mathrm{d}U_r}{\mathrm{d}\theta} = \frac{\mathrm{d}H_r}{\mathrm{d}\theta} - P\frac{\mathrm{d}V_r}{\mathrm{d}\theta} - V_r\frac{\mathrm{d}P}{\mathrm{d}\theta} \tag{C.10}$$

Applying the mentioned considerations to Eq. C.6, Eq. C.11 is obtained.

$$\frac{\mathrm{d}H_r}{\mathrm{d}\theta} - P\frac{\mathrm{d}V_r}{\mathrm{d}\theta} - V_r\frac{\mathrm{d}P}{\mathrm{d}\theta} = \frac{\mathrm{d}Q_r}{\mathrm{d}\theta} - P\frac{\mathrm{d}V_r}{\mathrm{d}\theta} + c_{p,r}T_r\frac{\mathrm{d}m_r}{\mathrm{d}\theta} \tag{C.11}$$

The differential of mass crossing the boundaries of the unburned zone is a function of the rate of mass burning $\frac{\mathrm{d}x_b}{\mathrm{d}\theta}$, presented in Eq. C.12.

$$\frac{\mathrm{d}m_r}{\mathrm{d}\theta} = -m\frac{\mathrm{d}x_b}{\mathrm{d}\theta} \tag{C.12}$$

The extensive enthalpy is a function of mass and intensive enthalpy, which is function of specific heat and temperature, as indicated in Eq. C.13.

$$H_r = m_r c_{p,r} T_r \tag{C.13}$$

By applying these considerations to C.11, Eq. C.14 is obtained.

$$m_r c_{p,r} \frac{\mathrm{d}T_r}{\mathrm{d}\theta} + c_{p,r} T_r \frac{\mathrm{d}m_r}{\mathrm{d}\theta} = \frac{\mathrm{d}Q_r}{\mathrm{d}\theta} + V_r \frac{\mathrm{d}P}{\mathrm{d}\theta} - c_{p,r} T_r m \frac{\mathrm{d}x_b}{\mathrm{d}\theta} \tag{C.14}$$

And substituting Eq. C.15 in Eq. C.14 leads to Eq. C.16.

$$c_{p,r} T_r \frac{\mathrm{d}m_r}{\mathrm{d}\theta} = -c_{p,r} T_r m \frac{\mathrm{d}x_b}{\mathrm{d}\theta} \tag{C.15}$$

$$m\left(1 - x_b\right) c_{p,r} \frac{\mathrm{d}T_r}{\mathrm{d}\theta} = \frac{\mathrm{d}Q_r}{\mathrm{d}\theta} + V_r \frac{\mathrm{d}P}{\mathrm{d}\theta} \tag{C.16}$$

By isolating the temperature differential $\frac{\mathrm{d}T_r}{\mathrm{d}\theta}$ in Eq. C.16, it is obtained Eq. C.17.

$$\frac{\mathrm{d}T_r}{\mathrm{d}\theta} = \frac{\frac{\mathrm{d}Q_r}{\mathrm{d}\theta} + V_r \frac{\mathrm{d}P}{\mathrm{d}\theta}}{m\left(1 - x_b\right) c_{p,r}} \tag{C.17}$$

The energy conservation law applied to the burned region of the cylinder is shown in Eq. C.18.

$$\frac{\mathrm{d}U_p}{\mathrm{d}\theta} = \frac{\mathrm{d}H_{comb}}{\mathrm{d}\theta} + \frac{\mathrm{d}Q_p}{\mathrm{d}\theta} - \frac{\mathrm{d}W_p}{\mathrm{d}\theta} + \frac{\mathrm{d}m_p}{\mathrm{d}\theta} h_r \tag{C.18}$$

The term $\frac{\mathrm{d}H_{comb}}{\mathrm{d}\theta}$ represents the energy released by the combustion process in Eq. C.18. In this case, it is being assumed that all of that energy is transferred to the burned gases. By applying the same considerations applied to the unburned zone from Eq. C.6 to Eq. C.14 to the burned zone, the following relation is obtained:

$$m_p c_{p,p} \frac{\mathrm{d}T_p}{\mathrm{d}\theta} + c_{p,p} T_p \frac{\mathrm{d}m_p}{\mathrm{d}\theta} = \frac{\mathrm{d}H_{comb}}{\mathrm{d}\theta} + \frac{\mathrm{d}Q_p}{\mathrm{d}\theta} + V_p \frac{\mathrm{d}P}{\mathrm{d}\theta} + c_{p,r} T_r m \frac{\mathrm{d}x_b}{\mathrm{d}\theta} \tag{C.19}$$

The energy released by combustion can be written as function of fuel mass m_{fuel}, the combustion enthalpy h_{comb} and the burning rate, as indicated in Eq. C.20

$$\frac{\mathrm{d}H_{comb}}{\mathrm{d}\theta} = m_{fuel} h_{comb} \frac{\mathrm{d}x_b}{\mathrm{d}\theta} \tag{C.20}$$

The rate of mass entering the burned zone is given as function of burning rate, presented in Eq. C.21.

$$\frac{\mathrm{d}m_p}{\mathrm{d}\theta} = m\frac{\mathrm{d}x_b}{\mathrm{d}\theta} \tag{C.21}$$

Substituting Eq. C.20 and Eq. C.21 in Eq. C.19 leads to C.22.

$$x_b m c_{p,p}\frac{\mathrm{d}T_p}{\mathrm{d}\theta} + c_{p,p}T_p m\frac{\mathrm{d}x_b}{\mathrm{d}\theta} = m_{fuel}h_{comb}\frac{\mathrm{d}x_b}{\mathrm{d}\theta} + \frac{\mathrm{d}Q_p}{\mathrm{d}\theta} + V_p\frac{\mathrm{d}P}{\mathrm{d}\theta} + c_{p,r}T_r m\frac{\mathrm{d}x_b}{\mathrm{d}\theta} \tag{C.22}$$

By isolating the differential of temperature $\frac{\mathrm{d}T_p}{\mathrm{d}\theta}$ in Eq. C.22, the differential equation C.23 can be found.

$$\frac{\mathrm{d}T_p}{\mathrm{d}\theta} = \frac{\left[m_{fuel}h_{comb} + m\left(c_{p,r}T_r - c_{p,p}T_p\right)\right]\frac{\mathrm{d}x_b}{\mathrm{d}\theta} + \frac{\mathrm{d}Q_p}{\mathrm{d}\theta} + V_p\frac{\mathrm{d}P}{\mathrm{d}\theta}}{m x_b c_{p,p}} \tag{C.23}$$

To obtain an expression for $\frac{\mathrm{d}x_b}{\mathrm{d}\theta}$, a balance of volume is performed in Eq. C.24.

$$V = V_r + V_p \tag{C.24}$$

The differentiation of Eq. C.24 leads to Eq. C.25.

$$\frac{\mathrm{d}V}{\mathrm{d}\theta} = \frac{\mathrm{d}V_r}{\mathrm{d}\theta} + \frac{\mathrm{d}V_p}{\mathrm{d}\theta} \tag{C.25}$$

The equation of state for ideal gases is presented in Eq. C.26.

$$PV = mRT \tag{C.26}$$

The differential form of Eq. C.26 is presented in Eq. C.27.

$$\frac{1}{P}\frac{\mathrm{d}P}{\mathrm{d}\theta} + \frac{1}{V}\frac{\mathrm{d}V}{\mathrm{d}\theta} = \frac{1}{m}\frac{\mathrm{d}m}{\mathrm{d}\theta} + \frac{1}{T}\frac{\mathrm{d}T}{\mathrm{d}\theta} \tag{C.27}$$

Applying the differential form of the ideal gases equation to each zone, Eqs. C.28 and C.29 are obtained.

$$\frac{\mathrm{d}V_r}{\mathrm{d}\theta} = V_r\left(\frac{1}{m_r}\frac{\mathrm{d}m_r}{\mathrm{d}\theta} + \frac{1}{T_r}\frac{\mathrm{d}T_r}{\mathrm{d}\theta} - \frac{1}{P}\frac{\mathrm{d}P}{\mathrm{d}\theta}\right) \tag{C.28}$$

$$\frac{\mathrm{d}V_p}{\mathrm{d}\theta} = V_p\left(\frac{1}{m_p}\frac{\mathrm{d}m_p}{\mathrm{d}\theta} + \frac{1}{T_p}\frac{\mathrm{d}T_p}{\mathrm{d}\theta} - \frac{1}{P}\frac{\mathrm{d}P}{\mathrm{d}\theta}\right) \tag{C.29}$$

Substituting Eqs. C.28 and C.29 in C.25 yields to Eq. C.30.

$$\frac{\mathrm{d}V}{\mathrm{d}\theta} = \frac{V_r}{m_r}\frac{\mathrm{d}m_r}{\mathrm{d}\theta} + \frac{V_r}{T_r}\frac{\mathrm{d}T_r}{\mathrm{d}\theta} - \frac{V_r}{P}\frac{\mathrm{d}P}{\mathrm{d}\theta} + \frac{V_p}{m_p}\frac{\mathrm{d}m_p}{\mathrm{d}\theta} + \frac{V_p}{T_p}\frac{\mathrm{d}T_p}{\mathrm{d}\theta} - \frac{V_p}{P}\frac{\mathrm{d}P}{\mathrm{d}\theta} \tag{C.30}$$

The sum of the volumes of each zone is equal to the whole volume of the combustion chamber, as indicated in Eq. C.31.

$$\frac{V_p}{P}\frac{\mathrm{d}P}{\mathrm{d}\theta} + \frac{V_r}{P}\frac{\mathrm{d}P}{\mathrm{d}\theta} = \frac{V}{P}\frac{\mathrm{d}P}{\mathrm{d}\theta} \tag{C.31}$$

Substituting Eq. C.31 in Eq. C.30 leads to Eq. C.32.

$$\frac{\mathrm{d}V}{\mathrm{d}\theta} + \frac{V}{P}\frac{\mathrm{d}P}{\mathrm{d}\theta} = \frac{V_r}{m_r}\frac{\mathrm{d}m_r}{\mathrm{d}\theta} + \frac{V_r}{T_r}\frac{\mathrm{d}T_r}{\mathrm{d}\theta} + \frac{V_p}{m_p}\frac{\mathrm{d}m_p}{\mathrm{d}\theta} + \frac{V_p}{T_p}\frac{\mathrm{d}T_p}{\mathrm{d}\theta} \tag{C.32}$$

Multiplying both sides of Eq. C.32 by P yields to C.33.

$$P\frac{\mathrm{d}V}{\mathrm{d}\theta} + V\frac{\mathrm{d}P}{\mathrm{d}\theta} = P\frac{V_r}{m_r}\frac{\mathrm{d}m_r}{\mathrm{d}\theta} + P\frac{V_r}{T_r}\frac{\mathrm{d}T_r}{\mathrm{d}\theta} + P\frac{V_p}{m_p}\frac{\mathrm{d}m_p}{\mathrm{d}\theta} + P\frac{V_p}{T_p}\frac{\mathrm{d}T_p}{\mathrm{d}\theta} \tag{C.33}$$

Since $\frac{PV}{m} = RT$ and $\frac{PV}{T} = mR$, Eq. C.33 can be re-written as Eq. C.34.

$$P\frac{\mathrm{d}V}{\mathrm{d}\theta} + V\frac{\mathrm{d}P}{\mathrm{d}\theta} = R_rT_r\frac{\mathrm{d}m_r}{\mathrm{d}\theta} + m_rR_r\frac{\mathrm{d}T_r}{\mathrm{d}\theta} + R_pT_p\frac{\mathrm{d}m_p}{\mathrm{d}\theta} + m_pR_p\frac{\mathrm{d}T_p}{\mathrm{d}\theta} \tag{C.34}$$

By substituting the following identities:

- $m_r = m\left(1 - x_b\right)$
- $m_p = mx_b$
- $\frac{\mathrm{d}m_r}{\mathrm{d}\theta} = -m\frac{\mathrm{d}x_b}{\mathrm{d}\theta}$
- $\frac{\mathrm{d}m_p}{\mathrm{d}\theta} = m\frac{\mathrm{d}x_b}{\mathrm{d}\theta}$

to Eq. C.34, it is possible to obtain Eq. C.35.

$$P\frac{\mathrm{d}V}{\mathrm{d}\theta} + V\frac{\mathrm{d}P}{\mathrm{d}\theta} = m\left(R_pT_p - R_rT_r\right)\frac{\mathrm{d}x_b}{\mathrm{d}\theta} + m\left(1 - x_b\right)\frac{\mathrm{d}T_r}{\mathrm{d}\theta} + mx_b\frac{\mathrm{d}T_p}{\mathrm{d}\theta} \tag{C.35}$$

The differential $\frac{\mathrm{d}T_r}{\mathrm{d}\theta}$ is dependent of $\frac{\mathrm{d}x_b}{\mathrm{d}\theta}$. Therefore, it is necessary to substitute Eq. C.23 in C.35, leading to Eq. C.36.

$$P\frac{\mathrm{d}V}{\mathrm{d}\theta}+V\frac{\mathrm{d}P}{\mathrm{d}\theta}-m\left(1-x_b\right)\frac{\mathrm{d}T_r}{\mathrm{d}\theta}=m\left(R_pT_p-R_rT_r\right)\frac{\mathrm{d}x_b}{\mathrm{d}\theta}+ \\ +\frac{mx_bR_p}{mx_bc_{p,p}}\left\{\left[m_{fuel}h_{comb}+mc_{p,r}T_r-mc_{p,p}T_p\right]\frac{\mathrm{d}x_b}{\mathrm{d}\theta}-\frac{\mathrm{d}Q_p}{\mathrm{d}\theta}+V_p\frac{\mathrm{d}P}{\mathrm{d}\theta}\right\} \quad \text{(C.36)}$$

Re-organising the terms in Eq. C.36 yields to Eq. C.37.

$$P\frac{\mathrm{d}V}{\mathrm{d}\theta}+V\frac{\mathrm{d}P}{\mathrm{d}\theta}\frac{R_p}{c_{p,p}}\left(\frac{\mathrm{d}Q_p}{\mathrm{d}\theta}-V_p\frac{\mathrm{d}P}{\mathrm{d}\theta}\right)-m\left(1-x_b\right)\frac{\mathrm{d}T_r}{\mathrm{d}\theta}= \\ m\left\{R_pT_p-R_rT_r+\frac{R_p}{c_{p,p}}\left[\frac{m_{fuel}h_{comb}}{m}+c_{p,r}T_r-c_{p,p}T_p\right]\right\}\frac{\mathrm{d}x_b}{\mathrm{d}\theta} \quad \text{(C.37)}$$

Isolating $\frac{\mathrm{d}x_b}{\mathrm{d}\theta}$ Eq. C.37 leads to Eq. C.38.

$$\frac{\mathrm{d}x_b}{\mathrm{d}\theta}=\frac{P\frac{\mathrm{d}V}{\mathrm{d}\theta}+V\frac{\mathrm{d}P}{\mathrm{d}\theta}+\frac{R_p}{c_{p,p}}\left(\frac{\mathrm{d}Q_p}{\mathrm{d}\theta}-V_p\frac{\mathrm{d}P}{\mathrm{d}\theta}\right)-m\left(1-x_b\right)R_r\frac{\mathrm{d}T_r}{\mathrm{d}\theta}}{m\left\{R_pT_p-R_rT_r+\frac{R_p}{c_{p,p}}\left[\frac{m_{fuel}h_{comb}}{m}+c_{p,r}T_r-c_{p,p}T_p\right]\right\}} \quad \text{(C.38)}$$

C.2 Pressure differentiaton

After filtering the pressure profile, measured in bench, a numerical differentiation is performed in order to obtain $\frac{\mathrm{d}P}{\mathrm{d}\theta}$. A compact scheme of fourth order was implemented. This scheme was actually adapted from finite differences methods for fluid mechanics simulations. The implemented differentiation is the Padé (LOMAX *et al.*, 2013), presented in Eq. C.39.

$$\frac{1}{6}\left.\frac{\mathrm{d}P}{\mathrm{d}\theta}\right|_{i+1}+\frac{2}{3}\left.\frac{\mathrm{d}P}{\mathrm{d}\theta}\right|_{i}+\frac{1}{6}\left.\frac{\mathrm{d}P}{\mathrm{d}\theta}\right|_{i-1}=\frac{P_{i+1}-P_{i-1}}{2\left(\theta_{i+1}-\theta_{i-1}\right)} \quad \text{(C.39)}$$

A matrix solution was computationally implemented for this method, following Eq. C.40, in which the coefficients matrix $[a]$ and $[b]$ were generated by assuming that the pressure profile is periodic, as indicated in Eqs. C.41 and C.42.

$$\frac{\mathrm{d}\vec{P}}{\mathrm{d}\theta}=[a]^{-1}[b]\,\vec{P} \quad \text{(C.40)}$$

$$[a] = \frac{1}{6}\begin{bmatrix} 4 & 1 & \dots & 1 \\ 1 & 4 & 1\dots & \\ & \ddots & & \\ \dots & 1 & 4 & 1 \\ 1 & \dots & 1 & 4 \end{bmatrix} \tag{C.41}$$

$$[b] = \frac{1}{2\Delta\theta}\begin{bmatrix} 0 & 1 & \dots & -1 \\ -1 & 0 & 1\dots & \\ & \ddots & & \\ \dots & -1 & 0 & 1 \\ 1 & \dots & -1 & 0 \end{bmatrix} \tag{C.42}$$

C.3 Determination of cylinder wall temperature

Only interaction of work and heat transfer occurs at the boundaries of the cylinder prior to combustion. Moreover, no chemical reaction occurs. Therefore, it is possible to calculate the temperature of the A/F mixture by the energy conservation, presented in Eq. C.43.

$$\frac{\mathrm{d}U}{\mathrm{d}\theta} = \frac{\mathrm{d}Q}{\mathrm{d}\theta} - \frac{\mathrm{d}W}{\mathrm{d}\theta} \tag{C.43}$$

Since work interaction is performed through boundary dislocation and internal energy is a function of temperature, the equation can be re-writen as indicated in Eq. C.44.

$$\frac{\mathrm{d}Q}{\mathrm{d}\theta} = mc_v\frac{\mathrm{d}T}{\mathrm{d}\theta} - P\frac{\mathrm{d}V}{\mathrm{d}\theta} \tag{C.44}$$

By assuming ideal gas behaviour and neglecting mass transfer effects, it possible to correlate temperature and pressure in a differential form, as presented in Eq. C.45.

$$P\frac{\mathrm{d}V}{\mathrm{d}\theta} + V\frac{\mathrm{d}P}{\mathrm{d}\theta} = mR\frac{\mathrm{d}T}{\mathrm{d}\theta} \tag{C.45}$$

Eq. C.46 can be found by substituting Eq. C.45 on Eq. C.44.

$$\frac{\mathrm{d}Q}{\mathrm{d}\theta} = \frac{c_v}{R}\left(P\frac{\mathrm{d}V}{\mathrm{d}\theta} + V\frac{\mathrm{d}P}{\mathrm{d}\theta}\right) - P\frac{\mathrm{d}V}{\mathrm{d}\theta} \tag{C.46}$$

Re-arranging the terms in C.46 yields to Eq. C.47.

$$\frac{\mathrm{d}Q}{\mathrm{d}\theta} = \frac{c_v}{R}V\frac{\mathrm{d}P}{\mathrm{d}\theta} + \left(\frac{c_v}{R} - 1\right)P\frac{\mathrm{d}V}{\mathrm{d}\theta} \tag{C.47}$$

And the temperature of gases can be calculated from the equation of state.

The temperature of cylinder T_w is assumed to be the same as the gases at the instant in which the heat transfer rate is observed to change the direction, *i.e.*, when the heat ceases to be added to the in–cylinder gases from the cylinder walls and it begins to be rejected from the gases to the cylinder walls as schemed in Fig. C.1.

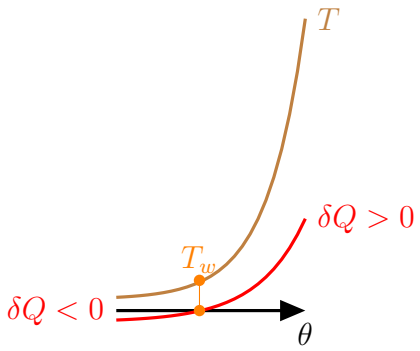

Figure C.1: Scheme for cylinder wall determination.

D. Additional results from the Combustion Diagnosis

D.1 Combustion duration in °CA

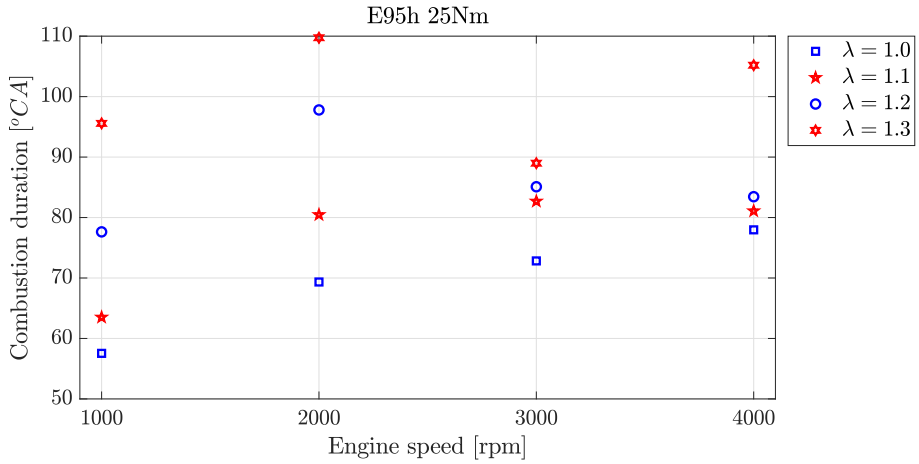

Figure D.1: Combustion duration in °CA for 25 Nm of load in the Lean Mixture test.

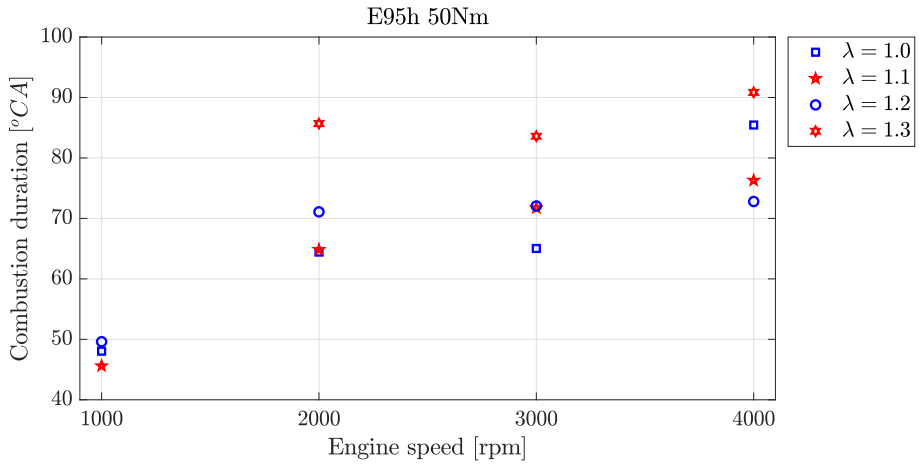

Figure D.2: Combustion duration in °CA for 50 Nm of load in the Lean Mixture test.

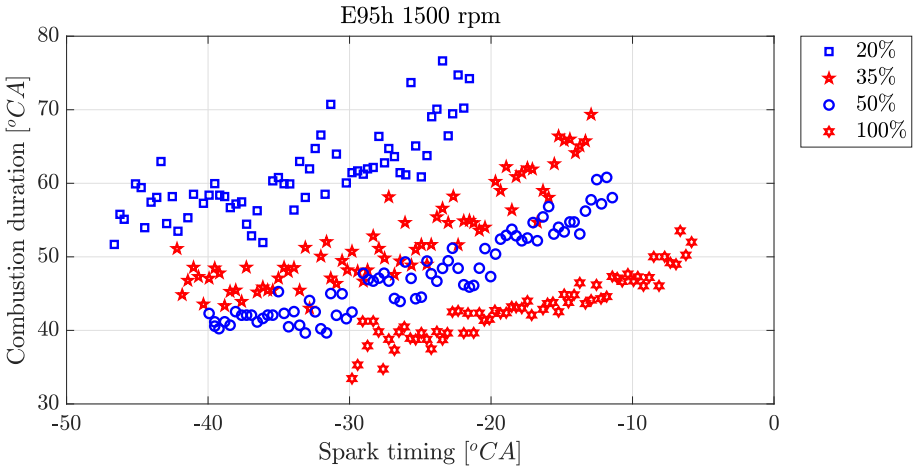

Figure D.3: Combustion duration in °CA for 1500 rpm of engine speed in the Spark advance sweep test.

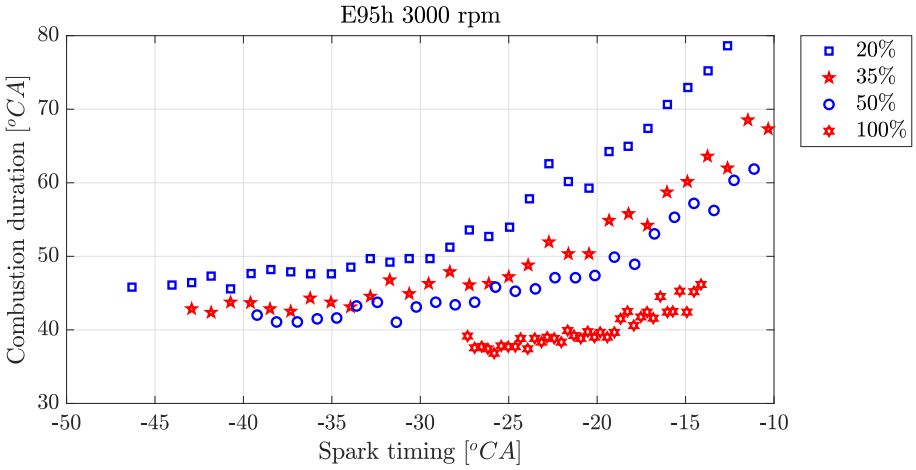

Figure D.4: Combustion duration in °CA for 3000 rpm of engine speed in the Spark advance sweep test.

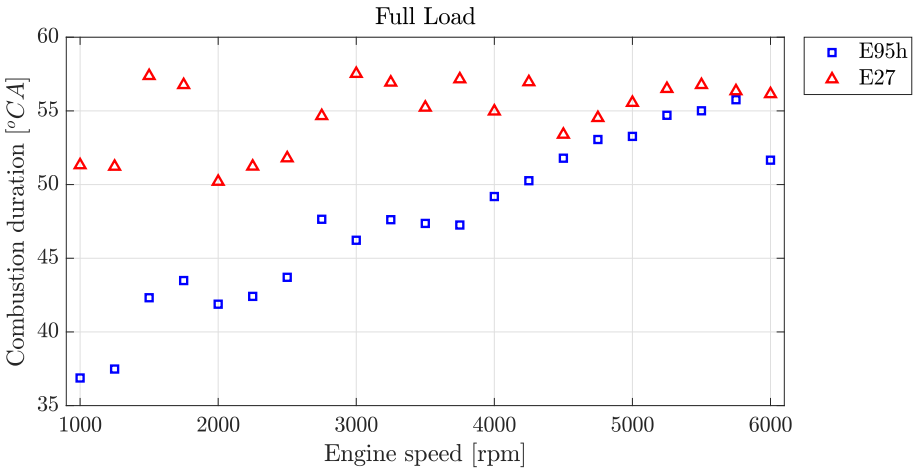

Figure D.5: Combustion duration in °CA in the Full load test.

D.2 Ignition delay in °CA

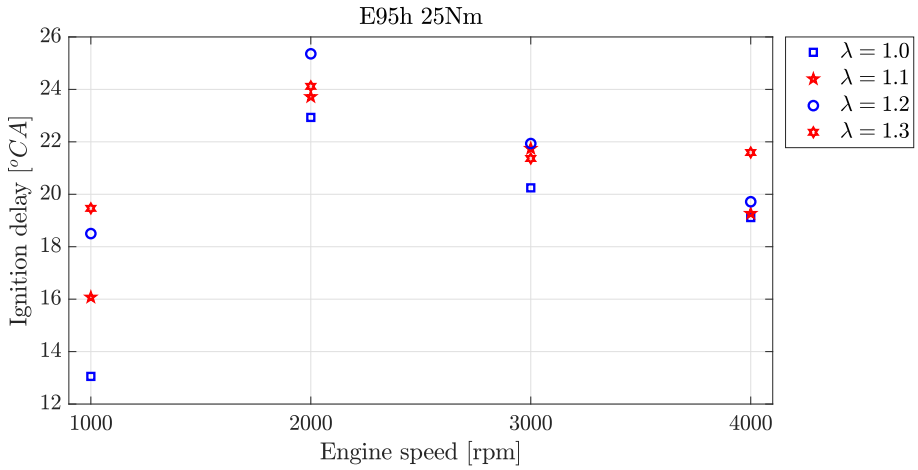

Figure D.6: Ignition delay in °CA for 25 Nm of load in the Lean Mixture test.

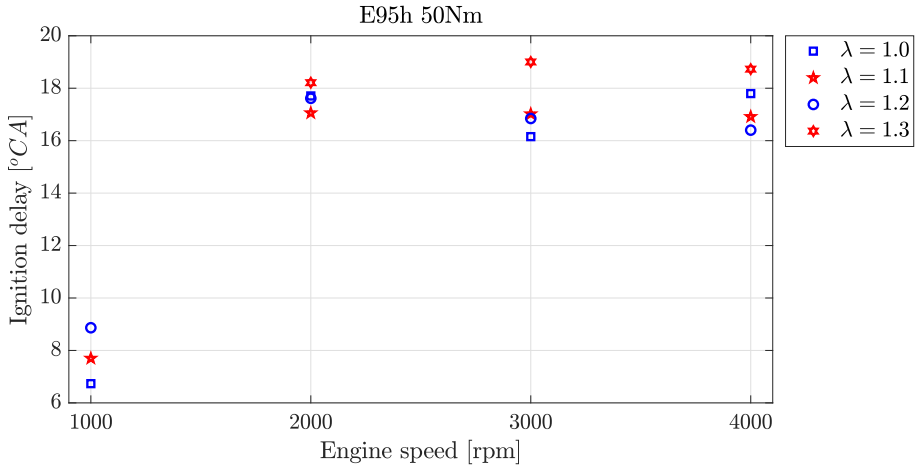

Figure D.7: Ignition delay in °CA for 50 Nm of load in the Lean Mixture test.

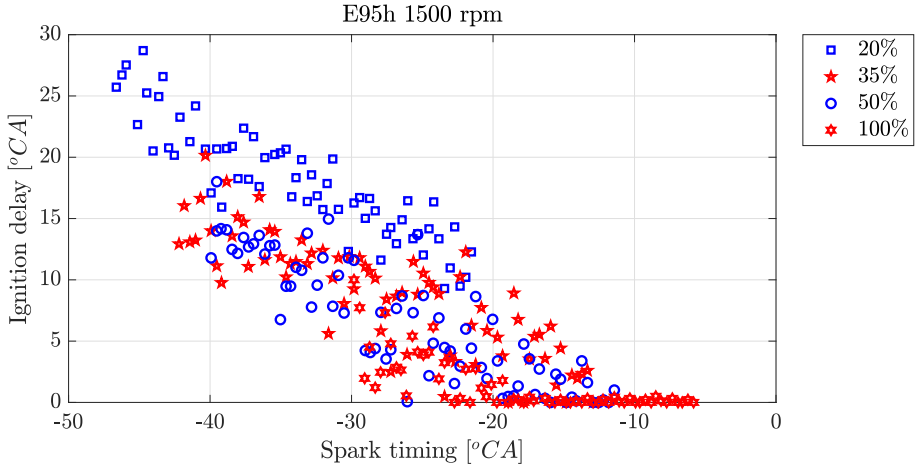

Figure D.8: Ignition delay in °CA for 1500 rpm of engine speed in the Spark advance sweep test.

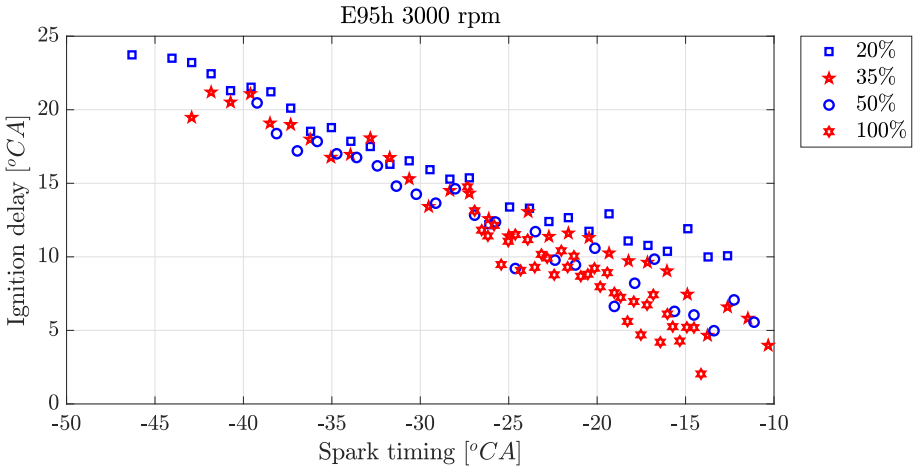

Figure D.9: Ignition delay in °CA for 3000 rpm of engine speed in the Spark advance sweep test.

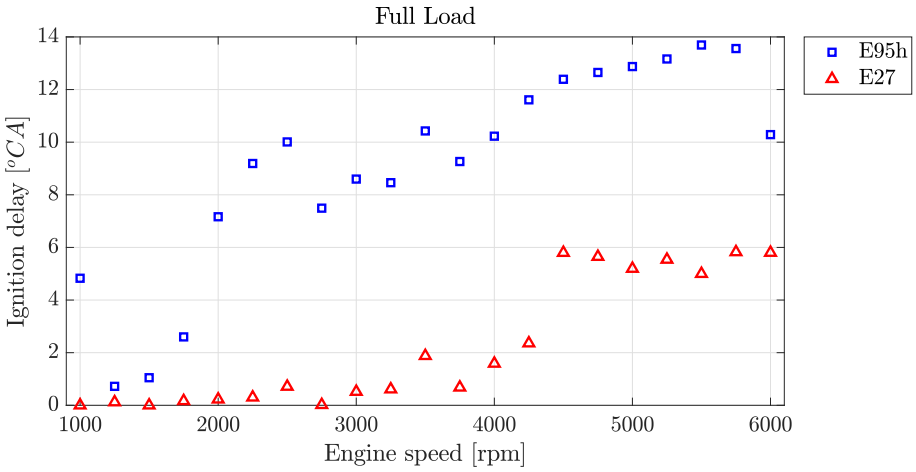

Figure D.10: Ignition delay in °CA in the Full load test.

D.3 Form factor for Lean mixture test

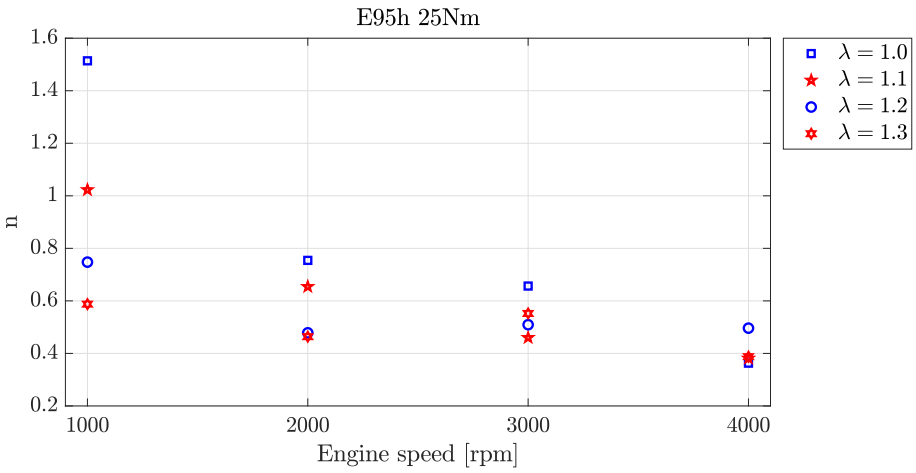

Figure D.11: Form factor for 25 Nm of load in the Lean Mixture test.

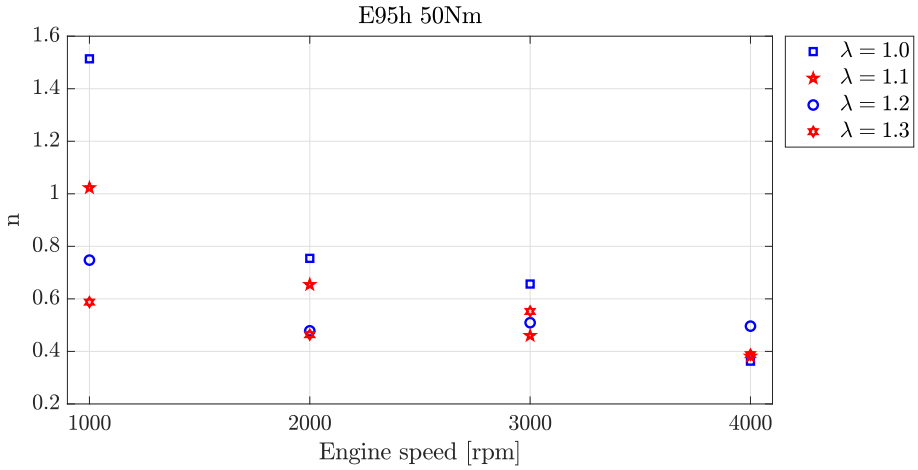

Figure D.12: Form factor for 50 Nm of load in the Lean Mixture test.

D.4 Spark advance sweep for all conditions of load

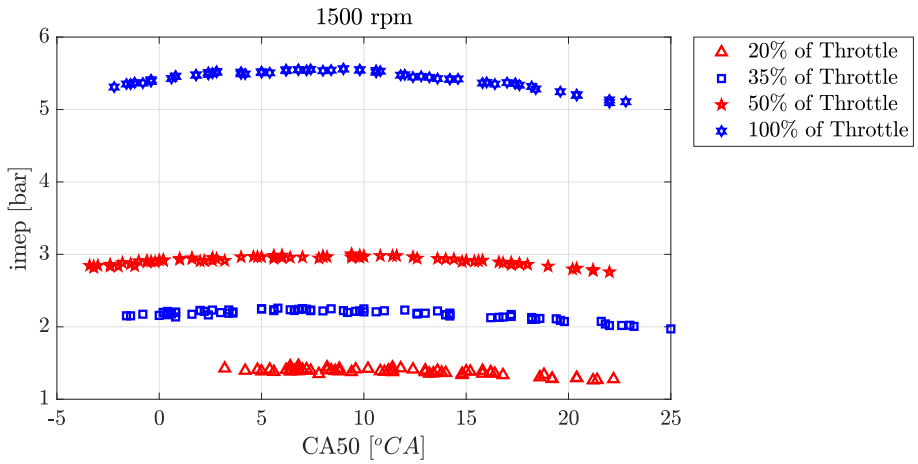

Figure D.13: Relation between CA50 and imep for all condition of load at 1500 rpm of engine speed.

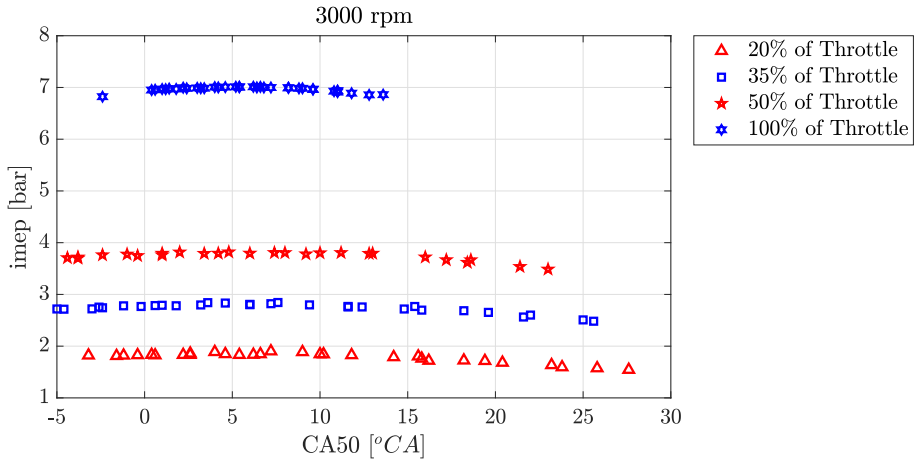

Figure D.14: Relation between CA50 and imep for all condition of load at 3000 rpm of engine speed.

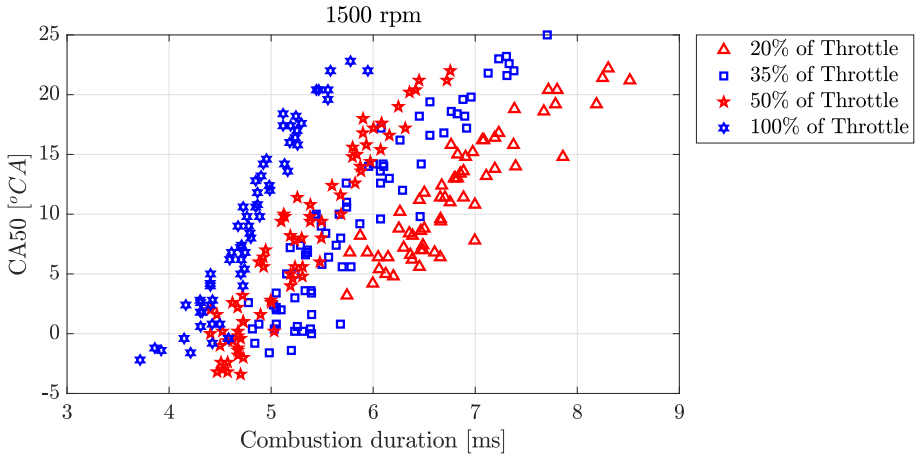

Figure D.15: Relation between Combustion duration and CA50 for all condition of load at 1500 rpm of engine speed.

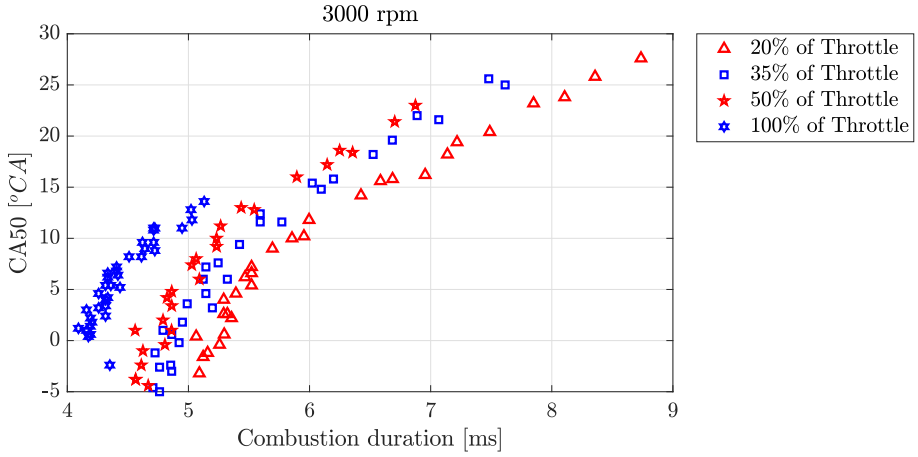

Figure D.16: Relation between Combustion duration and CA50 for all condition of load at 3000 rpm of engine speed.

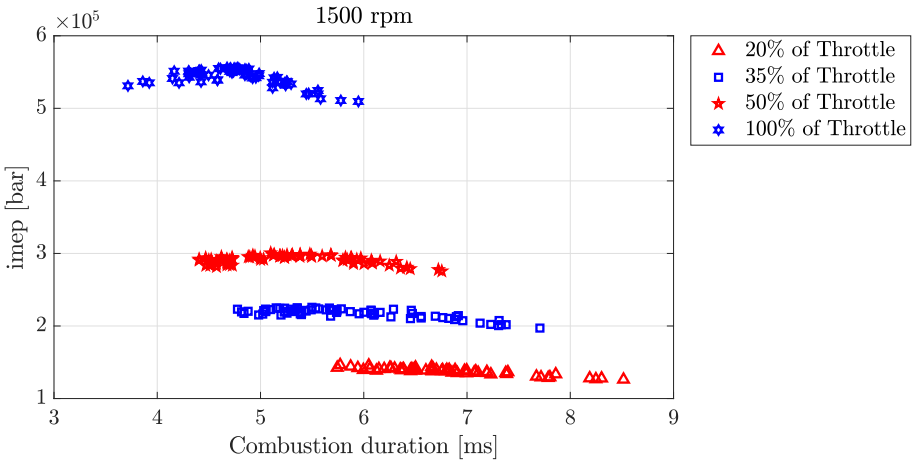

Figure D.17: Relation between Combustion duration and imep for all condition of load at 1500 rpm of engine speed.

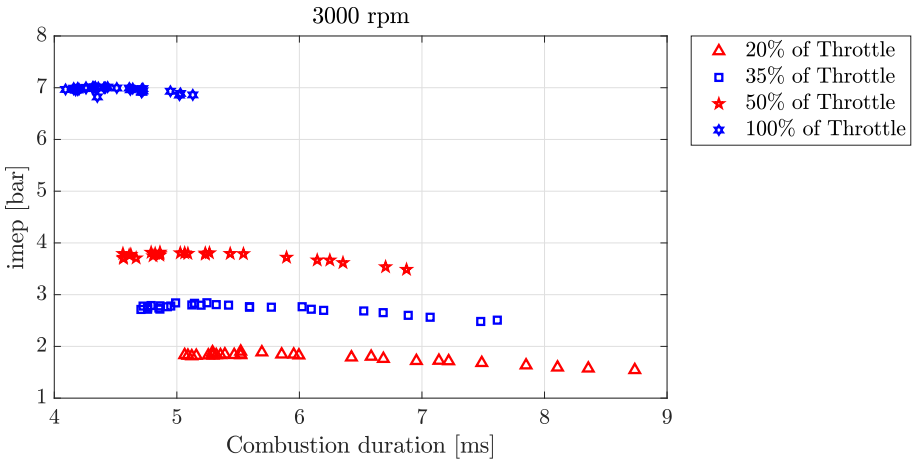

Figure D.18: Relation between Combustion duration and imep for all condition of load at 3000 rpm of engine speed.

D.5 Form factor for Spark advance sweep test

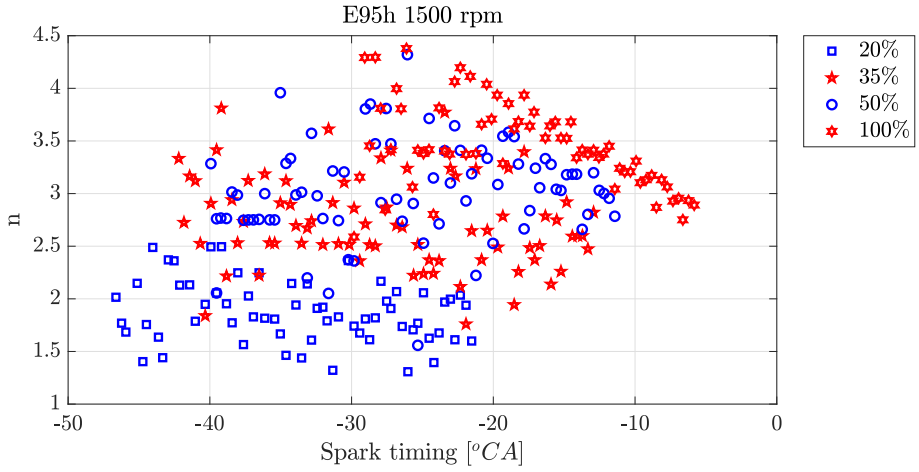

Figure D.19: Form factor for 1500 rpm of engine speed in the Spark advance sweep test.

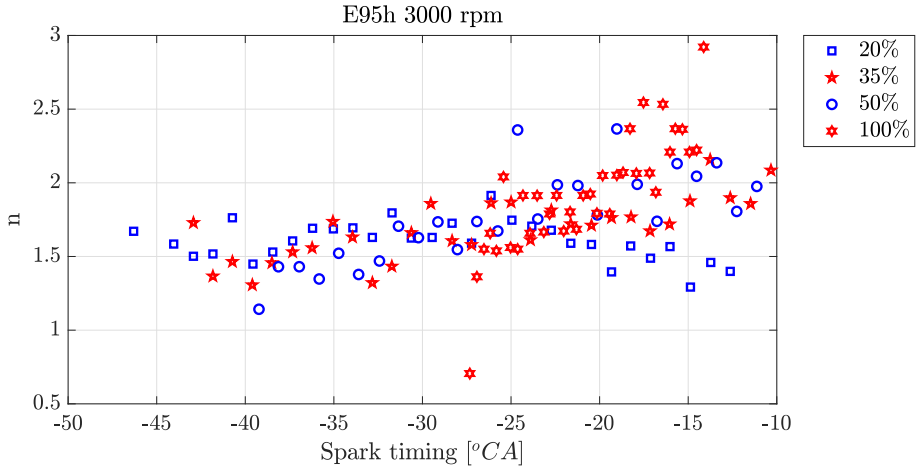

Figure D.20: Form factor for 3000 rpm of engine speed in the Spark advance sweep test.

D.6 Lean mixture for gasohol

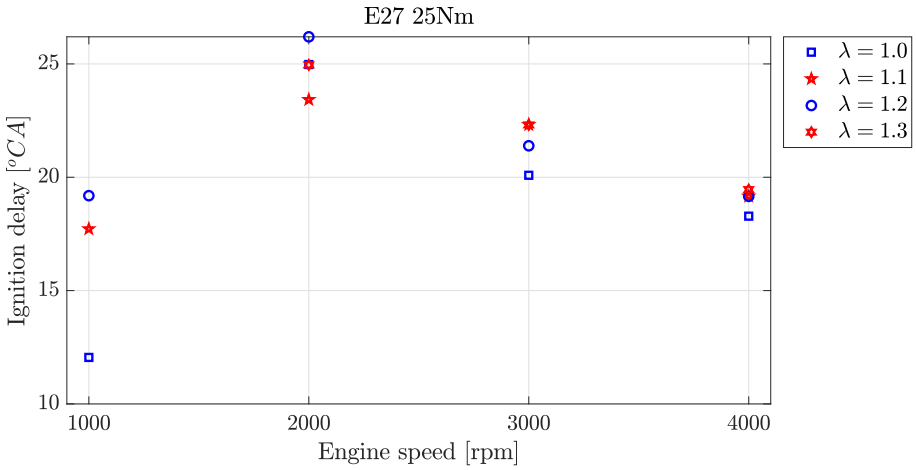

Figure D.21: Ignition delay in °CA for 25 Nm of load in the Lean Mixture test with gasohol.

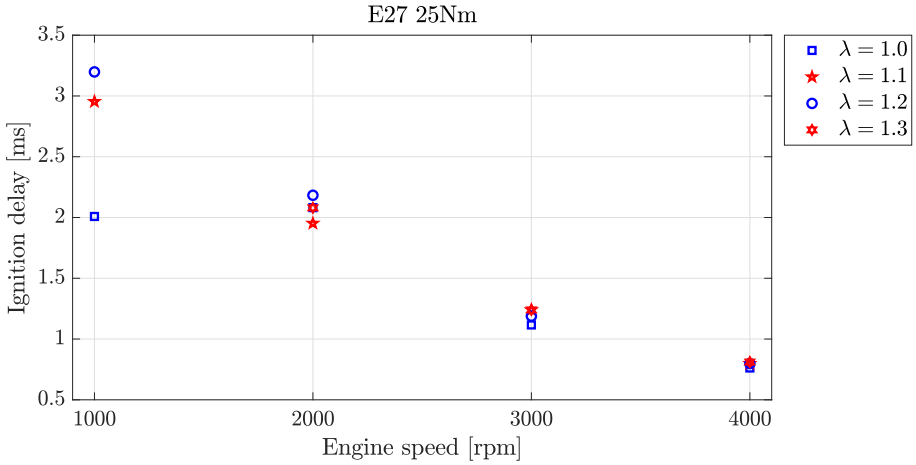

Figure D.22: Ignition delay in ms for 25 Nm of load in the Lean Mixture test with gasohol.

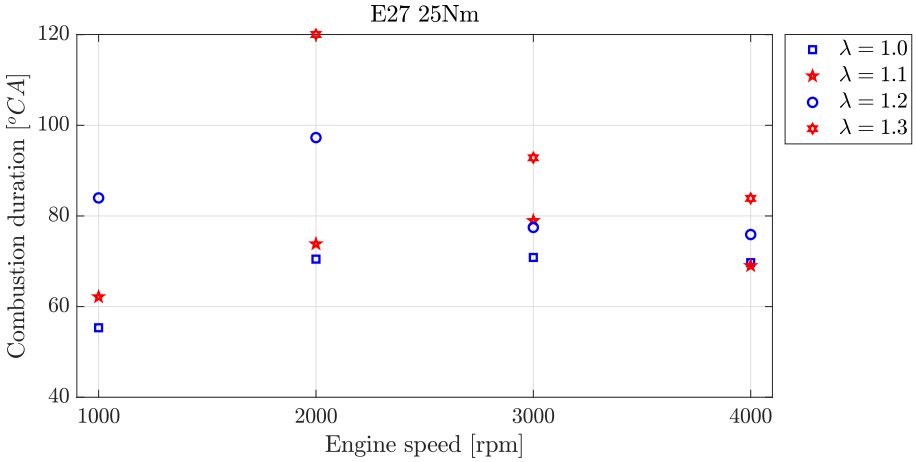

Figure D.23: Combustion duration in °CA for 25 Nm of load in the Lean Mixture test with gasohol.

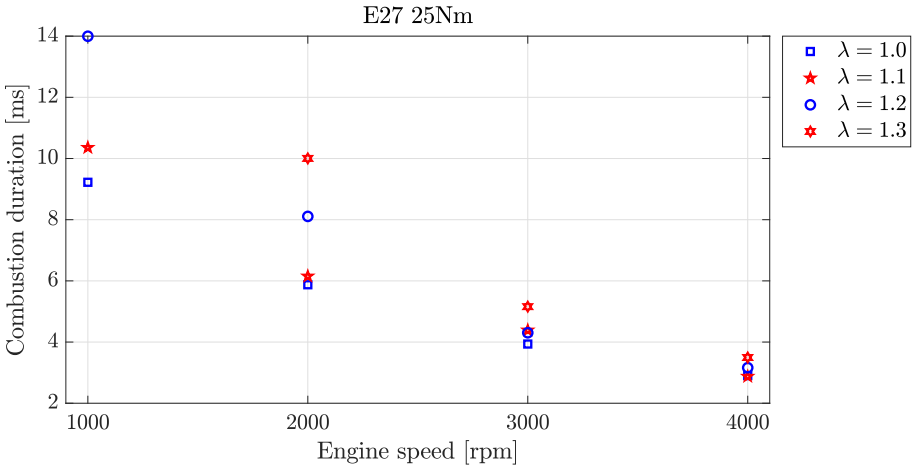

Figure D.24: Combustion duration in ms for 25 Nm of load in the Lean Mixture test with gasohol.

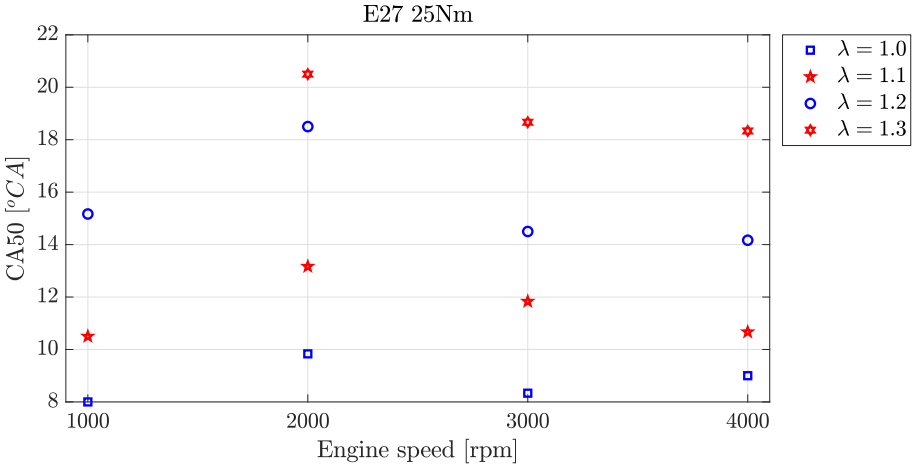

Figure D.25: CA50 for 25 Nm of load in the Lean Mixture test with gasohol.

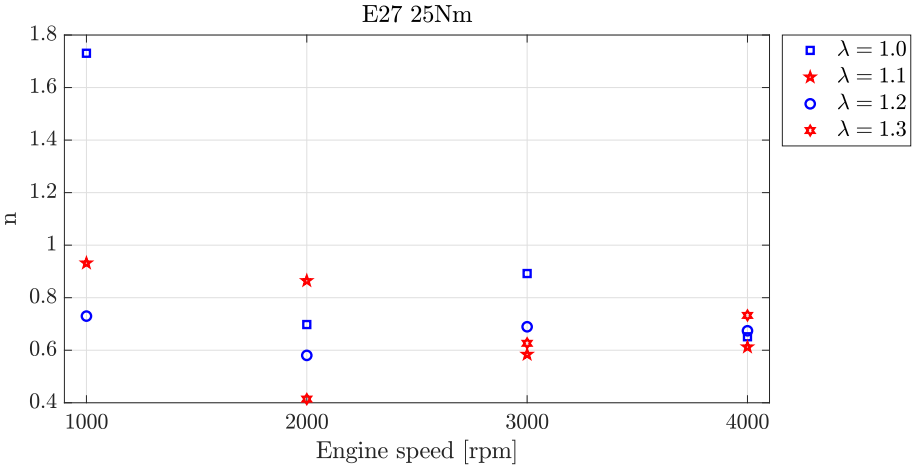

Figure D.26: Form factor for 25 Nm of load in the Lean Mixture test with gasohol.

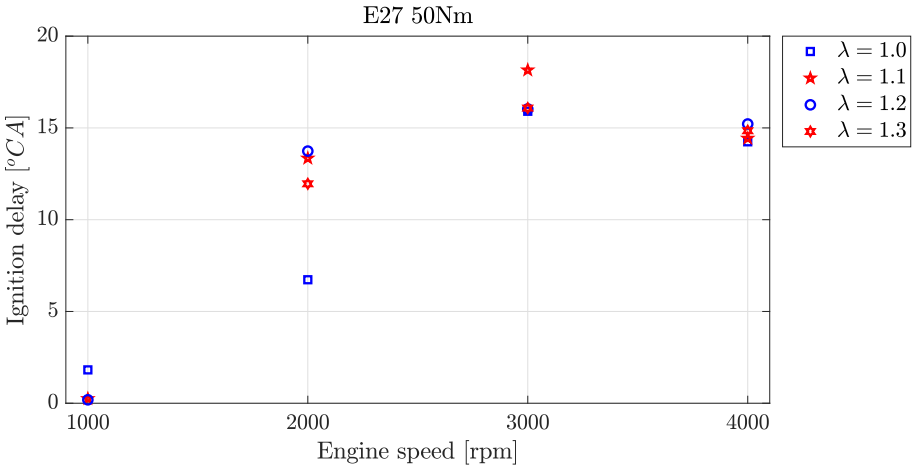

Figure D.27: Ignition delay in °CA for 50 Nm of load in the Lean Mixture test with gasohol.

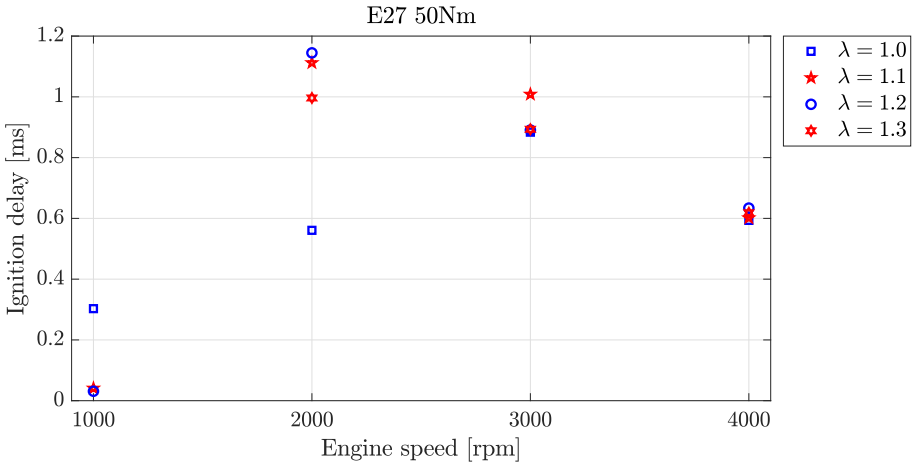

Figure D.28: Ignition delay in ms for 50 Nm of load in the Lean Mixture test with gasohol.

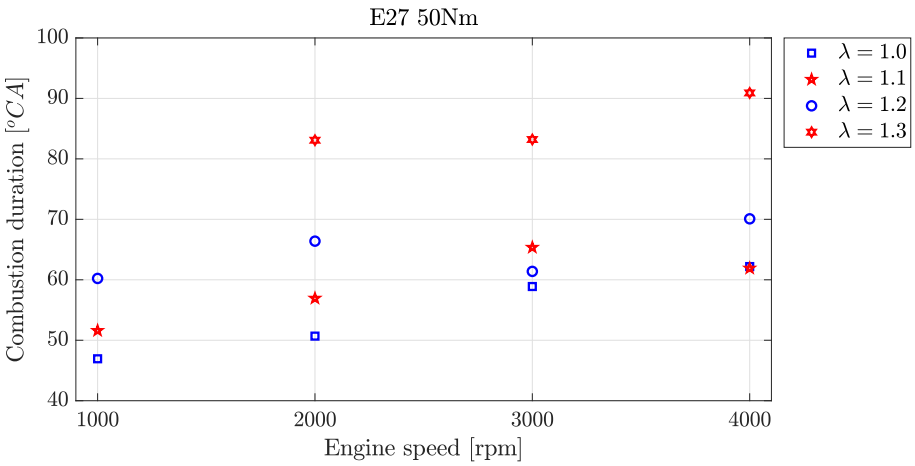

Figure D.29: Combustion duration in °CA for 50 Nm of load in the Lean Mixture test with gasohol.

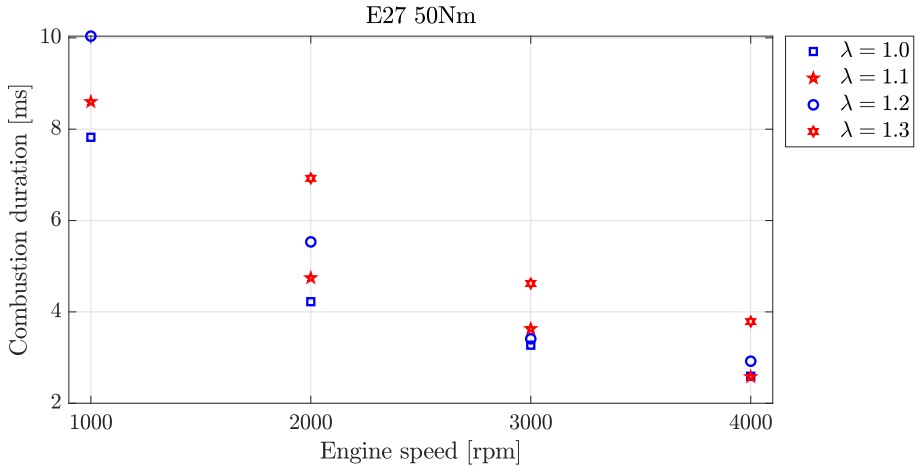

Figure D.30: Combustion duration in ms for 50 Nm of load in the Lean Mixture test with gasohol.

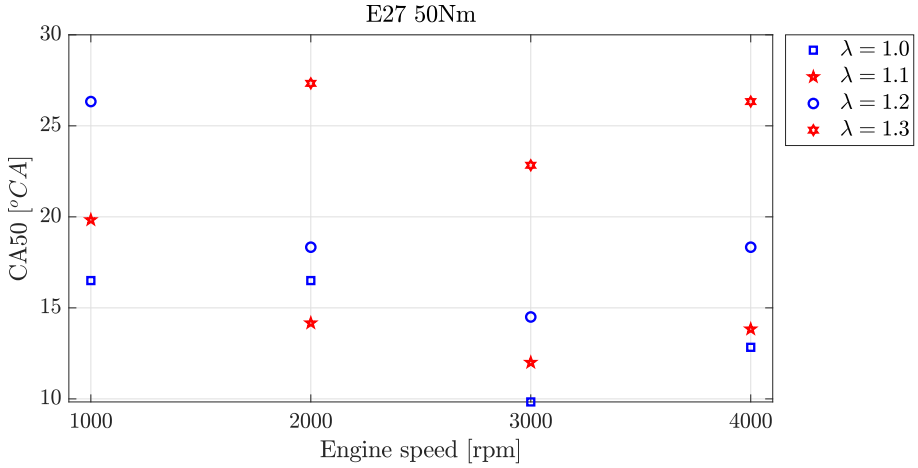

Figure D.31: CA50 for 50 Nm of load in the Lean Mixture test with gasohol.

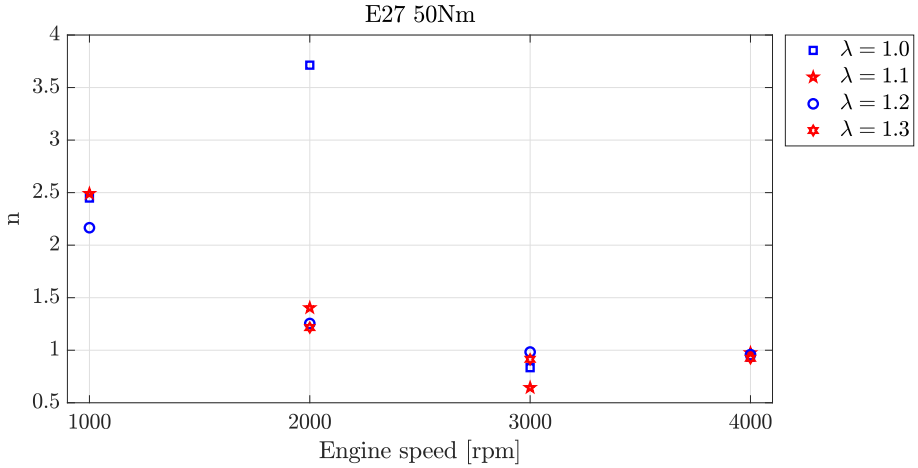

Figure D.32: Form factor for 50 Nm of load in the Lean Mixture test with gasohol.